Multiparametric analysis of embryonic, glial and endothelial cells cultured in microfluidic systems in standard or perturbed states

Vanessa Mancini

Submitted in accordance with requirements for the degree of Electronic and Electrical Engineering.

The University of Leeds
School of Electronic and Electrical Engineering

< October 2020>

The candidate confirms that the work submitted is her own and that appropriate credit has been given where reference has been made to the work of others.

Acknowledgments

First of all, I would like to thank my mum Carla and my dad Vittorio for all the support and affection they gave me. Thank you for always believing in me and helping me achieving my goals. Without you I wouldn't be where I am. I would like to thank my boyfriend Nicola, for always being at my side, supporting me and helping me during those intense years. Thank you for all your wise input, for always making me laugh and for the countless hikes and walks into the woods you had to do to make me happy. I would also like to thank my grandma Laura for her love and support, for the effort she put into learning how to use technology to stay in touch and also for trying so hard to understand the subject of my PhD. Finally, I would like to thank my best friend Sara, for always being at my side even though the distance, and my buddy Simone, for all the coffees, beers, chats and laughs we shared during those years. Thanks also to all my lovely friends in Leeds. You guys were all part of my success and made my life happier!

I want to thank my supervisor Virginia Pensabene for being a great mentor and for guiding me through my PhD. You were always there for me, for professional and personal matters, and all the input you gave me helped me to become a better scientist. You have been a great example and I learnt a lot from you. I want to thank my other supervisors, Sikha Saha, for the amount of shared knowledge on cerebrovascular medicine and for the support and great help you gave me during my PhD, and Prof Pietro Valdastri, for supporting me and for being an inspiring example. A special thank you to Prof Helen Picton, for your guidance, all the precious input and shared knowledge on reproductive biology. It has been an amazing experience to work in your group. Thanks to my colleague, Paul, for all the help, patience and shared knowledge. It was great to work with you and to share moments at conferences! A big thank to my friend and colleague Francesco, for the help in the lab and in the designing of the microfluidic device. It was great to have you around and to share not only moments at work, but also meals, coffees and drinks. I want to thank also everyone from the Bioelectronics group for the help and great time together.

Last but not least, I want to thank our collaborators at the Center for Innovative Technology (CIT) at Vanderbilt University, Stacy, Alexandra and Simona for the knowledge on metabolomics, for running the mass spectrometry analysis and for helping me with data analysis.

Abstract

Microfluidic devices have been applied to perform the functions required in assisted reproduction, including culture and mechanical manipulation of embryos and oocytes. However, this technology is not yet established in the field, being the impact of the microfluidic culture on the health and developmental competence of *in vitro*-derived embryos still uncertain.

In this project, a novel user-friendly microfluidic platform for the culture of murine zygotes was developed to produce viable and competent blastocysts, and to investigate potential effects of microfluidics and material toxicity on embryo development and metabolic activity. Culture medium analysis by untargeted metabolomics provided, for the first time, enhanced understanding of embryo metabolic activity and identification of metabolite changes throughout embryo development in the device, compared to traditional microdrops. Culture was also improved by using mouse uterine epithelial cells-conditioned media (CM), which significantly ($p < 0.05$) enhanced blastocyst development (blastocysts rates in CM were 71.8 ± 4.3%, *vs.* control 54.6 ± 6.6%) and had a significant impact on embryo metabolic activity and gene expression.

Microfluidic techniques have also been applied to recreate *in vitro* models of the blood brain barrier (BBB), allowing for co-culture of several BBB cell types. However, those models often require the use of complex liquid handling systems and suboptimal flow rates. In this work, a simple microfluidic model was developed to study BBB endothelial cells and to provide optimal shear stress without the need of complex instrumentation. It was shown that endothelial cells cultured in 200 µm-wide microchannels using a flow rate of 5 µl/min were able to align and elongate in the direction of flow.

The work described in this thesis demonstrates that microfluidic devices offer an attractive solution for *in vitro* toxicity studies and can be successfully coupled with analytical techniques for morphokinetic, genetic and metabolomic studies.

Table of Contents

List of Figures

List of Tables

List of Abbreviations

AA	Amino acid
ACN	Acetonitrile
AD	Alzheimer’s disease
ANOVA	Analysis of variance
ART	Assisted reproductive technology
Aβ	Amyloid β
BBB	Blood brain barrier
BL	Basal lamina
BMEC	Brain microvascular endothelial cells
BWS	Beckwith-Wiedemann syndrome
CAD	Computer-aided design
CD31	Cluster of differentiation 31
CE	Capillary electrophoresis
CIT	Centre for Innovative Technology
CM	Conditioned media
CNS	Central nervous system
COC	Cyclic olefin copolymer
CV	Coefficient of variance
DAPI	4′,6-diamidino-2-phenylindole
DMEM	Dulbecco's modified eagle medium
DMSO	Dimethyl sulfoxide
DNA	Deoxyribonucleic acid
DNMT	DNA methyltransferases
dNTP	Deoxynucleoside triphosphate
DTT	Dithiothreitol
EBM	Endothelial basal medium
EC	Endothelial cells
ECBM	Epithelial cell basal medium
ECM	Extracellular matrix
EGF	Epidermal growth factor
ELISA	Enzyme-linked immunosorbent assay

ESI	Electrospray ionization
FBS	Foetal bovine serum
FC	Fold change
FCS	Fetal calf serum
FMS	Full mass spectrometry
GA	Genetically altered
GC	Gas chromatography
GOI	Gene of interest
HBMEC	Human primary brain microvascular endothelial cells
HBVP	Human brain vascular pericytes
HEPA	High-efficiency particulate air
HMDB	Human metabolome database
HPLC	High-performance liquid chromatography
HRP	Horseradish peroxidase
HUVEC	Human umbilical vein endothelial cells
IAR	Inverse aspect ratio
ICM	Inner cell mass
ICSI	Intracytoplasmic sperm injection
ID	Internal diameter
IPA	Isopropyl alcohol
IVF	In vitro fertilization
JAM	Junctional adhesion molecules
KEGG	Kyoto Encyclopedia of Genes and Genomes
KSOM	Potassium-supplemented simplex optimization media
LC	Liquid chromatography
LD-PCR	Long Distance-polymerase chain reaction
LOC	‘Lab-on-a-chip’
MEA	Mouse embryo assay
MEMS	Micro-electromechanical systems
MLA	Maskless aligner
MS	Mass spectrometry
MS/MS	Tandem mass spectrometry
MTT	3-(4,5-dimethylthiazol-2-yl)-2,5-diphenyl tetrazolium bromide

MUEC	Mouse uterine epithelial cells
NGS	Next generation sequencing
NIR	Near infrared
NIST	National Institute of Standards and Technology
NMR	Nuclear magnetic resonance
NSET	Nonsurgical embryo transfer
NVU	Neurovascular unit
OoC	Organ-on-a-chip
PBS	Phosphate-buffered saline
PC	Polycarbonate
PCA	Principle components analysis
PCR	Polymerase chain reaction
PDMS	Polydimethylsiloxane
PES	Polyethersulfone
PFA	Paraformaldehyde
PLA	Polylactic acid
PMMA	Poly (methyl methacrylate)
PS	Polystyrene
QC	Quality control
qPCR	Real-time PCR
QTOF	Quadrupole time-of-flight
RNA	Ribonucleic acid
ROI	Region of interest
RPLC	Reversed-phase liquid chromatography
RT	Reverse transcriptase
RT-PCR	Reverse-transcription PCR
SART	Society for Assisted Reproductive Technology
SEM	Standard error of the mean
SET	Surgical embryo transfer
TE	Trophectoderm
TEER	Transendothelial electrical resistance
TNF	Tumor necrosis factor
TOF	Time-of-flight

UDP	Deoxyuridine-5'-diphosphate
UHPLC	ultra-high-performance liquid chromatography
UV	Ultraviolet
WOW	Well-of-the-well
WSS	Wall shear stress
ZO-1	Zonula Occludens -1
µTAS	Micro total analysis systems

Chapter 1
Introduction to research project

This chapter describes the specific research aims and objectives of this project and outline the results reported in each of the following Chapters of work.

1.1 Research aim

The main aim of this research project was to design, fabricate and optimise microfluidic devices that support *in vitro* development of embryonic, glial and endothelial cells in standard or perturbed states and allow for multiparametric "omic" analyses to evaluate the effect of the microenvironment on the metabolomic, genetic and secretome profiles.

1.2 Research objectives

1.2.1 Objective 1

To develop a user-friendly microfluidic device for culturing mouse embryos from one-cell to blastocyst stage and for complete assessment of their developmental competence.

The objective of this research project was to demonstrate that this novel microfluidic device:

i) Is "user-friendly", thus simple to use either for trained or untrained embryologists, to facilitate the adoption in clinical assisted reproductive technology (ART) laboratory. This implies that the system can be integrated with conventional laboratory equipment (*e.g.*, incubators and microscopes) and can be efficiently used without the need of extensive training for laboratory personnel.

ii) supports the embryo development.

iii) facilitates the direct assessment of embryo quality and the genetic expression profiling of single blastocysts by real-time PCR.

iv) allows to identify endogenous and exogenous factors, organic and inorganic compounds in small volume samples of medium by global untargeted mass spectrometry and to correlate these with normal or altered expression of genes associated with embryo development.

The design, development and use of the microfluidic device is described in Chapter 3. In Section 3.3.1 the design and optimization of the microfluidic device to reduce risk of damage for the embryos are presented. Section 0 describes the assessment of embryo developmental competence in terms of blastocyst rates and analysis of gene expression profile. Section 3.3.4 reports results obtained from global metabolomic analysis of spent embryo culture media samples.

1.2.2 Objective 2

To develop a user-friendly microfluidic device for culturing brain microvascular endothelial cells to study the endothelial barrier which characterize the blood-brain-barrier (BBB).

The second objective of this research project was to demonstrate that this microfluidic device:

i) is simple to use and does not require extensive trainings for lab personnel and the use of complex liquid handling systems
ii) supports the formation of an endothelial barrier that mimics the physiological properties of the BBB under optimal shear stress.
iii) can be used to study the effects of amyloid-β on viability of BBB cells (endothelial cells, astrocytes and pericytes) and cytokine production under static or dynamic culture conditions.
iv) can be integrated with on-line and off-line analysis (*e.g.*, immunocytochemistry, immunoassays, polymerase chain reaction) of small volume samples and cultured cells.

Chapter 4 describes the design, development and use of a microfluidic device for culturing brain microvascular endothelial cells and the optimization of the shear stress to induce cell alignment, polarization and tightening of the endothelium (Sections 4.3.2, 4.3.3). Sections 4.3.4.3 and 4.3.4.4 describe the assessment of amyloid-ß treatment effects on viability of BBB cells and cytokine production.

Chapter 2
Literature Review

2.1 Microfluidics and its biomedical applications

In the past decades, microfluidic technologies have been successfully applied to cellular studies, such as for the isolation, culture, and analysis of cells (1–3) and applied in a wide range of fields within the biological sciences, such as analytical chemistry (4), biochemistry (5), molecular biology (6), genomics (7), proteomics (8) and clinical diagnostics and therapeutics (9–11). Importantly, microfluidics has been widely applied to the culture of mammalian cells demonstrating the feasibility of creating *in vivo*-like microenvironments that present cells with physiologic cues in a controllable and reproducible manner that could not be achieved with conventional culture platforms (12–17). Microfluidic devices exploit the micro-scale physical properties of fluids, which are very different compared with flow in large channels, to achieve functionalities that are either difficult or impossible to obtain with macroscale systems (18). Microfluidics offers great advantages over conventional macroscale platforms, such as:

- Reduction of the fluid quantity needed for system operation. Consumption of reagents is normally 10^2 to 10^3 times less than conventional methods, leading to less waste, reduced costs and more efficient assays. Reduced reagent consumption is especially advantageous for biological applications that involve expensive reagents, such as antibodies or anti-cancer drugs, and limited available sample volumes (19,20).
- Microscale dimensions better match with the structures present *in vivo* (similar cell-to-medium volume ratio) and favour cell development (20,21).
- Liquid travelling in a microchannel at low flow rates presents laminar flow, a type of flow in which the fluid travels smoothly or in regular paths. Laminar flow allows to reduce sample dispersion and the precise control of fluid flow, in contrast to turbulent flow that occurs at high flow rates or large dimensions and commonly in low viscosity fluids. This enables to design and to optimize the physical characteristics of the microfluidic system to obtain the desired fluid dynamic properties. Also, laminar flow allows to provide automatic and

controlled perfusion of media, by supplying nutrients and draining waste products by cellular activities (22,23).

- Chemical gradients can be created to mimic the complex and dynamic 3D microenvironment within living tissues (24).
- Parallelization of microfluidic chips allows high throughput and multiple analysis at a time, reducing the costs and reagents per analysis while increasing the output results (25).
- Mechanical cues, which represent an important factor that can trigger cell differentiation *in vitro*, can be achieved by using complex microscale systems or can be induced by the flow (26,27). For example, mechanical forces such as shear stresses are fundamental for certain cells (*i.e.,* endothelial cells) to maintain their phenotype and to promote skeletal organization and tight junction formation (28).
- Interactions between cell populations can be precisely controlled through the use of channels, membranes and other features incorporated into these systems (29,30).

To increase the biological relevance of microfluidic cell culture models, the physical characteristics of microfluidic devices need to be accurately selected together with other specific requirements such as geometries, flow control and medium turnover. These are fundamentals elements for understanding how to control the microenvironment *in vitro* and how to tailor the physical forces (*i.e.,* shear stress) and diffusion phenomena that cells experience *in vitro* (31).

The next section provides some background on the basic characteristics of microscale fluid flow.

2.1.1 Theoretical background in microfluidics

Microfluidics is defined as the science and technology of systems that process or manipulate small (10^{-9} to 10^{-18} litres) amounts of fluids, using channels with dimensions of tens to hundreds of micrometers (32). In order to understand and work with microfluidics, it is necessary to understand the physical phenomenon behind the behaviour of fluids within microfluidic systems. As mentioned before, the fluid that travel in a microchannel can be considered as laminar flow – *i.e.,* a fluid that flows in parallel layers with no disruption between the layers. Under laminar flow the viscous forces dominate over the inertial effects

of the fluid within the channels. Laminar flow conditions are determined by the Reynolds number (*Re*) (Equation 1.1). *Re* is a dimensionless parameter which quantifies the ratio of inertial to viscous forces and is used to determine the transition from laminar to turbulent regimes (33,34).

$$Re = \frac{\rho u l}{\eta} \tag{1.1}$$

Where *u* is the characteristic velocity of the fluid, η is the viscosity of the fluid, and *l* is the length scale or channel diameter and ρ the density of the fluid. The flow goes from turbulent to laminar at Re < 2300 and is always fully laminar at Re < 15 (35). Because $Re \propto l$, the reduced dimension of microfluidic channels results in very low Re characteristic of laminar flow ($Re \ll 1$), where the viscous forces are dominant. The Reynold's number is derived from the Navier-Stokes equation that describes the flow of incompressible fluids. In the case of Newtonian fluids (*i.e.,* fluids that have constant viscosity independent of stress) the Navier Stokes equation is (Equation 1.2) (33,36):

$$\rho\left[\frac{\partial u}{\partial t} + (u \cdot \nabla)u\right] = -\nabla P + \eta \nabla^2 u \tag{1.2}$$

Where *P* is the applied pressure and *u* the velocity vector. The left-hand side of the equation represents the inertial forces, and the right-hand side represents the forces on the fluid caused by applied pressure and viscosity. For laminar flow with "no-slip" boundary conditions (u=0 at the walls) it is possible to effectively ignore the left-hand side of the Navier Stokes equation. From this simplified version of the Navier Stokes equation is possible to derive the Poiseuille equation, a physical law that gives the pressure drop in an incompressible and Newtonian fluid in laminar flow flowing through a pipe of constant (circular) cross section that is substantially longer than its diameter. The assumptions made to derive this equation are that the fluid flow is steady (*i.e.,* a flow in which the velocity at a specific location does not vary with time), pressure-driven and fully developed (*i.e.,* a flow that has the same velocity profile at any cross-section within the fluidic channel), with "no-slip" conditions (37). The velocity profile for Poiseuille flow is parabolic with the velocity at the centre being the highest and the velocity at the boundary being zero. The volumetric flow rate *Q* that is obtained for this flow from a pressure drop ΔP in the channel depends on the fluidic resistance R_f of the channel:

$$Q = \frac{\Delta P}{R_f} \tag{1.3}$$

For a rectangular parallelepiped channel with *length* ≫ *width* ≫ *height* (typical of long, high-aspect ratio channels), R_f could be approximated by (36):

$$R_f = \frac{12\mu L}{wh^3} \tag{1.4}$$

Where μ is the fluid viscosity, L the channel length, w the channel width and h the channel height. The cross-section dimensions clearly affect the flow through a channel. Channels with large diameter are characterized by small hydraulic resistance and require reduced pressures to fill the channel with fluid. In contrast, a small channel diameter leads to a large hydraulic resistance, such that small channels require extremely high-pressure levels to push liquid through.

Another phenomenon to take into consideration is the fluid shear. If there are "no-slip" conditions, a shear stress is exerted at the wall of the channel. This can be modelled by the shear stress at the wall of parallel plates under parabolic flow (38):

$$\tau_{wall} = \frac{6\mu Q}{h^2 w} \tag{1.5}$$

Where μ is the fluid viscosity, Q the flow rate, h the channel height and w the channel width.

These theoretical assumptions and considerations are fundamental for the design of microfluidic devices for cell biology applications, like the ones developed in this project. A proper selection of dimensions and shear stress guarantees the liquid to pass with the use of reasonable liquid pressure levels and at the same time function efficiently (39), and allows adherent cells to proliferate and maintain their phenotypic characteristics (12,40,41).

2.1.2 Fabrication of microfluidic devices: Soft lithography and Polydimethylsiloxane (PDMS)

Microfluidics stems from the microelectronics industry and the technologies used for micro-electromechanical systems (MEMS) (42). Since the introduction of miniaturized systems, glass and silicon have been the favoured materials used for the fabrication of microfluidic systems. However, in the second half of the 90's decade the interest has shifted towards polymers which are suitable materials for

large scale production, cost-effective and simplified fabrication processes (43,44).

Most of the microfluidic fabrication techniques rely on polymer molding technologies, including replica molding (45), hot embossing (46,47) and injection molding (48). Replica molding (*e.g.*, soft lithography) is widely used for the creation of prototypes and for small scale production (*i.e.,* in a laboratory environment) because of its versatility and simplicity in fabrication. In contrast, for commercial purposes injection molding and hot embossing are popular due to their capacity for large scale high-throughput and cost-efficient production (49). There are many other established and emerging manufacturing techniques for polymer microfluidic devices (50,51). Among them, 3D printing have been increasingly employed in this field as it allows to reduces the time needed to transition from a concept to a device and is thus suitable for rapid prototyping of microfluidic chips in industrial or research applications (52,53). Despite its promising manufacturing potential, 3D printing is still under development and, in its current state, does not guarantee the same resolution as replica molding technique, which continues to provide a valuable platform for prototyping and for research applications in academia (49).

One of the most commonly used microfabrication approach for constructing microfluidic devices is soft lithography, a technique that was popularized by Whitesides and his group at Harvard in the late 1990s (54). This technique involves the fabrication of a master (or mold) substrate and uses an elastomer to generate a negative replicate of the master (Figure 2.1). The procedure generally starts with the design of the pattern using computer-aided design (CAD) software (*e.g.*, Autodesk AutoCAD). The pattern created with the CAD software program is used to fabricate a photomask through high-resolution printing. Chrome photomasks are typically used when high resolutions down to 1 μm are required. On the other hand, printed transparency masks are significantly less expensive and faster than ordering and fabricating a chrome mask, but are typically suitable for the fabrication of feature sizes up to 8 μm (55,56). The photomask is then used to transfer the design pattern on substrates spun with a positive or negative photoresist by means of ultraviolet (UV) light using photolithographic techniques (44). SU-8 is a common negative photoresist used in mold fabrication due to its high resolution, mold durability, and capacity for high aspect ratios (57). The

fabricated substrates serve as templates for molding a prepolymer: a liquid precursor is casted against the master, cured and finally peeled off from the master, generating a negative replica of the master (55). The photolithographic step is carried out in cleanroom facilities with the equipment required for fabrication of microelectronic devices, which is relatively costly to build and maintain in a research laboratory environment. However, at prototyping phase, once the master is available, most of the fabrication tasks can be conducted outside the cleanroom in a chemical laboratory equipped with high-efficiency particulate air (HEPA) filters to avoid contamination of the polymers and the assembled devices. This step considerably reduces the costs involved in the prototyping of test patterns and devices for research applications.

Soft lithographic technique offers experimental simplicity and flexibility as it enables to generate various type of nanoscale and microscale structures on planar, curved and flexible substrates, in opposition to photolithography, a high cost micro-fabrication technology based mainly on glass and silicon substrates (43,55,58). Since the mold is typically rigid, the use of elastomeric materials facilitate the separation of the replica from the mold. Additionally, multiple molded polymeric layers can be easily bonded to each other or to glass or plastic substrates by conformal contact generating complex three-dimensional structures.

Currently, polydimethylsiloxane (PDMS) is vastly used for the fabrication of the replica in soft lithography, although other elastomeric polymers can also be used (59–61). PDMS is liquid at room temperature and can be readily converted into solid elastomers by cross-linking with the addition of a curing agent containing a catalyst (54). PDMS has many advantages compared to other materials, including chemical and thermal stability, low cost (compared to glass and silicon), versatile surface chemistry, mechanical flexibility and durability. In addition, since PDMS has a low free surface energy (2.16×10^{-2} J m^{-2}) (62,63), the pre-polymer mixture can be cast on the master forming an accurate negative replica of the relief. PDMS has also the highly desirable properties for cell culturing and manipulation: it is biocompatible, optically transparent, impermeable to water, permeable to gas (19,64). Since PDMS is strongly hydrophobic, oxygen plasma treatment can be used to create hydrophilic PDMS surface through oxidation (65). This process is commonly used because it can be

completed in only in less than a minute and does not require the use of chemicals; however, the hydrophilic surface is unstable and PDMS completely recover its hydrophobic nature in two weeks (66–68).

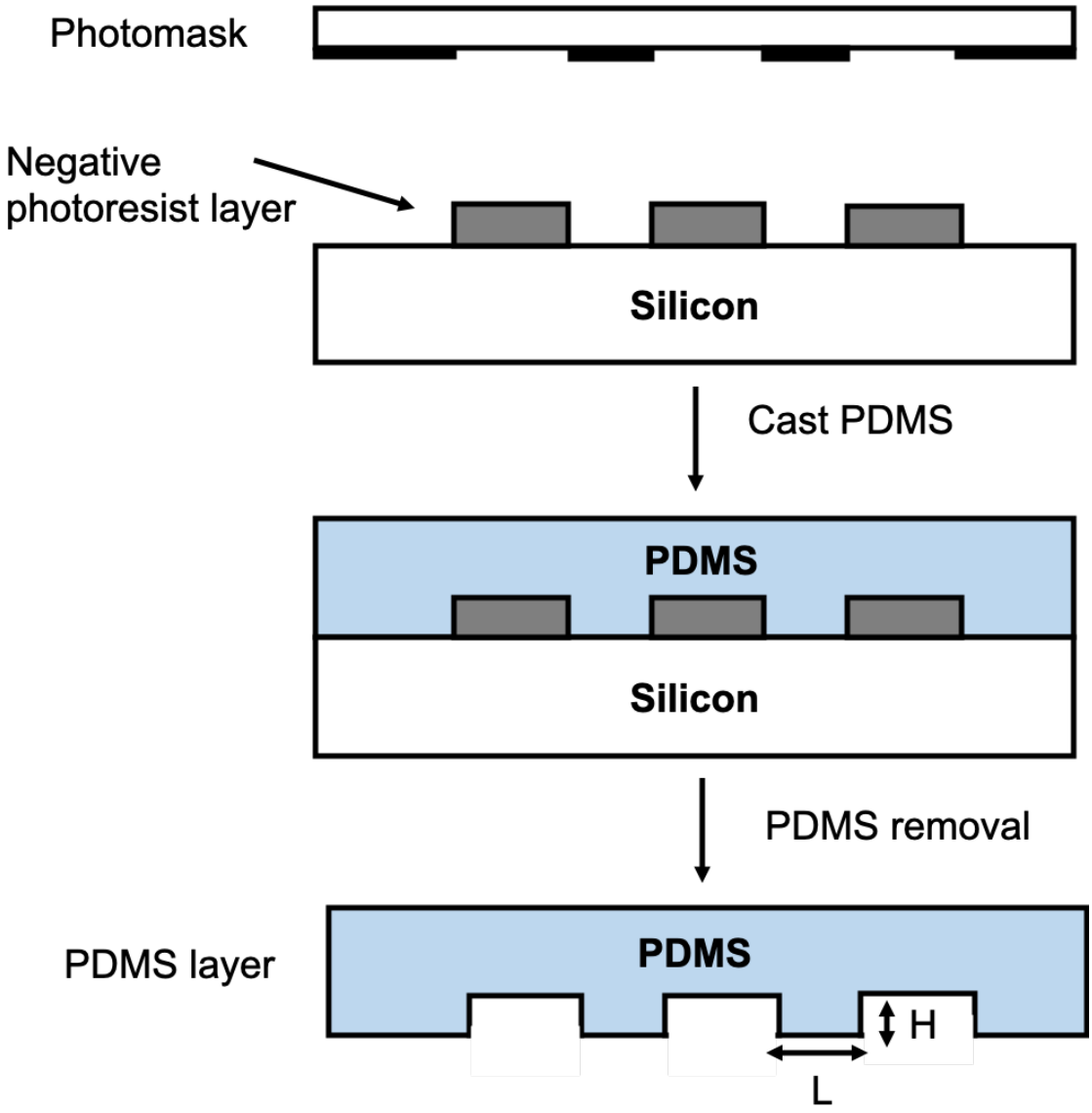

Figure 2.1 Schematic illustration of soft lithographic process.

PDMS presents some challenges and limitations. For instance, the softness of the material limits the *aspect ratio* (the ratio of the height, to the width, L, of the desired feature) of microstructures that can be realized. To prevent channel collapse after fabrication, a general rule is to use aspect ratios above 1:10 and below 4:1 (69). For this reason, microstructure dimensions need to be selected accordingly to avoid deformation or distortion of the PDMS features which generate defects in the pattern (70). From a material prospective, there are some issues related to the chemical nature of PDMS which have an impact on cell

culture microfluidic systems applications. For instance, incomplete curing of PDMS leaves uncross-linked oligomers within the material that can leach out and contaminate the medium used for cell culture (71). Furthermore, due to its hydrophobic nature, PDMS tends to absorb from the liquid organic solvents and small hydrophobic molecules (*e.g.*, steroids) (71,72). This phenomenon could lead to a significant alteration of cellular microenvironment and hormone-dependent cell behavior, negatively interfering with cellular signalling pathways. Thus, cell culture experiments that aim at the study of effects that biomolecules or hormones have on cell behavior need to be accurately optimized to avoid material artefacts introduced by the PDMS microfluidic platform. Those issues (absorption and release of small molecules) can be mitigated by adopting specific coatings or processing methods of PDMS devices. PDMS leaching can be reduced by surface treatments, which provide a reliable barrier against oligomer escape, by crosslinking reactions forced toward completion during curing, or by removing un-crosslinked oligomers from the polarized network after curing, for example through Soxhlet extraction with ethanol (72). However, none of these methods can completely overcome the leaching of uncrosslinked PDMS oligomers. Absorption of small molecules can be leveraged for instance by coating with parylene (73) or with paraffin wax (74), but PDMS is still not suitable for studies focused on cell signalling (75). Another issue of PDMS is the gas permeability which leads to evaporation of water. The media in microfluidic chambers can evaporate if the environment is not properly humidified, increasing the concentration of soluble factors in the media which may ruin stable gradients established in the microfluidic chamber (76) and is critical for cells (*e.g.*, mammalian gametes and embryos) particularly sensitive to changes in osmolarity (77–79). For the same reason, PDMS devices are also prone to the formation of air bubbles which can block the entire microchannel or impede fluid to flow through the system causing clogging of medium and then alteration of the cell culture environment (80).

From a processing perspective, PDMS fabrication methods based on soft lithography involves several sequential steps which cannot always be scaled up and can limit mass production and automation (81). Therefore the translation of microfluidic designs from the research to the mass market production and successful commercialization is possible, but not frequent (52,82). Additionally,

shipping, packaging, and storage of surface-treated PDMS microdevices remain challenging given that hydrophobic recovery tends to revert surface treatments to their original state (75).

Other materials with different chemical properties and requiring different manufacturing techniques are used in microfluidics, including cyclic olefin copolymer (COC) (83), poly (methyl methacrylate) (PMMA) (84), polycarbonate (PC) (85), polylactic acid (PLA) (86) and polystyrene (PS) (87), the most common plastic used for traditional macroscopic cultureware (Petri dish, flasks and multi-well plates). While their advantages for microfluidic device fabrication and their comparative properties have been discussed in literature (94), the evaluation of their performance is outside the goal of this project.

2.1.3 Microfluidics for cell culture applications: "Organ-on-a-chip"

Microfluidic devices represent promising platforms for high-throughput screening, drug discovery and toxicity testing as they can facilitate the study of cell behavior *in vitro* and the manipulation of cell growth environments. (88,89) They are also known as 'lab-on-a-chip' (LOC) or "micro total analysis systems" (μTAS) and typically combine microchannels with pumps, valves, filters and sensors for flow control and integrated measurements (90).

Over the past two decades, the emerging growth of microfluidic-based technologies have led the development of innovative 3D cell-culture models, called "organs-on-a-chip" (OoC) (1). OoC recapitulate *in vitro* characteristic functions of tissues or organs by enabling the co-culture of multiple cell types under physiologically relevant conditions, such as mechanical, chemical stimuli or perfusion (91). One of the main applications of these systems is in the pharmaceutical industry. The drug discovery and drug testing process recorded several failures in the last years, due to the extensive use of animal experiments, which may produce results inconsistent with human trials. Recent reports show that, of thousands of compounds entering the first stages of screening, only 11% is makes it through development and gets approved by regulatory authorities (92). This process thus has elevated costs and can last 15 years (93). These issues lead to a decrease of number of new drugs approved per year (94). OoC aim to provide key advantages in this process:

- Use of human cells: this favours the replacement of animal models with 3D *in vitro* systems and the reduction of number of animals sacrificed for collection of tissues and cells. More importantly, it allows to use patient derived cells, thus enabling testing the effect of new compounds on healthy patients or on patients presenting specific pathologies.
- Reduction of volumes: in an OoC the microfluidic compartments have micrometric dimensions and volumes smaller than the industry standard 96 well plate (>75 μL). By controlling the specific gradients and static or dynamic perfusion into the system, the availability of nutrients and stimuli to the cell population is augmented and the dilution of molecules and nutrient is limited thus providing a much more consistent and physiologically relevant environment for pharmacokinetic-pharmacodynamic studies (95).
- High-throughput screening: OoC can be designed to be compatible with real time microscopic imaging techniques and with a multiple array of analytical techniques that allow to extract information from living cells and effluents, such as lysis of cells and subsequent RNA analysis, quantitative polymerase chain reaction (PCR), enzyme-linked immunosorbent assay (ELISA), or mass spectrometry, which are compatible with small sample volumes (96–98). By automated perfusion and sampling, parallelized and standardized tests can significantly increase the throughput of cell-based assays and screening methods (95).
- Long term culture: the underlined concept of OoC is the possibility to mimic the development and to keep an organ alive for at least 4 weeks; this allows the organ to fully form and to perform testing, or to reproduce *in vitro* complex physiological processes, such as the female menstrual cycle (99).

In order to be relevant for pharmacological and toxicological studies, OoCs need to recreate the main physiological units involved in absorption (i.e. from the delivery site into the bloodstream), distribution (from the bloodstream to the tissues) metabolism and eventually excretion of drugs or chemicals and their metabolites from the body.

One of the most popular examples of organ-on-a-chip models is the lung-on-chip developed by the Ingber group at the Wyss Institute a decade ago. This biomimetic microsystem recreates physiological breathing movements by

mechanical actuation of cultures of lung and vascular cells on-chip via cyclic mechanical strain. This model is capable of reproducing the critical functional alveolar-capillary interface of the human lung, by culturing in close proximity epithelial cells and endothelial cells (Figure 2.2) (14,100). The availability of a fully functional endothelial barrier enabled to visualize and quantify the effects of drugs and exogenous factors (such as bacteria or cigarette smoke) on the lung vascular permeability.

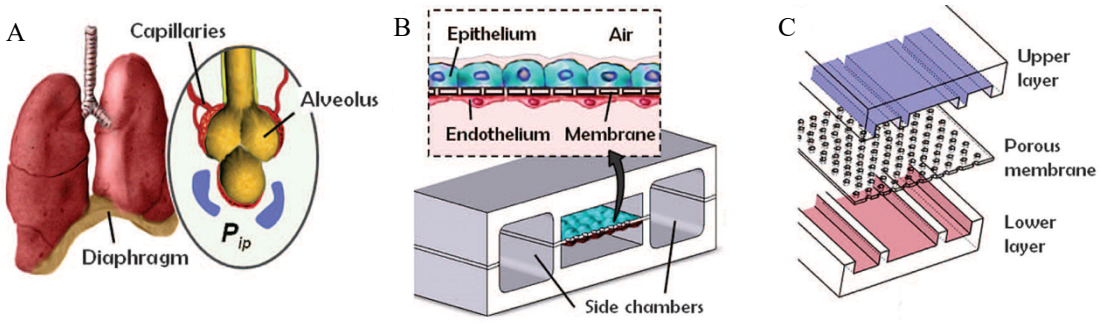

Figure 2.2 Biologically inspired design of a human breathing lung-on-a-chip microdevice.

(A) Schematic image of the lung and alveoli. (B) The microfabricated device uses compartmentalized PDMS microchannels to form an alveolar-capillary barrier on a thin, porous, flexible PDMS membrane coated with ECM. The device recreates the physiological breathing movements by applying vacuum to the side chambers and causing mechanical stretching of the PDMS membrane forming the alveolar-capillary barrier. (C) Three PDMS layers are aligned and irreversibly bonded to form two sets of three parallel microchannels separated by a 10-μm-thick PDMS membrane containing an array of through-holes with an effective diameter of 10 μm (100).

Microfabricated OoC systems of liver (101), kidney (102,103), heart (104), blood-brain-barrier (105) and reproductive organs (106–109) have contributed to the testing and understanding of specific cellular mechanisms involved in the permeability and extravasation of molecules through the endothelial barrier. These phenomena rely on cell-cell junction complexes and cell attachments to the ECM and basement membrane which maintain the integrity of the barrier through intricate mechanisms. To recreate an endothelium *in vitro* is fundamental a clear understanding of the tissue physiology and of its characteristic chemical and physical cues. For example, the vascular endothelium is exposed to hemodynamic shear stress (external physical forces) and complex biochemical cues that regulate barrier functions (76).

Thus, as discussed in Chapter 4, in order to model *in vitro* the endothelium, it is essential to control and to be able to assess the establishment of a physical

barrier, the contribution of other cell types involved in the barrier formation and stability, and the response of the endothelial cells to physical and biochemical stimuli.

2.2 Current techniques *for in vitro* culture of mouse embryos

2.2.1 Introduction to *in vitro* embryo culture: the mouse model

Assisted Reproductive Technology (ART) includes medical procedures and therapies that are primarily used to treat human infertility. *In vitro* fertilization (IVF), the most common type of ART, consists in removing eggs from the woman's ovaries and their fertilization with sperm in a laboratory. The fertilized egg (zygote) is cultured *in vitro* and then implanted back in the woman's uterus (Figure 2.3) (110,111). In the biomedical research community ART and IVF are widely used procedures to generate genetically altered (GA) mice, to breed large animals as models to study human disorders and diseases and also to preserve endangered animal species. The implantation rate following IVF (*i.e.,* the percentage of embryos which successfully implant compared to the number of transferred embryos) varies with species, but it is in general suboptimal (112). For instance, Table 2.1 reports data relative to the average human IVF success rates in the United States per age group according to a summary compiled by the Society for Assisted Reproductive Technology (SART) in 2017.

Implantation failures, for both humans and GA mice, are often ascribed to the difficulties to control and preserve the microenvironment surrounding the embryo during its preimplantation development *in vitro* (113).

Table 2.1 Implantation rate (%) per age groups according to the 2017 SART report.

Age	<35	35-37	38-40	41-42	>42
Implantation rate (%)	47.1	40.6	30.9	18.8	7.8

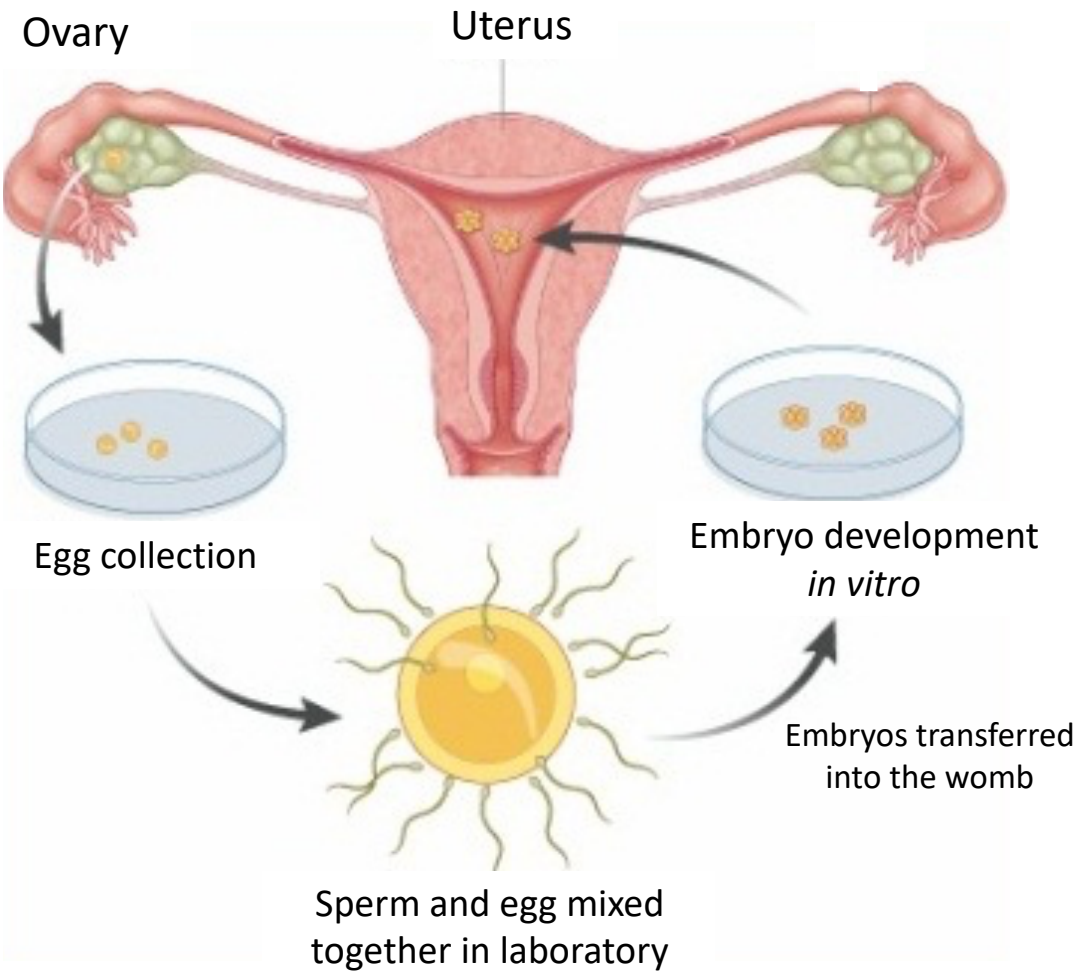

Figure 2.3 Schematic of IVF procedure.

Advances in the ART field have always been supported by the use of animal models. Mice are the main rodent species that has contributed in such development. Their main advantages are the small size, the high fecundity (1 to 10 pups per litter), short generation interval (19 to 21 days of gestation) and the ease with which they can be bred (114). These characteristics make them an attractive relatively inexpensive choice in comparison with other species, accompanied by less logistical and ethical issues. Furthermore, their extended use in ART is due to the similarities between their genome and the human one: 99% of mouse genes have equivalent homologous genes in humans, genes are located in the same order and gene knockouts have similar phenotypes (115). Concerning the embryo development, the morphological changes at different stages in mouse and human (Figure 2.4) are similar, but the timing varies (Table 2.2) (116). The changes in substrate utilization during the preimplantation

development are also similar between both species: the main energy source in early embryos during the first half of preimplantation is pyruvate, whereas after compaction (8 cell stage), the utilization of exogenous glucose increases in both species (117).

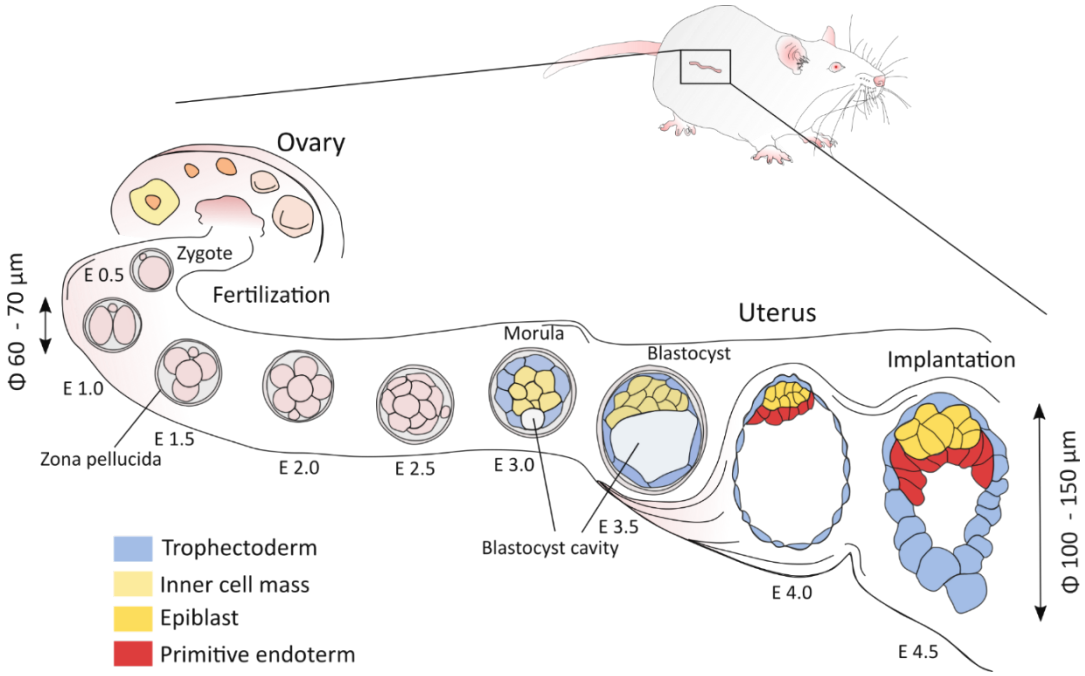

Figure 2.4 Mouse preimplantation embryo development.

After fertilization in the oviduct, the embryo undergoes a series of symmetrical divisions according to the day of development, in mouse represented as E. Eventually, a cell mass structure, known as morula, is formed. Following morula compaction, the embryo cavity, blastocoel, starts to form and two different cell populations arise: the inner cell mas (ICM) and trophectoderm (TE). Around the fifth day of development, the embryo hatches and differentiates to produce further cell types (epiblast, primitive endoderm). The embryo is then able to start the implantation process in the uterine wall.

Table 2.2 Comparison of human and mouse embryo developmental timing.

Time to reach (h)	Mouse	Human
2-cell stage	12	30
Blastocyst	70	120
Hatching	100	150

Compared to other animal models, the mouse has also the great advantage of being suitable for genetic modification, enabling the creation of inbred strains. Mice from an inbred strain are nearly identical genetically and can be used in the same experiment reducing phenotypic variability (118). GA mice are widely used to study the role of gene function and gene regulation in human development and health for decades: almost 50% of the total amount of animals used for scientific research are genetically modified animals, the majority of which are mice (119).

Specifically in medical research and pharmaceutical industry, GA mouse models provide new insight in pharmacology and toxicology thanks to the recent introduction of sequencing, genetic engineering technologies (such as CRISPR/Cas9, Microinjection, Embryonic Stem Cell Injection or Nuclear Transfer) and to the use of “humanised” mice, in which a particular mouse gene is replaced by its human counterpart known to be associated with a specific human disease. To date, mouse models have been applied for the study of important diseases, such as ageing (120,121) breast cancer (122,123), metabolic disorders, diabetes, obesity as well as for drug discovery applications (124,125).

2.2.2 Traditional culture systems

The traditional most widely used method for *in vitro* embryo culture in IVF relies on 5-100 µL drops (i.e. “microdrops”) of specialised embryo culture medium (126) in Petri dishes covered with mineral oil to prevent evaporation (Figure 2.5). Embryos are kept into these medium drops and allowed to develop undisturbed in the incubator. When ready to be transferred, developed blastocysts are aspirated and injected in the oviduct or in the uterus by traditional Surgical Embryo Transfer (SET) techniques or by Non-Surgical Embryo Transfer (NSET) (127). Manipulation of the embryos is performed by manual pipetting and is a labour intensive, time consuming, and not repeatable procedure, also complicated by the presence of oil. The success of these techniques depends on many factors including embryo quality, embryonic stage, number of embryos transferred, experience of the person performing the transfer, age and weight of the recipient and hormonal status of the recipient (128). Thus, the ability to control the culture environment to the exquisite sensitivity of the embryo, producing developmentally competent embryos at the required developmental stage, is of fundamental importance for the success of embryo transfer procedures. Higher success rates have been reported when culturing embryos to the morula or blastocyst stage before transfer, a procedure requiring up to 4 days of *in vitro* culture in the mouse and up to 8 days in other mammalian species (129–131).

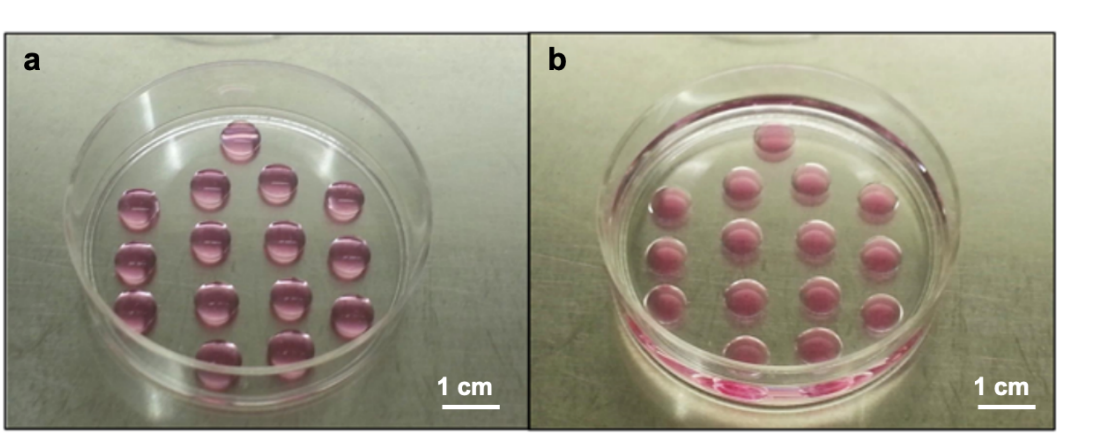

Figure 2.5 Traditional microdrop culture.

50 µL medium drops on the bottom of a 60 mm Petri dish before (a) and after (b) covering with mineral oil.

Numerous studies revealed that increased embryo density and decreased spacing of embryos can also improve embryo development, likely due to the increased production and exposure to autocrine/paracrine factors which are otherwise diluted in larger microdrops (132–136). This has prompted a revision of the culture protocols and the adoption, over the past two decades, of smaller volumes of media (137–139). For instance, Ali *et al.* used extremely low volumes (1.5 to 2 µL) of medium in human ART, so called ultramicrodrop culture (139). Although this technique enabled very high clinical pregnancy rates of 50% and live birth delivery rates of 35%, the handling of such small volumes requires careful attention and is technically challenging. A variation of the traditional microdrop has been developed by Vajta *et al.* in 2000 and entails small microwells engraved at the bottom of a 35 mm plastic dish. This platform, called well-of-the-well (WOW), allows for positioning of individual or small groups of embryos in each single well, covered afterwards by a common drop of medium. As further development of this approach, a WOW Petri dish containing 25 wells was integrated with time-lapse microscope to continuously track developing embryos showing promising results in terms of oxygen consumption and pregnancy rates following transfer (140). This approach combines the benefits of group culture with the possibility to keep in place and monitor individual embryos. Although the WOW approach significantly reduces the surface area and volume of media around the embryos, the volumes required for the culture are still not comparable to those found *in vivo* (110), the time required for individual embryo loading is long and the effective clinical advantage has not been proved yet.

2.2.3 Methods to assess embryo quality and developmental competence

Predictive indexes of embryo quality and methods to assess the competence of the embryo at preimplantation stage are, for ethical reason, mainly based on non-invasive assessment of embryo morphology (142,143). Typical parameters that are taken into account are cell number, degree of fragmentation, pronuclear morphology, early cleavage to the 2-cell stage and the quality of the trophectoderm and the inner cell mass on successive days (144).

In addition to morphological characteristics, adjunctive technologies have been recently investigated for the biochemical assessment of embryo viability and developmental competence. These approaches include non-invasive metabolic studies, *i.e.,* measurement of the depletion and/or appearance of culture medium components such as glucose, lactate, pyruvate (145), measurement of the amino acid turnover (146) and assessment of oxygen consumption by the embryo (147,148).

With the recent advances in omics technologies, such as transcriptomics, proteomics, and metabolomics, novel non-invasive quantitative methods for embryo viability have been investigated. Proteomic technologies have allowed the profiling of mammalian embryonic proteome (the complete set of proteins produced by the embryo) and secretome (proteins that are produced by the embryo and secreted into the surrounding environment), enabling a direct non-invasive investigation of mammalian embryonic developmental process (149,150). Genomic and proteomic screening expands the current knowledge of early embryogenesis by allowing the identification of metabolic biomarkers as predictive indexes of embryo competence, (151). Importantly, developments in genomics technologies, including microarrays, real-time polymerase chain reaction (qPCR) and next generation sequencing (NGS), have allowed comprehensive chromosome screening and have led to the identification of thousands of genes that are expressed and have specific functions during mouse embryo preimplantation development (152–157).

Most recently, analytical examination of the embryonic metabolome has also been evaluated, particularly applying spectroscopic methods (158–163). The metabolome refers to the complete array of small compounds, such as metabolic

intermediates and signalling molecules that are found within a biological sample and reflect the functional phenotype. Metabolomics is the systemic and comprehensive analysis of this dynamic set of metabolites, and constitutes a proper means to study functional biological systems (164). This technique attempts to determine metabolites associated with physiologic and pathologic states and provides valuable information that are complimentary to those obtained from genomics and proteomics studies (165). The techniques predominantly used in metabolomics are nuclear magnetic resonance (NMR) spectroscopy and mass spectrometry (MS). For the detection of low abundance metabolites or complex mixture of compounds, MS-based metabolomics are commonly used due to their higher sensitivity (163). This instrumental setup also allows for multiple sample analysis in a rapid manner compared to NMR, where sample automation is less efficient than gas or liquid chromatography (GC and LC, respectively) . Raman and near-infrared (NIR) spectroscopy have also been successfully applied to analyse spent culture media and quantify biomarkers (166–169). Compared to MS, those methods have the benefits of lower instrumentation costs, rapid simultaneous analysis and do not require the sample preparation before analysis (170); however, they are not always suitable for target metabolite identification (171).

Thus, by coupling proteomics/metabolomics studies with time-lapse morphokinetics it is possible to facilitate the identification of the embryos that are most competent for development (172). In turn, this will allow the more accurate selection of the best embryo, improving ART outcome and reducing the change of multiple pregnancies (161).

In this work, among the techniques available to assess *in vitro* embryo development, the feasibility of integration of qPCR and MS analysis with the microfluidic culture platforms were assessed and used for a comprehensive evaluation of the genetic profile of individual mouse blastocysts and embryo metabolome. Moreover, this study showed for the first time a comparison of metabolic and genetic signatures between embryos developed in microfluidic devices or in traditional microdrops, providing important knowledge for future studies involving microfluidics and ART. The following sections briefly described the characteristics, principles and limits of those analytical methods.

2.2.4 Real-time PCR (qPCR)

Polymerase chain reaction (PCR) is one of the most powerful technologies in molecular biology. This relatively simple technique amplifies specific sequences within a DNA or complementary DNA (cDNA) template using sequence-specific oligonucleotides, heat-stable DNA polymerase, and thermal cycling. In traditional PCR, detection and quantification of the amplified sequence are performed at the end of the reaction after the last PCR cycle, and involve post-PCR analysis such as gel electrophoresis and image analysis. In real-time quantitative PCR (qPCR), PCR product is measured at each cycle. By monitoring reactions during the exponential amplification phase of the reaction, it is possible to determine the initial quantity of the target with great precision. PCR theoretically amplifies DNA exponentially, doubling the number of target molecules with each amplification cycle. In qPCR, the amount of DNA is detected and quantitated after each cycle via fluorescently labelled oligonucleotide probes or fluorescent DNA-binding that yield increasing fluorescent signal in direct proportion to the number of PCR product molecules generated. Data collected in the exponential phase of the reaction yield quantitative information on the starting quantity of the amplification target. If a particular sequence (DNA or RNA) is abundant in the sample, amplification is observed in earlier cycles; if the sequence is scarce, amplification is observed in later cycles. The change in fluorescence over the course of the reaction is measured by an instrument that combines thermal cycling with fluorescent dye scanning capability. By plotting fluorescence against the cycle number, the real-time PCR instrument generates an amplification plot that represents the accumulation of product over the duration of the entire PCR (173). This technique is limited to the analysis of DNA samples. To apply PCR to the study of RNA, the RNA sample must first be converted to cDNA to provide the necessary DNA template for the heat-stable polymerase. This process is called reverse-transcription PCR (RT-PCR) and uses a reverse transcriptase (a RNA-directed DNA polymerase) to catalyse the synthesis of a cDNA of the target RNA molecules (174).

Although qPCR represents a powerful tool in gene expression analysis and quantification, the technique has limitations related to technical and experimental variation. For instance, sampling conditions, sample purification, stabilization,

and storage conditions all affect the results of an experiment and need to be carefully controlled. Moreover, the analysis of gene expression profiling in individual preimplantation embryos is complicated by the limited amount of RNA from blastocysts (between 100 and 200 cells) and require the implementation of techniques for RNA amplification and appropriate normalization strategies (175,176). The optimization of this method for the analysis of blastocysts developed in the microfluidic device developed in this project in standard and altered conditions is reported in Chapter 3.

2.2.5 Mass Spectrometry and untargeted metabolomics

The progress of advanced omics technologies and their application to the analysis of extremely reduced volumes is of extreme interest for the investigation of embryo physiology and viability. Metabolomic studies allow in fact to non-invasively measure metabolic profiles in spent culture medium and to identify metabolic markers of embryo embryo development, quality (163), and outcome (177). Indeed, spent culture medium profiling can be used to predict developmental competence and genetic integrity of mammalian embryos (178). and to study teratogenic effects of exposure to drugs and environmental chemicals (179).

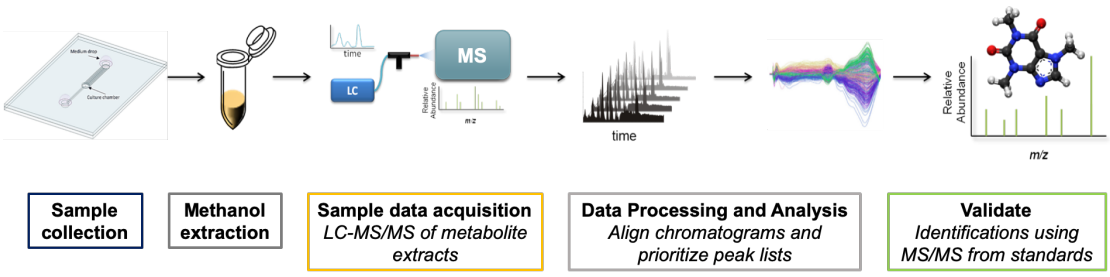

Figure 2.6 General Overview of an Untargeted Molecular Omics Workflow

MS-based metabolomics can implement both targeted (measuring a predefined set of metabolites) or untargeted (measuring all detectable metabolites, both known and unknown) approaches. For metabolomics studies, MS is typically combined with a separation technique, such as liquid chromatography (LC), gas chromatography (GC), capillary electrophoresis (CE), or ultra-high-performance liquid chromatography (UHPLC), that reduces the complexity of the mass spectra due to metabolite separation in a time dimension and provides additional information on the physical-chemical properties of the

metabolites (180). Reversed-phase liquid chromatography (RPLC) uses a hydrophobic stationary phase with a stronger affinity for hydrophobic or less polar compounds, resulting in hydrophilic molecules passing through the column an being eluted first, and in hydrophobic molecules being adsorbed to the stationary phase. RPLC is currently the most widely used separation mode for metabolomics studies, as it is directly compatible with the analysis of aqueous samples. However, it has limitation for the analysis of polar and/or ionic species which are not retained on the stationary phase and typically elute with the void volume (181). Recently developed UHPLC use columns with very small particle size (< 2 μm), which leads to increased graphic resolution and peak capacity, resulting in lower detection limits and increased sensitivity compared to conventional high-performance liquid chromatography (HPLC) (180). LC-MS and UHPLC-MS can be used for separation, identification and quantification of a broad range of metabolites and offer the benefits of inherent high sensitivity and high selectivity. Additionally, these techniques are suitable for thermo-labile compounds and do not require chemical derivatization prior to analysis, which is normally used to enhance the MS efficacy and selectivity and to improve the chromatographic separation (182,183). The chromatography step reduces the number of competing compounds entering the mass spectrometer facilitating the separation of complex mixtures of metabolites, which allows production of high quality MS data (184).

In terms of basic principle of MS, a mass spectrophotometer consists of an ion source for production of a charged species in the gas phase, and mass analyzers to separate these ions by their mass-to-charge (m/z) ratio. Electrospray ionization (ESI) is the preferred ionization technique in MS, by which a high voltage is applied to the sample in liquid phase producing an aerosol. The ionized molecules reach the analyzer and then a detector which counts the ions for every m/z ratios (151). For LC-MS, different mass analyzers can be used including ion trap, triple quadrupole, time-of-flight (TOF), quadrupole time-of-flight (QTOF) or Orbitrap. Hybrid instruments (*e.g.* Quadrupole-Orbitrap) allow to perform tandem MS (MS/MS), in which ions are selectively isolated, then fragmented and their m/z ratio is measured and used for structural characterization, providing high-resolution data on fragment ions (185).

By using LC-MS-based untargeted metabolomic approaches, the analysis of a biological sample results in the detection of thousands of peaks, each one referring to a detected ion (metabolite feature) with a unique m/z ratio, unique retention time and MS/MS fragmentation data (186). After data acquisition, the results are processed by using dedicated commercial or freely available bioinformatic software. With the evolution of advanced bioinformatics techniques, those tools are able to perform the series of processes typically involved in a MS data processing pipeline, such as filtering, peak detection, peak deconvolution, retention time alignment, and finally feature annotation (186). The m/z values for the peaks of interest are searched in metabolite databases, such as the Human Metabolome Database (HMDB) and METLIN, to obtain putative identifications. Putative identifications are then confirmed by comparing tandem MS/MS data and RT data to that of standard compounds (185). Metabolite identification is a critical step in untargeted metabolomics, because it is time consuming and typically performed manually by inspection. In addition, this process can be complicated by the fact that metabolite nomenclature is not entirely standardized among the available libraries and there is the possibility that a considerable amount of detected metabolite features do not return any matches. Similarly, in some cases it is not possible to reduce the results of a feature to a single candidate (181,185). In an effort to better communicate the confidence of annotation, specific classification systems can be used to guide metabolite annotation (186).

MS techniques provide highly valuable qualitative and quantitative analytical data on biological samples. However, the coupling with analysis performed on microfluidic platforms may require complex instrumentation such as integrated nanospray emitters (187,188). Typically, small sample volumes (microliter to picoliter) are collected from devices and analyzed offline after any chip-based analysis or treatment of interest is performed (189). This step prevents the dilution of signalling factors and biomolecules existing in traditional culture systems, but the detection of low concentration species in such small volumes remains a possible challenge.

A detailed discussion of the selection and optimization of the methods for the analysis of spent media sampled from the microfluidic systems is provided in Chapter 3.

2.2.6 Culture conditions: Conditioned media

Despite advances in Assisted Reproductive Technologies (ART) (111) and the evolution of *in vitro* embryo culture systems, the quality of *in vitro* derived mouse embryos still remains lower than those produced *in vivo* (190). The media composition for *in vitro* embryo culture has been considered a prominent cause for this failure and the effect of the different supplements has been deeply investigated (191,192). The design of media is complicated, because the components and their concentrations should be determined in order to minimize stress for the cultured embryos and to reflect the concentration of nutrients, electrolyte and macromolecules (*e.g.*, paracrine and autocrine factors, growth factors) present in the lumen of the female reproductive tract (*i.e.,* the oviduct) (193–195). Two possible formulations have been considered: one is based on single embryo culture medium in which the embryo is cultured in a constant medium containing all the supplements needed for its development (196); and the other is based on the so-called sequential culture media designed to mimic the chemical environmental changes that the embryos experiences *in vivo* moving through the fallopian tube and the uterus (112,197).

Despite the important contributions in the field of early mammalian embryo development, the optimal culture media formulation, able to reduce developmental arrest and improve *in vitro* pre-implantation development, has not yet been manufactured (198). Currently, one of the most widespread media used for mouse embryo culture is the potassium-supplemented Simplex Optimization Media (KSOM) (199). KSOM was greatly improved when Ho *et al.* supplemented the medium with essential and non-essential amino acids, which are present in high concentration in female reproductive tract fluids and are required to maintain cell viability *in vitro* (200,201). This allowed to significantly augment embryo development *in vitro* (202).

To clarify aspects of embryo implantation failure and embryo maternal communication, researchers cultured embryos in contact with a feeder layer of uterus derived cells, aiming to mimic the *in vivo* natural chemical and physical environment. These studies demonstrated that the co-culture with uterine cells improve *in vitro* early embryonic development and quality of mouse embryos (203–207). Cells release diffusible factors, such as bioactive molecules, growth

factors and cytokines, that favour embryo development (208), but the molecular mechanisms involved in this embryo-maternal communication still remain not completely understood (209). Other works suggest that cell-to-cell contact between cells and embryos is not required and an alternative to co-culture may come from the use of conditioned media. Conditioned media culture systems can pose several advantages over co-culture models, such as the absence of foreign cells and the presence of embryotrophic factors (210). Although several studies demonstrated that the use of oviductal epithelial cells-conditioned media support the development of early embryos in cattle (211–213), fewer works have been conducted in mouse. For instance, Lee *et al.* observed no significant changes in blastulation rate when a porous insert was placed between Vero cells and mouse embryos (50%) or when embryos were cultured directly on the cellular monolayer (57%) (214). However, these values were significantly higher than that of the control (29%), revealing the beneficial effects of cells-conditioned media on embryo culture and viability.

Based on these preliminary studies, Chapter 3 reports evidences of the alterations of the genetic and metabolomic profiles of fully developed blastocysts stimulated in a controlled microfluidic device with a conditioned medium, previously exposed to endometrial cells.

2.3 Microfluidic devices for studying the blood-brain-barrier

2.3.1 Blood-brain-barrier: basic physiology and pathology

Neurological diseases (*e.g.*, Alzheimer's disease, Parkinson's disease, brain tumors, epilepsy and multiple sclerosis) are increasingly recognized as major causes of death and disability worldwide. They affect up to one billion people worldwide and caused an estimated 9 million deaths (16.5 % of global deaths) in 2016 (215,216). For instance, Alzheimer's disease (AD) caused 122,019 deaths in the United States in 2018, making it the sixth leading cause of death in the United States and the fifth leading cause of death among Americans age 65 and older (217). AD is the common cause of dementia and is characterized by a progressive deterioration of cognitive functions due to degeneration of synapses and the death of neurons (218,219). This results in a significant reduction of the volume of the brain in AD patients as compared to healthy subjects. One of the main challenges in Alzheimer's research is to develop preventive and therapeutic drugs able to cross the 'blood-brain barrier' (BBB), i.e. the barrier separating the circulating blood from the brain.

The BBB is the interface between the blood and the central nervous system (CNS) that is responsible for the maintenance of the cerebral homeostasis in the CNS (Figure 2.7). The BBB regulates the transport of biological substances needed for the brain metabolic processes and neuronal functions and prevents the entry of toxins circulating in the blood, such as bacteria and virus, that can potentially lead to neuron cell death. Because of the BBB function in regulating the active and passive transport of solutes into the CNS, there are substantial obstacles to drug delivery for the treatment of neurological disease (220). Therefore, the functional and structural integrity of the BBB is of vital importance for healthy brain functioning (221).

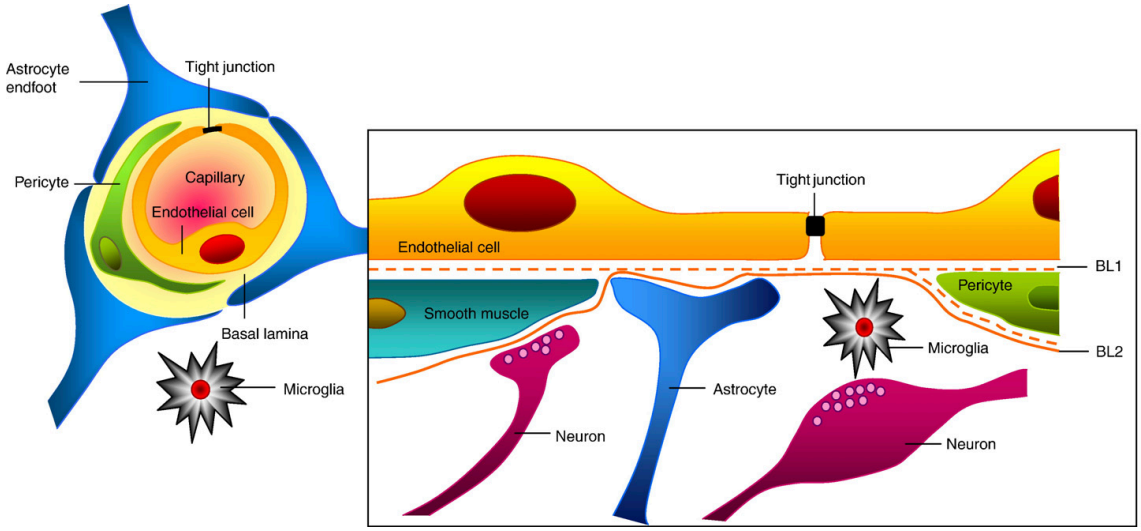

Figure 2.7 Cellular constituents of the blood-brain barrier (BBB).

The BBB is formed by brain microvascular endothelial cells (BMECs), which are connected by tight junctions. Represented on the right, the endothelium, together with the basal lamina (BL1, BL2), pericytes, and astrocytic end-feet forms the neurovascular unit (221).

At the cellular level, the BBB consists of specialized cerebrovascular endothelial cells (ECs), that line the blood vessels of the vascular system of the CNS, surrounded by the basal lamina and astrocytic perivascular end-feet (222). ECs are interconnected by junctional complexes including tight junctions and adherens junctions which control the paracellular transport, providing the highly selective and protective role of the barrier (223). Pericytes, supporting glial cells (astrocytes and microglia), basement membranes and the extracellular matrix (ECM) also play a fundamental role in maintaining the integrity of the BBB (224,225). The term neurovascular unit (NVU) has been recently used to refer to the functional network constituted by ECs, along with neurons, pericytes, astrocytes, microglial cells, and extracellular matrix (226,227). The NVU is a highly dynamic system regulated by specific biochemical and biomechanical signals produced by neuronal and non-neuronal cells that are responsible for the physical, biochemical and immune barriers of the CNS (221). In particular, astrocytes and pericytes have a vital role in BBB regulation and influence the BBB phenotype of the cerebrovascular endothelium (228,229). Astrocytes provide nutrition for neurons, regulate extracellular potassium balance, carry out the clearance of neurotransmitters, regulate proliferation of stem cells and maintenance of the BBB (230–232). Astrocytes interact with the ECs through the end-feet protrusions, highly specialized and polarized structures that wrap around

the capillary (222,233). On the other hand, pericytes wrap around the abluminal surfaces of cerebral vessels walls including those of capillaries, precapillary arterioles and postcapillary venules (234). Morphologically, pericytes tend to align with the vessel axis and are separated by a thin basement membrane from ECs and astrocyte end-feet. They perform various neurovascular tasks, including contributing to vessel stability, regulating capillary diameter and blood flow and controlling BBB integrity and function (235). However, the influence of pericytes on BBB permeability and functions is still not well understood and may be dependent on their stage of differentiation (236). The tight junctions in the brain microvasculature prevent transcellular passage of molecules of all size or polar molecules such as water-soluble compounds (electrolytes). Transport for nutrients and biologically important substances from the peripheral circulation into CNS requires specialized carrier-mediated transport systems. Some of these transport proteins are localized into either the luminal (blood-facing) or the abluminal (brain-facing) membrane or into both membranes of the endothelial cells. The localization of these transporters determines the polarity of the barrier, which is responsible to maintain functional integrity and homeostatic brain microenvironment (237,238). A further function of tight junctions is to prevent the movement of these proteins from one side of the endothelium (luminal or abluminal membrane) to the other, preserving the polarity of the endothelial barrier (239). At the molecular level, tight junctions consist of at least three integral protein types, such as claudins, occludins, and junctional adhesion molecules (JAM). These tight junction membrane proteins are connected to the actin cytoskeleton via *zonula occludens* (ZO) adaptor molecules (ZO-1 and ZO-2) (240,241). Antibodies to claudin-5, occludin, and ZO-1 are commonly used as markers of tight junction formation in monolayers of cerebrovascular ECs (242).

In addition to cellular interaction of ECs with other BBB cells, there are other factors which play an important role in maintaining BBB functions. For instance, the morphology of microvascular ECs is also dependent in part on biomechanical signals derived from the vascular system, such as shear stress associated with blood flow. Those inputs result in elongation and alignment of the ECs in the direction of flow, as well as in the differentiation of these endothelial cells into a BBB phenotype (243)(244). Additionally, studies suggested that tight junction formation between cerebral ECs in culture can be induced by the use of

astrocyte-conditioned medium, as this contain secreted chemical factors that can induce aspects of the BBB phenotype in the ECs *in vitro* (233,245,246).

Malfunction of the BBB, linked to increased BBB permeability, tight junctions disruption and impaired transporter functions, can lead to increased extravasation of immune cells and dysregulated transports of molecules and ions across the BBB (228).

2.3.2 *In vitro* models of the BBB

For the reasons explained above, preclinical models of the BBB are important for understanding the structural, physiological, and biochemical functions of the BBB and its role in pathogenesis of neurological diseases. Indeed, the development of physiologically relevant platforms that can accurately recapitulate BBB phenotypes and the complex cellular communication could help the understanding of BBB structural and functional properties as well as the development of new therapies. So far, animal *in vivo* models have been used to study drug delivery and transport across the barrier as they can reflect the real state of the microenvironment. However, those models are typically time consuming, costly, low throughput and do not predict clinical outcomes in human due to cross-species differences, causing high failure rates in late stage clinical trials (247–249).

In vitro transport measurements are usually performed using a Transwell assay where a confluent monolayer of endothelial cells is formed on a porous support separating two chambers. Transwell-based models typically use brain microvascular endothelial cells obtained from different species, including rat (250), mouse (251), bovine (252), porcine (253–255) or human (256). For BBB models, the use of primary cells is generally preferred as they provide the closest approximation to their *in-situ* counterpart, both for healthy or pathological tissues (257). *In vitro* models of non-human origin have provided valuable information on the physiology of the BBB and have allowed cross-validation between models. However, animal-derived endothelial cells have the drawback of limited physiological relevance compared to human cells-based model and may respond differently to specific treatment and drug testing compared to human cells. On the other hand, cell-based human models are difficult to establish due to the limited availability of primary, healthy, patient derived human cells and the complexity of

the isolation and purification process (258,259). Commercial sources of primary human BBB endothelial cells are available and represent a more accessible alternative for BBB models compared to freshly isolated cultures, even though they are relatively expensive. Nonetheless, primary cells might not be a convenient choice for studies that require high throughput and cost effectiveness, where the use of immortalized cell lines remain viable alternative for reduced culture preparations costs and relatively increased affordability (259).

More complex models have been developed and include the co-culture of ECs with astrocytes and/or pericytes, since they play an important role in the development and integrity of the BBB (246,260,261). Those three non-neuronal BBB cell types are currently considered, according to leading opinions, the key components for a BBB *in vitro* model that better correspond to the anatomical situation in the cerebral microvessels (222,262). Astrocytes-conditioned media has also been widely used in Transwell models, because it contains secreted soluble factors that have been shown to increase the expression of thight junction molecules (222,263).

Although Transwell inserts are widely used for their simplicity, cost-effectiveness and ability to assess BBB integrity, permeability and metabolic functions, they suffer from the major drawbacks of lack of physiological relevance and ability to effectively mimic the NVU milieu (264). Moreover, Transwell platforms are static culture models; they cannot reflect fluid characteristics of the BBB and cannot provide shear forces critical to induce proper physiological junction formation and to establish polarized tissues (244).

The use of 3D dynamic *in vitro* models of the BBB which allows the use of co-cultures and creates intraluminal flow through artificial capillary-like structural supports have also been investigated (265,266). In these systems, BBB ECs are cultured inside hollow fiber structures coated with fibronectin or ECM matrices, and exposed to pulsatile flow. Astrocytes can be seeded on the abluminal surface of the same hollow fibers and transendothelial electrical resistance (TEER) can be measured in real time through electrodes embedded in the system. Despite being suitable for co-culture studies and TEER measurements, those models do not allow for visualization of the intraluminal compartment and require time and technical skills to be implemented, which limits the adoption of this system among researchers.

2.3.2.1 Microfluidic models of the BBB

In recent years, microfluidic chips have been used to construct BBB models, and have become increasingly popular (267). Microfluidic platforms offer precise control of fluid transport at microscale dimensions and the possibility to integrate sensors (*e.g.*, TEER, pH, temperature, oxygen), which make it possible to simulate the BBB microenvironment and to study BBB dysregulation or CNS drugs transport (268). The precise fluid control enables the generation of shear stress that mimic those in natural microenvironments and have critical role in cell growth, morphology, cell function, gene expression and phenotype differentiation. BBB models can be easily customized to diverse experimental requirements and designed to obtain microstructure sizes similar to microvascular structures, to better resemble the microenvironment *in vivo* (269). The advantages and limitations of microfluidics and currently available *in vitro* BBB models are reported in Table 2.3.

Table 2.3 Advantages and disadvantages of *in vitro* BBB models

***In vitro* BBB models**	**Advantages**	**Drawbacks**
Transwell	• Very low-cost fabrication • Allows co-culture • Simple fabrication • Moderate scalability • High-throughput	• No shear stress • Limited cell differentiation • Lack of physiological relevance
3D dynamic models	• Low-cost fabrication • Allows co-culture • Complex fabrication • Enables the effect of shear stress • Allows for hemodynamic studies	• Setup require high cell numbers • Time consuming • Technically challenging • Not ideal for high throughput screening • Not permissive for visual microscopy
Microfluidics	• Low-cost fabrication • Flexibility in the design • Reduced cell numbers • Realistic microenvironment • Control over microenvironment	• Limited scalability • Complex fabrication • Lack of standardized quantification of parameters

	• Resembles more closely the actual *in vivo* brain anatomy • Can reproduce shear stress • Allows permeability measurements • Improvement in paracellular barrier functions • Allows for cell inspection via visual microscopy

To date, different designs, materials and strategies have been explored (Figure 2.8). Most microfluidic models contain relatively independent and closed compartments and use a porous membrane to separate the luminal and abluminal layers. Endothelial cells and other cells are cultured on the two sides of the membrane to form a neural chamber and a vascular chamber (105,270–273). Another widely used BBB design is the planar parallel configurations, which consists in two aligned channels separated by an array of PDMS micropillars. This structure creates two communicating compartments – the “brain” and the “blood” compartments – and do not require the use of a physical membrane to separate the different cell types improving cell-cell interactions (274–278). However, the thickness of the central separating channel is still not comparable with the thickness of native basal lamina. Innovative designs use 3D microvascular tube structures constructed using collagen gel. The use of cylindrical microchannels results in constant and more uniform shear stress along the inner walls of the structure, compared to rectangular channels. These 3D structures can be used to co-culture ECs with astrocytes or pericytes to better mimic the *in vivo* conditions, although they are, currently, not compatible with TEER measurements of barrier integrity (279–282). In Figure 2.8 are reported some examples of microfluidic BBB models from literature.

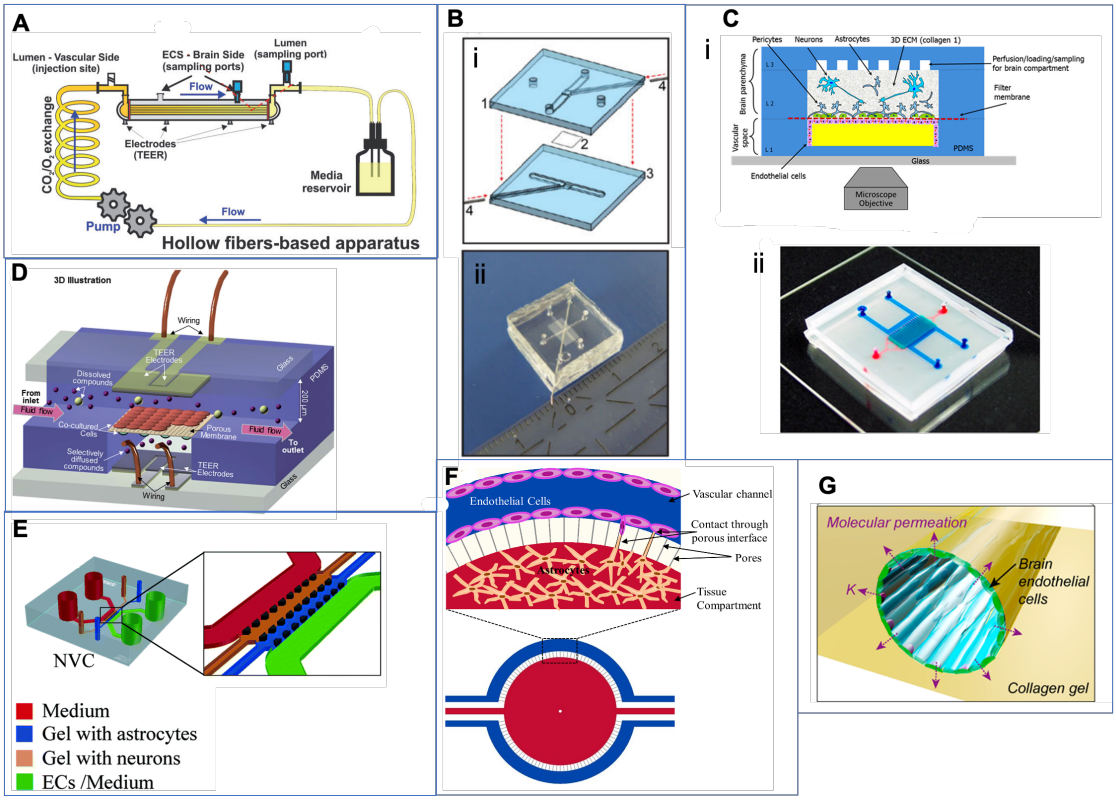

Figure 2.8 Examples of BBB *in vitro* models from literature:

(A) Schematic illustration of a 3D dynamic *in vitro* BBB model. BBB endothelial cells are cultured inside hollow fiber structures (lumen) coated with fibronectin or ECM matrices, and astrocytes can be seeded on the abluminal surface of the same hollow fibers. (266) **(B)** (i) Schematic representation of (1) top part, (2) Transwell membrane and (3) bottom part of the BBB chip, with side-channels to incorporate (4) TEER electrodes, and (ii) picture of the BBB chip made in PDMS. (105) **(C)** Microfluidic model of the Neuro Vascular Unit. (i) Schematic view of the chip indicating endothelial cells lining the lower, vascular chamber, astrocytes and pericytes lining the other side of the filter membrane, with neurons in the collagen gel in the upper brain chamber; (ii) picture of the BBB chip made in PDMS (273). **(D)** Multi-layered channel structure made from patterned PDMS substrate with dynamic flows, co-cultured cells and two sets of electrodes. (270) **(E)** Microfluidic BBB with planar configuration. Schematic layout of the BBB chip and enlarged view of the channels: two central hydrogel regions for co-culturing astrocytes (blue) and neurons (orange), and two side channels for hosting endothelial cells and media (green and red, respectively). (277) **(F)** Schematic illustration of a BBB device showing one of two vascular channels (blue) with endothelial cells lining the channel walls, the tissue compartment (red) containing astrocytes, and the porous interface (white) separating the vascular channel and tissue compartment. (275) **(G)** Microfluidic device to model the brain microvasculature. Schematic illustration of a 3D printed microvascular structure that support the culture of brain mouse brain endothelial cells on the luminal surface of collagen microchannels (281).

Importantly, microfluidic BBB systems enable sensor and omics integration and provide opportunities for high-throughput or single-cell manipulation. These versatile tools support a wide range of potential applications, including the development of novel therapeutics (283), personalized medicine (284), toxicology studies (285,286), fundamental brain research and the study of glioblastoma

(278). This technology also presents a promising alternative to reduce animal testing and shows a great potential to further BBB research.

Nonetheless, there are currently several challenges which limit the success of these innovative platforms for BBB-related studies. For instance, there are some aspects that need to be taken into account for each platform, such as cell numbers, culture volumes, perfusion conditions and the possibility to enable analysis of small volumes (*i.e.,* RT-PCR, Western blotting, ELISA) to measure changes in permeability-related genes or biomolecules that can be coupled with data obtained from immunocytochemistry analysis (259,287). Furthermore, as for other microfluidics applications, the lack of standardization in cell manipulation procedures and the complexity of fabrication and operation of the device, makes difficult the integration of microfluidic tools into non engineering-focused laboratories. Moreover, although these models provide several advantages over traditional BBB Transwell-based platforms, there is still a significant gap between the characteristics of microfluidic models and the *in vivo* environment.

As a consequence, microfluidic-based BBB models are still not ready for commercial use and progress (*e.g.*, materials and fabrication techniques) is needed to improve the reproducibility and efficiency of such devices (19,264,268). Proper optimization of these microfluidic BBB models and culture conditions will enable the adoption such models in pharmaceutical and toxicology applications.

Chapter 3
Microfluidics to improve *in vitro* embryo culture and toxicity assessment

3.1 Introduction

Over the past 2 decades, research on improving the culture medium has greatly enhanced *in vitro* development of embryos. However, the culture techniques used to grow mouse embryos *in vitro* have changed very little and both cleavage rates and embryo viability are suboptimal*,* indicating that present *in vitro* systems are still not efficient. Since the nineties, microfluidic miniaturized platforms have been proposed as innovative systems to support IVF procedures with the aim to solve most of the issues associated with traditional culture systems (288–294). In particular, this new culture strategy aims to reduce the handling of medium and zygotes during embryo development, to optimize the concentration of autocrine and paracrine factors in the close proximity of the embryo, and to recreate the mechanical stimulation that occurs *in vivo* in the oviduct (294,295). The main advantage of the microfluidic approach is the reduction of volumes below the standard microdrop technique, thus the reduction of the ratio between media and embryos. Volumes used in microfluidics (0.01-10 mL) are comparable to the fluid volume found in the reproductive tract (*i.e.,* an oviduct is about 10 cm long and has a diameter of approx. 1 mm), recreating a microenvironment that better resembles that found *in vivo*.

Microfluidic culture systems could potentially support most parts of an ART cycle and so far have been successfully used to perform gamete selection, IVF and development (289–291,293,296–299). In 2002, Hickman *et al.* observed impaired development for embryos exposed to a continuous flow rate (0.1-0.5 µL h^{-1}) in a silicon-glass microfluidic device compared to static cultures (300). In contrast, in 2006 and 2010 Cabrera and Heo shown that pulsatile dynamic culture conditions were critical to enhance blastocyst development in a funnel-shaped microfluidic device, observing increased percentage of hatching blastocysts and blastocyst cell numbers. (Figure 3.1i) (299,301). While implantation rates and numbers of ongoing pregnancies were similarly improved by the dynamic culture, the new approach was not more successful than traditional drop culture. A work

conducted by Ma *et al.* in 2011 proposed an innovative system able to integrate each step of IVF, including single-oocyte positioning, motile sperm screening, fertilization, medium replacement, embryo culture, and embryo in situ analysis, within a microfluidic device (Figure 3.1iv). This system utilized different microchannel shapes and oocyte traps designs to select the fertilizing sperm, based on the swimming quality of the sperm, and to enable fast and efficient medium replacement, obtaining embryo growth rate similar to that of conventional IVF systems (291). In 2013, Swain summarized the benefits and limitations of the microfluidic approach for clinical procedures in IVF (including maturation, manipulation, culture, cryopreservation and non-invasive quality assessment) (302). Specifically, while the use of microfluidic devices would reduce the stress induced during embryo manipulation, optimize the culture environment and reduce the variability between different embryology laboratories, their design and operation still limit the adoption of microfluidics in clinical ART laboratory. In the same year, Severine Le Gac's group reported a comprehensive assessment of the beneficial effect of reduced culture volume on single and group embryo culture, using a microfluidic system that supported blastocyst development with birth rates comparable to microdrop culture (Figure 3.1 ii) (293). Despite the interest in using these microfluidic systems for ART is significant, there are still concerns regarding the safety, consistency and accuracy of such systems and the long-term (*i.e.,* after implantation) impact of microfluidic culture on the embryo, which remain not completely understood. Importantly, microfluidic technology has not yet been introduced into the clinics and human IVF laboratories, since those platforms result complex and less practical to use for not-trained embryologists. Material toxicity is one of the principal issues, mainly because these prototypes are fabricated "in-house" using manufacturing processes difficult to control and not yet standardized. The chemical and physical characteristics of polymers used for the fabrication of these systems significantly affect the safety and efficacy of IVF procedures, particularly if they are not medical graded, impure or not completely polymerized. Plastics and chemical residues present in manufacturing consumable plastics can not only affect the viability of the embryos, but also trigger long-term adverse effects on the foetal development (303–307). Microfluidic devices are typically constructed using soft lithography technique in polydimethylsiloxane (PDMS) (55). Despite PDMS has

no detrimental effect on embryo development and has several advantages in microfluidic applications for embryo culture (*i.e.,* ease of use, optical transparency, gas permeability and biocompatibility), there are some possible adverse aspects that might affect microscale embryo culture (75). As discussed in Section 2.1.2 these include small molecule absorption, deformation of the channels features, media evaporation and consequent increase of osmolarity, hydrophobic recovery, and leaching of small molecular weight species and un-crosslinked PDMS (71,75,79). Figure 3.1 and Table 3.1 report some examples of PDMS-based microfluidic devices that support *in vitro* culture and development of mouse embryos, summarizing some of their key-features.

Alternative materials are PS, widely used for common plasticware in ART/IVF laboratories, and thermoplastic materials, such as PMMA, PC, COC, PLA, which can be used for industrial manufacturing of disposable devices using inexpensive and fast processes, but their long term toxicity is still uncertain (86). In 2004, Raty *et al.* compared the development of embryos cultured in a microfluidic channel under static conditions, manufactured in silicon/borosilicate and PDMS/borosilicate showing in both cases improvement of cleavage and blastocysts rates compared to microdrop culture (Figure 3.1iii) (298).

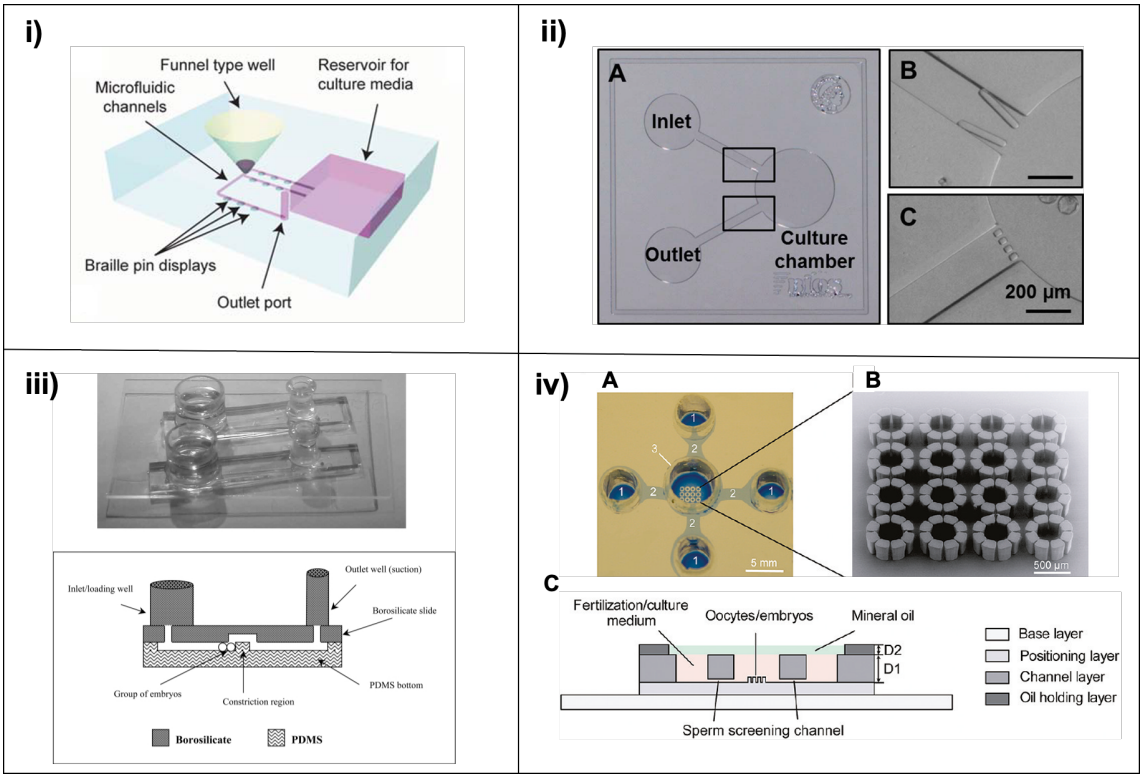

Figure 3.1 Examples of microfluidic devices for *in vitro* culture of mouse embryos.

i) Dynamic microfunnel culture device: schematic drawing of the device placed on an array of piezoelectric pin actuators provided by Braille displays. Embryos are loaded and cultured in the microfunnel under the flow-through condition created by the pin actuation sequence (299) ii) Microfluidic device for embryo culture in PDMS. Embryos are introduced from the inlet reservoir (B), guided in the chamber and trapped with the help of grids (C) (293) iii) A PDMS/borosilicate device. The basic structure of the device is a PDMS bottom covered with a borosilicate slide that forms the top of the microchannels. (298) iv) Microfluidic IVF device. The device has three regions: (1) sperm inlet pools, (2) sperm screening channel, (3) oocyte-embryo positioning well. (B) Scanning electron micrograph of the 4 × 4 array of oocyte traps. (C) Schematic side view of the microdevice: oocytes-embryos are cultured in a four-layer structured PDMS-glass device (291).

Table 3.1 Examples of microfluidic devices for *in vitro* culture of mouse embryos (308)

	Research group	**Raty *et al.*, 2004** (298)	**Heo *et al.*, 2010** (299)	**Ma *et al.*, 2011** (291)	**Esteves *et al.*, 2013** (293)
	Embryo species	Mouse	Mouse	Mouse	Mouse
Culture environment	***Medium***	M16	KSOM + ½ AA with D-Glucose and phenol red	KSOM	α-MEM + 0.2 % w/v bovine serum albumin + 50 μg mL^{-1} gentamicin sulphate
	Temperature	37 ˚C	37 ˚C	37 ˚C	37 ˚C
	pH	N.A.	N.A.	N.A.	N.A.
	O_2 tension	N.A.	20%	N.A.	N.A.
	CO_2	5%	5%	5%	7%
	Single vs. group culture	Group culture (10 embryos)	Group culture (13 – 15 embryos)	4x4 array of single embryos	Single and group culture (5 and 20 embryos)
Device characteristics	***Volume***	10 μL	10 μL	0.5 – 10 μL	30 and 270 nL
	Material	Silicon/ borosilicate PDMS/ borosilicate	PDMS-Parylene-PDMS	PDMS	PDMS
	Retrieval	Yes	Yes	Yes	Yes
	Automatization	No	Pulsatile or peristaltic pumping performed using computer-controlled, piezoelectric and movable pins	No	Passive pumping
Culture characteristic	***Refreshed medium***	No	Yes	No	Yes
	Mineral oil	Yes	Yes	Yes	No
	Static vs. dynamic culture	Static	Static/Dynamic	Static	Static/Dynamic

Unfortunately, the majority of microfluidic devices reported in the literature still require the use of mineral oil to stabilize temperature, osmolality and pH (291,298,299). Quality and composition of the oil have been correlated with markers of embryo developmental competence rate, such as embryo cleavage (to morula and blastocyst stages) and embryo viability (309). Additionally, since

the fundamental aim of these systems is their adoption for human fertility treatment, the toxicity of all the materials needs to be thoroughly tested. The Mouse Embryo Assay is currently the gold standard bioassay used in research and industry to evaluate the toxicity of any material, compound or device that may be exposed to embryos (310) and it is specifically designed to ensure consistent quality, reliability and safety of new culture products to be used in IVF clinics. The standard MEA consists in monitoring the growth of mouse embryos in contact with the novel material or device from 1- or 2-cells stage to the blastocyst stage by assessing embryo morphology and viability at different time points.

Additional evaluation of embryo quality indexes provides a thorough understanding of the impact of the microfluidic culture and the use of reduced volumes on the health and developmental competence of *in vitro*-derived mouse embryos. Morphokinetics (cell cleavage, timing, cell counting, morphology) (311–315), energy metabolism (316–318), outgrowth assay (319), total cell count, cell allocation and blastocyst rate (320–322), represent biomarkers of blastocyst competence that can be evaluated *in vitro* to optimize the microfluidic technology before moving to *in vivo* testing, reducing the need of animal models. While some of these methods have been used for validation of microfluidic prototypes, metabolic and genetic signatures of embryos developed in microfluidic devices have never been compared with those of embryos cultured in traditional microdrops.

As mentioned above, currently there are no commercially available microfluidic devices for human IVF or for GA mouse breeding. This is mainly due to the fact that the technology still requires progress and need to be improved in order to achieve the challenging outcomes – *i.e.*, high throughput for GA mouse breeding and very good quality embryos for human IVF procedures – to guarantee high pregnancy rates.

This Chapter discusses the design, fabrication and evaluation of a microfluidic device for the culture of murine zygotes to produce viable and competent blastocysts. The device design was optimized by computational simulations using COMSOL Multiphysics® in order to control and reduce fluid dynamic shear stress during the loading and culture of the embryos in the device. Compared to currently available microfluidic devices, the device presented in this work aimed to limit stress and detrimental effects during culture by avoiding the

use of physical barriers, and to ensure a sufficient ease of operation during loading. Potential toxicity of PDMS was firstly assessed by performing the Mouse Embryo Assay (MEA) using cleavage and blastocyst development rates as predictive indexes of implantation (323). Gene expression profile of blastocysts developed inside the device was compared with that of those cultured in traditional microdrop by real-time PCR analysis, in order to exclude potential genetic alterations induced by the different environment and culture methods.

Additionally, global untargeted metabolomics was used to analyse culture media extracted from the microfluidic device or traditional microdrops either in presence or absence of the embryos to investigate PDMS-release of biomolecules and embryo metabolic activity.

Furthermore, the effects of culture in uterine epithelial cells-conditioned media was assessed in terms of blastocyst developmental competence by measuring blastocyst rates, gene expression profile and metabolomic profiling of embryo culture media.

Thus, the microfluidic device described in this work provides a novel simple and user-friendly platform for the culture of murine embryos which could be easily set up in a conventional ART/IVF laboratory. Additionally, the current study showed for the first time useful information on the comparison between the metabolic and genetic signatures of embryos developed in microfluidic devices compared with those of embryos cultured in traditional microdrops.

3.2 Materials and Methods

3.2.1 Device design and fabrication

Microfluidic devices were fabricated in polydimethylsiloxane (PDMS, Sylgard® 184, Down Corning, MI, USA). Each device is composed of two PDMS layers fabricated using a standard soft lithographic process using SU-8 photoresist and bonded together using oxygen-plasma (55). The master molds for the two layers were fabricated on a silicon wafer with SU-8 2050 and 2035. Subsequently, a 10:1 PDMS pre-polymer: curing agent mixture was poured on the obtained silicon mold, then thoroughly degassed and cured overnight at 70 °C afterwards. PDMS layers were cut, released from the molds, and assembled using oxygen-plasma treatment (600 mT, 100 W, 40 s). This process allowed for contamination removal (chemical), oxidation and activation of the surfaces. The assembled devices were immediately filled with sterile embryo-tested water and stored at 4 °C until used to preserve hydrophilicity. Before embryo culture, devices were sterilized by exposure to UV light (wavelength 254 nm for 30 min).

3.2.2 Device preparation and loading

The microfluidic device was placed inside a 60 mm MEA tested ART culture dish (Nunclon®, Scientific Lab Supplies, UK) and surrounded with 4 mL embryo-tested sterile-filtered water (Sigma, UK) (Figure 3.2), in order to preserve the humidity inside the dish and to avoid evaporation of the media during the culture. Devices were prepared by adding a 10 μL culture medium drop to the channel inlet and drawing the media from the channel outlet, repeating this procedure ten times. 10 μL drops of fresh medium were then added to inlet and outlet before. pre-equilibration overnight at 37 °C under 5% CO_2, 5% O_2 in a humidified nitrogen atmosphere. The total volume of these drops did not change significantly during a 3-day culture period, although media tended to flow to the outlet side by capillarity.

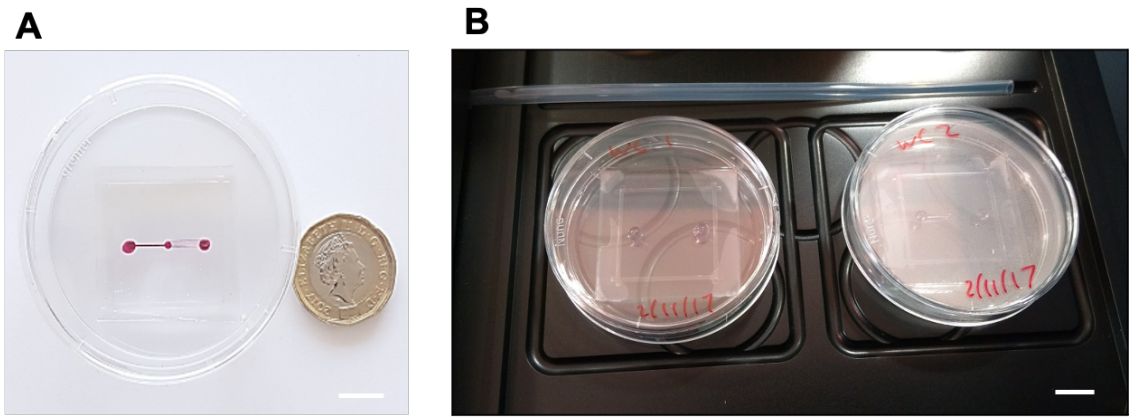

Figure 3.2 Device preparation and culture.

The fabricated PDMS microfluidic device in a traditional 60 mm petri dish for embryo culture (A), and two devices placed inside a MINC benchtop incubator (B) during culture. Scalebar: 10 mm.

3.2.3 Microfluidic device flow and shear stress analysis

The optimization of the device design and computational simulations were carried out by a former PhD student, Francesco Colucci, in the School of Electronic and Electrical Engineering at the University of Leeds. To characterize the fluid flow within the device, computational simulations were performed using COMSOL Multiphysics® 5.2a. Results were used to evaluate and compare flow rate, velocity field and predict shear stress as function of microfluidic device geometry. A 3D model of the microfluidic device was created using computer-aided design software (Autodesk AutoCAD 2017) and then imported into COMSOL. The fluid inside the device was simulated as an incompressible, homogeneous, Newtonian fluid with density (ρ=1000 kg m^{-3}) and viscosity (μ=1x10^{-3} Pa s) (324).

To measure the flow, a solution of 4.8 µm fluorescent polystyrene beads (Thermo Fisher Scientific inc., UK) was manually loaded using an embryo handling pipette with 170 µm tip (EZ-Grip, RI). The flow was monitored and recorded with a non-inverted fluorescent microscope (Olympus BX60) with a mercury lamp, using a Hamamatsu camera. Images and videos were taken using a 521 nm emission filter. Image frames were assessed measuring the length of the beads path divided by the exposure time using ImageJ software. The estimated inlet velocity was applied to a COMSOL model to predict the shear stress in the chamber during embryo loading.

For further characterization of the flow within the microfluidic device, a solution of fluorescein 0.05 mg mL^{-1} was flowed into the chamber. Images were acquired using an AMG EVOS fluorescence microscope for time lapse evaluation of the fluorescein flow chamber profile over time.

3.2.4 Embryo culture and blastocyst development

3.2.4.1 *In vitro* embryo culture in microdrops

Two different strains of murine embryos were used in this study. For embryo development studies, murine cryopreserved presumptive 1 cell zygotes were kindly provided by the Mary Lyon Centre (MRC Harwell Institute, Oxford, UK) and obtained from mature murine metaphase II oocyte-cumulus-complexes retrieved from superovulated C57BL/6NTac mice after IVF. According to the manufacturer's protocol, straws containing frozen 1 cell zygotes were held in air for 30 s, and plunged into room temperature water until the contents had visibly thawed. The straws were cut at the seal and the plug bisected to push the contents into a 60 mm, hydrophobic culture dish. Embryos were incubated for 5 min and washed two times in 100 µL drops of M2 medium (EmbryoMax®, Millipore, UK) at 37 °C. Embryos were then washed three times in 10 µL microdrops of pre-equilibrated medium KSOM (+AA w/D-Glucose w/Phenol Red, EmbryoMax®, Millipore, UK) under oil before transfer to devices or culture drops. Culture drops were 10 µL, 1 µL/embryo, in 35 mm hydrophobic IVF certified dishes (Nunc), covered with 5 mL of Bio-Ultra mineral oil (Sigma Aldrich, UK).

For metabolomics analysis, commercially available one-cell murine embryos, derived from the B6C3F1xB6D2F1 strain, were purchased from Embryo-Tech (Haverhill, MA, USA). Embryo straws were removed from liquid nitrogen, exposed to room temperature for 3 min and plunged into a 37 °C water bath for 1 min. The straws were cut at the seal and the plug bisected before pushing the contents into a 40 µL drop of M2 medium in a 60 mm IVF hydrophobic culture dish. Finally, embryos were rinsed twice in pre-warmed KSOM medium and allowed to rehydrate for 10 min in the final rinse droplet before transfer to devices or culture drops. Culture drops were prepared in advance, at least 2 hours before embryo thawing, and equilibrated in a MINC incubator at 30 °C under 5% CO_2, 5% O_2 in humidified nitrogen atmosphere. Embryos were washed in 3 additional drops of

KSOM before transfer to the culture drop. For qPCR experiments, 10 μl drops (1 μL/embryo) were used. For mass spectrometry analysis, 40 μl drops (4 μL/embryo) were used to obtain the same embryo to media ratio of the devices.

3.2.4.2 Device culture

Thawed embryos were cultured in group of ten in the microfluidic device. Before embryo loading, the 10 μL media drops were removed from inlet and outlet ports of the device. Embryos were then loaded through the inlet port by using an EZ-grip embryo handling pipette with a 145 μm diameter tip, which is traditionally used for embryo culture and has a tip size compatible with the inlet port. Medium was then drawn through from the channel outlet port until all embryos entered the central chamber (Figure 3.3). Next, 10 μL drops of pre-warmed KSOM were then added to channel inlet and outlet ports before culture at 37 °C under 5% CO_2, 5% O_2 in a humidified nitrogen atmosphere in a MINC benchtop incubator. At the end of the culture embryos were retrieved by simply aspirating from the inlet channel mouth using the same 135 μm pipette tip until all the loaded embryo are retrieved. Embryo loading was equally successful and practical using a range of bulb and pipettor embryo handling devices common to clinical and research ART laboratories. This confirmed the ease of operation of the device which resulted simple to use for both experienced embryologists and unexperienced personnel. The loading procedure was indeed facilitated by the absence of oil and by the compatibility of the device with bench top incubators and optical microscopes.

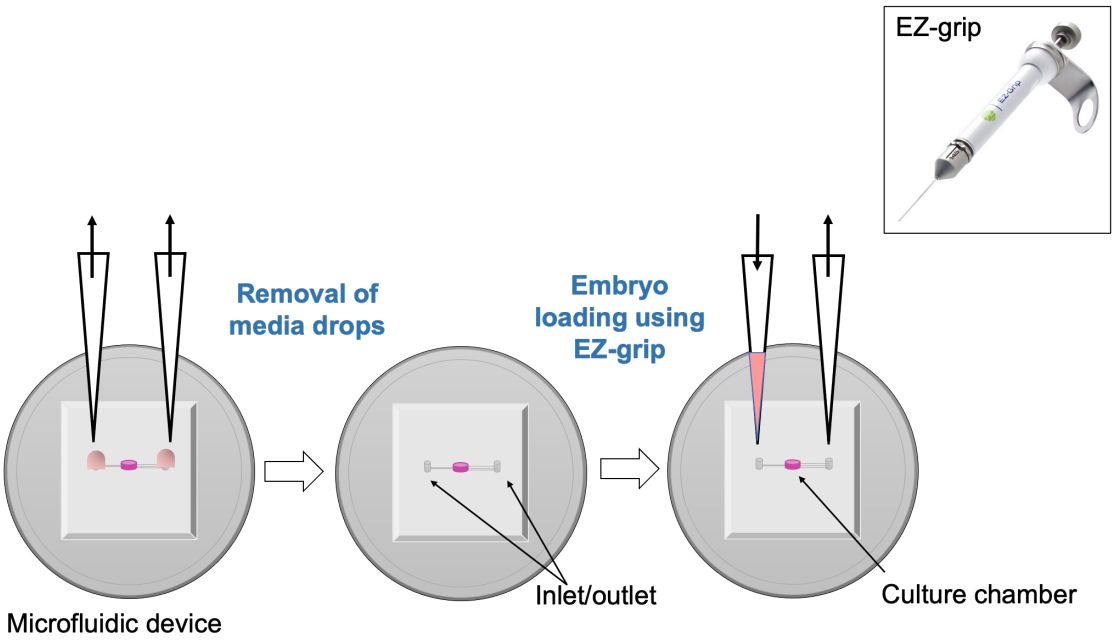

Figure 3.3. Schematic of the embryo loading procedure.

After removing the 10 µL media drops from inlet and outlet ports, embryos are loaded through the inlet port by using an EZ-grip embryo handling pipette (shown in the insert). To ensure loading, medium is slowly drawn through from the channel outlet until embryos enter the culture chamber.

Embryo cleavage rates were assessed after 24 h and blastocyst rates were assessed after 120 h of culture. Embryos were examined under a Nikon Intracytoplasmic Sperm Injection (ICSI) microscope with RI viewer with Tokai Hit heated stage set to 37 ºC.

3.2.5 Mouse uterine epithelial cells culture

Mouse uterine epithelial cells (MUECs) were purchased from Creative Bioarray (CSC-C9063J, NY, USA) and cultured in SuperCult® Complete Epithelial Cell Basal Medium (ECBM, Creative Bioarray, USA) containing 2% fetal bovine serum (Creative Bioarray, USA), 1% L-Glutamine (Creative Bioarray, USA) and 1% Antibiotic-Antimitotic Solution (Creative Bioarray, USA). Cells were maintained in a humidified 5% CO_2 environment at 37 °C. Trypsinized cells were seeded at a density of 25 × 10^3 cells/cm^2 on a 12 well plate coated with 0.1% gelatin solution (EmbryoMax®, Merck Millipore, UK). Culture medium was replenished every 2 days until cells reached 70% confluence, determined using a standard phase contrast inverted microscope.

To prepare conditioned medium, ECBM medium was replaced with fresh KSOM when MUECs were 70 % confluent. Cells were then incubated for 24 h at

37 °C. Conditioned medium was sterilized by passage in a 0.2 μm-pore-diameter Millipore filter and immediately used.

3.2.6 Embryo culture in uterine epithelial cells-conditioned media

Uterine epithelial cells-conditioned media (called from here on “KSOM cm”) was used to culture mouse embryos in microdrops or in devices and results were compared with embryos cultured in KSOM (control KSOM).

For drop culture, embryos were cultured in oil-covered 40 μL drops (4 μL/embryo) in either control KSOM or KSOM cm, for 5 days or until the developmental stage of fully expanded blastocyst was reached. At the end of culture, blastocysts were recovered for qPCR and spent media samples were collected and immediately frozen at -80 °C for mass spectrometry analysis. Each experiment was performed in triplicate and replicated three times (n=9 drops, 90 embryos for each experimental group).

For device culture, ten embryos were loaded in each device and cultured in either control KSOM or KSOM cm for 5 days or until the developmental stage of fully expanded blastocyst was reached. Each experiment was performed in triplicate and replicated five times (n=15 devices, 150 embryos for each experimental group). At the end of the culture blastocysts were recovered and snap frozen for qPCR analysis. Spent media samples were collected from inlet and outlet ports from each device and immediately frozen at -80 °C for mass spectrometry analysis.

3.2.7 qPCR: gene expression profiling of individual blastocyst

Individual expanded blastocysts were recovered from microdrops or devices and analysed using a bespoke real-time PCR (qPCR) array to identify changes in expression of genes associated with blastocyst development and to assess effects of culture in uterine epithelial-cell conditioned media. The procedure used for cDNA libraries preparation and qPCR is described in the sections below.

3.2.7.1 Sample preparation

Individual stage-matched expanded blastocysts were recovered from microdrops or microfluidic devices, carefully rinsed in Dulbecco’s phosphate buffered saline (PBS) twice and dispensed into 0.5 mL RNA-free PCR tubes

containing 2 µL of *RNA*GEM-extraction reagent mastermix (RNAGEM Tissue Plus®, MicroGem International PLC, Southampton, UK) with less than 0.5 µL PBS (see Table 3.2). Samples tubes were kept on ice during the whole process and then transferred into -80 °C freezer until analysis.

Table 3.2 RNAGEM-Extraction Reagent Mastermix Preparation.

REAGENT	VOLUME
10X buffer silver	5 µL
Rnagem	1µL
RNase-free H_2O	44µL
Total	50 µL

3.2.7.2 Cell lysis and DNA degradation

The samples and reagents were kept on ice during preparation for the DNAse treatment. The DNAse cocktail was prepared by mixing 0.3 µL/reaction of 10X DNAse buffer (ZyGEM, Southampton, UK) with 0.2 µL/reaction of 1 U/µL DNAse I (ZyGEM, Southampton, UK). DNAse cocktail was prepared for all reactions plus one additional reaction by adding the two components in a 0.5 mL PCR tube. Samples were spun down (700 x g for 10 s at room temperature) to collect the liquid at the bottom of the tube before running the PCR program. A Veriti™ thermal cycler (Applied Biosystems) machine was used to run the program listed in Table 3.3. In detail, samples were first incubated at 75 °C for 10 min to achieve cell lysis. After cooling down to 37 °C for 5 min, 0.5 µL of the prepared DNAse cocktail was added into each sample tube. The solution was mixed well by pipetting keeping samples in ice. Then, samples were incubated for 5 min at 75 °C to allow completion of the DNA decontamination reaction. Next, reactions were heated up to 75 °C for 5 min for degradation of DNAse activity before cooling down to store at 4 °C for the further process.

Table 3.3 Cell lysis and DNA degradation Program.

TEMPERATURE	TIME	PURPOSE
75 °C	10 min	Cell lysis
37 °C	5 min	DNA decontamination reaction
75 °C	5 min	Degradation of DNase activity
4 °C	Hold	Safe storage

3.2.7.3 cDNA Library construction

For the construction of cDNA libraries of individual blastocysts, a modified version of an existing protocol (176) was used and the total RNA was reverse-transcribed to cDNA using a first strand cDNA synthesis kit (Thermo Fisher Scientific Inc., UK). The master mix of the Reverse Transcriptase (RT) reaction for the first stranded cDNA was prepared for all reactions plus one additional reaction by adding the reagents listed in (Table 3.4) into a 0.5 mL PCR tube. The prepared RT reaction mix was added to each DNA-decontaminated blastocyst sample tube containing approximately 3 µl of total blastocyst RNA (sample volume ~2.5 µl plus 0.5 µl DNAse mix) keeping samples at 4 °C or in ice to avoid hybridization of ssDNA. Samples were spin down (700 g for 10 s at room temperature) to collect the liquid at the bottom of the tubes, and the reaction was then incubated in the thermal cycler with a heated lid, as detailed below in Table 3.5. Samples were finally inserted in the machine after program started and the temperature set for the first step (42 °C) was reached.

Table 3.4 Composition of the first strand cDNA construction reaction.

REAGENT	CONCENTRATION	VOLUME PER REACTION (µL)
5X First strand buffer	5X	3.2
Betaine	5 M	3.0
$MgCl_2$	50 mM	1.8
Superscript II Reverse Transcriptase	200 U/µL	0.75
RNase-out (RNA inhibitor)	40 U/µL	0.4
Dithiothreitol (DTT)	0.1 M	0.75
TSO (5'primer)	10 mM	1.0
3CDS (3'primer)	10 mM	1.0
Deoxynucleoside triphosphate (dNTP)	10 mM	1.0
DNA-decontaminated RNA template		3.0
Total		15.9

Table 3.5 RT Program.

CYCLES	TEMPERATURE	TIME	PURPOSE
1	42 °C	90 min	RT and template-switching
10	50 °C	2 min	Unfolding of RNA secondary structures
	42 °C	2 min	Completion/continuation of RT and template-switching
1	70 °C	15 min	Enzyme inactivation
1	4 °C	Hold	Safe storage

3.2.7.4 Long distance PCR for cDNA amplification

The first strand DNA product synthesized from total RNA in single blastocyst lysates was subsequently amplified by using a Long Distance PCR (LD PCR)-based method. Reagents were prepared as shown in Table 3.6 to make a LD

PCR master mix for all reactions plus one additional reaction. The prepared LD PCR reaction mix was added to each sample tube, producing a final volume of 50 µl. Samples were vortexed to mix, and spun down (700 g for 10 s at room temperature) to collect the liquid at the bottom of the tubes. Finally, the PCR was performed in a Veriti™ thermal cycler by using the program listed in Table 3.7. The LD PCR product was held at 4 °C after cDNA amplification was completed and the cDNA libraries were then kept at -20 °C until later use.

Table 3.6 Preparation for Master Mix Reaction of Long Distance PCR for cDNA Amplification.

REAGENTS	CONCENTRATION	VOLUME PER REACTION (µL)
DNA/RNA-free H2O		25.5
10X Advantage 2 PCR Buffer (Takara Bio Europe/Clontech)	10X	5.0
50X Advantage 2 Polymerase Mix (Takara Bio Europe/Clontech)	50X	1.0
TaKara LA Taq® Hot-Start (Takara Bio Europe/Clontech)	5U/µL	0.5
dNTP	10 mM	1.0
Nest universal primer	10 mM	1.0
1st strand DNA template		16.0
Total		50

Table 3.7 LD-PCR Program.

CYCLES	DENATURE	ANNEAL	EXTEND	HOLD
1	95 °C, 1 min	-	-	-
25	95 °C, 15 s	60 °C,1 min	72 °C, 5 min	-
1	-	-	-	4 °C

3.2.7.5 Real time PCR

Real-time PCR (qPCR) was performed to determine transcript abundance of selected genes in cDNAs generated from individual, stage matched blastocysts

cultured either in the microfluidic device or in traditional microdrops. qPCR was carried out using an ABI 7500 RT-PCR System (Applied Biosystems) with SYBR Green Master PCR mastermix (Thermo Fisher Scientific Inc., UK), following the PCR cycling program outlined in Table 3.8 below. After a 2 minute incubation at 50 °C to eliminate RNA residues, denaturation was performed at 95 °C for 10 min, then amplification was performed at 95 °C or 15 seconds and 60 °C for 1 minute.

Table 3.8 PCR Cycling conditions.

CYCLES	TEMPERATURE	TIME	PURPOSE
1	50 °C	2 min	RNA decontamination
1	95 °C	10 min	Initial Denaturation
40	95 °C	15 s	Denaturation
	60 °C	1 min	Annealing/ Extension

Data were analysed with a 7500 Software (Applied Biosystems) by relative quantification analysis using the comparative threshold cycle (C_t) method ($\Delta\Delta C_t$ method) (325). This is a very popular technique that compares results from experimental samples with both a calibrator (*e.g.,* untreated sample) and a normalizer (*e.g.,* housekeeping gene). With this method, C_t values for the gene of interest (GOI) in both the test sample and the calibrator sample are adjusted in relation to a normalizer (norm) gene C_t from the same two samples. The resulting $\Delta\Delta C_t$ value is incorporated to determine the fold difference in expression.

$$\text{Fold difference} = 2^{-\Delta\Delta Ct}$$

$$\Delta C_{t\ \text{sample}} - \Delta C_{t\ \text{calibrator}} = \Delta\Delta C_t$$

$$C_{t\ \text{GOI}}{}^{s} - C_{t\ \text{norm}}{}^{s} = \Delta C_{t\ \text{sample}}$$

$$C_{t\ \text{GOI}}{}^{c} - C_{t\ \text{norm}}{}^{c} = \Delta C_{t\ \text{calibrator}}$$

In this work, we considered as a normalizer the mean of C_t values of 8 housekeeping genes (*Eif1, Rpl13a, Gapdh, Rplp0, Ywhaz, Actb, 18s, Pgk1*) for the sample of interest, and as a calibrator a sample which expressed all the genes analyzed (Table 3.9).

Table 3.9 Summary of gene symbol, accession number, product length and primer sequences of the housekeeping genes.

Symbol	Name	Accession	Size (bp)	Sequence of nucleotides (5'⟶3')	
Eif1	Eukaryotic translation initiation factor 1	NM_011508	186	**Forward**	AAGGGCTACCTTTCCAGAGA
				Reverse	GCACTGGCTCGTACTGAGTT
Rpl13a	Ribosomal protein L13A	BC086896	215	**Forward**	ATGACAAGAAAAAGCGGATG
				Reverse	CTTTTCTGCCTGTTTCCGTA
Gapdh	Glyceraldehyde-3-phosphate dehydrogenase	BC083080.1	223	**Forward**	CTGGAGAAACCTGCCAAGTA
				Reverse	TGTTGCTGTAGCCGTATTCA
Rplp0	Ribosomal protein, large, P0	NM_007475	202	**Forward**	AACCCAGCTCTGGAGAAACT
				Reverse	GGAAGAAGGAGGTCTTCTCG
Ywhaz	Tyrosine 3-monooxygenase/ tryptophan 5-monooxygenase activation protein, zeta polypeptide	NM_011740	181	**Forward**	AGCAGGCAGAGCGATATGAT
				Reverse	TTCTCAGCACCTTCCGTCTT
Actb	Actin, beta	NM_007393	160	**Forward**	AAGAGCTATGAGCTGCCTGA
				Reverse	TACGGATGTCAACGTCACAC
18s	18s ribosomal RNA	NR_003278	298	**Forward**	ATTCCGATAACGAACGAGACT
				Reverse	AGCTTATGACCCGCACTTACT
Pgk1	Phosphoglycerate kinase 1	NM_008828	185	**Forward**	GCAGATTGTTTGGAATGGTC
				Reverse	TGCTCACATGGCTGACTTTA

3.2.7.6 Gene expression analysis to investigate effect of device culture

To identify potential effects of the microfluidic environment on embryo development, the expression of 53 genes associated with blastocyst developmental competence was measured using array qPCR. Gene expression was measured for blastocysts cultured in the microfluidic device or in traditional microdrop culture. Specifically, 10 expanded blastocysts were analyzed for each experimental group. Particular interest was addressed to marker genes involved in ICM/epiblast development including Nanog homeobox, *Nanog* (326), Signal transducer activator of transcription 3, *Stat3* (327), POU domain, class 5, transcription factor 1, *Pou5f1* (328), sal-like 4 (Drosophila), *Sall4* (327), GATA binding protein 6, *Gata6* (329), or trophoblast differentiation (sno, strawberry notch homolog 1, *Sbno1* (330), Kruppel-like factor 5, *Klf5* (331), caudal type

homeobox, *Cdx-2* (326), TEA domain family member 4, *Tead4* (332) and E74-like factor, 5 *Elf5* (333), GATA binding protein 3, *Gata3* (334), keratin 18, *Krt18* (326). A summary of gene accession number, size and primer sequence of nucleotides is presented in Table 3.10.

Table 3.10 Summary of gene symbol, accession number, product length and primer sequences of the target genes.

Symbol	Name	Accession	Size (bp)	Sequence of nucleotides (5'⟶3')	
Nanog	Nanog homeobox	NM_028016	207	**Forward**	GGACAGGTTTCAGAAGCAGA
				Reverse	CAATGGATGCTGGGATACTC
Stat3	Signal transducer activator of transcription 3	NM_213659	187	**Forward**	ATCTGTAACCACAGGGCAAA
				Reverse	GTAAGCTGAGTGAGCGAAGC
Pouf5f1	POU domain, class 5, transcription factor 1	NM_013633	160	**Forward**	AAGCAACTCAGAGGGAACCT
				Reverse	GGTGATCCTCTTCTGCTTCA
Sall4	sal-like 4 (Drosophila)	NM_175303	125	**Forward**	TTAAGCAGCCATGTGTCTCA
				Reverse	GGTAGCTTGGCTTGTTTCAA
Gata6	GATA binding protein 6	NM_010258	168	**Forward**	TAGAAATGCTGAGGGTGAGC
				Reverse	ACAGAGCCACTGCTGTTACC
Sbno1	sno, strawberry notch homolog 1	NM_001081203	193	**Forward**	GCAGCTGAGCTTTACTGGAG
				Reverse	CTGGTGAGCAGACCAGAACT
Klf5	Kruppel-like factor 5	NM_009769	248	**Forward**	CACCATGCCAAGTCAGTTTC
				Reverse	TCTCCAGATCCGGGTTACTC
Cdx2	caudal type homeobox 2	NM_007673	150	**Forward**	TCAGGGGAAGACATGGTTTA
				Reverse	AGGCTGATAGCTTCATGTCG
Tead4	TEA domain family member 4	NM_011567	62	**Forward**	TCACCTGCTCTACGAAGGTC
				Reverse	CTCCGTCTCAACTTTCTCCA
Gata3	GATA binding protein 3	NM_008091	189	**Forward**	CCCTTTATTCCTCCGTGTCT
				Reverse	GAGAGGGGTCGTTTAATGGT
Elf5	E74-like factor 5	NM_010125	112	**Forward**	GTGCACCCTGAATACTGGAC
				Reverse	CGCTGATGTTGAAGTGACAG
Krt18	Keratin 18	NM_010664	173	**Forward**	ACCTGAGGGCTCAGATCTTT
				Reverse	GGTGTCATCTACCACCTTGC

3.2.7.7 qPCR array of blastocysts cultured in conditioned media

To investigate the effect of conditioned media, the gene expression profiles of blastocysts cultured in the device using conditioned media and using control KSOM were compared. A bespoke primer library was used, which included

primer sequences for 96 different genes associated with blastocyst development and cell differentiation after the pluripotent mid-pre-implantation stages.

3.2.8 Mass spectrometry of spent media samples

In order to identify changes in metabolomic profiles of embryos induced by the microfluidic environment and to assess the effects of culture in uterine epithelial-cells conditioned media, MS analysis was performed on media samples collected from microfluidic devices and from microdrops (control). The analysis was performed by reverse phase liquid chromatography and untargeted tandem mass spectrometry analysis (RPLC-MS/MS) using facilities at the Centre for Innovative Technology (CIT) at Vanderbilt University in Nashville, US (Figure 2.6). The procedures used for sample preparation, sample analysis and data analysis are described in the sections below.

3.2.8.1 Embryo culture and sample collection

For microdrop culture, groups of 10 embryos were cultured in individual oil-covered 40 µL drops in PS dishes at 37 °C under 5% CO_2, 5% O_2 in a humidified nitrogen atmosphere. Embryos were cultured from 1-cell to the expanded blastocyst stage. At the end of the culture, typically on day 4, medium was aspired from the microdrop, carefully avoiding contact of the pipette tip with the mineral oil, and kept at -80 °C before MS analysis.

Similarly, for device culture, groups of 10 embryos were cultured in each microfluidic device from 1-cell to the expanded blastocyst stage. To prevent media evaporation, 20 µL drops of media were added to inlet and outlet ports of the device. At the end of culture, typically on day 5, the total 40 µL of medium were collected from each device (including the 20 µL drops of media added onto inlet and outlet ports) and kept at -80 °C before MS analysis.

In this experiment, three biological replicates were considered for each experimental groups: group 1 - samples of spent media from microdrops; group 2 - samples of spent media from microfluidic devices; group 3 - samples of spent conditioned media from microdrops; group 4 - samples of spent conditioned media from microfluidic devices.

3.2.8.2 Metabolite extraction

All solvents used for metabolite extraction (methanol (MeOH), water (H_2O), acetonitrile (ACN), Ammonium Bicarbonate and formic acid (FA)) were LC-MS grade (Fisher Scientific, Fair Lawn, NJ, USA). Aliquots of each media sample (100 µL) were added to a new Eppendorf tube containing 100 µL ice cold lysing buffer (1:1:2, ACN:MeOH:Ammonium Bicarbonate (0.1M, pH 8.0). Heavy labelled standard molecules, Biotin-D2 and Phenylalanine-D8, were added to each sample as a measure of process variability and to help later assess the metabolite extraction quality. Samples were subjected to protein precipitation by addition of 800 µL of ice cold methanol (4x by volume), then vortexed for 30 s and incubated at -80 °C overnight. On the next day, samples were centrifuged at 10,000 rpm for 10 min to eliminate methanol precipitated proteins and the metabolite containing supernatant was dried via speed-vacuum and stored at -80 °C until further LC-MS analysis.

3.2.8.3 Global, Untargeted UHPLC-MS/MS Analysis

Dried extracts were reconstituted in 60 µL of 98:2 H_2O:ACN with 0.1% formic acid for RPLC analysis, and centrifuged for 5 min at 5,000 rpm to remove insoluble material. Heavy labelled standard molecules, Tryptophan-D3, Carnitine-D9, Valine-D8 and Inosine-4N15, were added to each sample as a measure of the instrument variability to help with the quality assessment of the MS analysis. Quality control (QC) samples were prepared by pooling equal volumes from each experimental sample. Full MS (FMS) data was acquired for this QC pool, in RPLC positive method, to use as a retention time alignment reference within Progenesis QI for subsequent normalization and data quantitation. MS/MS (data dependent) acquisitions for pooled QCs were run to assess instrument performance over time and used for feature annotation.

The instruments were set by the CIT collaborators following quality approved protocols. MS analyses were performed on a Q-Exactive HF hybrid mass spectrometer (Thermo Fisher Scientific, Bremen, Germany) equipped with a Vanquish UHPLC binary system and autosampler (Thermo Fisher Scientific, Germany). Full MS analyses were acquired under an ESI positive profile mode. Data dependent MS/MS spectra were acquired using a data dependent scanning mode in which one full MS scan (m/z 70-1050) was followed by 2, 4 or 6 MS/MS scans. To assess instrument performance and reproducibility throughout the

entire experimental run sequence, the retention times and peak areas for the heavy labelled molecules spiked in before and after the metabolite extraction were monitored. These data demonstrate the reliability of the UHPLC-MS/MS platform minimizing the importance of technical replicates (335).

3.2.8.4 Metabolite data processing and analysis

Data analysis has been performed as described previously (186,285,336,337). Briefly, UHPLC-MS/MS raw data were imported, processed, normalized, and reviewed using Progenesis QI v.2.1 (Non-linear Dynamics, Newcastle, UK). All data file was imported as an ion intensity map (used for visualization in both m/z and retention time dimensions) and all FMS sample runs were aligned against a FMS QC pool reference, with alignment to the reference being ≥ 96%, demonstrating the reproducibility of the RPLC column separation method. Peak picking, with a minimum threshold of 100,000 ion intensity, was performed for individual aligned runs based on an aggregate run (representative of all ion peaks detected in all samples). Following peak picking, unique ions (retention time and m/z pairs) were grouped (a sum of the abundancies of unique ions) using both adduct ([M + H]+, [M + Na]+ , [M + K]+ , etc.) and isotope deconvolutions to generate unique “features” (retention time and m/z pairs) representative of unannotated metabolites. Data were normalized to all features using Progenesis QI. Briefly, all runs have a measurement for every feature ion, therefore a ratio can be calculated for the feature ion abundance in a particular run relative to the value in the normalization reference. Progenesis applies a Log10 transformation to the ratio to yield a normal distribution on all ratio data within each run for all samples, and scalar estimations shift the Log10 distributions onto that of the normalization reference. Resulting FMS data was utilized for relative quantitation. Compounds with <20% coefficient of variance (%CV) (calculated within all FMS QC pool injections) were retained for further analysis.

Principle Components Analysis (PCA) was used to visualize clustering of data groups (all features included) prior to statistical tests of significance. Additionally, within Progenesis QI, a one-way analysis of variance (ANOVA) test was used to assess significance between groups and returned a *p*-value for each feature (retention time_m/z descriptor), with a nominal *p*-value ≤ 0.05 required for

significance. Significant features were further filtered using a fold change (FC) threshold calculated by Progenesis from combined abundance data, with a cut-off of FC ≥ |2| deemed as significant. Visualizations of dysregulated metabolites were represented by volcano plots (log2 (fold change) *vs.* -log10 (*p*-value)). Feature lists generated from different individual comparisons were visually compared using Venn diagrams generated by the Venny software package.

Tentative and putative annotations were determined within Progenesis using accurate mass measurements (<5 ppm error), isotope distribution similarity, and manual assessment of fragmentation spectrum matching (when applicable) from the Human Metabolome Database (HMDB) (338), Metlin (339), MassBank (340), and the National Institute of Standards and Technology (NIST) database (341). The MetaboAnalyst 3.0 program (www.metaboanalyst.ca) was used for pathway and metabolite set enrichment analyses using the list of statistical significance annotated features in the discovery dataset (186,342). Increased confidence in the annotation of many features was achieved by manually assessing spectral match and retention time consistencies between experimental data and chemical standards within a curated in-house library (285,335).

3.2.9 Statistical analysis

Data were analysed using GraphPad Prism 8 software. For statistical analysis of embryonic cleavage and blastocyst development all data sets were first tested for fit to the normal distribution by D'Agostino-Pearson test for normality. All normal data sets were compared by Student's t-test, while all non-parametric data were compared by Mann-Whitney U test. In all instances, significance was determined as $p < 0.05$.

qPCR results were analysed by the comparative threshold cycle (C_t) method (325). Relative expression ratios were obtained using as internal control the mean of C_t values of eight housekeeping genes from the sample of interest. Student t-test statistics was used to compare gene expression levels between samples from the different groups. Gene expression fold differences with $p<.05$ were considered statistically significant.

For MS, compounds with < 20 % coefficient of variance (% CV) were retained for further analysis. Within Progenesis QI, a one-way analysis of variance (ANOVA) test was used to assess significance between groups and returned a

p-value for each feature (retention time_m/z descriptor), with a nominal *p*-value ≤ 0.05 required for significance. Significant features were further filtered using a fold change threshold ≥ |2| deemed as significant.

3.3 Results and Discussion

3.3.1 Device design and fabrication

The microfluidic device presents a central culture chamber connected to two fluidic ports by microfluidic channels (Figure 3.4). The device dimensions were chosen in accordance to mouse embryos size which range from approximately 100 µm for expanded blastocyst and 150 µm for hatched blastocyst (290). Details of the dimensions of the device are presented in Table 3.11.

Table 3.11 Inlet and outlet cross-section dimension (width × height, w × h) for the proposed design.

Inlet cross-section dimension [w × h]	250 x 200 µm
Outlet cross section dimension [w × h]	(200^1, 150^2, 100^3) x 30 µm
Number of outlet channels	5
Flow rate necessary to guarantee WSS below 1.2 dyn cm^{-2}	13.91 µL/min (Re=1.03)*

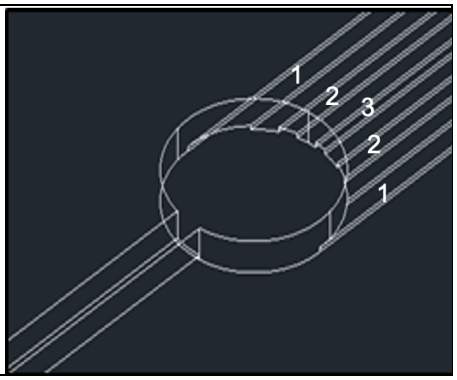

*Reynolds number for a square channel with width *w* (*Re* = $\boldsymbol{\rho Q/\eta w}$)

[1] External outlet channels, [2] Middle channels, [3] Central outlet channel

The culture chamber contains a medium volume of 400 nL, thus significantly reduced compared to the traditional 5-50 µL used in microdrop cultures, and even below the limit of 1.5-2 µL used in ultramicrodrops. The inlet and outlet channels present different height and are positioned at different levels: the single inlet channel is 200 µm in height and 250 µm in width. These dimensions allow the embryos to be loaded and to reach the culture chamber, where they cannot flow any further. The narrow outlet channels are at lower level and have height of 30 µm, thus smaller than the size of a mouse embryo at early stage of development (diameter approximately 60 µm (290)). The outlet channels have different widths: the two most external channels are 200 µm wide, the two middle channels are 150 µm wide and the central channel is 100 µm wide. This specific design was adopted to optimize the flow profile within the culture chamber as discussed below in Section 3.3.1.1. The choice of designing five narrow outlet channels instead of one single outlet channel as wide as the culture chamber diameter, which would equally allow to improve the flow profile within the device, was

dictated by fabrication requirements, *i.e.*, the need to prevent PDMS structure from collapse. Indeed, the presence of five channels with an height/width ratio less than 1:10 was found to be the optimum compromise in terms of fabrication limits and optimal flow rate profile.

After loading, embryos are left undisturbed to grow up to blastocysts (diameter approximately 100 μm) and then aspirated back from the inlet channel for further analysis or, considering the final use in IVF, to proceed with the transfer to the recipient mouse. The final device measures four by four cm and can be placed in an IVF 60 mm Petri dish, sterilized and used in a MINC™ Mini incubator (Figure 3.2).

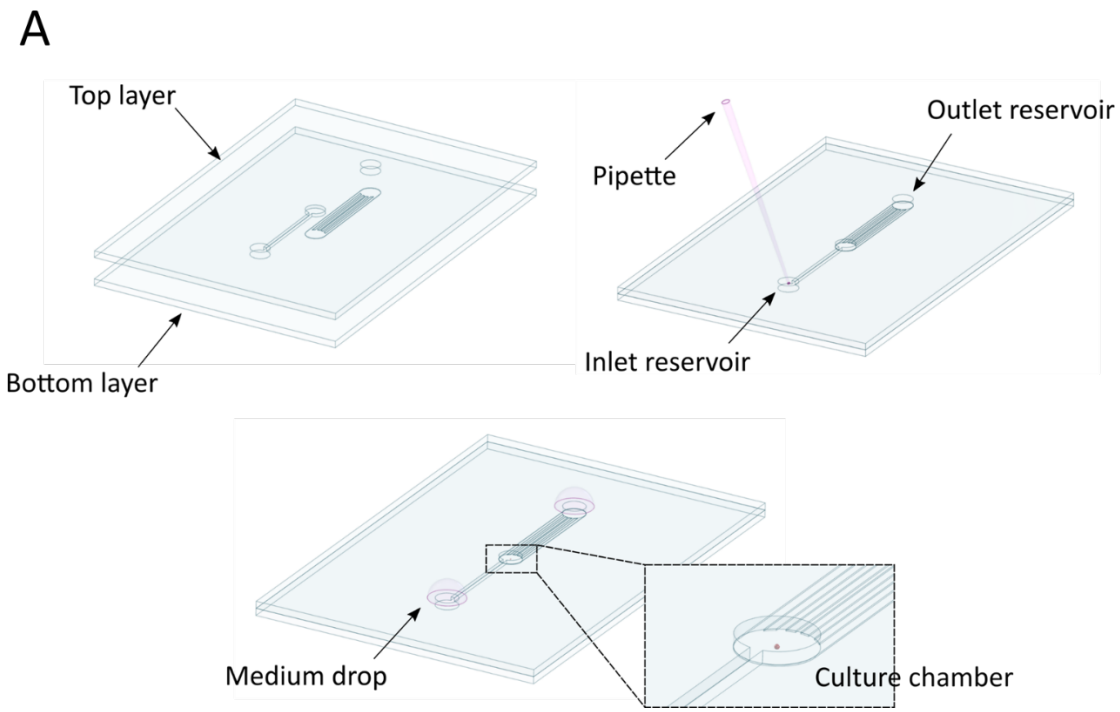

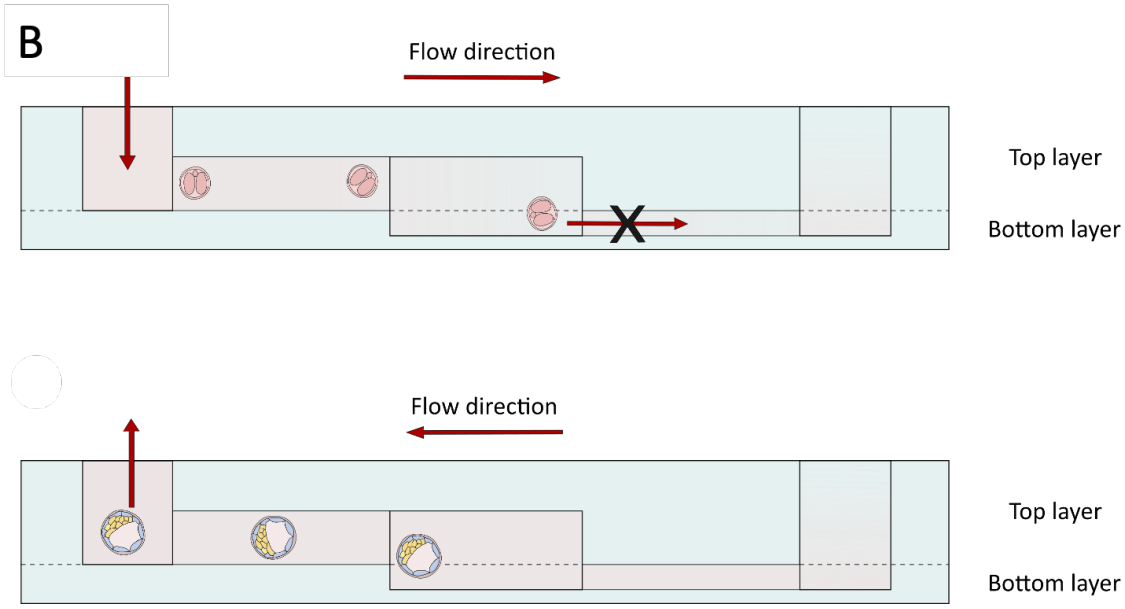

Figure 3.4 Microfluidic device design.

A) The device consists in two PDMS layers containing the features of the culture chamber (400 nL) and of the microfluidic channels characterized by two different heights. B) Schematic drawing of the novel microfluidic device. top) Embryos are introduced from the inlet port, guided by the pipette pressure and the capillarity force in the culture chamber through the inlet channel. bottom) Developed blastocysts are then aspirated back from the inlet port.

3.3.1.1 Flow and loading simulations and analysis

The criteria for the design were:

- to minimize wall shear stress (WSS) within the channels during loading and retrieval, considering as maximum threshold WSS value 1.2 dyn cm^{-2}, which has been reported to cause lethality within 12 h for E3.5 blastocysts (343).
- to facilitate a fast loading of the embryos into the main chamber and to avoid clustering into the inlet channel.
- to favour the spreading of the embryos into the main chamber maintaining close proximity between embryos, to exploit benefit of secreted embryotrophic factors (53).

From flow characterization experiments performed using fluorescent beads, the maximal velocity in the inlet channel was estimated to be respectively about 0.4 mm s^{-1} which corresponds to a flow rate equal to 1.17 µL min^{-1} (Re = 0.087). The design of the device allows for the capture of the embryos in the middle chamber thanks to the increased hydraulic resistance encountered when reaching the chamber, which prevents embryos to be stressed by lethal WSS

during loading into the device (344). Indeed, the WSS generated within the channel during loading and retrieval reaches maximum values of 0.17 dyn cm^{-2}, which is seven times lower than harmful values presented in literature (343) (Figure 3.5A). Critical values of shear stresses (~3.5 dyn cm^{-2}) were only found at the edges of the interface between the culture chamber and the outlet channels, although those areas cannot be reached by the embryos due to the narrow outlet channels dimensions (Figure 3.5B). During fluid loading, the velocity profile in the inlet channel (hydraulic resistance in the order of 10^{10} Pa s m^{-1}) is significantly reduced in the culture chamber (where an evenly blue spectrum is obtained, Figure 3.5B). In contrast, in the outlet channel the velocity increases above the initial value, due to an increased hydraulic resistance ($\propto 10^{12\text{-}13}$ Pa s m^{-1}). Fluid velocity profiles are similar in the inlet and outlet channels. For simulation purposes, those results were obtained using COMSOL by modelling the flow behaviour and properties in the device without including the presence of the embryos.

Importantly, the device design was also chosen to adapt the width of the outlet channels to the width of the culture chamber, thus the resulting velocity profile along the cross-sectional direction of the culture chamber is relatively wide. This favours the spreading of the embryos in the whole chamber and ensures a homogeneous perfusion of medium in the chamber. Moreover, the flow characterization of fluorescein diffusion suggested an homogeneous distribution of soluble nutrient factors within the chamber (Figure 3.5D). Those results are promising considering that previous data demonstrated that the culture of embryos at a specific reciprocal distance of approximately 165 µm enhances embryo growth by favouring paracrine signalling between embryos, and avoiding detrimental accumulation of secreted products in the medium surrounding them (345).

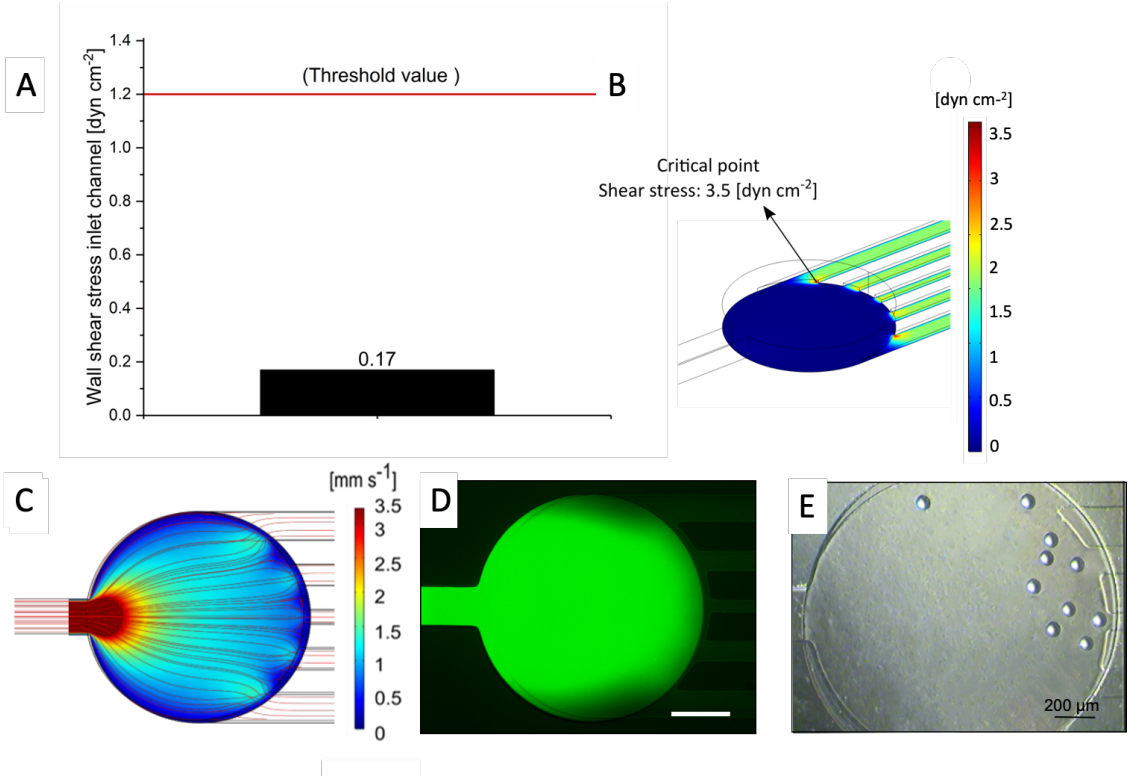

Figure 3.5 COMSOL simulations and flow characterization within the culture chamber.

A) Computational estimation of the wall shear stress in the inlet channel in dyn cm^{-2} is below the threshold value of 1.2 dyn cm^{-2} (represented by the right line in the graph). B) The fluid flow computational model of shear stress field surface plot during manual loading shows a maximum value of 3.5 dyn cm^{-2} at the beginning of the outlet channels, an area that the embryos cannot reach. The colour spectrum bar shows the shear stress field ranges between 0 and 3 dyn cm^{-2}. C) Velocity magnitude surface (in colours) and stream lines (in red) plot shows the fluid velocity generated in the culture chamber; The colour bar ranges between 0 and 3.5 mm s^{-1}. D) Single frame showing fluorescein diffusion within the culture chamber during real flow characterization (scale bar 400 μm). E) Brightfield image showing polystyrene beads at equilibrium spreading within the culture chamber (scale bar 200 μm).

The culture conditions within the microfluidic device are static, thus the transport of nutrients occurs mainly by diffusion between the embryo's culture chamber and the inlet/outlet ports. The microfluidic device provides a confined microenvironment which ensures local accumulations of growth factors secreted by the embryos that promote their development and the formation of gradients of nutrients in the embryo environment, as found *in vivo*. Beneficial autocrine factors, such as leukemia inhibitory factor (346), insulin-like growth factor (347), epidermal growth factor (EGF) (348) and platelet derived growth factor (349), accumulate in the close proximity of the embryos, while a very slow diffusion occurs along the channels from the medium drops.

As a measure of the diffusion process within the device, the time taken by a molecule to diffuse over the whole length of the device (18 mm), can be calculated from the formula (350,351):

$$t = \frac{x^2}{2D} \quad (3.1)$$

Where *t* is the diffusion time (s), *x* is the distance between inlet and outlet ports (m) and *D* the molecular diffusion coefficient for the molecule of interest (cm^2/s). For instance, at 37 °C the diffusion coefficient of glucose in water is 9.59×10^{-6} cm^2/s, thus the estimated diffusion time in the device is 17 s. In the case of EGF, which is known to be a relevant growth factor for embryo development, D is 1.66×10^{-10} cm^2/s (352), thus the diffusion time is around 271 h. Similarly, the estimated diffusion time in the device for other small molecules, such as amino acids (D ~ 1×10^{-10} cm^2/s) (353) is around 450 h.

In term of oxygen transport, this first occurs in the device by diffusion at the medium drop/air interface and then by diffusion through the media to the embryos. Additionally, since PDMS is gas permeable (oxygen diffusion coefficient: 3.5×10^{-10} cm^2/s), diffusion occurs also through the PDMS layer to the media.

From these considerations can be deduced that, in the device, a fine balance exists between the amount of essential (e.g., growth factors) and deleterious molecules released by the embryos themselves, as well as the availability of the right physical conditions (such as availability of nutrients and oxygen).

3.3.2 Embryo culture and blastocyst development

Assessment of morphology at distinct time points is regularly used for evaluating embryos quality. In this work, developmental quality of *in vitro* cultured mouse embryos was assessed by measuring early cleavage rate (occurring on average at 24 h after pronuclear fusion), blastocysts rate and hatching rate. Successively, gene expression analysis of individual blastocysts was performed by real-time PCR (qPCR) to assess the effect of the microfluidic environment on embryo development.

3.3.2.1 Cleavage, blastocyst and hatching rate measurements

Measurement of cleavage, blastocyst and hatching rates were used to compare developmental competence of mouse embryos cultured in the microfluidic device or in traditional microdrop culture. As summarized in Figure 3.6, embryo development was not altered in the microfluidic system, compared to traditional culture. No significant differences in terms of cleavage rate rates (94.62 ± 1.7%, n=30 vs control 94.84 ± 1.08%, n=30, p=0.48), blastocyst rates (90.48 ± 3.2%, n=30 vs control 86.40 ± 4.6%, n=30, p=0.6) and hatching rates (32.18 ± 10.35%, n=30 vs control 46.61 ± 10.28%, n=30, p=0.32) were observed between the two culture systems.

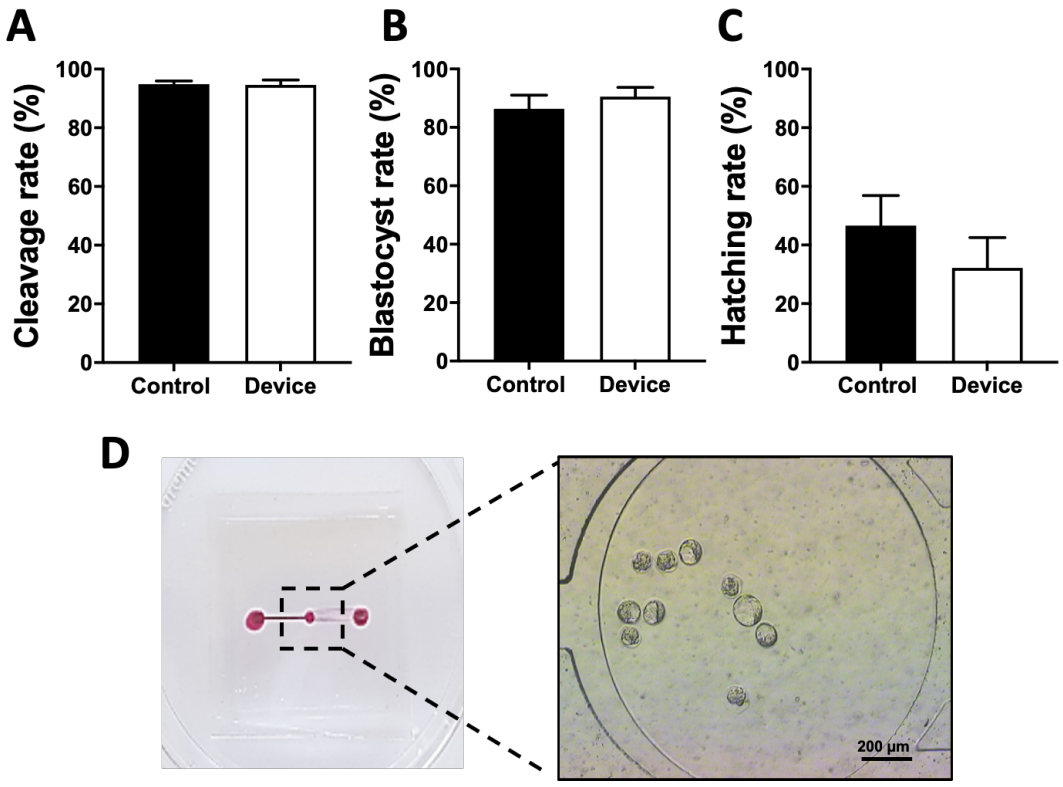

Figure 3.6 Comparison of pre-implantation embryo development achieved with microdrop culture and microfluidic device.

Cleavage rates (%) (n=30, A), blastocyst rates (% out of total embryos cultured) (n=30, B) and hatching rates (% out of total blastocysts) (n=30, C) achieved with microdrop culture (in black) and microfluidic device (in white). Bars represents standard deviations. D) Picture of the microfluidic device with a magnification of the chamber showing murine blastocysts at day 4 of culture.

3.3.2.1 Gene expression analysis to investigate effect of device culture

Figure 3.7 shows relative abundance of 53 different genes associated with blastocyst developmental competence measured using array qPCR. Specifically,

relative expression of selected marker genes involved in trophectoderm differentiation or ICM/epiblast development, including *Sbno1*, *Klf5*, *Cdx2*, *Tead4*, *Gata*, *Elf5*, *Krt18*, *Stat3*, *Nanog*, *Pou5f1*, *Sall4*, *Gata6*, was observed in each analysed blastocyst (Figure 3.8). Relative transcript abundance of those genes was relatively different between blastocysts cultured in the microfluidic device and those cultured in traditional microdrops, with high variability within each experimental group. Those results could be justified by the reduced sample size (number of expanded blastocysts for each experimental group) and need to be further investigated, particularly to explore the effect of each specific genetic alteration on embryo function and development.

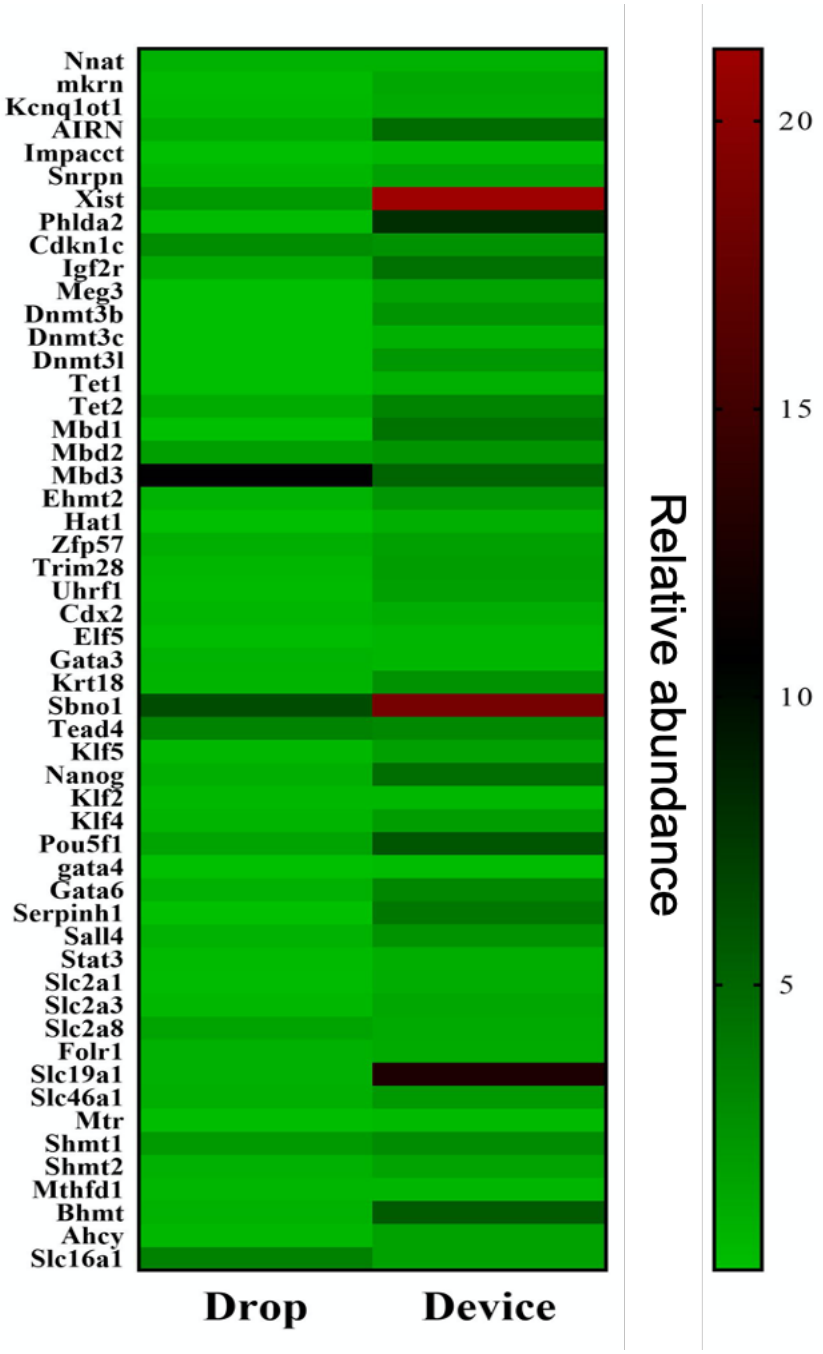

Figure 3.7 qPCR results of genes associated with blastocyst development.

Heatmap representing gene expression of mouse blastocysts cultured in the device compared to microdrop culture. Scale bar ranges from red for high expression (20) and green for low expression (0).

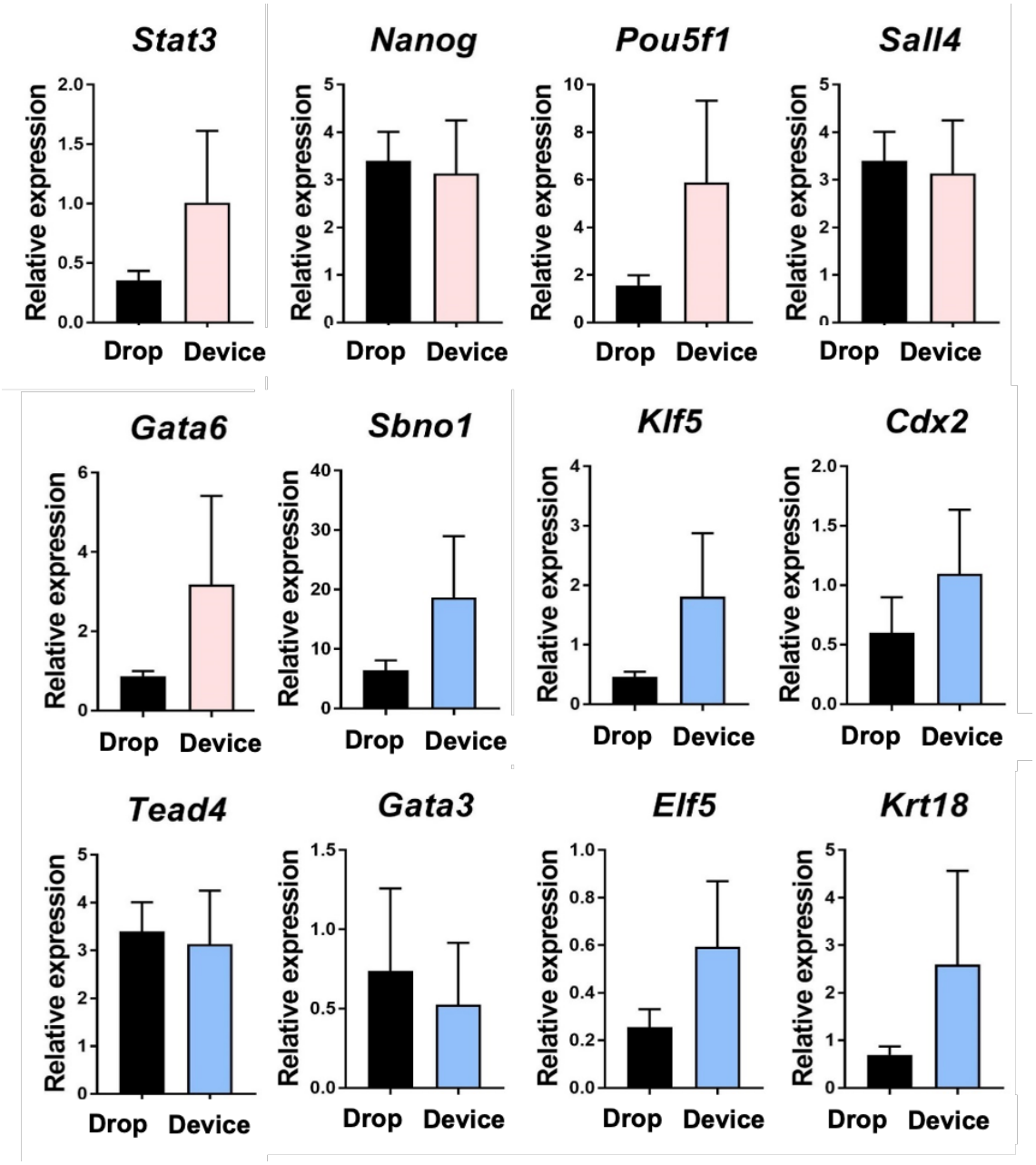

Figure 3.8 qPCR results of genes associated with blastocyst development.

Relative mRNA expression of selected genes (pink: markers of ICM/epiblast differentiation; blue: markers of trophectoderm differentiation) in expanded blastocysts cultured in the device (light blue bars), compared with control (black bars). Data are presented as mean ± SEM. Number of blastocysts examined in each group = 10.

3.3.3 Effect of cells-conditioned media on embryo development

Effect of conditioned media (KSOM cm) on blastocyst development was first assessed by measuring cleavage and blastocysts rates of embryos cultured in devices or traditional microdrops. Results were compared with culture in control media (KSOM). Cleavage rates were comparable for embryos cultured in drops and in devices. In drops, cleavage rates were 96.89 ± 1.59% (N=10) and 95.09 ±

1.64% (N=10) for embryos cultured in conditioned media and control media, respectively. In devices, cleavage rates were 98.7 ± 0.7% (N=23) and 94.9 ± 2.7% (N=21) for embryos cultured in conditioned media and control media, respectively. In terms of blastocyst rate, results were relatively different between drops and microfluidic devices. In drops, the use of conditioned media had no effect on blastocysts development and blastocyst rates were 92.1 ± 2.5% (N=10) for embryos cultured in KSOM and 85.4 ± 3.9% (N=10) for those cultured in conditioned media. In contrast, blastocysts rates were 54.6 ± 6.6% (N=19) and 71.8 ± 4.3% (N=20) for embryos cultured in devices using KSOM or conditioned media, respectively (Figure 3.9A,B).

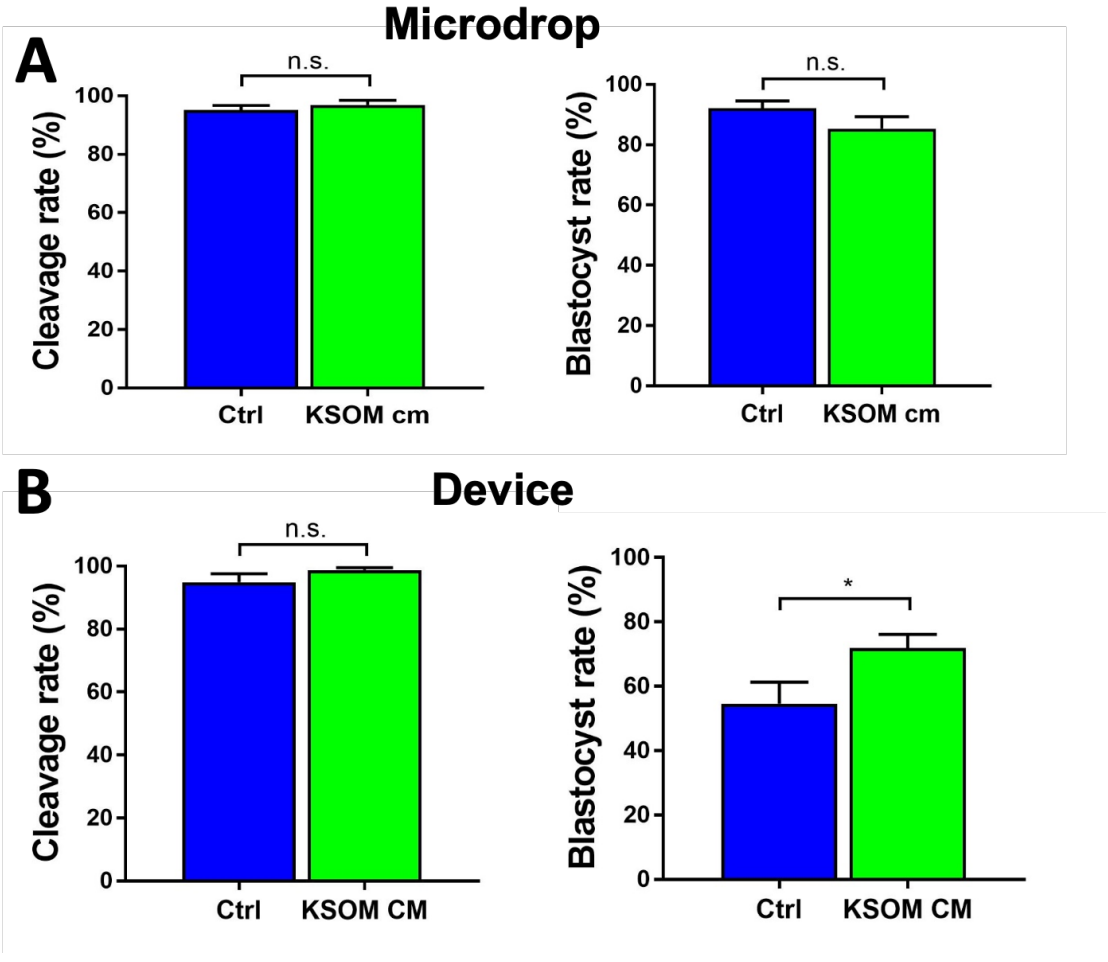

Figure 3.9 Effects of CM on embryo development.

Cleavage rates (left) and blastocyst rates (right) of embryos cultured in drops (A) or in microfluidic devices (B). Data presented as mean ± SEM. *=p<0.05.

The level of blastocyst rates observed in microfluidic devices compared to control microdrops was lower than the one obtained in the previous experiment. This can be ascribed to the different mouse strains used for this experiment, the

different batches of media and the intrinsic variability observed in literature for mouse embryo blastocysts rate (114,354). These values are however still comparable (293) or higher (299) than the ones achieved with other comparable microfluidic systems. In particular, results showed that in devices the use of cells-conditioned media, significantly (p=0.037) improved blastocyst production compared to control KSOM. This might be associated with the reduced culture volume and optimized biomolecule gradients provided by the device microenvironment which better resembles that found *in vivo*. Biomolecules and growth factors produced by cells and present in the conditioned media might have a greater effect on embryos cultured in such reduced volume, rather than in bigger culture drops, because of reduced embryo-to-media ratio and optimized gradients.

3.3.3.1 qPCR array of blastocysts cultured in conditioned media

Array qPCR results of blastocysts cultured in microfluidic devices or traditional microdrops revealed that the use of conditioned media had a considerable effect on gene expression profile (Figure 3.10). Among the 96 genes analysed using the bespoke primer array, significantly (p<0.05) altered expression of several genes, including Kcnq1 overlapping transcript 1 (*Kcnq1ot1*, p=0.005), DNA Methyltransferase 3b (*Dnmt3b*, p=0.006), DNA Methyltransferase 3C (*Dnmt3c*, p=0.048), Methyl-CpG Binding Domain Protein 3 (*Mbd3*, p=0.031), Histone Acetyltransferase 1 (*Hat1*, p=0.006), and Caudal Type Homeobox 2 (*Cdx2*, p=0.058) was observed between blastocysts cultured in devices using conditioned media (KSOM cm) or control media (KSOM) (Figure 3.10A).

In particular, 5 genes (*Dnmt3b, Dnmt3c, Mbd3, Hat1, Cdx2*) had significantly (p<0.05) increased expression in blastocysts cultured in conditioned media compared to KSOM, whereas only the imprinting gene *Kcnq1ot1* had significantly decreased expression in conditioned media. Additionally, differential expression of other two genes, Neuronatin (*Nnat*, p=0.059) and Makorin Ring Finger Protein (*Mkrn*, p=0.064), showed a trend toward significance. While *Nnat* had increased abundance in the conditioned media group, *Mkrn* was highly abundant in blastocysts cultured in control media. Those results indicated that the majority of genes differentially expressed between the two experimental groups were up-

regulated in blastocysts cultured in the microfluidic device using conditioned media.

Some of those genes are associated with key epigenetic and genomic imprinting mechanisms. For instance, the two DNA (cytosine-5)-methyl-transferases *Dnmt3b* and *Dnmt3c* are directly involved in DNA methylation, an epigenetic mechanisms required for regulating gene expression and maintaining genomic integrity, which is essential for normal embryonic development (355). This process consists in adding a methyl group to the fifth carbon atom of cytosine residues within cytosine-phosphate-guanine (CpG) and non-CpG dinucleotides sites, representing the only known epigenetic modification of the mammalian genomic DNA. DNA methylation functions in various biological phenomena (356,357) and is catalysed by specific DNA methyltransferases (DNMTs) enzymes. To date, five different DNMTs, DNMT1, DNMT2, DNMT3A, DNMT3B, DNMT3L, have been identified in mammals (358). Specifically DNMT1 is involved in the maintenance methylation, while the DNMT3A and DNMT3B enzymes are essentially responsible for carrying out *de novo* methylation in embryonic stem cells and during embryonic development (359,360). Additionally, the DNMT3B enzyme is exclusively specialized for methylation of the CpG dinucleotides in the repeated DNA sequences present in the pericentric satellite regions of chromosomes (360,361). The knockout of the *Dnmt3b* gene has shown to cause embryonic lethality (360). Furthermore, studies demonstrated that mutations in the DNA methyltransferase gene *Dnmt3b* can cause ICF (Immunodeficiency, Centromeric instability and Facial anomalies) syndrome, which is a rare autosomal recessive disease (362), and that DNMT3B protein is essential for the survival of T cells in the thymus of newborn mice (363). It is also known that the DNA *de novo* methylation mechanisms may contribute to the differentiation of the ICM and TE at the blastocyst stage (364) and that the DNMT3B protein is specifically localized in the ICM of mouse blastocysts (365). Another DNA methyltransferase gene, *Dnmt3c,* has recently been identified as a new member of the *Dnmt3* family in mice. This gene is required for the methylation and repression of retrotransposon in the male germ line, thus essential for mouse fertility (366). From these considerations, is possible to deduct that the increased expression of the *Dnmt3b* and *Dnmt3c* genes in blastocysts cultured in the

microfluidic device using conditioned media may suggest a beneficial effect of the media in supporting mouse pre-implantation embryo development *in vitro*.

In terms of functions of the other differential expressed genes, *Nnat, Mkrn* and *Kcnq1ot1* are imprinted genes, thus genes that are expressed differently on maternal and paternal chromosomes. Those genes have an important role in embryo development, fetal growth and behaviour after birth (367). Specifically, *Nnat*, a paternally expressed imprinted gene found in neuroendocrine systems, plays important roles in neuronal differentiation in the brain and in glucose-mediated insulin secretion in pancreatic β cells (368–370). However, specific function of *Nnat* on pre-implantation mouse embryo development remains undefined. *Mkrn1* gene acts downstream of *Oct4*, a transcriptional factor which has a role in establishment and maintenance of totipotency or pluripotency of embryonic and undifferentiated stem cells (371). *Mkrn1* expression has been reported in murine embryonic nervous system and testis, suggesting its important role in embryonic development and neurogenesis (372). *Kcnq1ot1* has a role in the maintenance of transcriptional gene silencing (373) and also in the regulation of imprinting domains, but its function in imprinted gene regulation during embryo pre-implantation development is not fully understood yet (374). However, hypomethylation of *Kcnq1ot1* has been identified as the underlying molecular mechanism of Beckwith-Wiedemann syndrome (BWS) disease. This is an heterogeneous congenital overgrowth syndrome resulting from genetic and epigenetic alterations (375,376), which has also been considered among the imprinting disorders that could emerge in children conceived by ART (377).

Similarly to *Dnmt3b* and *Dnmt3c*, *Mbd3* and *Hat1* genes represent epigenetic and genomic imprinting regulators. Specifically, MBD3 protein is implicated in transcriptional repression and is indispensable for embryonic development as deletion of *Mbd3* has been shown to cause embryonic lethality (378). HAT1 is a type B histone acetyltransferase that is thought to be responsible for the acetylation of newly synthesized histones during the process of chromatin assembly, and is known to be essential in mammalian development and for viability in the mouse (379). Finally, the transcription factor *Cdx2* has been identified as a marker for TE differentiation during mouse pre-implantation development (326) and inactivation of this gene leads to pre-implantation embryonic lethality (380).

The significantly increased expression of some DNA methylation and genomic imprinting regulators in the conditioned media group might suggest enhanced blastocyst development and a potential improvement in the quality of *in vitro* produced embryos.

However, no significant differential expression of the genes listed above was observed in traditional microdrop culture (Figure 3.10B). Those results could be explained by the different culture environment and, mostly, by the presence of diluted soluble factors concentration in larger culture drops which consequently could impact embryo development and blastocyst gene expression.

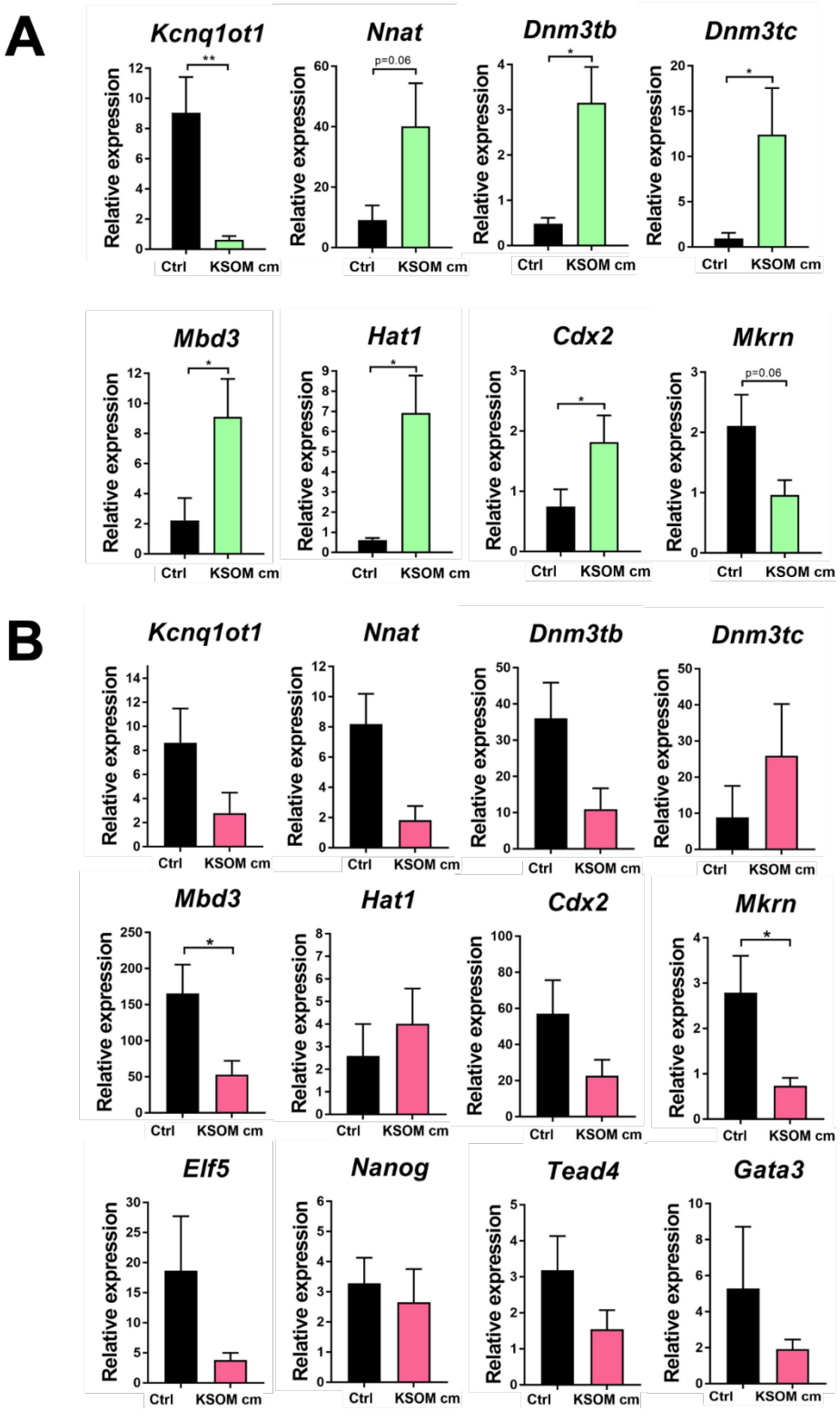

Figure 3.10 Effect of conditioned media on gene expression.

Relative mRNA expression of differentially expressed genes in blastocysts cultured in conditioned media (KSOM cm) or control (KSOM) in (A) the device or (B) traditional microdrop culture. Data are presented as mean ± SEM. Number of blastocysts examined in each group=12. *=p<0.05, **=p<0.005.

Table 3.12 lists details of genes that were differentially expressed in blastocysts cultured in the microfluidic device using conditioned media or control, including gene name, accession number, size and primer sequences.

Table 3.12 Primers used for array qPCR

Symbol	Accession	Size (bp)	Sequence of nucleotides (5'⟶3')	
Kcnq1ot1	NR_001461	234	**Forward**	CCCAAACCTTAGTCCTCCAT
			Reverse	TAACAAAGGGCACACGGTAT
Nnat	NM_010923	174	**Forward**	TTGAATCCCACCTTTACCAA
			Reverse	CCTGTCTCCAGGAGCTTACA
Dnmt3b	NM_001003961	155	**Forward**	ACTTGGTGATTGGTGGAAGC
			Reverse	CCAGAAGAATGGACGGTTGT
Dnmt3c	XM_021192798	241	**Forward**	TGATGATCAATGCCATCAAG
			Reverse	ATGTCGTCTTTGCCATTCAT
Mbd3	NM_013595	246	**Forward**	GTGGATTGAGTGCCTTTGAC
			Reverse	TGATGTCGTCATCTGTCACC
Hat1	NM_026115	150	**Forward**	GTGCCGTGGAGAAGAAACTA
			Reverse	CAGTTTCATCATCCCCAAAG
Cdx2	NM_007673	150	**Forward**	TCAGGGGAAGACATGGTTTA
			Reverse	AGGCTGATAGCTTCATGTCG
Mkrn	NM_018810	218	**Forward**	TTGTGGGTATCTGCCTCATT
			Reverse	AGAGCAACAAAATGCAAAGG
Elf5	NM_010125	112	**Forward**	GTGCACCCTGAATACTGGAC
			Reverse	CGCTGATGTTGAAGTGACAG

3.3.4 Mass spectrometry analysis of media composition

Global, untargeted liquid chromatography tandem mass spectrometry (LC-MS/MS) analyses were performed to investigate metabolite composition of spent media collected from the microfluidic device at the end of embryo culture or after incubation of the media in the device at 37 °C under 5% CO_2, 5% O_2 in a humidified nitrogen atmosphere. As a control, data were compared to metabolite content of medium at day 0. Next, the impact of uterine epithelial cells-conditioned medium (CM) was assessed by measuring metabolite content in spent CM collected from the microfluidic device and comparing it with control medium (KSOM).

In comparison, the analysis was carried out for equal volumes (100 µL) of samples collected from 40 µL microdrops for both control and treatment conditions. Finally, data obtained for the microfluidic devices were compared to those obtained for control microdrops to further elucidate effects of PDMS on embryo metabolomics and potential material embryotoxicity.

3.3.4.1 Metabolomics of murine embryos cultured in the device

This section reports LC-MS/MS data obtained from samples of spent culture medium collected from the microfluidic devices.

In Figure 3.11 are schematized the experimental groups of spent medium samples taken into account in this experiment and the pairwise comparisons of interest (indicated by the arrows).

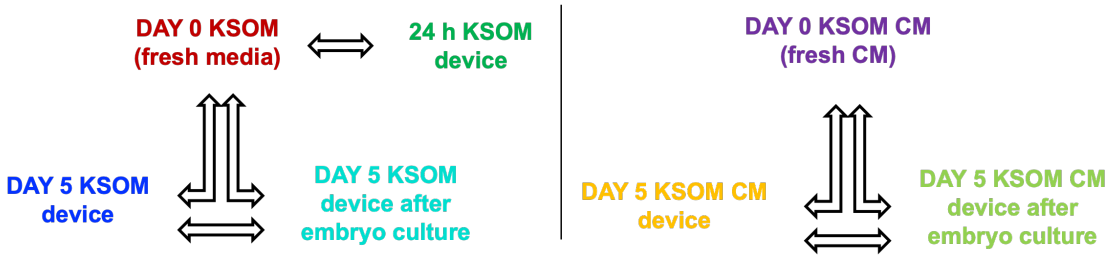

Figure 3.11 Schematic of experimental groups and pairwise comparisons of interest.

3.3.4.1.1 PDMS biomolecules leaking/absorption

In a first experiment, untargeted metabolomics analysis was used to identify potentially toxic PDMS-released compounds in spent media (KSOM) incubated in devices without embryos for 24 h or 5 days. These incubation times were chosen to investigate PDMS-related molecules released during the 24 h equilibration period (device priming) and during 5 days in the incubator (corresponding to the time needed for the embryos to reach the expanded blastocyst stage). Fresh media at day 0 (day 0 KSOM) was used as a control.

Statistical evaluation by principal component analysis (PCA) showed distinct clustering of the three experimental groups considered in this experiment – day 0 KSOM (red), 24 h KSOM (green), and day 5 KSOM (blue) (Figure 3.12i).

By a global comparison of the metabolic compounds (Figure 3.12ii) observed for each group of samples it was possible to detect a total of 2338 compounds among all the experimental groups. The heatmap visualization presents compounds as rows and sample replicates as columns. Data were processed using Euclidean distance and Ward clustering via Metaboanalyst 4.0 for Pareto scaled, log transformed, and averaged group data. From the heatmap it is possible to recognize four main clusters of compounds, identified by the curly brackets in Figure 3.12ii:

- Cluster 1 represents compounds which are decreased in media after 24 h incubation but not in media incubated for 5 days, compared to control. Those might correspond to metabolites that are temporarily sequestered by PDMS and released again into the media during culture.
- Clusters 2 and 4 include compounds which have different and not unique abundance in the three experimental groups.
- Cluster 3 likely refers to metabolites directly associated with PDMS and released into the media by the material regardless the incubation time.

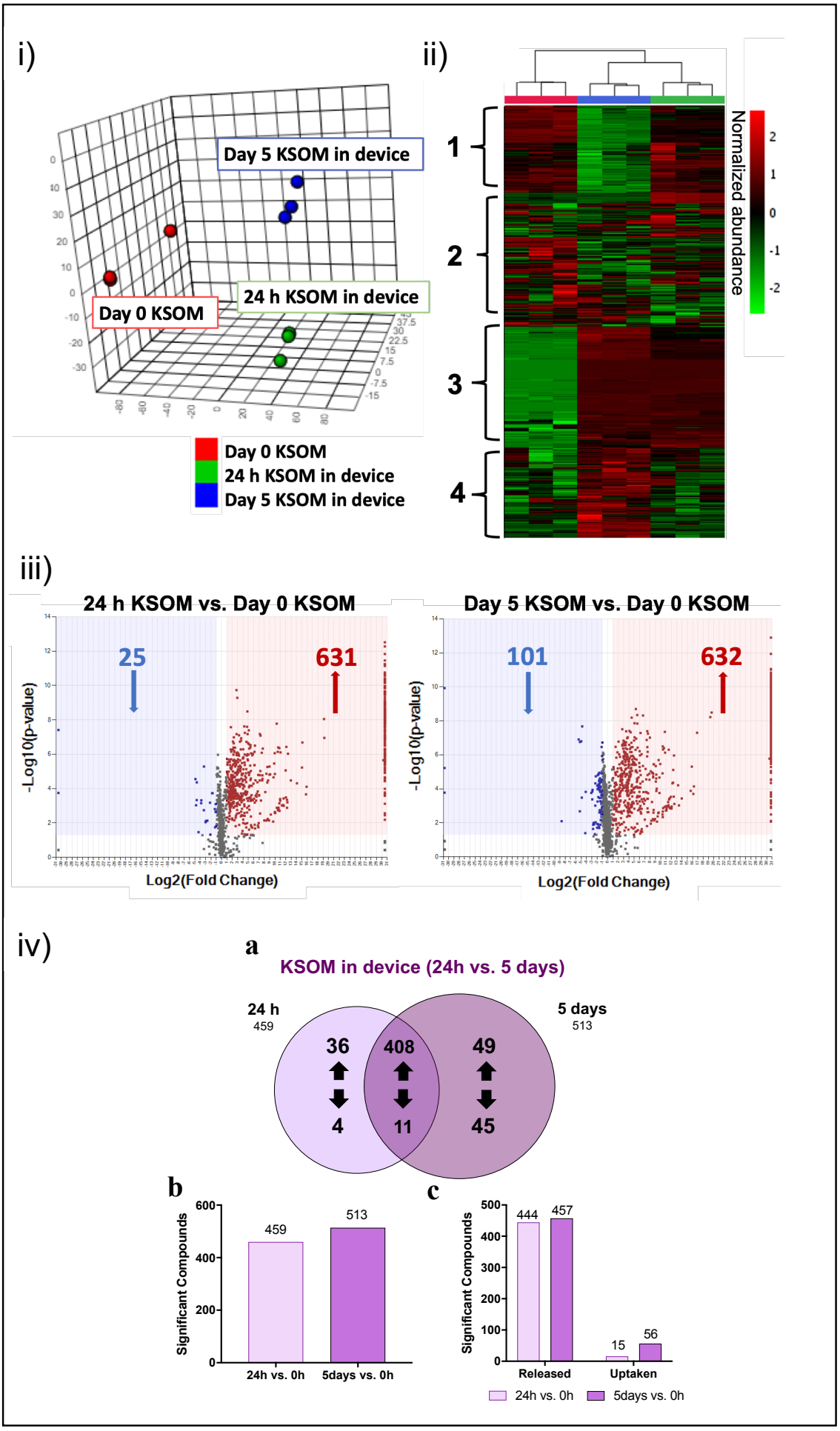
i)
Day 5 KSOM in device
24 h KSOM in device
Day 0 KSOM
Day 0 KSOM
24 h KSOM in device
Day 5 KSOM in device
ii)
1
2
3
4
Normalized abundance
2
1
0
-1
-2
iii)
24 h KSOM vs. Day 0 KSOM
25
631
-Log10(p-value)
Log2(Fold Change)
Day 5 KSOM vs. Day 0 KSOM
101
632
-Log10(p-value)
Log2(Fold Change)
iv)
a
KSOM in device (24h vs. 5 days)
24 h
459
5 days
513
36
4
408
11
49
45
b
Significant Compounds
459
513
24h vs. 0h
5days vs. 0h
c
Significant Compounds
444
457
15
56
Released
Uptaken
24h vs. 0h
5days vs. 0h

Figure 3.12 LC-MS/MS results of media samples collected from devices after 24 h or 5 days.

i) PCA plot for LC-MS/MS data of medium samples collected from devices after 24 h (N=3) or 5 days (N=3) and control KSOM (N=3). **ii)** Heatmap representing LC-MS/MS data. Colours are displayed by normalized abundance, ranging from low (green) to high (red). **iii)** Volcano plots showing the distribution of metabolic compounds for pairwise comparisons as stated above. (Left) 24 h PDMS leaching/molecule absorption *vs.* control, (right) 5 days PDMS leaching/molecule absorption *vs.* control. **iv)** Comparison of metabolites significantly altered in media incubated in PDMS devices for 24 h or 5 days. a) Venn diagram of metabolites/compounds observed in media incubated with PDMS for 24 h or 5 days. b) Graphical representation of the total number of features observed in 24h-PDMS media and day 5-PDMS media, compared to control. c) Graphical representation of the increase (released compounds) and decrease (uptaken compounds) in the total number of features found in 24 h KSOM (light pink) and 5 days KSOM (purple), compared to control.

Visualizations of dysregulated metabolites were also represented by volcano plots (Figure 3.12iii). Volcano plots combine the *p*-value measured by ANOVA, expressed as $-\log_{10}(p\text{-value})$, with the magnitude of the change in relative abundance, expressed as $\log_2$(fold change), between the groups considered in a particular pairwise comparison. This representation enables a quick visual identification of the features that display large magnitude changes that are also statistically significant (significance criteria: $p \leq 0.05$, fold change $\geq |2|$). In the plot, the most up-regulated species are towards the right (in red), the most down-regulated species are towards the left (in blue), and the most statistically significant species are towards the top.

These results showed that:

- **the metabolite composition of the media was significantly different among the three sample groups.** In particular, 656 features were significantly altered in the 24 h KSOM group compared to control, and 736 in day 5 KSOM group compared to control (Table 3.13).
- **the amount of compounds that are up-regulated in spent media form devices (PDMS-media) is relatively higher than the number of compounds that are down-regulated in PDMS-media, when compared to control media.** From the comparison between 24 h KSOM and control, 631 species had significantly increased abundance and 25 significantly decreased abundance in PDMS-media compared to control media. Additionally,127 features were unique to the 24 h KSOM and 2 to the control. Those are graphically represented, respectively, by the compounds on the extreme right and the extreme left of the volcano plot. Similarly, increased abundance of 632 features and decreased abundance of 101 features was measured in day 5

KSOM compared to control, with 141 features unique to samples of day 5 KSOM and 3 to the control.

- **Compounds identified only in PDMS-media**, represented by the ones on the extreme right of the two plots, **can have different origins.** Those can be in fact compounds present in the media as a consequence of the plastic or the degradation of the media during incubation. Importantly, low molecular weight species, which can be related to un-crosslinked PDMS (molecular weight of dimethylsiloxane monomer = 74.15 Da), were detected in media samples extracted from the devices, confirming possible leaching of PDMS oligomer into the culture media.

Table 3.13 Pairwise comparisons of experimental conditions.

Pairwise Comparison		Total # of Significant Compounds $p \leq 0.05$ and FC≥ |2|	Total # of Compounds CV<20%
Cond A	**Cond B**		
Day 0 KSOM	**24h KSOM**	656	2338
Day 0 KSOM	**Day 5 KSOM**	736	2338

The differential metabolites were searched against spectral libraries (HMDB, METLIN, NIST) and in-house databases to guide confident metabolite annotation. Among the compounds that were significantly dysregulated in 24 h KSOM (*vs.* control) or in day 5 KSOM (*vs*. control), 459 and 513 metabolites were respectively putatively identified using available libraries (Figure 3.12iv-b).

These lists of compounds were compared using Venn diagram as shown in Figure 3.12iv-a and highlighted:

- 419 compounds common to the two groups (24 h KSOM and the day 5 KSOM), 40 compounds unique to the 24 h KSOM group and 94 unique to the day 5 KSOM group.
- Of these, the expression of 408 compounds was significantly higher ($p < 0.05$) of more than 2-fold in both the 24 h KSOM and the day 5 KSOM compared to control. Those included 3''-chloro-3''-deoxytriphasiol, (2E)-hexene dioylcarnitine, 2-phthalimidoglutaric acid, pyridoxamine, (S)C(S)S-S-methy lcysteine sulfoxide, diethyl oxalpropionate, 3,5-bis(trifluoromethyl) diphenyla-mine, seryllysine and hydroxyprolyl-Isoleucine all of which had an expression value of >10-fold higher in the PDMS-media compared to control. **Even**

though the origin of those species is unclear, they could represent compounds released by PDMS into the culture medium, breakdown molecules produced by media degradation as a consequence of incubation at 37 ºC for short (24 h) and long (5 days) incubation periods.

- Presence of potentially toxic compounds, such as dimethyl sulfoxide and necatorine, was found in spent media from devices, revealing possible negative impact of plastic on embryo development. In contrast, the remaining 11 identified species might represent compounds sequestered from culture media by PDMS either after short or long incubation periods and include 4-O-alpha-D-galactopyranosylcalystegine B2, 1-Isopropyl citrate, and isoleucyl-phenylalanine and 2-methoxyestrone 3-glucuronide.
- **It was also possible to identify compounds which are significantly altered in PDMS-media *vs.* control only after 24 h,** including 36 compounds released into the culture media and 4 absorbed from the media, **or after 5 days**, including 49 compounds released into the culture media and 45 absorbed from the media.

3.3.4.1.2 Untargeted metabolomics of mouse embryos cultured in the device

After the identification of compounds released or absorbed by PDMS into the culture medium at different incubation periods, the metabolite composition of day 5 spent embryo culture media was assessed to investigate effect of device culture on embryos metabolome. For doing this, spent media was collected from devices after 5 days of embryo culture of after 5 days without embryos and compared to control KSOM by LC-MS/MS. The global metabolomic profile of the three experimental groups – day 0 KSOM (red), day 5 KSOM (green), and day 5 embryo culture KSOM (blue) – was analysed by principal component analysis (PCA) as presented in Figure 3.13i.

This showed distinct clustering of the groups, illustrating that three distinct metabolic signatures were observed in the LC-MS/MS analysis. The metabolic profile of *in vitro* cultured murine embryos can be thus distinguished from compound composition of media incubated in the device in absence of embryos. The heatmap visualization (Figure 3.13ii) further indicates that the three groups could be separated based on abundance of the detected metabolites. From this

map is possible to recognize four main clusters of compounds, identified by the curly brackets in Figure 3.13ii.

- Cluster 1 identifies features that are particularly increased in day 5 KSOM compared to either control or day 5 embryo culture media. Those could be compounds released by PDMS or media components which are rather consumed by embryos during culture.
- Cluster 2 shows compounds decreased in media collected from devices compared to control, which could be compounds either taken up by embryos or absorbed by PDMS during culture.
- Cluster 3 includes a relevant number of species which are increased in spent media from devices and are likely to be released into the media either by the plastic or by the embryos.
- Cluster 4 contains compounds that are not significantly different between the day 5 KSOM and the control, but rather an increased abundance in spent embryo culture media compared to control and day 5 KSOM. Those metabolites could be directly produced by embryos into the medium during culture.

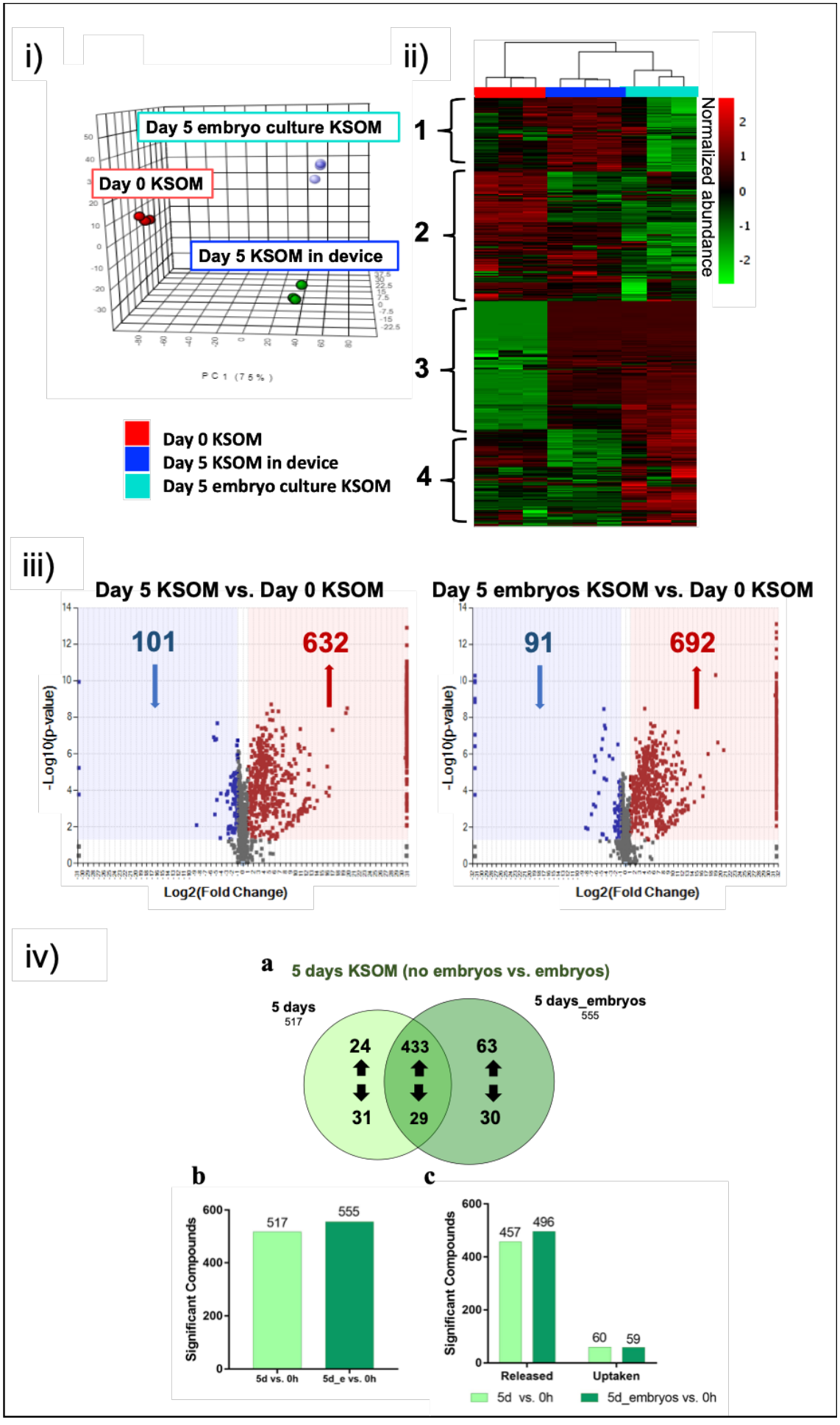
i)
Day 5 embryo culture KSOM
Day 0 KSOM
Day 5 KSOM in device
PC 1 (75%)
Day 0 KSOM
Day 5 KSOM in device
Day 5 embryo culture KSOM
ii)
1
2
3
4
Normalized abundance
2
1
0
-1
-2
iii)
Day 5 KSOM vs. Day 0 KSOM
101
632
-Log10(p-value)
Log2(Fold Change)
Day 5 embryos KSOM vs. Day 0 KSOM
91
692
-Log10(p-value)
Log2(Fold Change)
iv)
a
5 days KSOM (no embryos vs. embryos)
5 days
517
5 days_embryos
555
24
433
63
31
29
30
b
Significant Compounds
517
555
5d vs. 0h
5d_e vs. 0h
c
Significant Compounds
457
496
60
59
Released
Uptaken
5d vs. 0h
5d_embryos vs. 0h

Figure 3.13 LC-MS/MS results of media samples collected from devices after 5 days in the presence or without embryos.

i) PCA plot for LC-MS/MS data of medium samples collected from devices after 5 days in the presence (N=3) or without (N=3) of embryos, and control KSOM (N=3). **ii)** Heatmap representing LC-MS/MS data. Colours are displayed by normalized abundance, ranging from low (green) to high (red). **iii)** Volcano plots showing the distribution of metabolic compounds for pairwise comparisons as stated above. (Left) Day 5 KSOM *vs.* day 0 KSOM, (right) day 5 embryo culture KSOM *vs.* day 0 KSOM**. iv)** Comparison of metabolites significantly altered in media incubated in devices for 5 days in the presence or without embryos. a) Venn diagram of metabolites/compounds observed in media incubated in PDMS for 5 days without (light green) or with (dark green) embryos. b) Graphical representation of the total number of features observed in day 5 KSOM and day 5 embryo culture media, compared to control. c) Graphical representation of the increase (released compounds) and decrease (uptaken compounds) in the total number of features found in day 5 KSOM (light green) and day 5 embryo culture media (dark green), compared to control.

Table 3.14 provides an overview of differentially abundant metabolites in the pairwise comparisons – day 5 KSOM *vs*. control and day 5 embryo culture KSOM *vs*. control.

Analysis of the metabolite content in day 5 embryo culture KSOM identified 783 significant compounds. These data were compared to the list of 733 compounds identified in spent media incubated in microfluidic devices for 5 days without embryos. Volcano plots showing the differential metabolites in those two groups are displayed in Figure 3.13iii. Those results showed that:

- **Most of the metabolites are increased in spent media collected from devices compared to control.** In particular, among the 783 compounds identified in day 5 embryo culture media, 692 were significantly increased and 91 significantly decreased ($p < 0.05$, FC $\geq \left| 2 \right|$), when compared to control.
- **From the comparison between day 0 KSOM and day 5 embryo culture KSOM, 162 features were unique to the spent embryo culture media and 7 to the control.** The first ones are graphically represented by the compounds on the extreme right of the volcano plot and might be produced either by embryos or PDMS as a result of 5 days incubation. The 7 features only detected in control media, presented on the extreme left of the plot, might be compounds absorbed by PDMS or components of the media which have been degraded during culture.

Table 3.14 Pairwise comparisons of experimental conditions.

Pairwise Comparison		Total # of Significant Compounds $p \leq 0.05$ and $FC \geq \lvert 2 \rvert$	Total # of Compounds CV<20%
Cond A	**Cond B**		
Day 0 KSOM	**Day 5 KSOM**	733	2338
Day 0 KSOM	**Day 5 embryo KSOM**	783	2338

Among the compounds that were significantly dysregulated in day 5 KSOM or day 5 embryo culture KSOM, 517 and 555 metabolites, respectively, were putatively identified using available libraries (Figure 3.13iv-a,b). The comparison between these two groups allowed the generation of a list of metabolites present in spent media after embryo culture in the device as well as lists of metabolites unique to the embryo culture group (*i.e.,* produced by the embryo during culture) or to the PDMS-media group (*i.e.,* associated with the fabrication process or released/absorbed by PDMS). Comparison of these lists of compounds identified:

- 55 metabolites with significantly altered abundance uniquely in day 5 KSOM *vs.* control, 93 with significantly altered abundance uniquely in day 5 embryo culture KSOM *vs*. control and 462 common to the two groups (Figure 3.13iv-a).
- Among those common 462 metabolites, the expression of 433 was significantly higher ($p < 0.05$) of more than 2-fold in both the day 5 embryo culture KSOM and the day 5 KSOM compared to control, including alpha-methylphenylalanine, triethylene glycol, N-(1-Deoxy-1-fructosyl) glycine, pyroglutamic acid, trifluridine, N1,N8-diacetylspermidine, itaconic acid, dimethicone, all of which had an expression value of >10-fold higher in the device media compared to the control.
- **Increased presence of toxic compounds, such as dimethyl sulfoxide and necatorine, was found in spent media from devices** and might result detrimental for embryo development. This might suggest a different behaviour and metabolic activity of the embryos in the device culture environment and a slightly altered composition of the media due to the plastic. However, blastocyst rate results (see Section 3.3.2.1) showed that the culture environment did not negatively affect *in vitro* embryo growth and blastocyst development.

- In contrast, the relative abundance of **29 compounds** was at least 2-fold higher ($p < 0.05$) in the control compared to spent media collected from devices with or without embryos. Those are compounds **possibly sequestered by PDMS from the culture medium** and include muramic acid, 1H-indole-3-acetamide and geranyl diphosphate.

Compounds that are significantly increased in spent media collected from devices (day 5 KSOM or day 5 embryo culture KSOM) **can be compounds released by PDMS or embryos, or can be breakdown molecules produced by media degradation** as a consequence of incubation at 37 ºC.

- After 5 days of incubation, a total of 457 and 496 compounds were significantly ($p \leq 0.05$ and FC $\geq |2|$) increased into culture media samples collected from devices without embryos and into culture media samples collected from devices after embryo culture, respectively (Figure 3.13iv-c). Among them, **433** were common between the two groups, representing **compounds released into the culture medium only as a result of PDMS leakage or media degradation**. In contrast, 24 features were unique to day 5 KSOM and 63 were only increased in day 5 embryo culture KSOM. Those **63 species** might be directly associated with compounds **released by embryos during culture.**

On the other hand, **features that are significantly decreased in spent media samples collected from devices represent compounds absorbed by PDMS or metabolites taken up by embryos during culture**.

- In detail, a total of 60 and 59 metabolites were decreased in day 5 KSOM and day 5 embryo culture KSOM, respectively (Figure 3.13iv-c). Among them, 29 metabolites were common between the two groups, indicating compounds that are potentially degraded into culture media or absorbed by PDMS during culture. The remaining compounds were either unique to day 5 KSOM (31 features) or to day 5 embryos culture KSOM (30 features). While the former have unclear origins, the latter indicate compounds which might be taken up by embryos from the medium during culture.

The pairwise comparison between the day 5 embryo culture KSOM and the day 5 KSOM identified a list of 293 compounds. These data were compared to the list of 783 compounds identified in spent embryo culture KSOM (Table 3.15).

Volcano plots showing the differential metabolites in those two pairwise comparisons are displayed in Figure 3.14i. The results showed that:

- Among the 293 compounds significantly different in the first pairwise comparison, 231 were significantly decreased and 62 significantly increased ($p < 0.05$, FC $\geq |2|$) in day 5 KSOM compared to day 5 embryo culture KSOM.
- The 231 features represent compounds which are highly abundant in spent media from embryo culture, thus metabolites potentially released by embryos during culture. Similarly, **62 compounds** are decreased in spent embryo culture media since they might have been **taken up by embryos during culture**. Moreover, 16 features were unique to spent embryo culture media, whereas 7 to the day 5 KSOM. The first ones, graphically represented by the compounds on the extreme left of the volcano plot in Figure 3.14i, are specifically produced by embryos in culture. In contrast, the 7 features only detected in day 5 KSOM, presented on the extreme right of the plot, might be components of the media that have been degraded or taken up by embryos during culture.

Table 3.15 Pairwise comparisons of experimental conditions.

Pairwise Comparison		Total # of Significant Compounds $p \leq 0.05$ and FC$\geq |2|$	Total # of Compounds CV<20%
Cond A	**Cond B**		
Day 5 embryo KSOM	**Day 0 KSOM**	783	2338
Day 5 KSOM	**Day 5 embryo KSOM**	293	2338

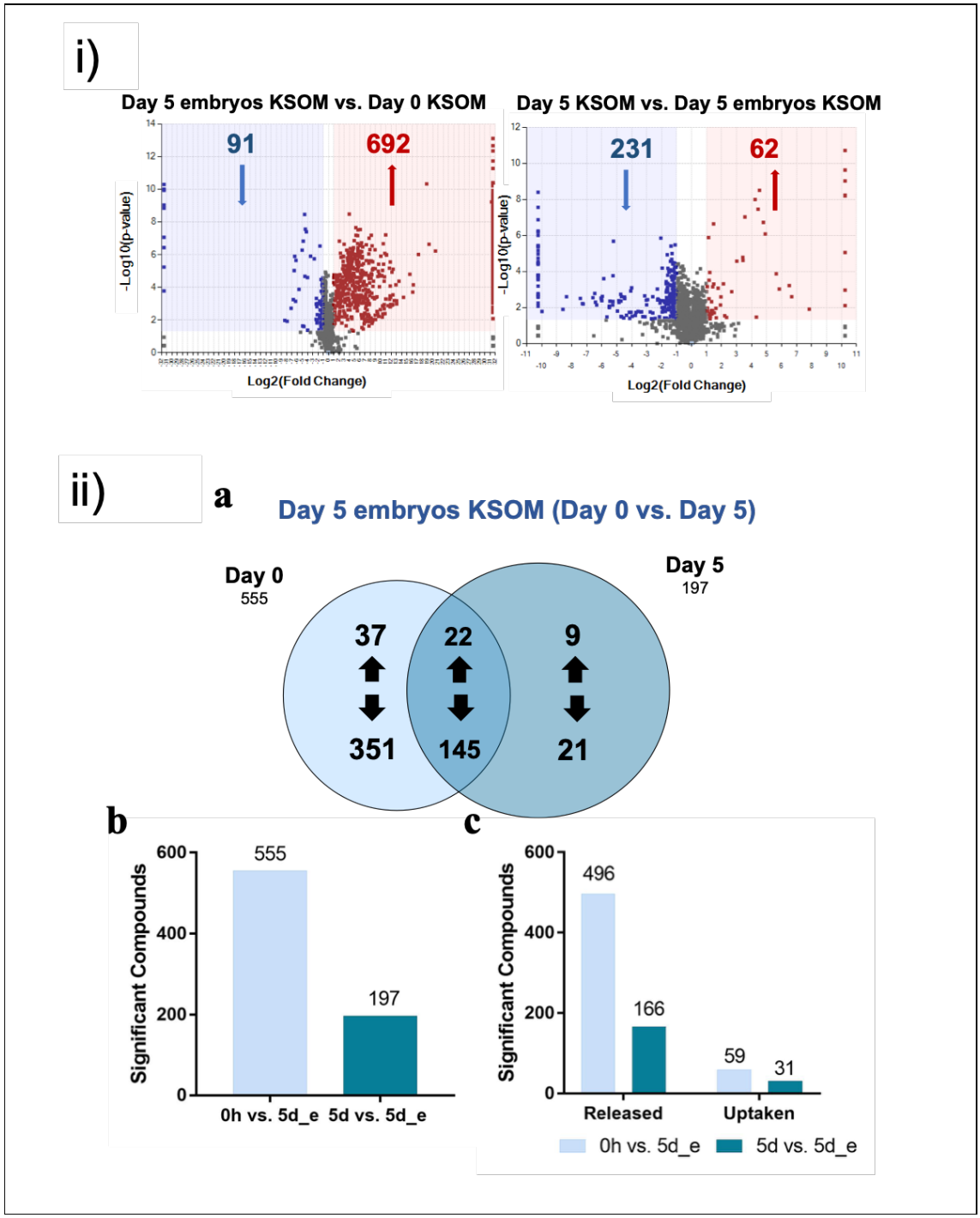

Figure 3.14 LC-MS/MS results of media samples collected from devices after 5 days in the presence or without embryos.

i) Volcano plots showing the distribution of metabolic compounds for pairwise comparisons as stated above. (Left) day 5 embryo KSOM *vs.* day 0 KSOM, (right) day 5 KSOM *vs.* day 5 embryo culture media. **ii)** Comparison of metabolites significantly altered in day 5 embryo culture media. a) Venn diagram of metabolites altered in control media (day 0 KSOM) (light blue) or day 5 KSOM (dark blue) compared to day 5 embryo culture media. b) Graphical representation of the total number of features significantly altered in control or day 5 KSOM, compared to day 5 embryo culture media. c) Graphical representation of the decrease (released compounds) and increase (uptaken compounds) in the total number of features found in control (light blue) and day 5 KSOM (dark blue), compared to day 5 embryo culture media.

Among the compounds that were significantly dysregulated in day 5 embryo culture KSOM *vs.* control or in day 5 embryo culture KSOM *vs*. day 5 KSOM, 555 and 197 metabolites, respectively, were putatively identified using available libraries (Figure 3.14ii-a, b). The comparison between this two groups allowed the generation of a list of metabolites which are present in spent media and uniquely associated with embryo culture.

- There are **145 features** which are common between the two pairwise comparisons and are significantly decreased in both control and day 5 KSOM, when compared to day 5 embryo culture KSOM. Those are known to be **compounds specifically released by embryos after 5 days *in vitro* culture in the device** and associated neither with PDMS nor with media degradation. Similarly, the **22** common features which are significantly increased in both control and day 5 KSOM, when compared to day 5 embryo culture KSOM, consist in **metabolites taken up by embryos during culture in the microfluidic device**.

  Those 145 compounds directly related to embryo metabolism are discussed in the next session to investigate whether they are involved in key metabolic pathways characteristic of *in vitro* pre-implantation embryo development.

3.3.4.1.3 Metabolite pathways associated to metabolites released and consumed by embryos during culture

The attributed metabolites that were common to the two pairwise comparisons described in the previous paragraph – and characterized by the same fold change direction – were combined and used for pathway overrepresentation analysis. The Musmusculus (mouse) KEGG pathway library was used to map the selected potential biomarkers using the web-based Metaboanalyst 4.0 program pathway analysis, which supports integrating enrichment and pathway topology analysis. **This analysis aimed to depict biological pathways associated with the list of metabolites which are consumed or released by the developing embryos during culture to investigate embryo metabolism.**

Firstly, the list (see Appendix) of **metabolites significantly increased in abundance in spent media from embryo culture, thus released into the**

culture medium by the embryos, were combined and imported into Metaboanalyst.

Figure 3.15 shows a metabolome view which contains all the pathways matched with this list of metabolites arranged by *p*-values (from pathway enrichment analysis) on Y-axis, and pathway impact values (from pathway topology analysis) on X-axis. Individual nodes in the map represent individual pathways. Colour gradient and circle size indicate the significance of the pathway ranked by *p*-value (yellow: higher *p*-values and red: lower *p*-values) and pathway impact score (the larger the circle the higher the impact score), respectively. Pathways with *p*-value < 0.1 and impact higher than 0 were deemed as important. **On day 5 of blastocyst development, there were 11 overrepresented biological processes** including pantothenate and CoA biosynthesis, tryptophan metabolism, cysteine, methionine, glycine, serine and threonine metabolism, purine and pyrimidine metabolism, caffeine metabolism, nicotinate and nicotinamide metabolism, glycerolipid metabolism, galactose metabolism, glutathione metabolism, arginine and proline metabolism and aminoacyl-tRNA biosynthesis. **The most affected metabolic pathway (*p* = 0.08) is pantothenate and CoA biosynthesis.** CoA (coenzyme A) is an essential cofactor that is involved in many metabolic processes (*e.g.,* synthesis and oxidation of fatty acids, complex lipid synthesis and, oxidation of pyruvate in the citric acid cycle) and is derived from pantothenate, or vitamin B5 (381). This is a required vitamin in mammals and can be obtained from the diet and from intestinal bacteria (382). Previous works showed that supplementation of pantothenate in culture media has a stimulatory effect on mouse blastocyst development (383); thus the confirmed activity of this metabolic pathway in blastocysts cultured in the microfluidic device might indicate enhanced blastocyst development. **Another pathway which was significantly affected is tryptophan metabolism,** since it was observed significant increase of intermediate metabolites (L-tryptophan, L-kynurenine, 5-hydroxy-L-tryptophan) in spent media from embryo culture. Moreover, activity of the metabolic pathways of other 5 amino acids (cysteine, methionine, glycine, serine and threonine) could explain the resulting activity of protein synthesis mechanisms fundamental during embryo development.

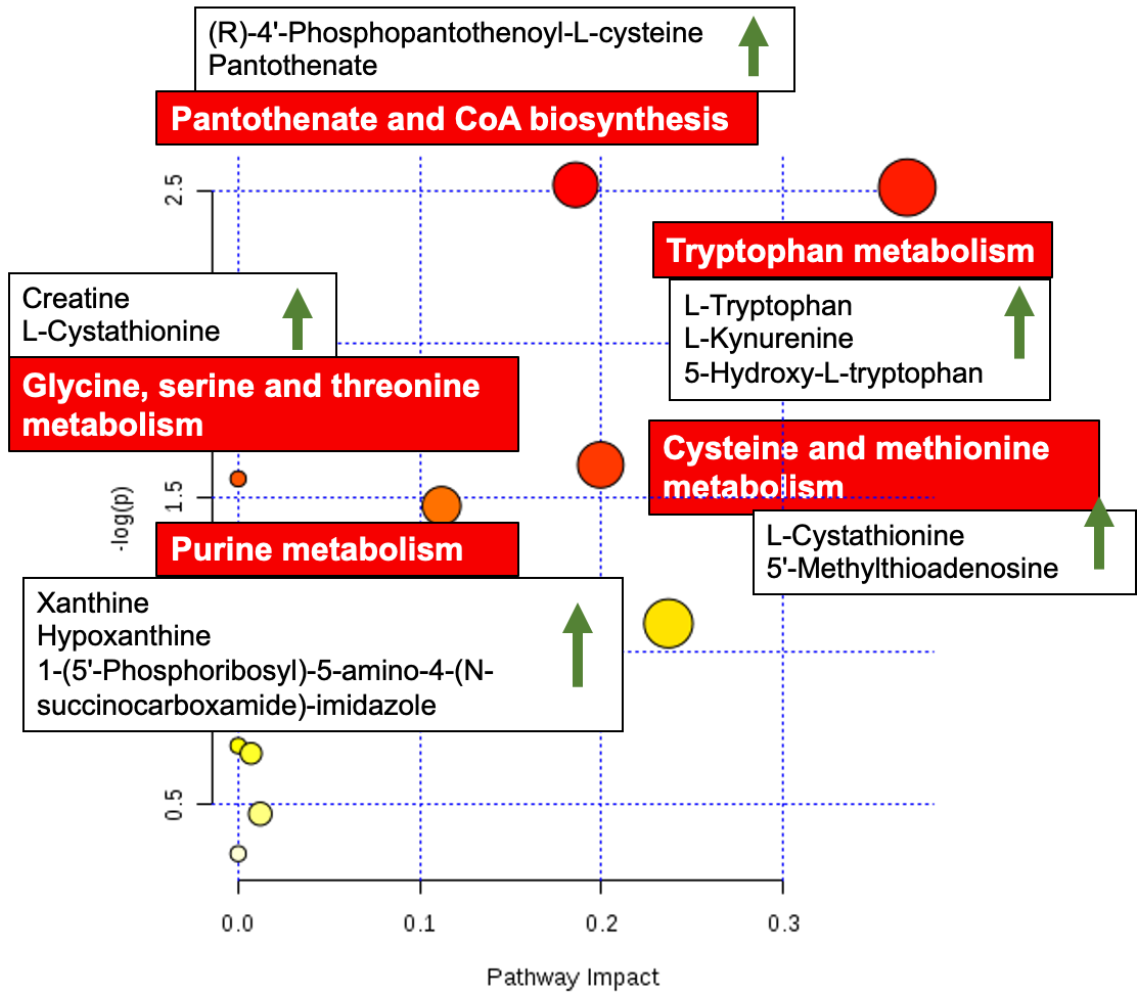

Figure 3.15 Pathways overrepresentation analysis. Summary of metabolic pathways of metabolites released into the culture medium by embryos cultured in KSOM in the microfluidic device.

Next, compounds that were significantly decreased in spent embryo culture media, thus metabolites potentially taken up by embryos during culture, were combined and imported into Metaboanalyst 4.0. **The biological pathway analysis revealed 3 overrepresented metabolic pathways, including caffeine metabolism, alanine, aspartate and glutamate metabolism, and purine metabolism**. Despite caffeine metabolism is not biologically relevant for mouse blastocyst development, detection of decreased level of 5-

phosphoribosylamine indicate activity of amino acids metabolism pathways as well as purine metabolism pathways (

Figure 3.16). However, **those pathways are not significant (p > 0.1)** and the number of compounds hits is not sufficient to draw meaningful conclusion about the effect of device culture on embryo metabolism.

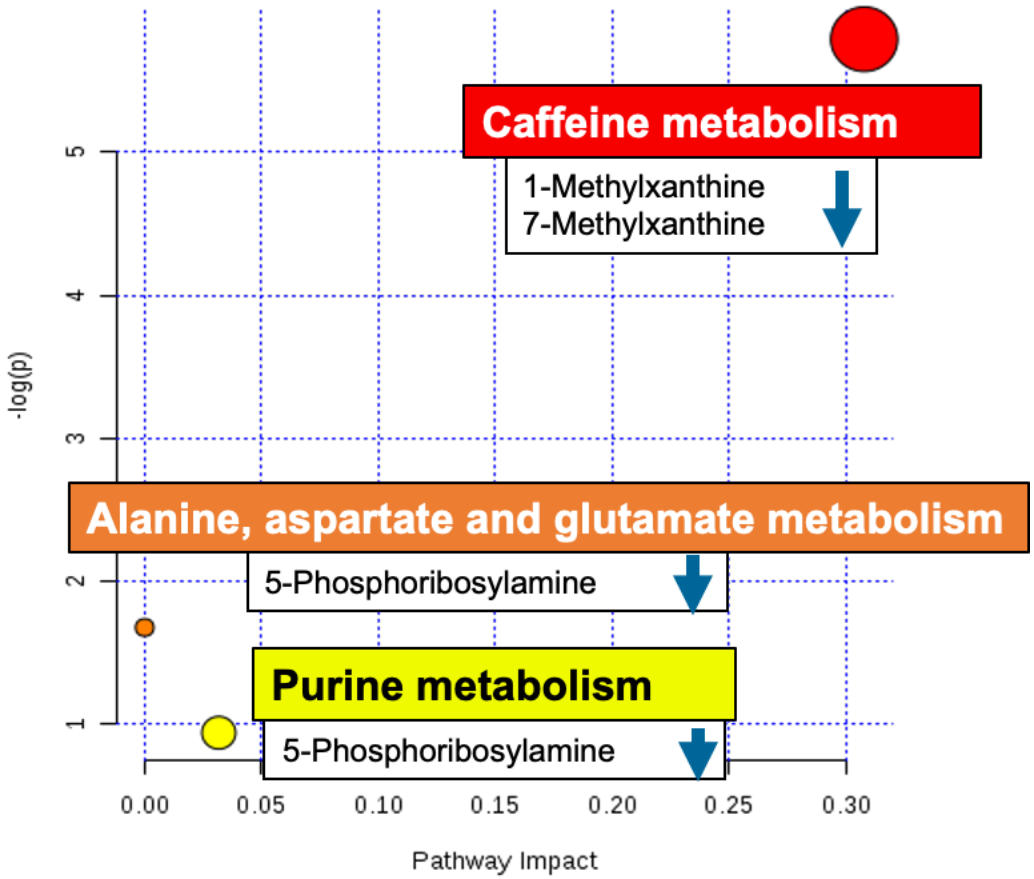

Figure 3.16 Pathways overrepresentation analysis. Summary of metabolic pathways of metabolites consumed from the culture medium by embryos cultured in KSOM in the microfluidic device.

3.3.4.1.4 Effect of cells conditioned media on embryo metabolomics

To assess the impact of culture using mouse uterine epithelial cell-conditioned media (CM), the metabolite composition of spent CM collected from microfluidic devices at day 5 of embryo culture was measured by untargeted LC-MS/MS. Data were compared either to control media, fresh KSOM CM at day 0 (Day 0 CM), or to media incubated in the device for 5 days without embryos (Day 5 CM), similar to what has been done for the experiment described above. As a control, results were compared to those previously obtained using KSOM. Figure 3.17 shows the overall LC-MS/MS results of the different experimental sample groups, including spent KSOM (blue) or CM (yellow) from devices without embryos, spent KSOM (cyan) or CM (green) from devices with embryos and the relative controls. **From a statistical evaluation by principal component analysis, a clearly different distribution of metabolic profiles was observed among all the analysed experimental groups** (Figure 3.17i). This confirmed also the quality of the analysis, since all the experimental groups are clearly separated and characterized by an altered levels of metabolites. For instance, each of the three replica of day 0 KSOM and day 0 CM (red and purple dots, respectively), are clearly distinguished between each other. Likewise, samples of KSOM and CM at day 5 without embryos cluster together, but away from the controls, and samples of KSOM or CM at day 5 of embryo culture clearly appear as distinct groups. This shows that **by conditioning the media with uterine epithelial cells the metabolite composition of the media used for embryo culture considerably changes**.

Those differences are also visible in the heatmap visualization shown in Figure 3.17ii where colours are displayed by relative abundance and all metabolic compounds are represented as rows. From the heatmap, is possible to identify three main clusters of metabolites:

- Cluster 1 is likely to be associated with metabolites taken up by embryos, as it includes features which are significantly reduced in spent media from embryo culture.
- Cluster 2 includes species differentially expressed in all the experimental groups, thus difficult to associate to any specific condition.

- Cluster 3 shows compounds significantly altered in spent media collected from devices compared to control, representing metabolites associated to embryo culture and to the microfluidic environment.

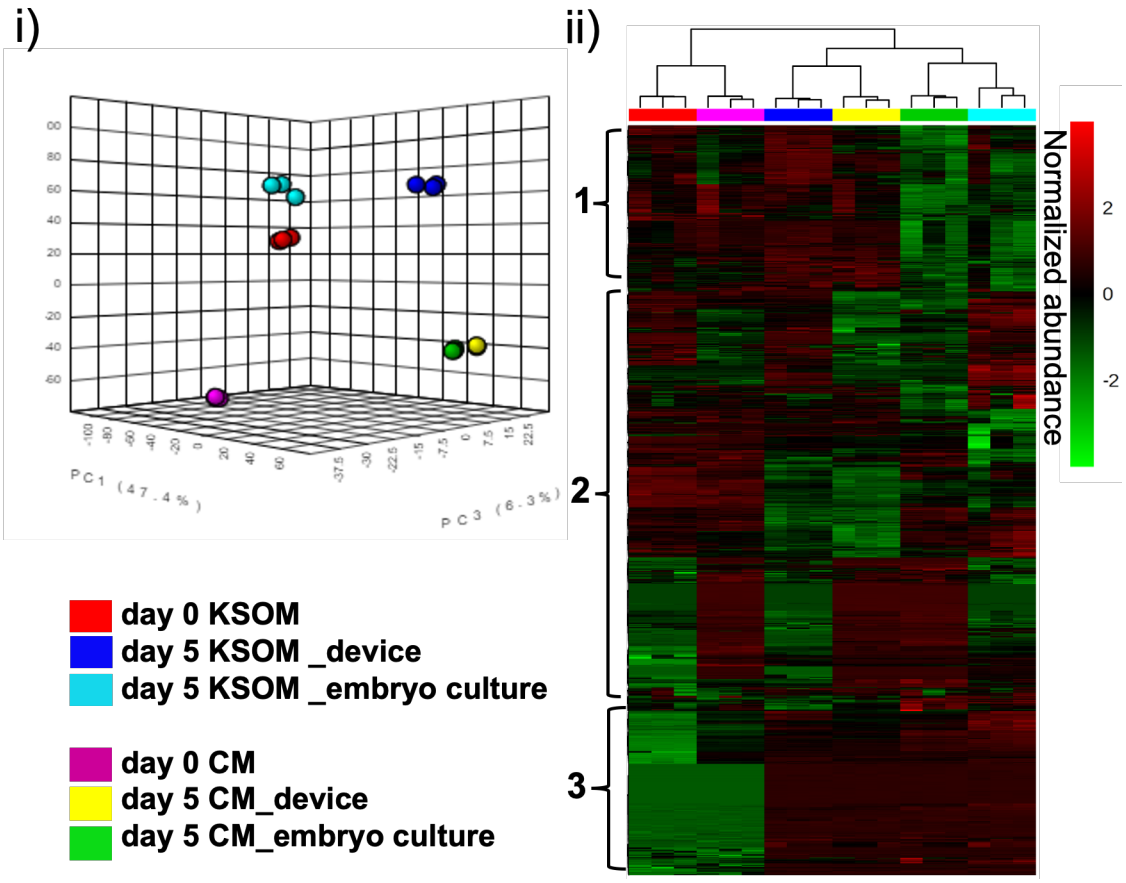

Figure 3.17 LC-MS/MS global metabolomic profile analysis of blastocysts cultured in KSOM or CM in devices.

i) PCA plot for LC-MS/MS data of medium samples collected from devices in different experimental conditions (N=3 for each group). **ii)** Heatmap representing LC-MS/MS data. Compounds are presented as rows and sample replicates as columns and processed by using Euclidean distance and Ward clustering via Metaboanalyst 4.0 for Pareto scaled, log transformed, and averaged group data. Colours are displayed by normalized abundance, ranging from low (green) to high (red).

To investigate metabolite composition of the different experimental groups, the pairwise comparisons described in section 3.3.4.1.2 were similarly carried out for samples of conditioned media collected from devices. Firstly, metabolite content of day 5 CM collected from devices without embryos (day 5 CM) was compared to metabolite content of day 5 embryo culture CM (Table 3.16).

- From the pairwise comparison between day 5 CM and control (day 0 CM) 683 significant compounds were detected. Among them, 487 were significantly

increased in spent media from devices, while 196 were increased in control media.

- Similarly, the pairwise comparison between day 5 embryo culture CM and control identified 661 significantly altered features. Among them, 548 were increased and 113 decreased in spent embryo culture media from devices, compared to control (Figure 3.18i).

Table 3.16 Pairwise comparisons of experimental conditions.

Pairwise Comparison		Total # of Significant Compounds $p \leq 0.05$ and $FC \geq \lvert 2 \rvert$	Total # of Compounds CV<20%
Cond A	**Cond B**		
Day 0 CM	**Day 5 CM**	683	2338
Day 0 CM	**Day 5 embryo CM**	661	2338

Following compounds annotation, the two pairwise comparisons were analyzed using Venn diagram (Figure 3.18ii) to highlight compounds of interest. Results showed that:

- **378 identified features** were common to the two groups and significantly altered in spent medium from devices compared to control. Those compounds **are specifically associated to PDMS**, for the reasons described above. In particular, 330 species were released into the culture media as a consequence of PDMS or media degradation, including plastic compounds or media breakdown molecules. In contrast, 48 compounds were absorbed from culture medium by PDMS since they have decreased abundance in spent media collected from devices compared to control.
- Overall, 423 identified compounds were found to be significantly altered between day 5 CM and control, whereas 449 were found to be significantly altered between day 5 embryo culture CM and control.
- Considering the compounds increased in spent CM compared to control, **380 were released into the media from the culture environment (culture medium and device), and 335 were released also by the embryos cultured in the device.** On the other hand, 63 compounds were decreased in spent CM as a consequence of PDMS molecule absorption, while 114 were either absorbed by PDMS or taken up by embryos after 5 days of culture.

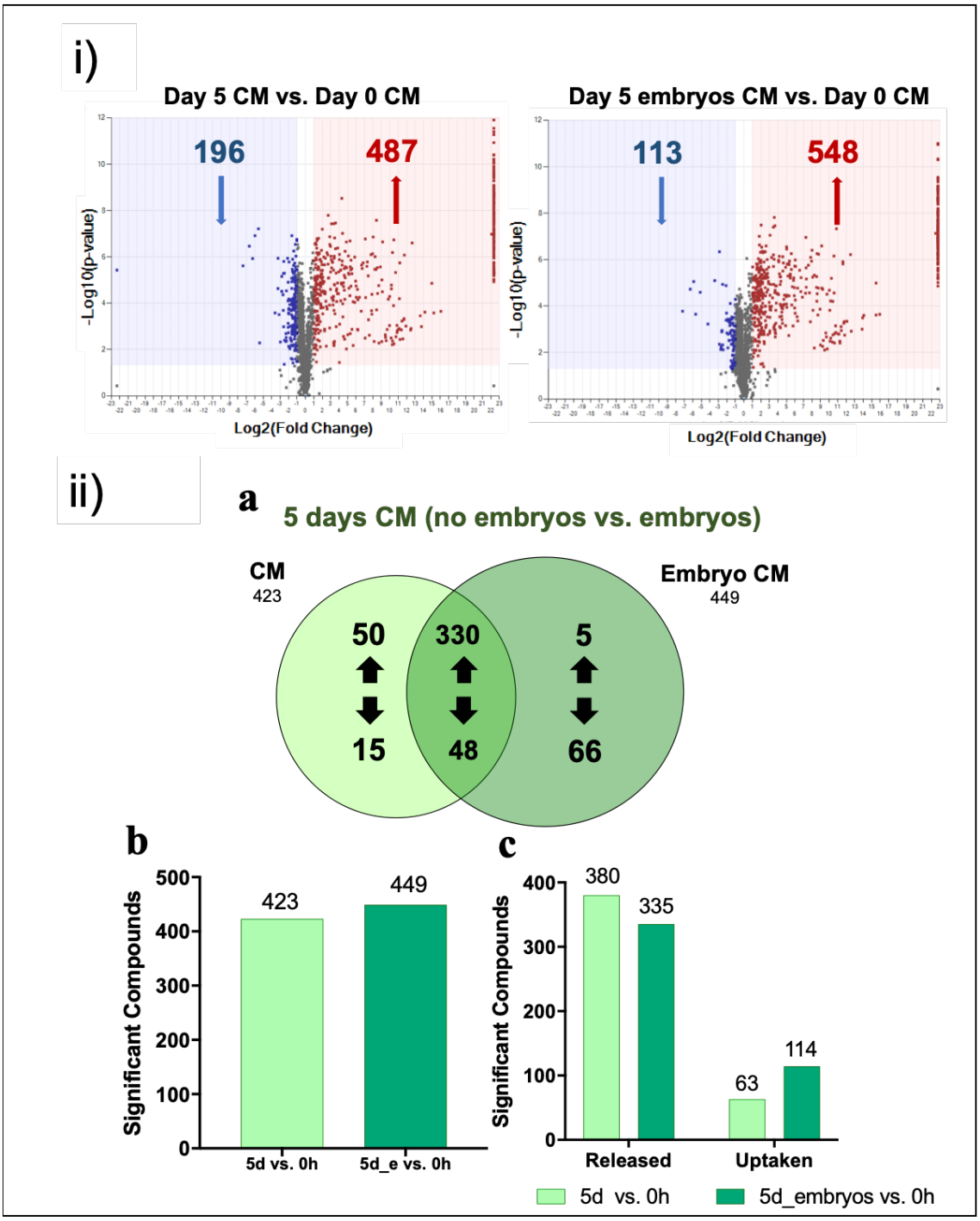

Figure 3.18 LC-MS/MS results of CM samples collected from devices after 5 days in the presence or without embryos.

i) Volcano plots showing the distribution of metabolic compounds for pairwise comparisons as stated above. (Left) Day 5 CM *vs.* Day 0 CM, (right) Day 5 embryos CM *vs.* Day 0 CM. **ii)** Comparison of metabolites significantly altered in day 5 CM. a) Venn diagram of metabolites altered in day 5 CM (light green) or day 5 embryo culture CM (dark green), compared to control (day 0 CM). b) Graphical representation of the total number of features significantly altered in day 5 CM or day 5 embryo culture CM, compared to control. c) Graphical representation of the increase (released compounds) and decrease (uptaken compounds) in the total number of features found in day 5 CM (light green) and day 5 embryo culture CM (dark green), compared to control.

The pairwise comparison between day 5 embryo culture CM and day 5 CM identified a list of 116 compounds. These data were compared to the list of 661 compounds identified in spent embryo culture CM (

Table 3.17). Volcano plots showing the differential metabolites in those two pairwise comparisons are displayed in Figure 3.19i. Among the 116 compounds significantly different in the first pairwise comparison, 32 were significantly decreased and 84 significantly increased ($p < 0.05$, FC ≥ | 2 |) in day 5 embryo culture CM compared to day 5 CM. The 84 features represent compounds which are highly abundant in spent media from embryo culture, thus metabolites potentially released by embryos during culture. Similarly, 32 compounds are decreased in spent embryo culture media because they are taken up by embryos during culture.

Table 3.17 Pairwise comparisons of experimental conditions.

Pairwise Comparison		Total # of Significant Compounds p ⩽ 0.05 and FC⩾ | 2 |	Total # of Compounds CV<20%
Cond A	**Cond B**		
Day 5 embryos CM	**0h KSOM**	661	2338
Day 5 embryos CM	**Day 5 CM**	116	2338

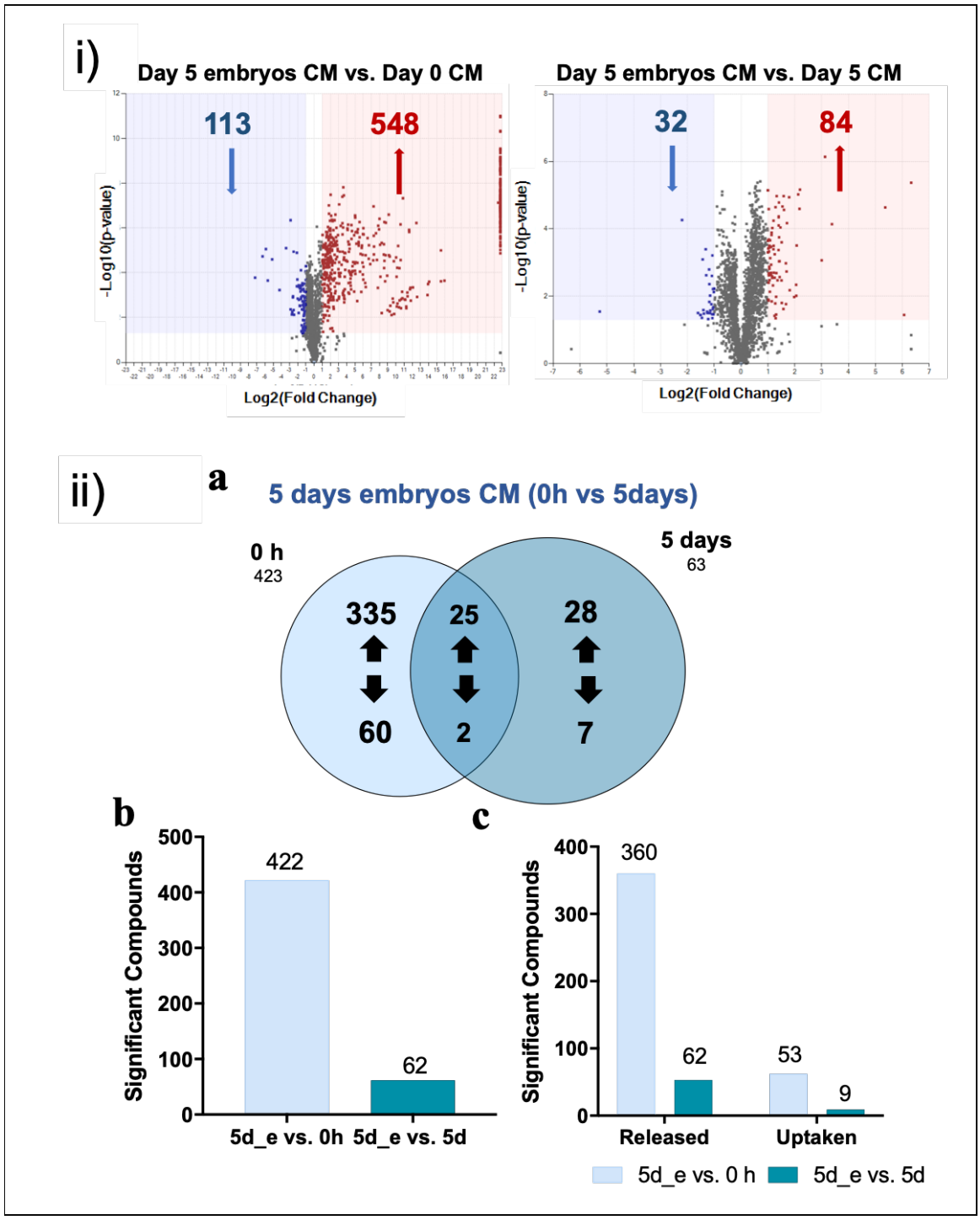

Figure 3.19 LC-MS/MS results of CM samples collected from devices after 5 days with or without embryos.

i) Volcano plots showing the distribution of metabolic compounds for pairwise comparisons as stated above. (Left) Day 5 embryos CM *vs.* Day 0 CM, (right) Day 5 embryos CM *vs.* Day 5 CM. **ii)** Comparison of metabolites significantly altered in day 5 embryo culture CM. **a)** Venn diagram of metabolites altered in control (Day 0 CM, light blue) or day 5 CM (dark blue) compared to day 5 embryo culture CM. b) Graphical representation of the total number of features significantly altered in control or day 5 CM, compared to day 5 embryo culture CM. c) Graphical representation of the increase (released compounds) and decrease (uptaken compounds) in the total number of features found in day 5 embryo culture CM compared to control (light blue) and day 5 embryo culture CM compared to day 5 CM (dark blue).

Compounds that were significantly dysregulated between **day 5 embryo culture CM *vs.* control** or **day 5 embryo culture CM *vs.* day 5 CM**, were putatively identified using available libraries. In detail, a total of 422 and 62 identified metabolites were found to be significantly altered in, respectively, each one of the two pairwise comparisons (Figure 3.19ii-a,b). As mentioned before, **the comparison between these two groups allowed the generation of a list of metabolites which are present in spent media and uniquely associated with embryo culture**.

- 25 features are common between the two pairwise comparisons and are significantly increased in day 5 embryo culture CM, when compared to either control or day 5 CM. Those are known to be **compounds specifically released by embryos after 5 days *in vitro* culture** in the device and associated neither with PDMS nor with media degradation.
- 2 features (identified as cycloalliin and clomethiazole) are common between the two pairwise comparisons and are significantly increased in either control of day 5 CM, when compared to day 5 embryo culture CM. Those could represent **metabolites taken up by embryos** during culture in the microfluidic device using CM.

By comparing compounds released by embryos in KSOM and those released by embryos in CM, 9 were common to the two groups, including (5-chloro-1H-indol-2-yl)(4-methyl-1-piperazinyl)methanone, 2-amino-4-({1-[(carboxymethyl)-C-hydroxycarbonimidoyl]-2-{[1-hydroxy-1-(4-methoxyphenyl)-4-methyl-3-oxopentan-2-yl]sulfanyl}ethyl}-C hydroxycarbonimidoyl) butanoic acid, 7-aminonitrazepam, glutamylmethionine, lepidine D, pyroglutamic acid, ribothymidine, tetrapropylene glycol and xanthine. Those represents metabolites produced by pre-implantation embryos during culture regardless the use of KSOM or CM.

To further investigate impact of uterine epithelial cells-conditioned media on metabolomics of pre-implantation embryo development, the metabolite content in spent KSOM collected from devices was compared to metabolite content in spent CM collected from devices. Table 3.18 aids in providing an overview of differentially abundant metabolites in the three pairwise comparisons considered here: day 5 embryo culture CM *vs*. day 5 embryo culture KSOM, day 5 CM *vs.* day 5 KSOM, and day 0 CM *vs.* day 0 KSOM. Overall, **621 features were**

significantly ($p < 0.05$, FC≥ ⎪2⎪) altered in embryo culture CM compared to embryo culture KSOM, meaning that the use of CM significantly changes metabolite composition of spent embryo culture media. In this analysis, spent media collected from devices in absence of embryos and fresh media at day 0 were considered as controls. In detail, 567 species were found significantly different by comparing day 5 CM and day 5 KSOM, and 589 by comparing day 0 CM and day 0 KSOM.

Table 3.18 Pairwise comparisons of experimental conditions

Pairwise Comparison		Total # of Significant Compounds p ⩽ 0.05 and FC⩾ ⎪2⎪	Total # of Compounds CV<20%
Cond A	**Cond B**		
Day 5 embryos CM	**Day 5 embryos KSOM**	621	2338
Day 5 CM	**Day 5 KSOM**	567	2338
Day 0 CM	**Day 0 KSOM**	589	2338

Of the 621 compounds identified from the comparison between day 5 embryo culture CM and day 5 embryo culture KSOM, 385 illustrated an up-regulated trend and 236 a down-regulated trend in the CM group compared with the control KSOM group (Figure 3.20). Following compound annotation and identification, overall, 208 compounds were identified with confidence level L1-L3 among the up-regulated features, and 145 among the down-regulated features. Interestingly, the volcano plot on the left of Figure 3.20 spotlights the dysregulated compounds detected only in one of the groups, represented by the metabolites on the extreme right and left of the graph. They include **7 compounds unique to spent embryo culture KSOM and 61 to spent CM from embryo culture**. The 61 species are metabolites produced by embryos as a consequence of culture in CM or compounds already present in CM due to the conditioning of the media with uterine epithelial cells, including N-gamma-L-glutamyl-D-alanine, N,N'-bis(4-nitrophenyl)-urea, 6-methyltetrahydropterin, glycerophosphocholine, glutaminylleucine, 1-methyladenosine, uracil, 3-dehydroxycarnitine, 7-methylguanine, inosine diphosphate, thiamine, guanine, L-alpha-aspartyl-L-hydroxyproline and 5-phosphoribosylamine.

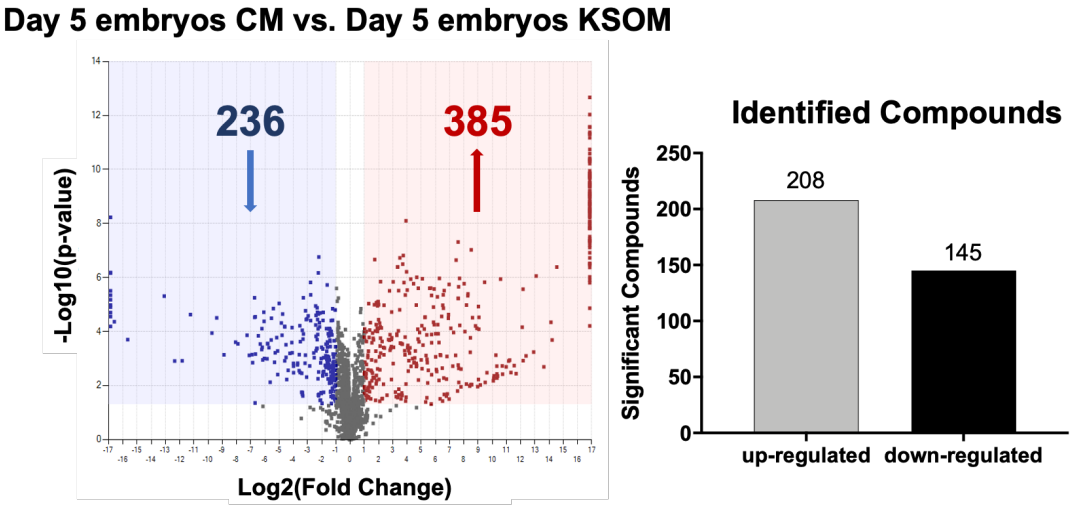

Figure 3.20 Pairwise comparison of day 5 embryo culture CM *vs.* day 5 embryo culture KSOM.

Left) Volcano plot showing the distribution of metabolic compounds for the pairwise comparison. Significance criteria: $p \leq 0.05$, fold change $\geq |2|$. Volcano plots combine the *p*-value measured by ANOVA, expressed as $-\log_{10}$(*p*-value), with the magnitude of the change in relative abundance, expressed as $\log_2$(fold change), between the groups considered in a particular pairwise comparison. Right) Total number of identified metabolites among the up-regulated and the down-regulated species shown in the volcano plot.

Putative metabolite identifications were used for pathway overrepresentation analysis using Metaboanalyst 4.0. Data below show results of the analysis generated by Metaboanalyst using the combined list of significant compounds ($p \leq 0.05$, fold change $\geq |2|$) for the day 5 embryo culture CM *vs.* day 5 embryo culture KSOM pairwise comparison. Up-regulated and down-regulated metabolites were explored in separate analyses.

Figure 3.21 presents a list of the matched overrepresented pathways for compounds significantly increased in day 5 embryo culture CM, compared to day 5 embryo culture KSOM. The metabolome view contains all the matched pathways arranged by *p*-values on Y-axis, and pathway impact values on X-axis. This view map revealed that the enriched pathways for the 208 increased metabolites identified in the CM group were arginine and proline metabolism, purine metabolism, pyrimidine metabolism, alanine, aspartate and glutamate metabolism, arginine biosynthesis, butanoate metabolism, nicotinate and nicotinamide metabolism, cysteine and methionine metabolism, pantothenate and CoA biosynthesis, nitrogen metabolism, D-glutamine and D-glutamate metabolism, glutathione metabolism, aminoacyl-tRNA biosynthesis,

phenylalanine metabolism, histidine metabolism, terpenoid backbone biosynthesis, tryptophan metabolism, selenocompound metabolism, ether lipid metabolism, citrate cycle (TCA cycle), beta-alanine metabolism, propanoate metabolism, phosphatidylinositol signaling system, porphyrin and chlorophyll metabolism, inositol phosphate metabolism, glyoxylate and dicarboxylate metabolism, glycine, serine and threonine metabolism, glycerophospholipid metabolism and tyrosine metabolism. Additionally, five of these pathways had a *p*-value < 0.1 and 16 had pathway impact value higher than 0, which are the cut-off values for relevance.

Results showed that:

- **The most affected metabolic pathway was arginine and proline metabolism,** with the increased abundance of L-glutamate, L-proline, creatine, S-adenosyl-L-methionine and hydroxyproline.
- The metabolic pathway of the amino acids alanine, aspartate and glutamate was also significantly affected, with the increased abundance of the metabolites L-alanine, L-glutamate, succinate and 5-phosphoribosylamine. This pathway is of fundamental importance during embryo development. Amino acids serve not only to provide energy but also to maintain embryo function by preventing cellular stress induced by suboptimal culture conditions *in vitro* (384,385). Noteworthy, **the increased abundance of S-adenosyl methionine might indicate an effect on the *de-novo* methylation of DNA process, which is essential for early mammalian development and for the critical process of gene imprinting** (359). S-adenosyl methionine is indeed necessary for the activity of DNA methyl transferase activity and its detection could be correlated to an increased activity of, not only arginine and proline metabolism, but also DNA methylation in blastocysts cultured in the device (116).
- An increased production of the metabolites uridine, thymine, deoxycytidine, deoxyuridine, uracil, guanine, xanthine, inosine diphosphate, deoxyinosine diphosphate, deoxyadenosine, hypoxanthine and 5-phosphoribosylamine, from embryos cultured in CM indicates an effect on DNA bases (purine and pyrimidine) metabolism pathways which

are critical during embryo growth. In particular, pyrimidine metabolism pathway is required throughout embryo development as inhibition of *de novo* pyrimidine nucleotide synthesis can prevent blastocyst development (386). Purine metabolism is a complex scheme of enzyme reactions which are described as two pathways: the purine salvage pathway and the *de-novo* synthesis pathway. These metabolic pathways are fundamental for pre-implantation embryo development as they allow synthesis of purine precursors for nucleic acid formation (387). The detection of two end-products, xanthine and hypoxanthine, confirmed that those two pathways are both active in pre-implantion embryo development. Xanthine has indeed been reported to be the end-product of purine degradation in the mouse pre-implantation embryo development, while hypoxanthine is an activator of purine salvage pathway (388,389).

Figure 3.22 shows the pathway views of the significantly affected pathways for the metabolites increased in CM including details of the matched compounds. The increased abundance of the metabolites involved in those pathways can be explained by an increased production of these compounds by mouse blastocysts cultured in CM, when compared to KSOM. The metabolic pathways linked to these species could be relatively more active in blastocysts cultured in CM, and this could reveal a beneficial effect on pre-implantation embryo development. On the other hand, another hypothesis might consider that these metabolites are consumed in a reduced amount by blastocyst cultured in CM, compared to KSOM. Despite being difficult to elucidate specific function and activity of these pathways, it is clear that the use of CM have a significant impact on embryo metabolomics and these data need to be investigated further.

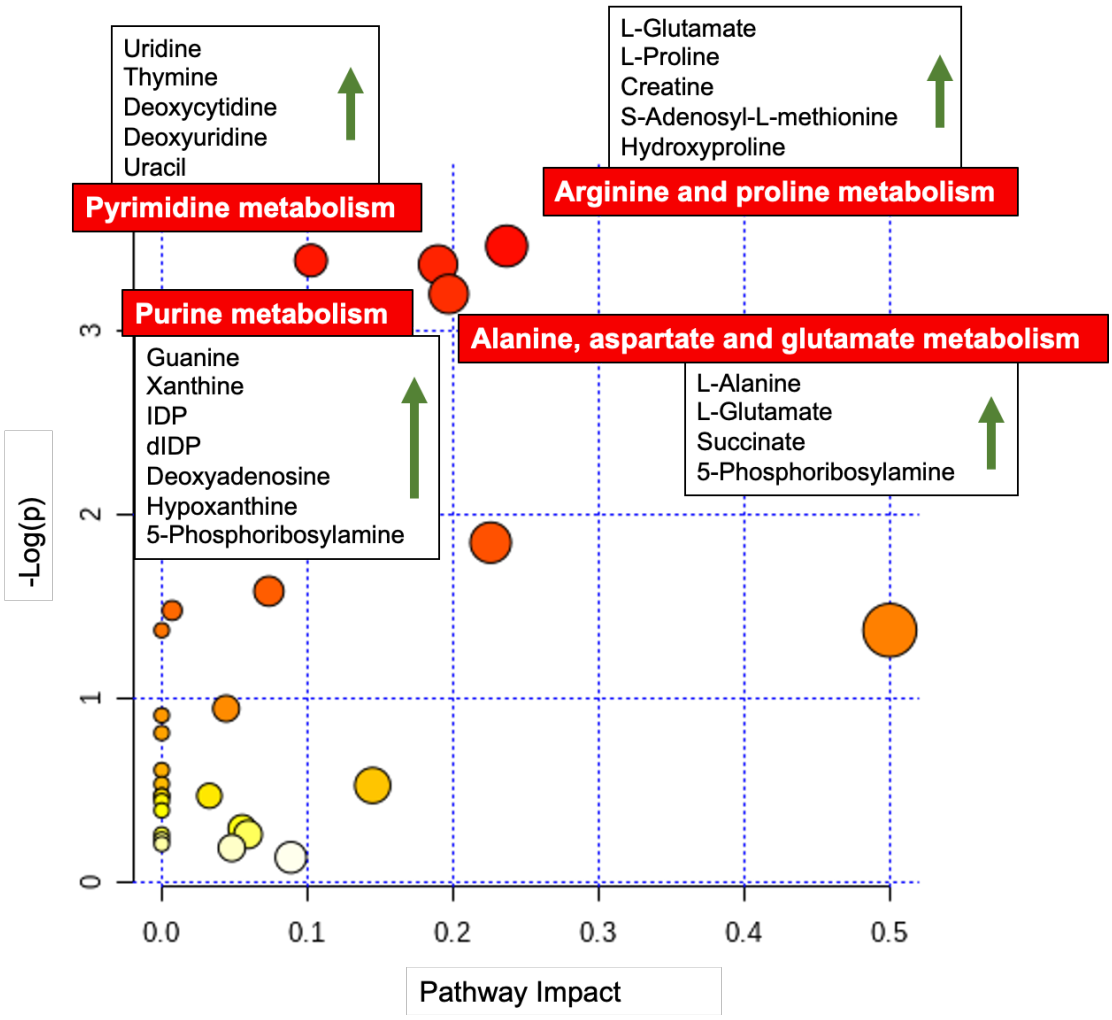

Figure 3.21 Pathways overrepresentation analysis.

Summary of metabolic pathways of significantly changed metabolites between day 5 embryo culture CM and day 5 embryo culture KSOM.

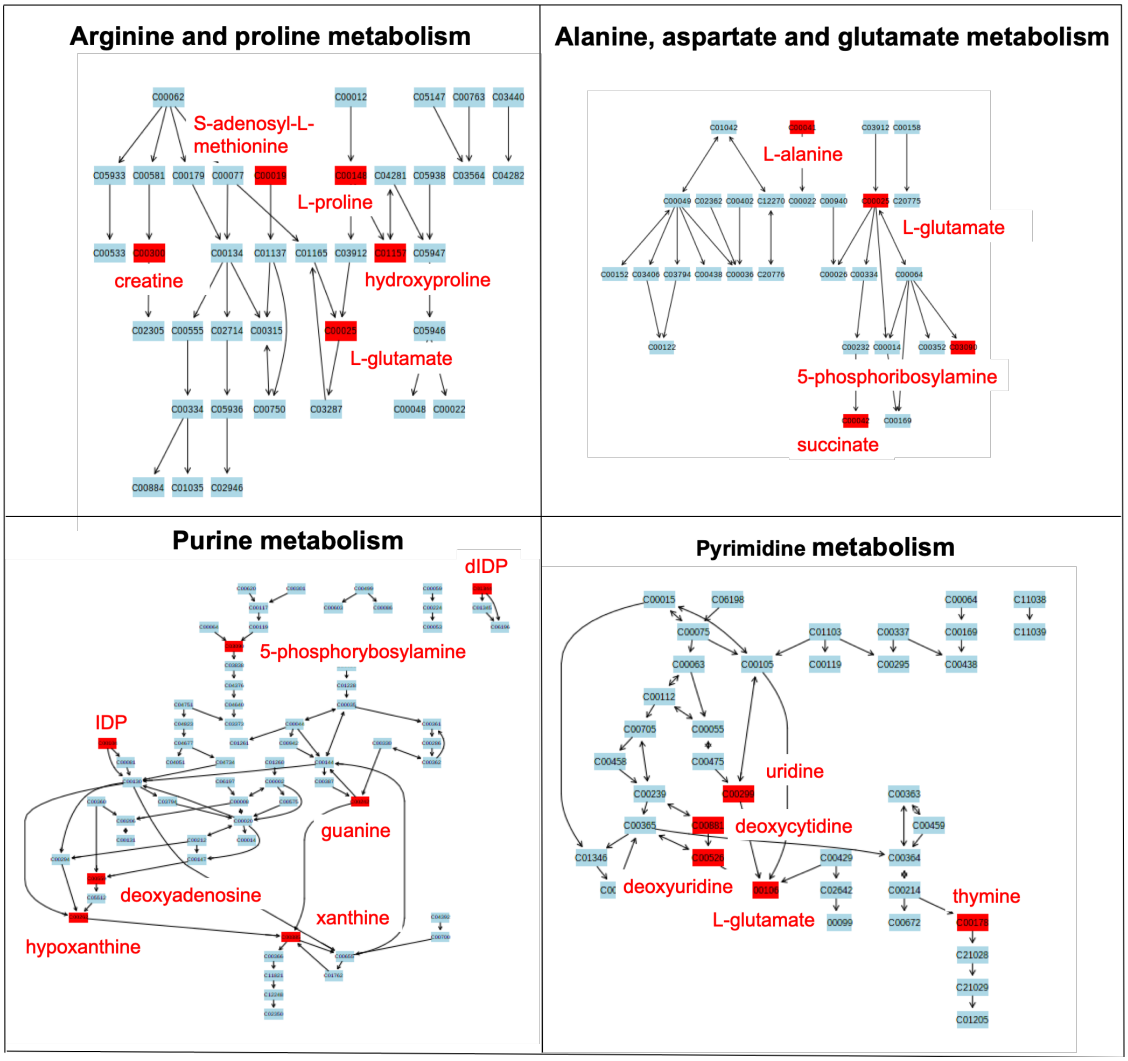

Figure 3.22 Pathway views of the significantly affected pathways for the metabolites increased in CM.

Red nodes reveal individual significant metabolites matched to the pathway and their localization of significance within a given canonical pathway.

Next, **the overrepresented KEGG pathways associated with the list of compounds significantly decreased in day 5 embryo culture CM, compared to day 5 embryo culture KSOM, were determined using Metaboanalyst**. Only pathways with *p*-value < 0.1 were considered significant. The metabolome view in Figure 3.23 revealed that the enriched pathways were aminoacyl-tRNA biosynthesis, phenylalanine metabolism, arginine biosynthesis, cysteine and methionine metabolism, pantothenate and CoA biosynthesis, phenylalanine, tyrosine and tryptophan biosynthesis, D-glutamine and D-glutamate metabolism, nitrogen metabolism, alanine, aspartate and glutamate metabolism, glyoxylate and dicarboxylate metabolism, ubiquinone and other terpenoid-quinone

biosynthesis, glycine, serine and threonine metabolism, caffeine metabolism, tryptophan metabolism, nicotinate and nicotinamide metabolism, histidine metabolism, beta-alanine metabolism, sphingolipid metabolism, purine metabolism, glutathione metabolism, pyrimidine metabolism, tyrosine metabolism and fatty acid biosynthesis. Of these pathways, 10 had impact value higher than 0 and 10 had a p value < 0.2. The most significantly affected ($p < 0.1$) metabolic pathways were aminoacyl-tRNA biosynthesis, phenylalanine metabolism, arginine biosynthesis and cysteine and methionine metabolism.

- Reduction in abundance of metabolites L-glutamine, L-aspartate, L-serine, L-tryptophan, and L-tyrosine implies a potential effect of CM on aminoacyl-tRNA biosynthesis.
- Other amino acid metabolism pathways were affected, such as phenylamine metabolism and cysteine and methionine metabolism, with the decreased abundance of L-tyrosine, phenylacetylglycine, L-serine, L-cystathionine, L-cystine, L-glutamine and L-aspartate.

Those results show that the use of CM can have a significant impact on key metabolic processes and protein synthesis during *in vitro* culture. However, is not well understood weather those pathways are characterized by reduced activity in blastocyst cultured in CM or if there is simply a reduced production of the metabolites involved in those pathways by the developing embryos. Therefore, **there is a need** to further investigate those results, **to better understand the specific role of these altered metabolites on embryo development and implantation potential.**

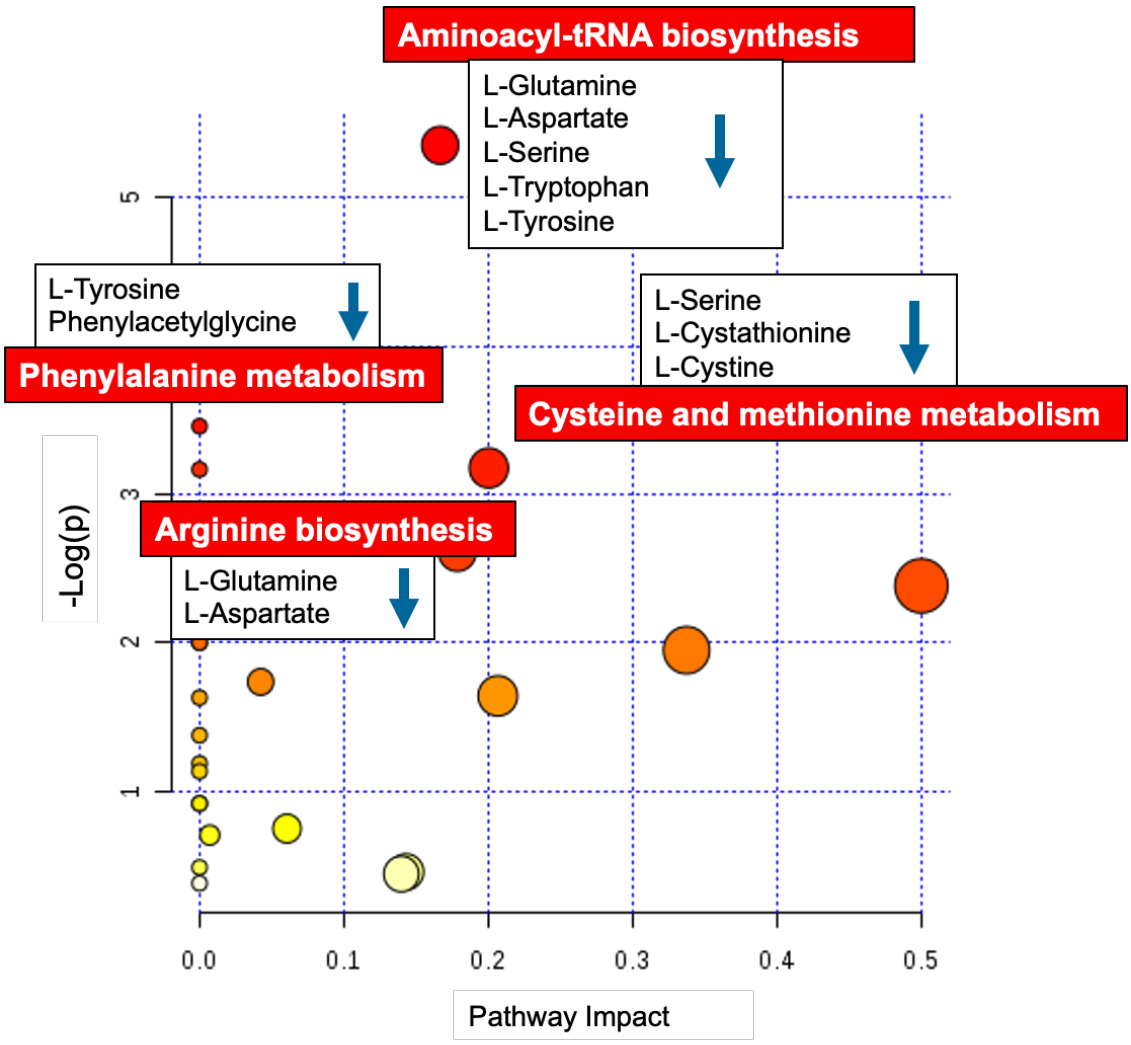

Figure 3.23 Pathways overrepresentation analysis.

Summary of metabolic pathways of significantly changed metabolites between day 5 embryo culture CM and day 5 embryo culture KSOM with Metaboanalyst.

To further investigate key metabolic markers that can be directly associated to the use of CM, the list of metabolites identified from the day 5 embryo culture CM *vs.* day 5 embryo culture KSOM pairwise comparison was compared with the lists of compounds identified in the other two pairwise comparisons, day 5 CM *vs.* day 5 KSOM and day 0 CM *vs.* day 0 KSOM (see Table 3.18). Among the 567 significant compounds detected by comparing day 5 CM and day 5 KSOM, 369 illustrated an up-regulated trend in CM, and 220 a down-regulated trend in CM, compared to the KSOM group. Of the 369 increased species, 84 were only found in the CM group and thus can represent compounds specifically released by uterine epithelial-cells into the medium. In contrast, 9 features were unique to the KSOM group and are purely related to the not-conditioned KSOM medium. Of the

589 significant compounds emerged from the comparison between the two medium at day 0, 491 showed an up-regulated trend in CM, and 76 a down-regulated trend in CM, compared to day 0 KSOM. Interestingly, 113 features were unique to day 0 CM and 3 to day 0 KSOM (Figure 3.24).

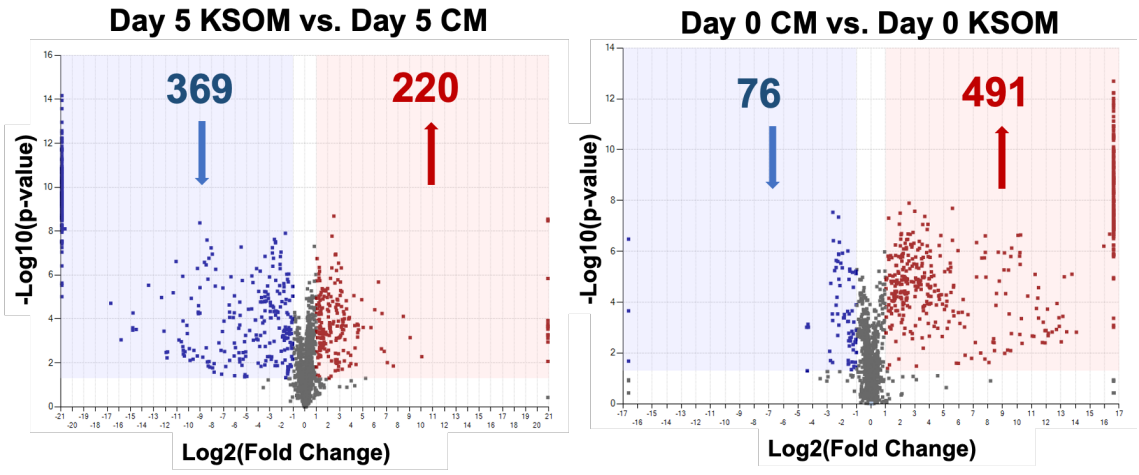

Figure 3.24 LC-MS/MS results of media (KSOM or CM) samples collected from devices after 5 days and controls.

Volcano plots showing the distribution of metabolic compounds for pairwise comparisons as stated above. (Left) Day 0 CM *vs.* Day 0 KSOM, (right) Day 5 CM *vs.* Day 5 KSOM.

Next, the significant compounds were putatively identified using available libraries. Overall, 308, were identified in the pairwise comparison day 5 embryo culture CM *vs.* day 5 embryo culture KSOM, 332 in the pairwise comparison day 5 CM *vs*. day 5 KSOM and 306 in the pairwise comparison day 0 CM *vs*. day 0 KSOM. Figure 3.25 shows in detail the features that were either up-regulated or down-regulated in the CM groups compared to the KSOM groups. The results shows that:

- 53 species are unique to the comparison between CM and KSOM at day 5 with embryos, 61 to the comparison between the two media at day 5 without embryos, and 86 unique to the comparison between the two media at day 0.
- Furthermore, 182 features were common between the three pairwise comparisons, representing compounds significantly increased (160 features) or decreased (22 features) in CM compared to KSOM regardless of incubation time and embryo culture.
- **The origin of the 53 species unique to the comparison between the two spent embryo culture media can be directly linked to metabolites produced or consumed by embryos as a result of culture in CM in the**

device. In detail, the expression of 24 metabolites was at least 2-fold higher (p < 0.5) in CM compared to KSOM including 5-phosphoribosylamine, S-adenosylmethionine and 5-hydroxy-L-trypthophan, which are involved in the metabolism pathways of purine and several amino acids (cysteine, methionine, alanine, arginine, aspartate, glutamate, proline, tryptophan). On the other hand, the relative abundance of 29 metabolites was at least 2-fold higher in KSOM compared to the CM, including glutamylmethionine, glutamyltyrosine, 9-methylxanthine and dodecanoic acid. None of these compounds were found to be involved in metabolic pathways characteristic of mouse embryo development. Thus, **the significant increase in production of metabolites involved in key metabolic pathways by embryos cultured in CM, might indicate another significant impact of the use of uterine epithelial cell-conditioned media on pre-implantation embryo development.**

- 86 compounds are significantly altered in CM compared to control purely due to the composition of the media at day 0, without considering effects of 5 days incubation with or without embryos. Of the **79 features increased of at least 2-fold in day 0 CM compared to day 0 KSOM**, were detected biological species including 5-oxoproline, spermidine, L-glutamine and deoxyribose, which are intermediate of some metabolic processes such as glutathione metabolism, glutamine and glutamate metabolism, nitrogen metabolism and arginine metabolism. These metabolites are likely to be **biomolecules produced by endothelial cells and released into the KSOM during the conditioning of the media**. Their increased abundance into the culture media can have an impact on *in vitro* pre-implantation embryo development. However, is not clear which is the mechanisms behind this process and further studies will investigate which are effectively the compounds contained in CM that can influence embryo grow and implantation potential. In contrast, CM presented reduced relative abundance of 7 metabolites, compared to control, including alanyl-Isoleucine, phenylalanyl-arginine, N-acetylisoleucine, arginyl-Isoleucine, m-methylhippuric acid, 1H-indole-3-acetamide and 2-diethylaminoethanol. Those could be species consumed by uterine epithelial cells during the conditioning of the media, and thus less available in the conditioned media.

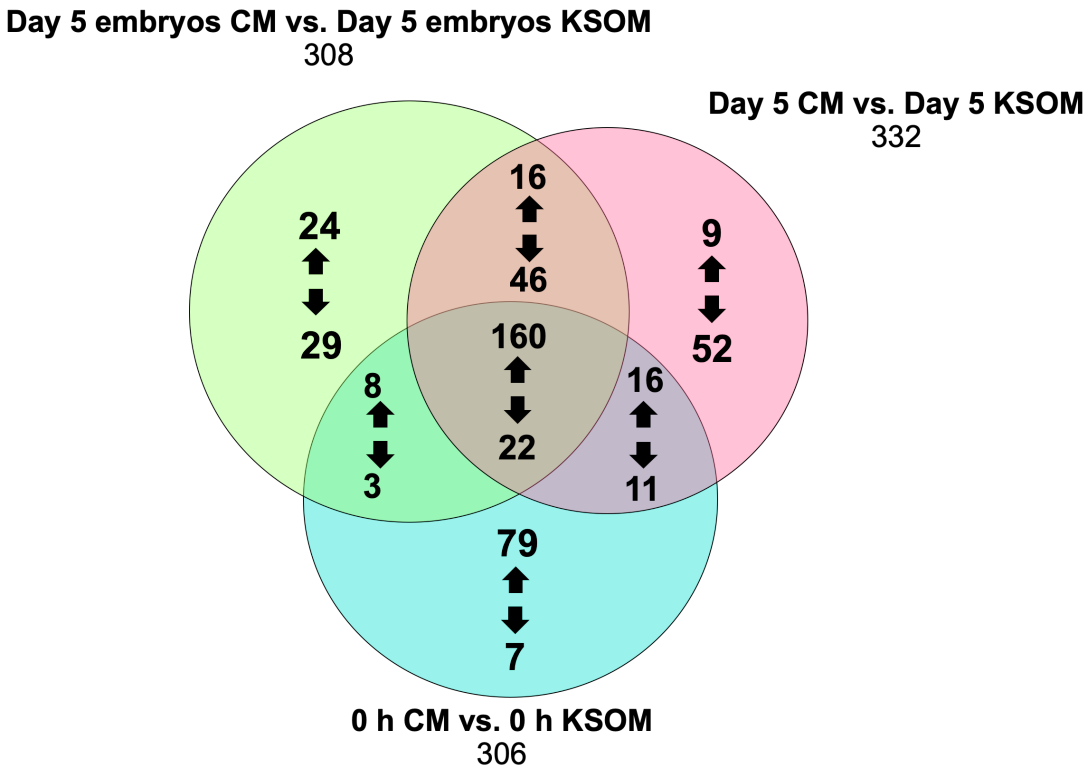

Figure 3.25 Venn diagram showing the distribution of the number of metabolites between the three pairwise comparisons.

3.3.4.2 Metabolomics of murine embryos cultured in microdrops

This section reports results of LC-MS/MS analysis of spent medium collected from 40 µL drops in the presence or without embryos after 4 days, compared to control (fresh medium at day 0). Those data were compared to LC-MS/MS data of spent media samples collected from microfluidic devices. The incubation time of microdrops was chosen according to the previous experiment in a way that culture ended when embryos developed to a fully expanded blastocyst stage. This was reached after approximately 4 days of microdrop culture. The slightly altered incubation time can be explained by the fact that embryo development in the device microenvironment is partially slowed down and embryos develop to blastocysts stage between 12 and 24 h later than in microdrop culture. However, as stated above, no significant reduction of blastocyst rate was observed in devices, compared to control microdrops.

The impact of uterine epithelial cells conditioned media on embryo metabolomics was also assessed and compared with results obtained previously from device culture. In Figure 3.26 are schematized the experimental groups of spent medium samples taken into account in this experiment and the pairwise comparisons of interest (indicated by the arrows).

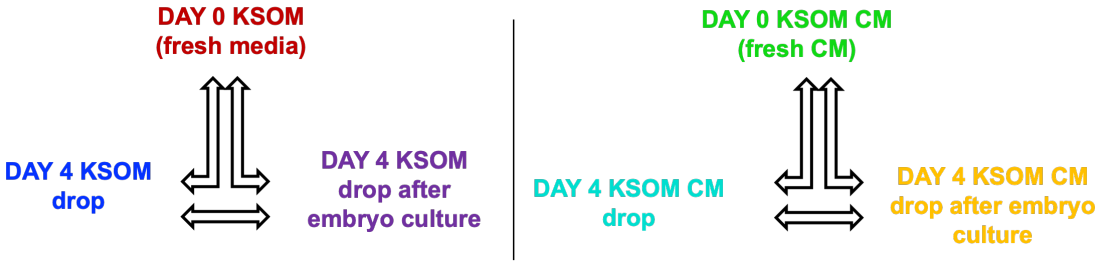

Figure 3.26 Schematic of experimental groups and pairwise comparisons of interest.

3.3.4.2.1 Untargeted metabolomics of mouse embryos cultured in KSOM drops

Similarly to what has been described in the previous sections, the metabolome of murine embryos cultured in 40 µL KSOM drops for 4 days was assessed by LC-MS/MS. For doing so, spent media was collected from KSOM microdrops after 4 days of embryo culture (day 4 embryo culture KSOM) of after 4 days without embryos (day 4 KSOM) and compared to control KSOM (day 0 KSOM). The global metabolomics profile of the three experimental groups was analysed by principal component analysis (PCA) as presented in Figure 3.29i. This showed distinct clustering of the groups, illustrating that three distinct metabolic signatures or profiles were observed in the LC-MS/MS analysis. Then, a comparison of the metabolic compounds observed for each of the three groups of samples was conducted, as shown in the heatmap visualization in Figure 3.29ii. Samples (columns) and features (rows) were processed using Pearson distance and Average clustering via Metaboanalyst 4.0.

The total number of compounds identified in the analysis and characterized by a coefficient of variance (CV) <20% were 2904. Successively, individual pairwise comparisons of the samples groups were considered. Table 3.19 aids in providing an overview of differentially abundant metabolites in pairwise comparisons as stated. Significance criteria were chosen as $p \leq 0.05$ and fold change (FC) $\geq |2|$.

Analysis of the metabolite content of day 4 culture media identified 479 compounds. These data were compared to the list of 393 compounds identified in spent media collected from microdrops after 4 days without embryos. Volcano plots showing the differential metabolites in those two groups are displayed in Figure 3.27.

The results showed that:

- **Most of the metabolites show an increase in spent media collected from drops compared to control** (day 0 KSOM).
- Among the 479 compounds significantly altered ($p \leq 0.05$, FC $\geq |2|$) in day 4 KSOM, 301 were significantly increased and 178 significantly decreased compared to control.

- Similarly, among the 393 compounds significantly altered in day 4 embryo culture media, 304 were significantly increased and 89 significantly decreased compared to control. Moreover, the 83 features graphically represented by the compounds on the extreme right of the volcano plot in Figure 3.27i were unique to the spent embryo culture media. Those might be either associated to drop culture (*i.e.,* medium breakdown molecules, mineral oil or plastic released compounds) or produced by embryos.

Table 3.19 Pairwise comparisons of experimental conditions

Pairwise Comparison		Total # of Significant Compounds $p \leq 0.05$ and FC≥ |2|	Total # of Compounds CV<20%
Cond A	**Cond B**		
Day 4 KSOM	**Day 0 KSOM**	479	2904
Day 4 embryos KSOM	**Day 0 KSOM**	393	2904

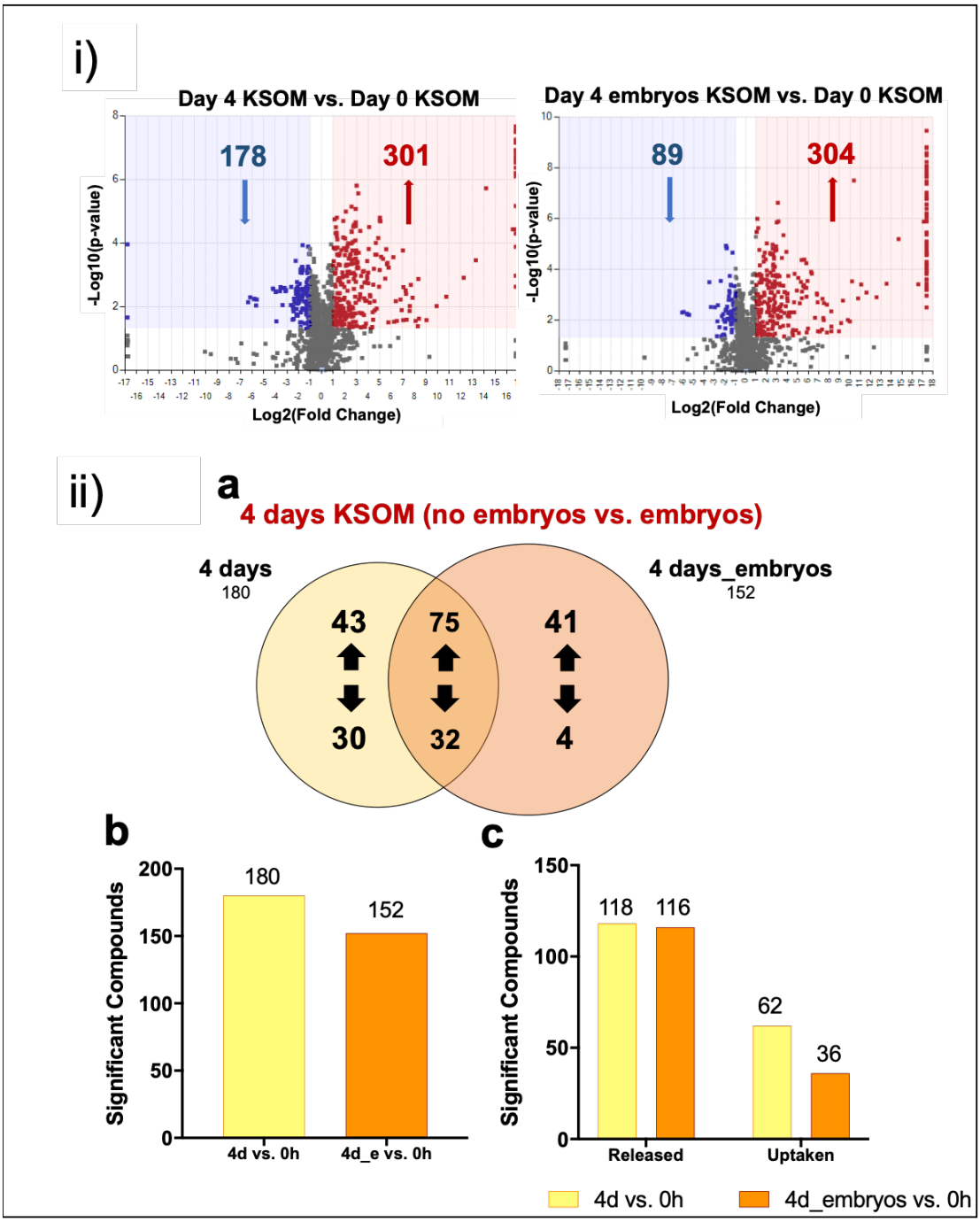

Figure 3.27 LC-MS/MS results of media samples collected from microdrops after 4 days in the presence or without embryos, compared to control.

i) Volcano plots showing the distribution of metabolic compounds for pairwise comparisons as stated above. (Left) Day 4 KSOM from microdrops *vs.* Day 0 KSOM, (right) Day 4 embryo culture KSOM from microdrops *vs.* Day 0 KSOM. ii) Comparison of metabolites significantly altered in day 4 KSOM. a) Venn diagram of metabolites altered in day 4 KSOM or day 4 embryo culture KSOM compared to control (Day 0 KSOM). b) Graphical representation of the total number of features significantly altered in day 5 KSOM or day 5 embryo culture KSOM, compared to control. c) Graphical representation of the increase (released compounds) and decrease (uptaken compounds) in the total number of features found in day 5 KSOM (yellow) and day 5 embryo culture KSOM (orange), compared to control.

Among the compounds that were significantly dysregulated in day 4 KSOM or day 4 embryo culture media, 180 and 152 metabolites, respectively, were putatively identified using available libraries (Figure 3.27ii-b). The comparison between this two groups allowed the generation of a list of metabolites present in spent media after embryo culture as well as a list of metabolites unique to embryos (*i.e.,* produced or consumed by the embryo during culture). In detail:

- 73 metabolites were unique to the microdrop media incubated without embryos, 45 metabolites to the embryo culture media, and 107 were common to the two groups (Figure 3.27ii-a). Among these 107 metabolites, the expression of 75 was significantly ($p < 0.05$) higher of more than 2-fold in both the day 4 embryo culture media and the day 4 KSOM, compared to control, including arginyl-glycine, histidinyl-hydroxyproline, 3-carbamoyl-2-phenylpropionic acid, ribothymidine, 5-oxoprolinate and S-allylcysteine, all of which had an expression value of > 10-fold higher in the day 4 media compared to the control. In contrast, the relative abundance of 32 compounds was at least 2-fold higher ($p < 0.05$) in the control compared to spent media from culture microdrops, including L-tyrosine, aspartylphenylalanine, phenylacetylglycine and threoninyl-histidine.

Compounds that are significantly increased in spent media collected from culture microdrops could represent metabolites produced by embryos, breakdown products of media components digestion or species released into the media from the plastic or mineral oil used for embryo culture as a consequence of incubation at 37 ºC. Overall, after 4 days of incubation, a total of 118 and 116 compounds were significantly ($p \leq 0.05$ and FC $\geq|2|$) increased into culture media samples collected from drops with or without embryos, respectively (Figure 3.27ii-b). Among them:

- 75 were common between the two groups and represent compounds released into culture media only as a result of media degradation or of the culture microenvironment (*i.e.,* mineral oil or plastic-related species).
- The remaining compounds were unique to day 4 KSOM (43 features) or to day 4 embryo culture media (41 features) (Figure 3.27i-a).

On the other hand, features that are significantly decreased in spent media samples collected from culture microdrops represent compounds either absorbed from the culture environment or consumed by embryos during culture. In detail,

a total of 62 and 36 metabolites were decreased in day 4 KSOM and day 4 embryo culture media, respectively. Among them:

- 32 metabolites were common between the two groups, including compounds that are potentially sequestered by the culture environment from the culture medium or media components which have been consumed during culture.
- The remaining compounds were unique to day 4 KSOM (30 features) or to day 4 embryo culture media (4 features) (Figure 3.27ii-a).

Species unique to day 4 embryo culture media represent metabolites released (increased compounds) or consumed (decreased compounds) from the culture medium by the developing embryos in culture and are thus directly associated with embryo metabolism. In particular, it was observed increased abundance of metabolites such as ornithine, L-proline, 5'-Methylthioadenosine hypoxanthine, deoxycytidine, 2-hydroxyglutarate, lactose, which are all involved in key metabolic pathways such as amino acids or DNA bases metabolisms and biosynthesis. Specifically, ornithine is involved in glutathione, arginine and proline metabolism pathways, whereas deoxycytidine is involved in pyrimidine metabolism.

Another pairwise comparison was carried out between day 4 embryo culture media and day 4 KSOM, identifying a list of 86 compounds. These data were compared to the list of 393 compounds identified in spent embryo culture media (Table 3.20). Volcano plots showing the differential metabolites in those two pairwise comparisons are displayed in Figure 3.28i. Among the 86 compounds significantly ($p < 0.05$, FC $\geq \left| 2 \right|$) different in the first pairwise comparison, 4 were significantly decreased and 82 significantly increased in day 4 embryo culture media when compared to day 4 KSOM. The 82 features represent metabolites released by embryos into the medium during culture, whereas the 4 decreased compounds are taken up by embryos during culture. Moreover, 16 features were unique to spent embryo culture media, whereas only 1 was unique to day 4 KSOM. The first ones are graphically represented by the compounds on the extreme right of the volcano plot on the right of Figure 3.28i, and the feature only detected in day 4 KSOM appears on the extreme left of the plot.

Table 3.20 Pairwise comparisons of experimental conditions.

Pairwise Comparison		Total # of Significant Compounds $p \leqslant 0.05$ and $FC \geqslant \lvert 2 \rvert$	Total # of Compounds CV<20%
Cond A	**Cond B**		
Day 4 embryos KSOM	**Day 4 KSOM**	86	2904
Day 4 embryos KSOM	**Day 0 KSOM**	393	2904

The differential compounds were searched against available libraries and 36 metabolites were identified from the pairwise comparison between day 4 embryo culture media and day 4 KSOM. The comparison between this group and the 152 species identified in day 4 embryo culture media (*vs.* control), allowed the generation of a list of metabolites which are present in spent media and uniquely associated with embryo culture (Figure 3.28ii). In particular:

- There are 28 features which are significantly decreased in either control or day 4 KSOM, when compared to day 4 embryo culture media. Those are known to be compounds specifically released by embryos after 4 days *in vitro* culture and associated neither with the culture environment nor with media degradation.
- The only feature significantly increased in both control and day 4 KSOM, when compared to day 4 embryo culture media, is 5-hydroxydantrolene and is likely to be taken up by embryos during culture.

Considering the remaining identified species, 7 were unique to the comparison between day 4 embryo culture media and day 4 KSOM, whereas 123 were unique to the comparison between day 4 embryo culture media and control. Among those 123 features:

- 35 were highly abundant in day 0 embryo media (*e.g.,* L-galacto-2-heptulose, glutamyllysine and deoxyadenosine) representing species absorbed from the culture medium simply as a consequence of the culture microenvironment and not by the embryos.
- 88 appeared to be significantly decreased in spent embryo culture media when compared to control. Those include media components degraded over time or species partially released by plastic or mineral oil used for culture, including N-acetyl-L-methionine, 5-oxoprolinate, pyroglutamic acid and ribothymidine.

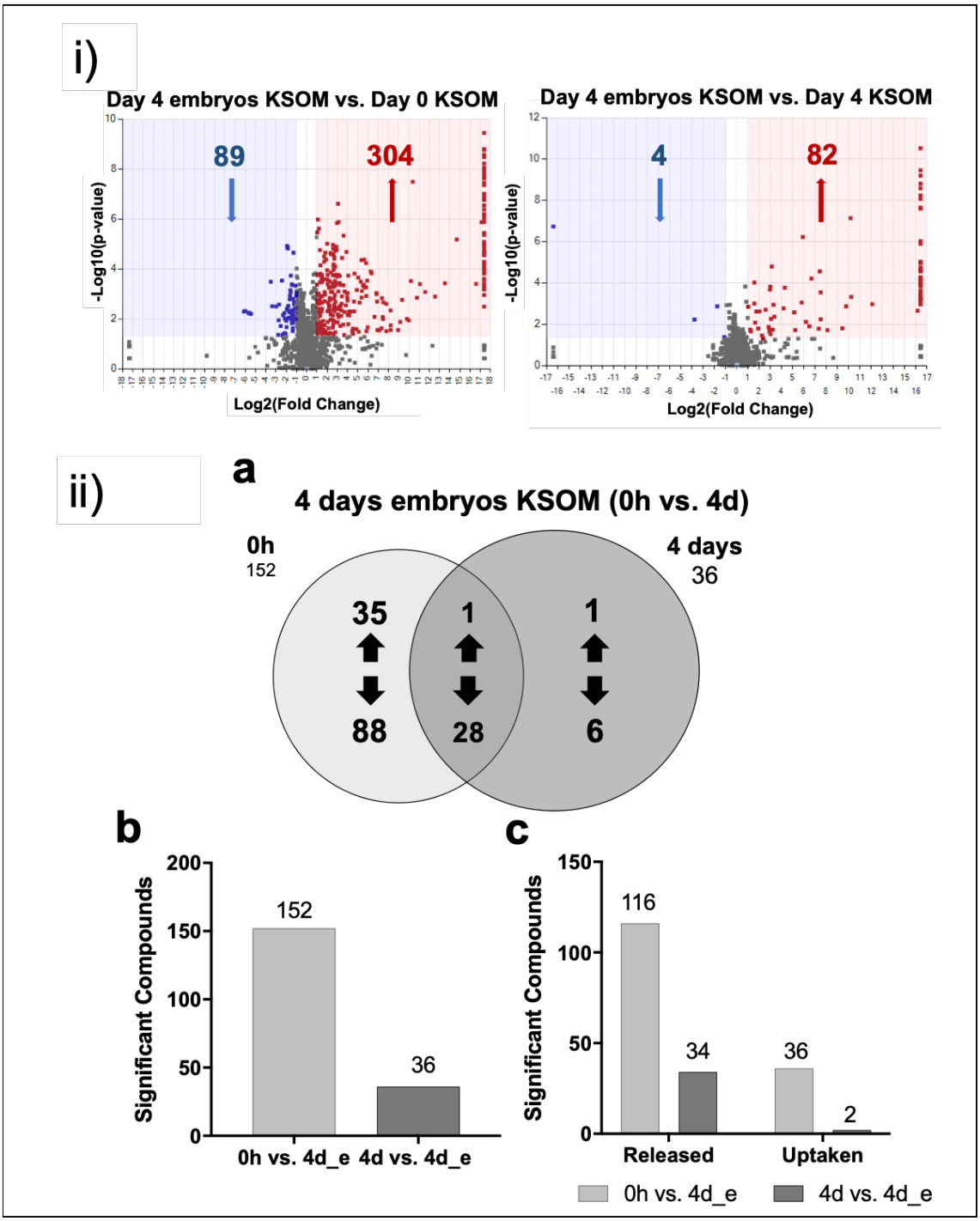

Figure 3.28 LC-MS/MS results of media samples collected from microdrops after 4 days in the presence or without embryos.

i) Volcano plots showing the distribution of metabolic compounds for pairwise comparisons as stated above. (Left) Day 4 embryo culture KSOM *vs.* Day 0 KSOM, (right) Day 4 embryo culture KSOM *vs.* Day 4 KSOM. **ii)** Comparison of metabolites significantly altered in day 4 embryo culture KSOM. a) Venn diagram of metabolites altered in control (day 0 KSOM) or day 4 KSOM compared to day 4 embryo culture KSOM. b) Graphical representation of the total number of features significantly altered in control or day 4 KSOM, compared to day 4 embryo culture KSOM. c) Graphical representation of the increase (uptaken compounds) and decrease (released compounds) in the total number of features found in day 4 embryo culture KSOM compared to control (light grey) and day 4 KSOM (dark grey).

3.3.4.2.2 Effect of cells conditioned media on embryo metabolomics

In accordance to what has been discussed in section 3.3.4.1.4, the impact of culture using mouse uterine epithelial cell-conditioned media (CM) was assessed by measuring metabolite content in spent CM collected from culture microdrops at day 4 of embryo culture using untargeted LC-MS/MS. Data were compared to metabolite content in control media, fresh KSOM CM at day 0 (day 0 CM), or metabolite content in media incubated for 4 days without embryos (day 4 CM). Those results were then compared to data previously obtained from microdrop culture in KSOM, to identify metabolites produced or consumed by embryos in response to presence of CM.

A statistical evaluation by global principal component analysis (PCA) of the different experimental sample groups and controls is shown below in Figure 3.29. The plot presents abundance data of medium extracted metabolites for the six biological conditions, illustrating a distinct shift in metabolic profiles between groups. The run samples are indeed separated based on overall variability, as the plot shows clear separation of KSOM samples *vs.* CM samples across the x-axis (Figure 3.29i). Those results confirm also the quality of the analysis and the presence of an altered level of metabolites among all the experimental groups. In detail, by comparing media at day 0, the CM is separated from KSOM, indicating a clearly different composition of the media. Similar considerations can be done for both day 4 media collected from microdrops without any embryos (CM *vs.* KSOM) and day 4 embryo culture media (CM *vs.* KSOM), which were all clearly distinct as groups. Those differences are also visible in the heatmap visualization shown in Figure 3.29ii where colours are displayed based on normalized abundance, ranging from low (green) to high (red) as shown in the legend, and all metabolic compounds are represented as rows. Each column of the map, which represents the group average of the samples, is easy distinguishable from the others. Moreover, **is possible to identify a cluster of compounds**, at the top of the map, **that includes a group of species remarkably increased in CM groups compared to KSOM groups. Those are likely to represent biomolecules released into the media from uterine epithelial cells and characteristic of CM**.

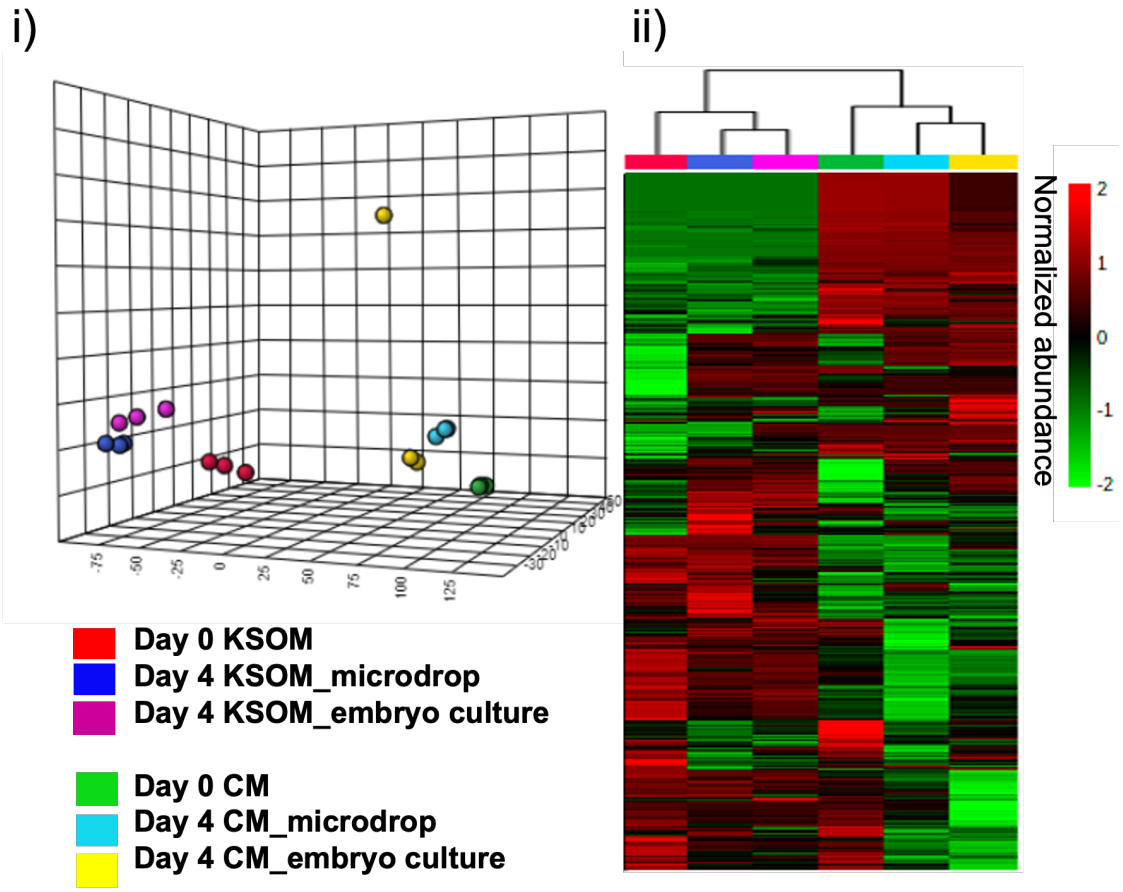

Figure 3.29 LC-MS/MS global metabolomic profile analysis of murine blastocysts cultured in microdrops in KSOM or CM.

i) PCA plot for LC-MS/MS data of media samples from all the experimental groups. **ii)** Heatmap representing LC-MS/MS data. Compounds are presented as rows and sample replicates as columns and processed by using Euclidean distance and Ward clustering via Metaboanalyst 4.0 for Pareto scaled, log transformed, and averaged group data. Colours are displayed by normalized abundance, ranging from low (green) to high (red).

To investigate metabolite content of the different experimental groups, the pairwise comparisons described in Section 3.3.4.2.1 were carried out for samples of conditioned media collected from microdrops.

- Firstly, metabolite content in day 4 CM collected from microdrop without embryos (day 4 CM) was compared to that of control media (day 0 CM), identifying a total of 511 significant ($p \leq 0.05$ and $FC \geq |2|$) compounds (Table 3.21). Among them, 266 were significantly increased in spent media from microdrops, while 245 were increased in control media.
- Similarly, from the pairwise comparison between day 4 embryo culture CM and control, were detected 367 significantly altered features. Of these, 271 were increased and 96 decreased in spent embryo culture media from devices, compared to control (Figure 3.30i), with 14 feature unique to spent

media from embryo culture and 4 to control media. Those particular species are displayed, respectively, by the compounds at the extreme right and left of the volcano plot shown on the right of Figure 3.30i and can have different origins. They can in fact be indicative of embryo metabolomics in CM as well as of media degradation or effects of the culture environment on medium metabolite content.

Table 3.21 Pairwise comparisons of experimental conditions

Pairwise Comparison		Total # of Significant Compounds p ⩽ 0.05 and FC⩾ | 2 |	Total # of Compounds CV<20%
Cond A	**Cond B**		
Day 4 CM	**Day 0 CM**	511	2904
Day 5 embryos CM	**Day 0 CM**	367	2904

Following compound annotation, the pairwise comparison between day 4 CM and control was compared to the one between day 4 embryo culture CM and control (Figure 3.30ii-a). Overall, the first one identified a total of 211 significantly altered annotated compounds, whereas the second one highlighted 157 species (Figure 3.30ii-b). Among them, 119 were common between the two groups, 92 unique to day 4 drop-media and 38 unique to day 4 embryo culture media. **Species that were found common between the two groups, are specifically associated to the effect of the culture environment on metabolite content of spent medium.** In particular:

- The 84 features significantly increased in day 4 media (without or with embryos) might represent breakdown products of media components digestion as well as species released into the media from the plastic or mineral oil used for embryo culture as a consequence of incubation.
- The 35 compounds significantly decreased in day 4 media (without or with embryos) compared to control, are compounds sequestered by the culture environment from the culture medium or media components which have been consumed during culture.

Similar considerations apply for the 38 species identified only in spent embryo culture media compared to control. They represent metabolites released into the medium or compounds consumed from the medium by embryos during 4 day of culture. The 35 compounds released into the medium and unique to the spent embryo culture media group included key metabolic markers such as ornithine,

lactose and kynurenine, known to be involved in several amino acids metabolism pathways.

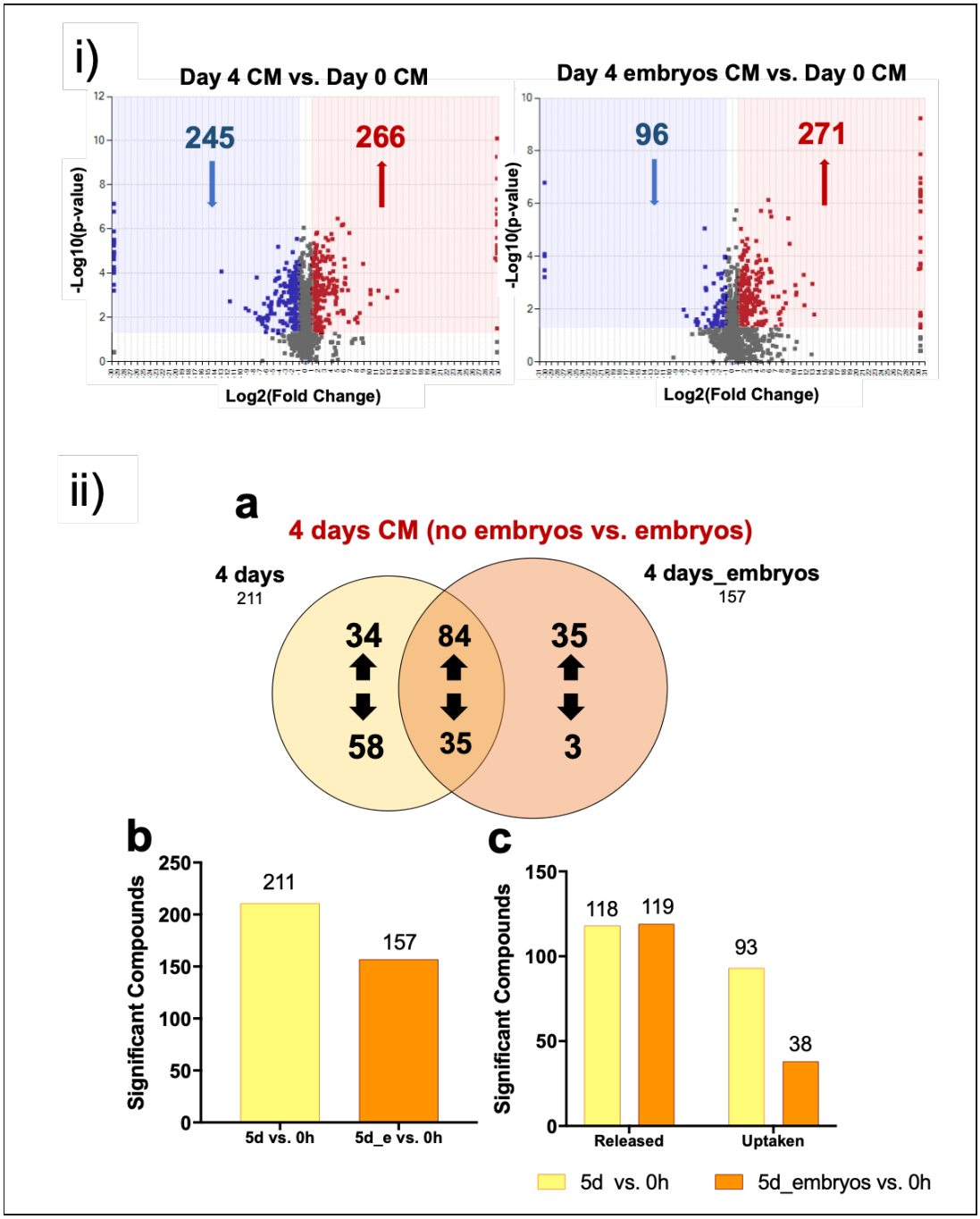

Figure 3.30 LC-MS/MS results of CM samples collected from microdrops after 4 days with or without embryos, compared to control.

i) Volcano plots showing the distribution of metabolic compounds for pairwise comparisons as stated above. (Left) Day 4 CM *vs.* Day 0 CM, (right) Day 4 embryo culture CM *vs.* Day 0 CM. **ii)** Comparison of metabolites significantly altered in day 4 CM. a) Venn diagram of metabolites altered in day 4 CM or day 4 embryo culture CM compared to control (day 0 CM). b) Graphical representation of the total number of features significantly altered in day 5 CM or day 5 embryo culture CM, compared to control. c) Graphical representation of the increase (released compounds) and decrease (uptaken compounds) in the total number of features found in day 5 CM (yellow) and day 5 embryo culture CM (orange), compared to control.

To further investigate impact of CM on embryo metabolomics, metabolite content of day 4 embryo culture CM was compared to that of day 4 CM, identifying a list of 75 differentially abundant compounds. Successively, these data were compared to the list of 367 significant compounds identified in spent embryo culture media (Table 3.22). Volcano plots providing an overview of differentially abundant metabolites in those two pairwise comparisons are displayed in Figure 3.31i. Of the 75 compounds significantly different in the first pairwise comparison, 6 were significantly decreased and 69 significantly increased in day 4 embryo culture CM when compared to day 4 CM. The 69 features represent metabolites released by embryos into the medium during culture in CM, whereas the 6 decreased compounds are consumed by embryos from the culture medium.

Table 3.22. Pairwise comparisons of experimental conditions.

Pairwise Comparison		Total # of Significant Compounds $p \leq 0.05$ and $FC \geq \lvert 2 \rvert$	Total # of Compounds CV<20%
Cond A	**Cond B**		
Day 4 embryos CM	**Day 0 CM**	367	2904
Day 4 embryos CM	**Day 4 CM**	75	2904

Compounds that were significantly dysregulated between day 4 embryo culture CM *vs.* control or day 4 embryo culture CM *vs.* day 4 CM, were putatively identified using available libraries. In detail, a total of 157 and 31 identified metabolites, respectively, were found to be significantly altered in each one of the two pairwise comparisons (Figure 3.31ii-a,b). Among them, 20 features were found to be significantly altered in both the two comparisons, and thus represent compounds uniquely associated with embryo culture. In particular, there are **19 features which are significantly increased in day 4 embryo culture CM,** when compared to either control or day 4 CM. Those can be interpreted as **compounds specifically released by embryos after 4 days of culture in CM** microdrops and include lactose, ornithine, and 5-hydroxy-L-tryptophan. In contrast, the abundance of only one feature ((2S)-2-amino-3-(4-hydroxy-3-methoxyphenyl)-2-methylpropanoic acid) was significantly reduced in day 4 embryo culture CM, and is likely to be taken up by embryos during culture using CM.

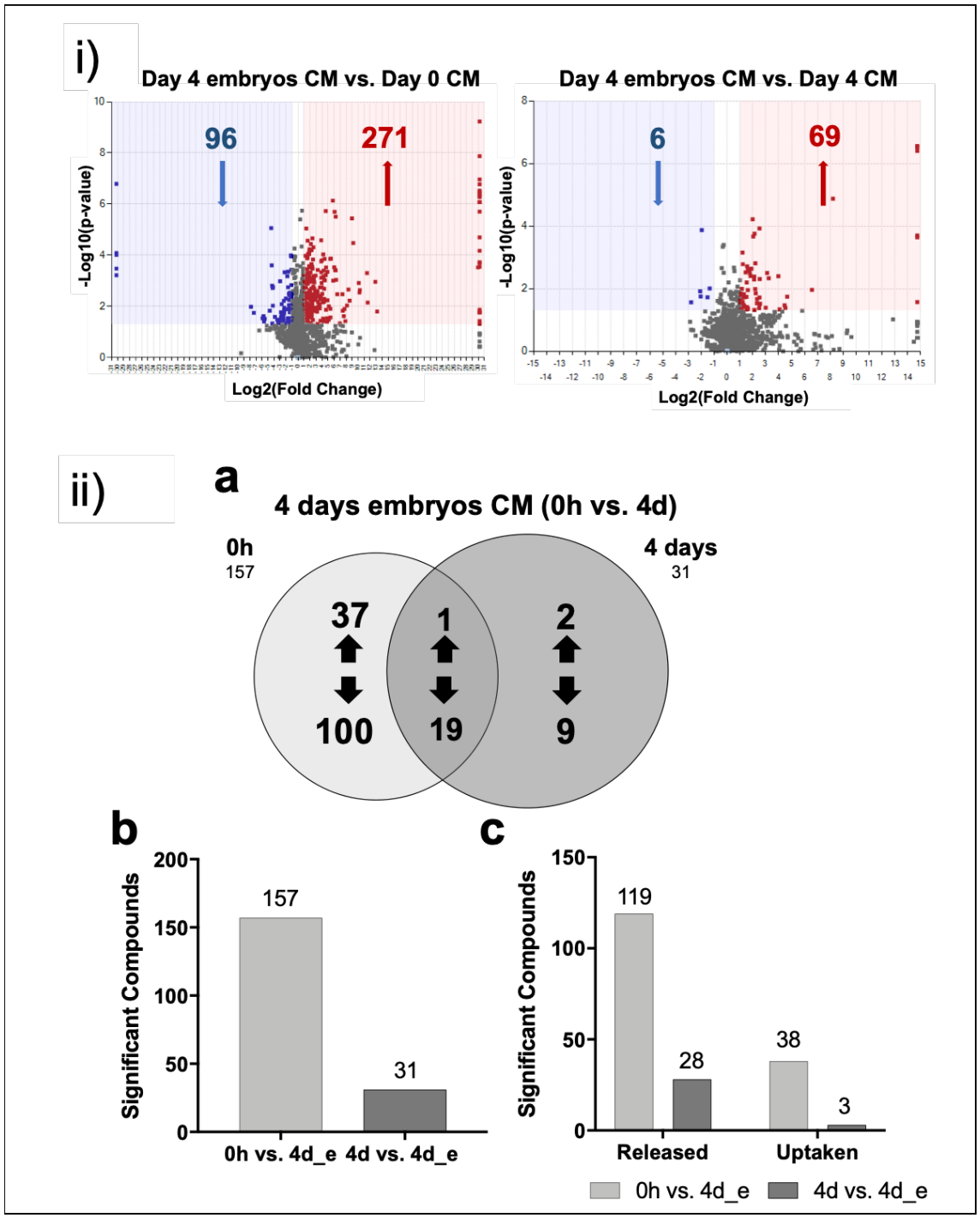

Figure 3.31 LC-MS/MS results of CM samples collected from microdrops after 4 days with or without embryos, compared to control.

i) Volcano plots showing the distribution of metabolic compounds for pairwise comparisons as stated above. (Left) Day 4 embryo culture CM *vs.* Day 0 CM, (right) Day 4 embryo culture CM *vs.* Day 4 CM. **ii)** Comparison of metabolites significantly altered in day 4 embryo culture CM. a) Venn diagram of metabolites altered in control (Day 0 CM) or day 4 CM compared to day 4 embryo culture CM. b) Graphical representation of the total number of features significantly altered in control or day 4 CM, compared to day 4 embryo culture CM. c) Graphical representation of the increase (uptaken compounds) and decrease (released compounds) in the total number of features found in day 4 embryo culture CM compared to control (light grey) and day 4 CM (dark grey).

Next, the metabolite content of spent CM and KSOM collected from culture microdrops were compared to further investigate impact of uterine epithelial cells-conditioned media on metabolomics of pre-implantation embryos. Table 3.23 provides an overview of differentially abundant metabolites in pairwise comparisons as stated. Overall, 560 features were significantly ($p < 0.05$, FC ≥ $|2|$) altered in embryo culture CM compared to embryo culture KSOM. Spent media collected from microdrops in absence of embryos and fresh media at day 0 were considered as a control. In detail, 1063 species were found significantly different by comparing day 4 CM and day 4 KSOM, and 1221 by comparing day 0 CM and day 0 KSOM. Therefore, those **results indicate that the use of CM has a considerable effect on medium composition as well as on embryo metabolites consumption and/or production**.

Table 3.23. Pairwise comparisons of experimental conditions

Pairwise Comparison		Total # of Significant Compounds p ≤ 0.05 and FC≥ |2|	Total # of Compounds CV<20%
Cond A	**Cond B**		
Day 4 embryos CM	**Day 4 embryos KSOM**	560	2904
Day 4 CM	**Day 4 KSOM**	1063	2904
Day 0 CM	**Day 0 KSOM**	1221	2904

The volcano plot in Figure 3.32 illustrates the differentially regulated compounds between the sample groups, with specific numbers for down-regulated and up-regulated compounds in the day 4 embryo culture CM samples *vs.* day 4 embryo culture KSOM ones. Of the 560 significantly altered compounds identified from this comparison, 375 illustrated an up-regulated trend and 185 a down-regulated trend in the CM group compared to the control KSOM group. Moreover, 7 compounds were unique to spent embryo culture KSOM and 29 to spent embryo culture CM. Those 29 species are metabolites produced by embryos as a consequence of culture in CM or compounds already present in CM after the conditioning of the media with uterine epithelial cells.

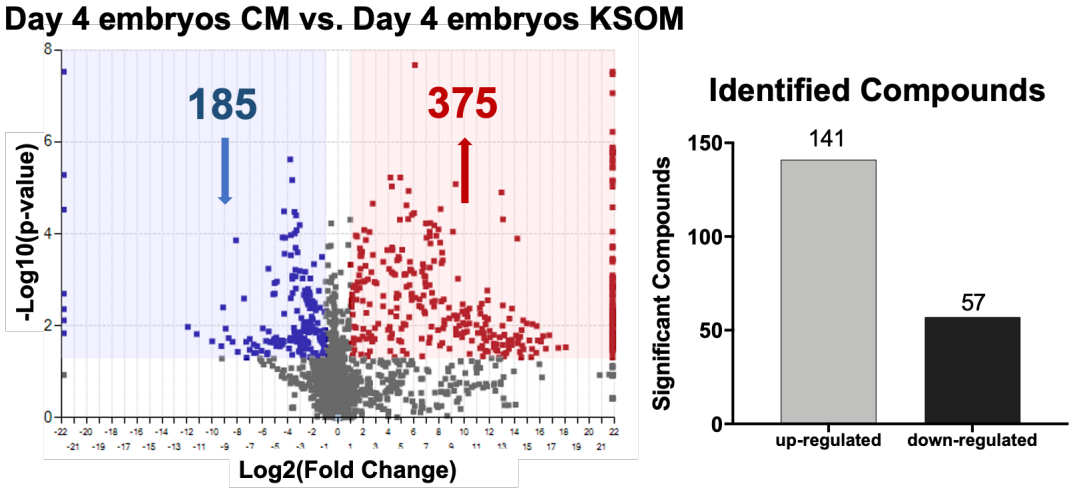

Figure 3.32 Pairwise comparison of day 4 embryo culture CM *vs.* day 4 embryo culture KSOM.

Left) Volcano plot showing the distribution of metabolic compounds for the pairwise comparison day 4 embryo culture CM *vs.* day 4 embryo culture KSOM. Significance criteria: $p \leq 0.05$, fold change $\geq |2|$. Right) Total number of identified metabolites among the up-regulated and the down-regulated species shown in the volcano plot.

Potential metabolite identifications were established using multiple databases and spectral libraries, as described above, and used for pathway overrepresentation analysis. Overall, 141 compounds were identified with confidence level L1-L3 among the up-regulated feature, and 57 among the down-regulated features. Data below show results of the analysis generated by Metaboanalyst using the combined list of significant compounds ($p \leq 0.05$, fold change $\geq |2|$) for the day 4 embryo culture CM *vs.* day 4 embryo culture KSOM pairwise comparison. Up-regulated and down-regulated metabolites were explored in separate analyses.

The metabolome view map in Figure 3.33 shows the matched overrepresented pathways for the 141 compounds significantly increased in day 4 embryo culture CM, compared to day 4 embryo culture KSOM. In detail, the enriched pathways were folate biosynthesis, glycine, serine and threonine metabolism, one carbon pool by folate, vitamin B6 metabolism, glycerophospholipid metabolism, biotin metabolism, arginine and proline metabolism, tryptophan metabolism, nicotinate and nicotinamide metabolism, glycerolipid metabolism, terpenoid backbone biosynthesis, pantothenate and CoA biosynthesis, pyruvate metabolism, glycolysis or gluconeogenesis, galactose metabolism, cysteine and methionine metabolism, pyrimidine

metabolism, aminoacyl-tRNA biosynthesis and purine metabolism. Additionally, four of these pathways had a *p*-value < 0.2 and thirteen had a pathway impact value higher than 0, which is the cut-off value for relevance. However, only the folate biosynthesis pathway had a *p*-value < 0.1, with the increased abundance of folate, dihydropteroate, tetrahydrobiopterin. **Despite showing reduced significance, some key metabolic pathways, such as amino acids and vitamins metabolism pathways, were overrepresented for the considered metabolites**. For instance, some up-regulated metabolites (*i.e.,* choline, creatine and L-proline) are involved in metabolic pathways of several amino acids (*i.e.,* glycine, serine, threonine, arginine and proline), while pyridoxine is involved in vitamin B6 metabolism. Folate (or vitamin B9) is involved also in one-carbon metabolism pathway which is a universal metabolic process that serves to activate and transfer one-carbon units for biosynthetic processes, including purine and thymidine synthesis and homocysteine remethylation (390). One-carbon metabolism plays thus an important role in nucleic acid synthesis and epigenetic maintenance.

The up-regulated species involved in those pathways are produced in higher amount by blastocysts cultured in CM compared to those cultured in KSOM. Therefore, **the mentioned metabolic pathways could be more active in blastocysts cultured in CM, revealing a potential beneficial effect on pre-implantation embryo development**. On the other hand, another hypothesis might be that these metabolites are consumed in a reduced amount by blastocyst cultured in CM, compared to KSOM. Despite being difficult to elucidate specific function and activity of these pathways, it is clear that the use of CM have a significant impact on embryo metabolomics and that these data need to be investigated further.

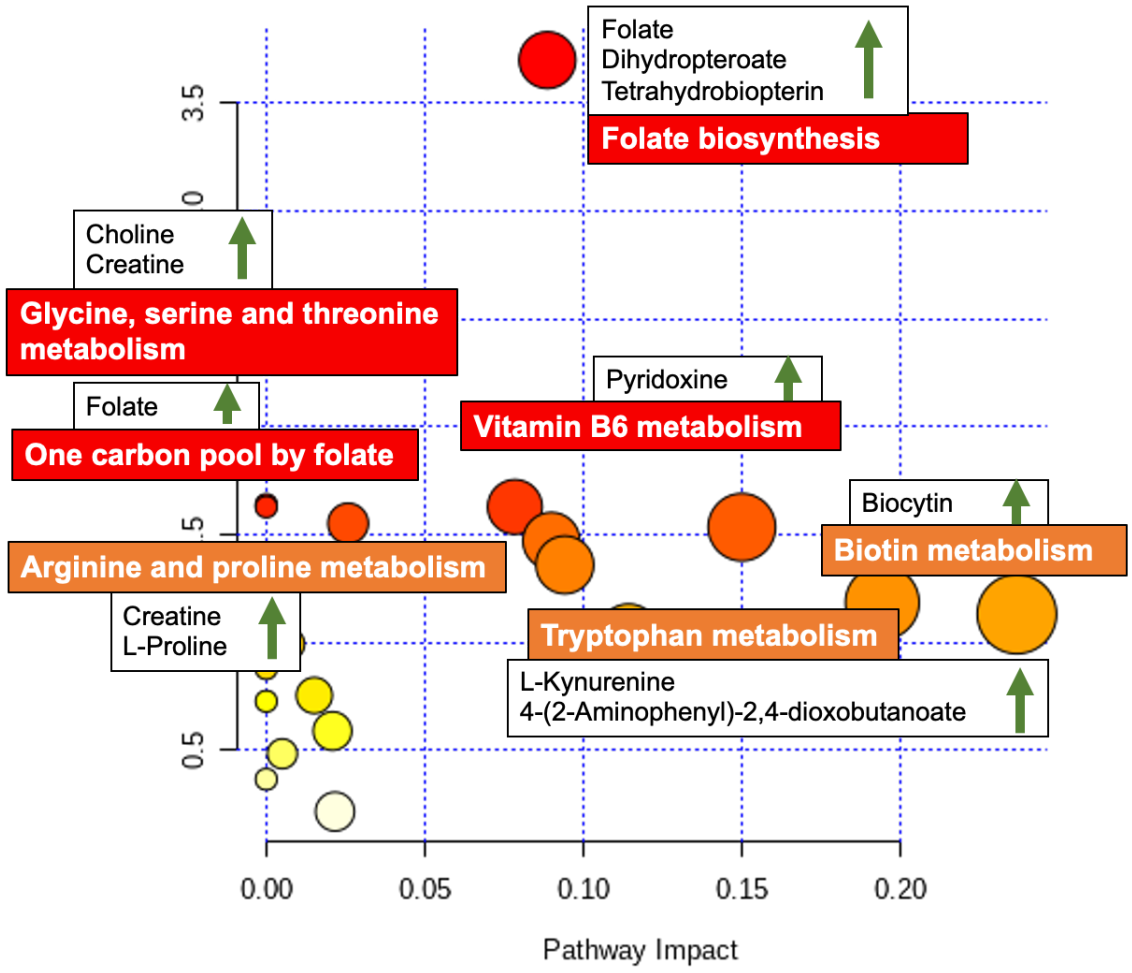

Figure 3.33 Pathways overrepresentation analysis.

Summary of metabolic pathways of significantly up-regulated metabolites in day 4 embryo culture CM compared to day 4 embryo culture KSOM with Metaboanalyst.

The biological pathway analysis of metabolites down-regulated in day 4 embryo culture CM *vs.* day 4 embryo culture KSOM revealed 6 metabolic pathways including neomycin, kanamycin and gentamicin biosynthesis, phenylalanine metabolism, starch and sucrose metabolism, galactose metabolism, and cysteine and methionine metabolism (Figure 3.34). Of these pathways, 4 had a p value < 0.2 and only two (starch and sucrose metabolism and galactose metabolism) had a pathway impact higher than 0. The most significantly affected metabolic pathways were neomycin, kanamycin and gentamicin biosynthesis and phenylalanine metabolism. However, it is not known whether those pathways have a relevant biological role on mouse pre-implantation embryo development. The significantly altered metabolites involved in those pathways are D-glucose and phenylacetylglycine. Reduced abundance of those metabolites in spent embryo culture CM indicates an increased

consumption of these compounds by blastocysts cultured in CM rather than in KSOM. However, it might also be possible that those species are produced in lower amount by blastocyst cultured in CM, thus the linked metabolic pathways are characterized by reduced activity.

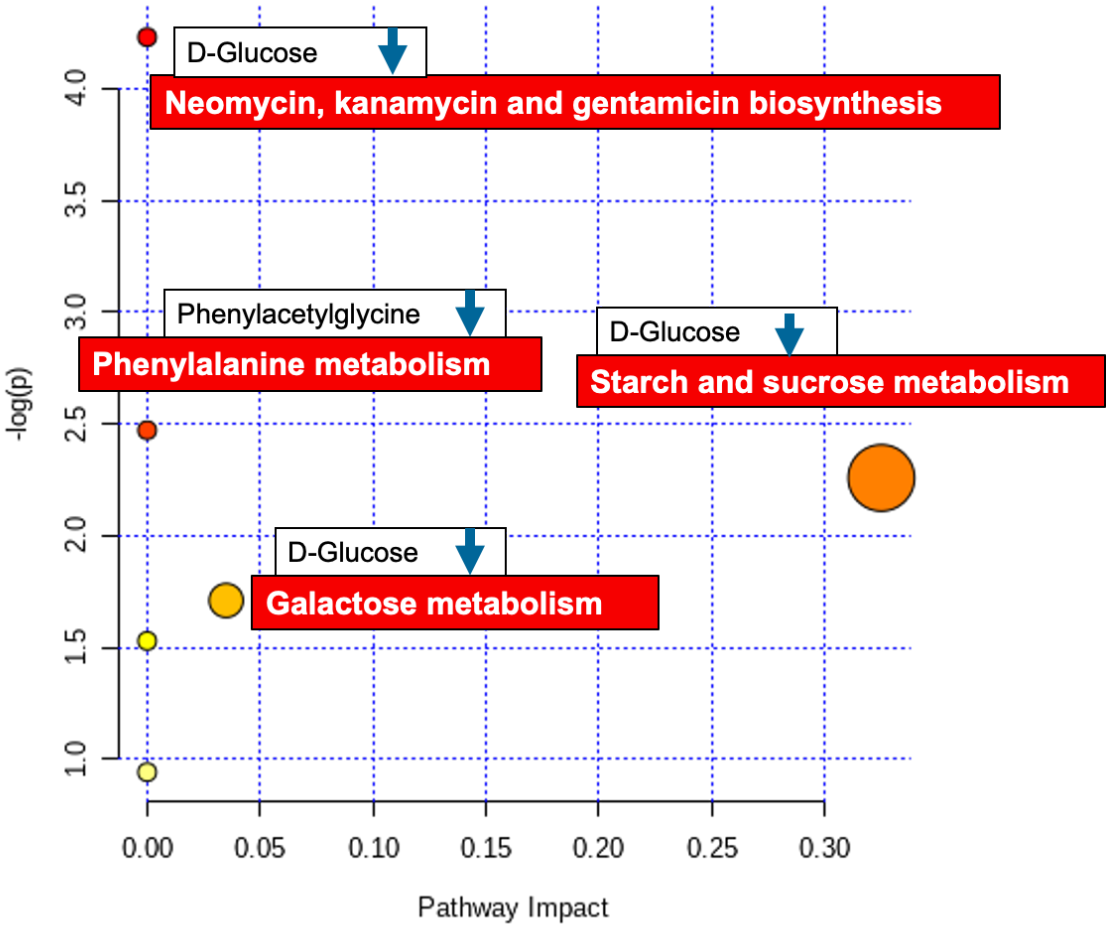

Figure 3.34 Pathways overrepresentation analysis.

Summary of metabolic pathways of significantly down-regulated metabolites in day 4 embryo culture CM compared to day 4 embryo culture KSOM with Metaboanalyst.

To further investigate key metabolic markers related to the use of CM, the list of metabolites identified from the day 4 embryo culture CM *vs.* day 4 embryo culture KSOM pairwise comparison was compared with the lists of compounds identified in the other two pairwise comparisons, day 4 CM *vs.* day 4 KSOM and day 0 CM *vs.* day 0 KSOM. **Among the 1063 significant compounds detected by comparing day 4 CM and day 4 KSOM, 699 illustrated an up-regulated trend in CM**, and 364 a down-regulated trend in in CM, compared to KSOM. Of the 699 increased species, **100 were only found in the CM group and thus can represent compounds specifically released by uterine epithelial-cells into**

the medium. In contrast, 9 features were unique to day 4 KSOM and are purely related to the not-conditioned medium. Of the 1221 significant compounds emerged from the comparison between the two media at day 0, 401 showed a down-regulated trend in CM, and 820 an up-regulated trend in CM, compared to day 0 KSOM. Interestingly, 99 features were unique to day 0 CM and 8 to day 0 KSOM (Figure 3.35).

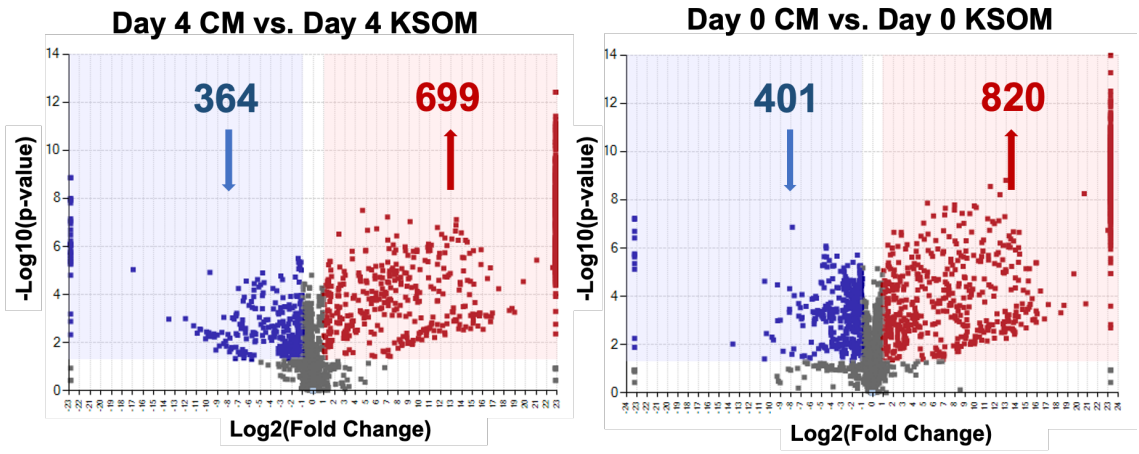

Figure 3.35 LC/MS results of media (KSOM and CM) samples collected from microdrops after 4 days without embryos.

Volcano plots showing the distribution of metabolic compounds for pairwise comparisons as stated above. (Left) Day 4 KSOM *vs.* Day 4 CM, (right) Day 0 CM *vs.* Day 0 KSOM.

Subsequently, the significant compounds were putatively identified using available libraries. Overall, 198, were identified in the pairwise comparison day 4 embryo culture CM *vs.* day 4 embryo culture KSOM, 351 in the pairwise comparison day 4 CM *vs.* day 4 KSOM and 402 in the pairwise comparison day 0 CM *vs.* day 0 KSOM. **Figure 3.36 shows in detail the features that were either up-regulated or down-regulated in the CM groups compared to the KSOM groups.**

The diagram shows 5 species which are unique to the comparison between day 4 embryo culture CM and KSOM. The origin of these species can be directly linked to metabolites produced or consumed by embryos as a result of culture in CM. In detail:

- 4-(2-Aminophenyl)-2,4-dioxobutanoic acid, norcisapride, 5-Chloro-1,3-dihydro-1-(4-piperidinyl)-2H-benzimidazol-2-one and dimethylurea were released in a higher amount in CM, compared to KSOM. The metabolites norcisapride and 5-chloro-1,3-dihydro-1-(4-piperidinyl)-2H-benzimidazol-2-

one were uniquely detected in spent embryo culture CM, whereas dimethylurea and 4-(2-aminophenyl)-2,4-dioxobutanoic acid had a 2-fold increase in CM compared to KSOM.

- Citreoviridin C was the only specie significantly decreased in CM compared to KSOM. This has been identified in both media but it was increased with a 2-fold change in spent KSOM compared to CM. Citreoviridin C is a mycotoxin and its decreased production in CM might be linked to a beneficial effect of CM on embryo development and on the release of toxic compounds from the developing embryos.

Of the 79 features unique to the comparison between media at day 0 were detected biological species including ribothymidine, 5-oxoproline, kyotorphin, cyclohexylamine, pyroglutamic acid and aspartylphenylalanine, all of which had increased abundance in CM. Similarly, other species such as L-lysine, L-pipecolate, L-tyrosine, thiamin monophosphate, 3-sulfino-L-alanine, 5,6-Dihydro-5-fluorouracil had increased abundance in KSOM compared to CM. This list of compounds needs to be further examined to fully understand differences in metabolite composition of the two types of media.

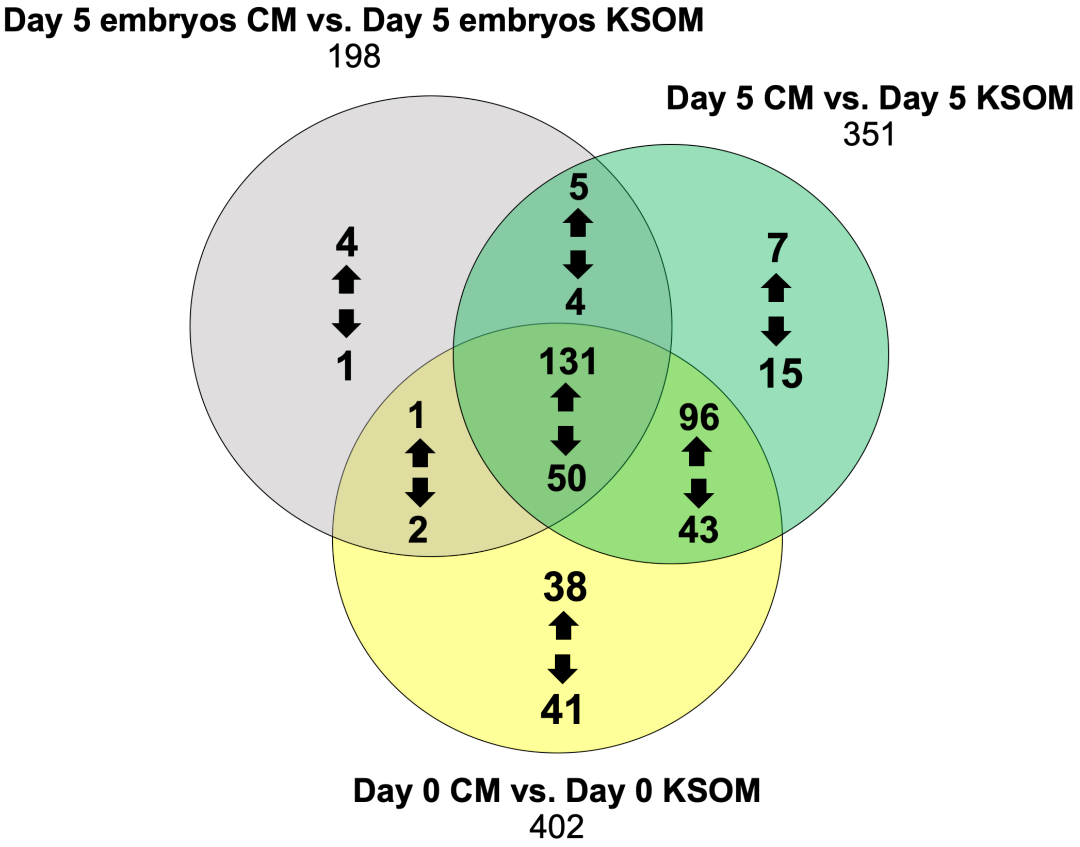

Figure 3.36 Venn diagram showing the distribution of the number of metabolites between the three pairwise comparisons.

3.3.4.3 Comparison between polystyrene and PDMS biomolecules release/absorption

The 2338 metabolites identified from the analysis of day 5 embryo culture media collected form microfluidic devices was finally compared with the list of 2904 compounds identified in day 4 embryo culture media collected from traditional microdrops. Specifically, LC-MS/MS analyses were performed to compare spent medium (KSOM) on days 4 or 5 of embryo culture between each experimental group (KSOM, KSOM + microdrop, KSOM + device). This allowed to identify potentially toxic compounds released by PDMS in culture media and to analyse metabolomics of *in vitro* cultured murine embryos. PCA analysis (Figure 3.37A) and heatmap visualization (Figure 3.37B,C) shows distinct clustering of the experimental groups. **These global views revealed that while the majority of the detected metabolites were stable in abundance, there was a modest subset of metabolites in culture medium with unique abundance profiles between device and microdrop technique**.

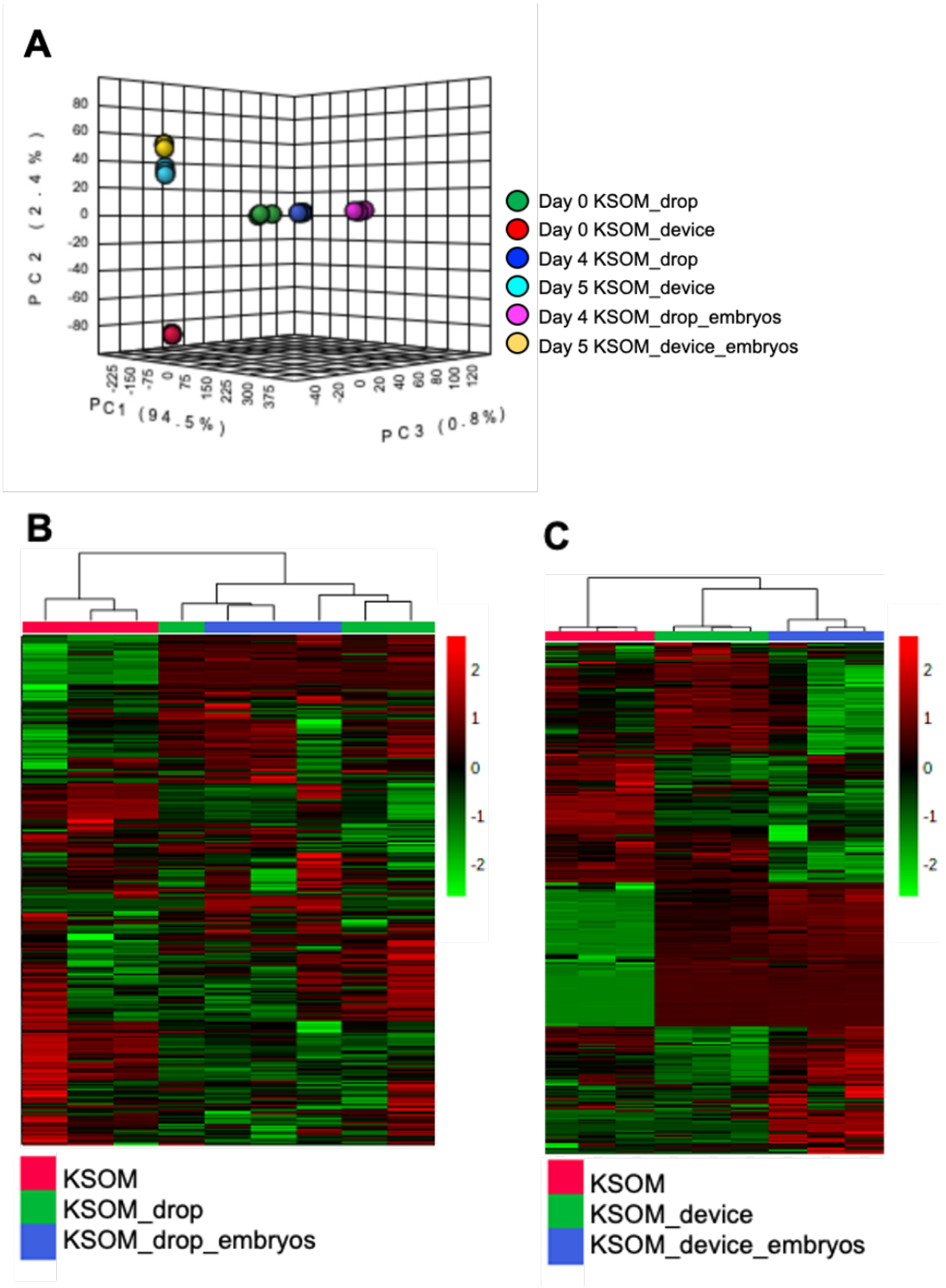

Figure 3.37 LC-MS/MS global metabolomic profile analysis of murine blastocysts cultured in device or microdrops.

A) PCA plot for the LC-MS/MS data of medium samples collected after 4 days in microdrops (N=3) or 5 days (N=3) in devices and control KSOM (N=3). B) Heatmap representing LC-MS/MS data of media samples collected from the microfluidic devices or from C) control microdrops. Compounds are presented as rows and sample replicates as columns. Scale: red indicates high expression and blue is low expression.

Second-order meta-analysis of the individual pairwise comparisons (Figure 3.38) allows prioritization of endogenous or xenobiotic compounds (specific to PDMS, PS or mineral oil exposure) that were altered in abundance by embryo culture method (device *vs.* microdrops). The Venn diagram shows shared and unique compounds for specific comparisons. A comparison of the compounds identified in spent media from devices ("PDMS-media") or spent media from control microdrops on standard Polystyrene dish ("PS-media") without the presence of embryos revealed a total of 547 compounds (Figure 3.38A). Using meta-analysis, 48 compounds were common to the two groups (device *vs.* microdrop), whereas 387 were unique to the PDMS-media group and 64 to the PS-media group. **Compounds unique to the device group, represent species (xenobiotics) directly associated with PDMS use**. These data show **339 xenobiotic compounds were released by PDMS into the culture medium and 48 compounds were absorbed by or adsorbed onto the PDMS from the culture medium**. Included in the 339 species released into the culture medium, plasticizers such as butyl lactate, dimethyl sulfoxide, ethanol, 2-[2-(2-butoxyethoxy)ethoxy]-, N,N-dimethylformamide, necatorine, pentaethylene glycol, triethylene glycol and tripropylene glycol were detected. The effects of these potentially toxic compounds on embryo development must be further investigated. The remaining detected compounds indicate breakdown products of media components produced by media degradation after 5 days of incubation at 37 °C. These include peptides, amino acids and other small endogenous molecules (*e.g.,* L-glutamine, L-tryptophan, N-phenylacetylglutamic acid, pyridoxamine, dihydrolipoamide).

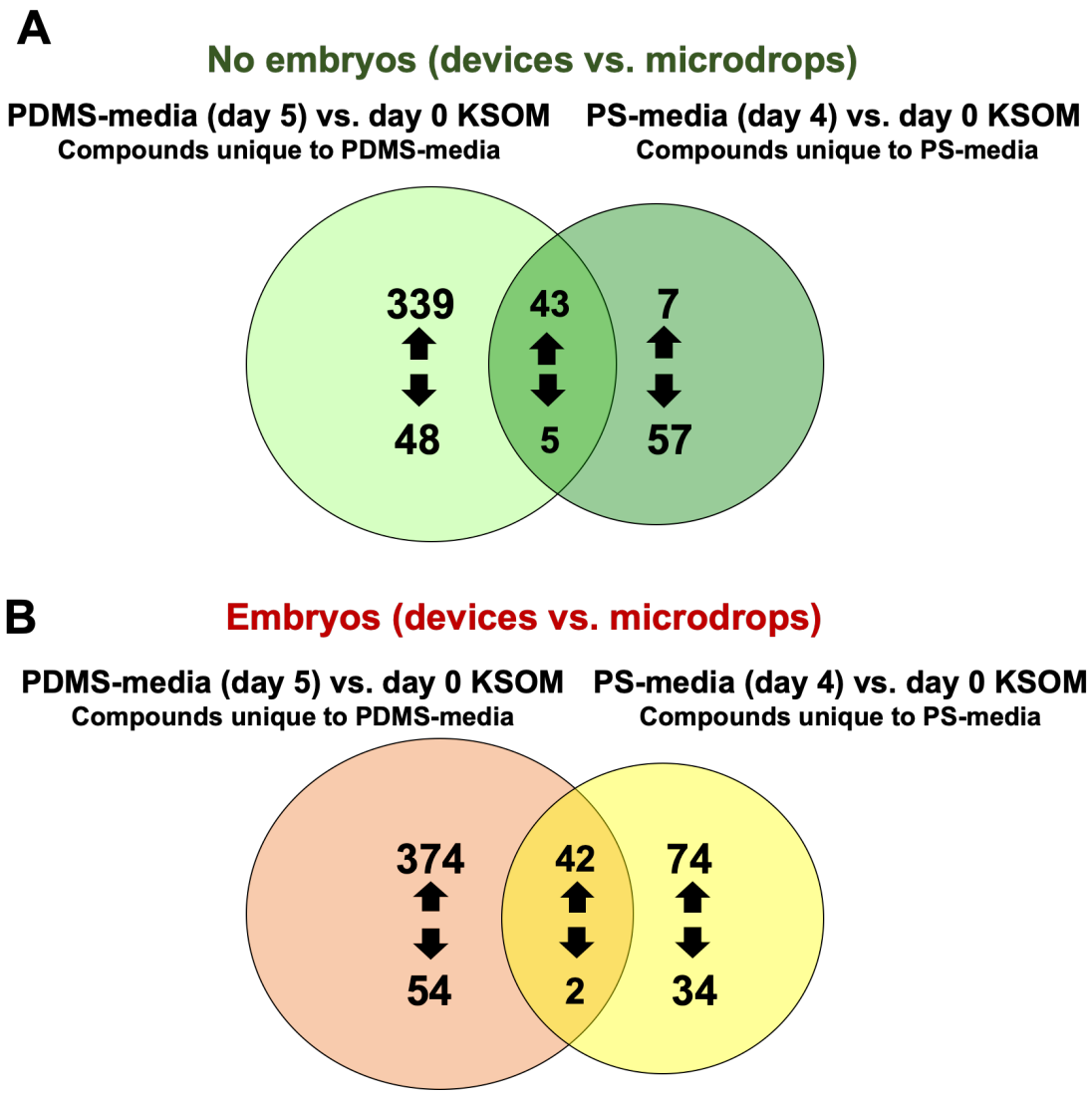

Figure 3.38 Venn diagram of dysregulated compounds in PDMS-media and PS-media compared to control (day 0 KSOM).

(A) Comparison of dysregulated compounds in day 5 PDMS-media and day 4 PS-media without embryos. **(B)** Comparison of dysregulated compounds in day 5 embryo culture PDMS-media and day 4 embryo culture PS-media.

Similarly, among the 48 species that were significantly decreased in spent media from the device, numerous biological compounds that were sequestered by PDMS from the culture medium were identified, including amino acids and dipeptides (*e.g.*, isoleucyl-isoleucine, isoleucyl-Leucine, isoleucyl-phenylalanine, N-acetyl-L-methionine, and valyl-leucine).

Among the species that were significantly decreased (57 compounds) in spent media from microdrop culture, peptides and amino acids, such as L-tyrosine, aspartylphenylalanine and phenylacetylglycine were identified. These data suggest that these molecules were absorbed or transformed by the plastic

or mineral oil. The remaining detected compounds represent breakdown products of culture media that degraded over time.

Other organic species appeared downregulated in PS-media and PDMS media suggesting a segregation of compounds from the medium both into the elastomer as well as in the plastic or the mineral oil used to prevent media evaporation. These molecules include tryptophol [xylosyl-(1->6)-glucoside], muramic acid, [3,5-dihydroxy-2-(hydroxymethyl)-6-[3,5,7-trihydroxy-2-(2,4,5-trihydroxyphenyl)-3,4-dihydro-2H-1-benzopyran-6-yl]oxan-4-yl]oxidanesulfonic, and 2-methoxyestrone 3-glucuronide.

Subsequently, second-order meta-analysis of spent media collected with embryos present in the device and in the microdrop method was performed. Specifically, embryo cultured spent media from devices (day 5) were compared to embryo present spent media from microdrops (control, day 4) (Figure 3.38B). **These analyses allow to determine metabolites and/or xenobiotics present in spent media after embryo culture (*i.e.,* produced or consumed by the embryo during culture) as well as xenobiotics unique to device culture (*i.e.,* associated with the fabrication process or released/absorbed by PDMS) or to control microdrop culture (*i.e.,* associated with PS or the mineral oil used to prevent medium evaporation)**. The Venn diagram shows 428 species to be only present in embryo cultured PDMS-media, 108 compounds were only observed in embryo culture PS-media and 44 species were present in both embryo culture PDMS-media and embryo culture PS-media. Notably, among these 44 common metabolites, the relative abundance of 42 of these compounds were statistically significantly increased ($p < 0.05$ and fold change ratios > 2) in both the embryo culture PDMS-media and the embryo culture PS-media when compared to control, these identified compounds include metabolic markers of pre-implantation embryo development, such as Pyroglutamic acid, 5'-methylthioadenosine (391), hypoxanthine (388,389), cytosine, N-acetyl-L-methionine, and phenylacetylglycine. Pre-implantation embryo development compounds represent metabolites produced by embryos in both culture conditions. Similarly, 2 compounds significantly decreased in spent embryo culture media compared to control (*i.e.,* muramic acid and meticillin) are known to be consumed by embryos from the culture medium.

These results allow to conclude that expected metabolomic changes can be detected by mass spectrometric analysis in samples of media collected during embryo culture, and these can be correlated with organic and inorganic compounds available to the embryo during its development.

3.4 Summary

In this chapter was presented the design and development of a microfluidic device, which resulted in a user-friendly and simple system for culturing murine embryos comparable to currently available traditional IVF platforms.

The microfluidic compartment of the device was designed to achieve efficient and reproducible loading and retrieval of the embryos. The culture procedure was also facilitated by the absence of oil and by the compatibility of the device with bench top incubators and optical microscopes. The possibility to load embryos using a reasonably straightforward and quick procedure, is of fundamental importance to reduce embryo manipulation and for the potential adoption of the device in conventional IVF laboratories. The system offers the possibility to non-invasively assess the impact of culture conditions on embryo development using several techniques. Embryo development was comparable to traditional group culture in microdrops, with both cleavage and blastocyst rates exceeding 90% in all the conditions. These data indicated that this microfluidic device supported embryo full-term development without the need for media changes or oil overlay.

Furthermore, the influence of the microfluidic culture conditions on embryo quality was assessed by the analysis of gene expression of individual fully developed blastocysts and by metabolomics analysis of spent culture media samples. Those two techniques provided complimentary results. Genomic data allowed to follow changes of embryo development at the gene and protein level, whereas metabolomics data allows us to identify at the molecular level metabolites released by the embryo or consumed by the embryo during development.

The LC-MS/MS culture medium analysis revealed the presence of specific compounds found uniquely in samples derived from the microfluidic system. Among them, numerous uncrossed-linked components of the PDMS were identified. Those species could explain leaching and sequestration of small molecules by the elastomer. The culture medium analysis also provided enhanced understanding of the embryo metabolic activity. Specifically, second-order meta-analysis allowed the identification of biologically important metabolite changes in the culture medium throughout embryo development. These data show that the presence of the embryo in culture altered the composition of the

medium in the device and in the microdrop method. The unexpected xenobiotic compounds observed in the medium did not induce significant alteration of the embryo development during culture. These data also show that the number of common compounds in the different culture settings (device *vs.* microdrops) were minimally changed.

Another improvement of culture conditions was obtained by using mouse uterine epithelial cells-conditioned media for the culture of murine embryos from 1-cell to blastocyst stage. Increased blastulation rates and significant changes in mRNA expression levels of DNA methylation and genomic imprinting regulators were observed in blastocysts cultured in cells-conditioned media when compared with control. Importantly, LC-MS/MS analysis of the culture medium allowed the identification of important biological markers revealing insights into embryo metabolic activity. Pathway overrepresentation analysis results showed that some key metabolic pathways were enriched for the metabolites consumed by the embryos during culture in microfluidic devices using conditioned media. Among them, metabolic pathways of several amino acids and DNA bases that have a critical role in embryo development were significantly affected. Those results indicate an effect of conditioned media in protein and DNA synthesis, fundamental process during embryo development, which may drive to higher cell number and improvement in pre-implantation embryo development. Therefore, the use of conditioned media has a significant impact on many aspects of embryo development, including metabolic activity and gene expression.

Further investigations are required to identify the link between the observed changes in gene expression and *in vitro* embryo development as well as to confirm further effects of the same genes on pregnancy outcomes after embryo transfer. In addition, future analyses of the medium composition will be used to search for specific toxins, such as peroxides derived from the mineral oil, zinc, and other unknown contaminants that may be released into the medium from the oil or the plastic. A more detailed analysis could be set up by collecting samples every 2 hours to correlate altered media composition with abnormal embryo developmental rates to morula or blastocyst stage.

Overall, those findings reveal the feasibility of performing both PCR and metabolomics analyses of blastocysts cultured in the microfluidic device and the potential of this novel platform for future *in vitro* studies and ART procedures. It

is now known that “omics” techniques can provide new means to monitor embryo development and assess embryo quality in a more comprehensive way than morphokinetics alone. Thus, the integration of such techniques with miniaturized and *in vivo*-like microfluidic culture systems will help the progress in ART techniques and IVF outcomes. Moreover, to further identify physiological requirements of pre-implantation embryos, future works will be addressed to integrate modular physical and/or biochemical sensors. Those sensing units will enable the detection of soluble biomarkers and the measurements of environmental parameters such as temperature, oxygen and pH.

This novel microfluidic technology presents innovative aspects compared to traditional embryo culture platforms and currently available microfluidic platforms. First, this system eliminates the need of potentially embryo-toxic mineral oil, thus reducing toxicity, failure, and costs of individual culture set-up. Second, the loading and retrieval are significantly simplified compared to the microdrop technique, allowing to load groups of embryos from the inlet reservoirs easily in a single step and avoiding the contact with the overlaid oil. This represents an additional value in high throughout facilities to maximize the costs and the success of the culture. Most importantly, this new method also favours the adoption of nonsurgical embryo transfer (NSET). Developed in 2009, NSET techniques are now adopted globally as they provide improved efficiency compared to SET techniques for the transfer of blastocyst stage embryos into pseudo-pregnant recipient rodents (127,392,393). By using this microfluidic device in combination with NSET, animal breeding laboratories will see reduction in costs related to bench and animal preparation for surgery (i.e. setting up, packaging, sterilisation and cleaning of surgical tools, health monitoring, anaesthetics, analgesics, etc.). In addition, the times required for embryo transfer will be reduced from one hour to 15 min, and the training for embryologists and practitioners will be reduced from four months to one month.

Lastly, this study represents the first untargeted metabolomic investigation of murine embryos cultured in a microfluidic devices which confirms the feasibility of the platforms for non-invasive embryo quality assessment.

Further investigation will explore the effects of microfluidic culture on post-implantation ability and embryo developmental competence after transfer. Embryo transfers in mice and assessment of birth rates will confirm the quality of

embryos cultured in the microfluidic device and will allow to quantify time and costs saving introduced by this protocol.

It will be interesting to see whether alternative plastics for manufacturing of the device could be used for this novel system, based on current limitation of PDMS in terms of stability and suitability with manufacturing processes.

Finally, this novel microfluidic device could be made adaptable for the culture of human embryos and compatible with clinical procedures. The design of the device could be easily changed to accommodate groups or individual human embryos. To this end, more data are required to move to preclinical trials, in order to prove the effective improvement of the embryo development and exclude any long term, epigenetic effect of the materials, as well as any interference with the current protocols and standards in IVF clinical settings.

Chapter 4
Microfluidic device to study BBB cells

4.1 Introduction

The blood brain barrier (BBB) is a critical structure that separates blood from brain interstitial fluids (221). The BBB regulates traffic of small molecules, hormones and nutrients between the brain and peripheral blood circulation and is crucial for maintaining the homeostasis of the brain microenvironment. This unique barrier also prevents entry of toxic substances (*e.g.*, drugs, toxins) into the central nervous system (CNS) and limits the exchange of inflammatory cells and mediators under physiological and pathological conditions (394). For these reasons, BBB models are fundamental to clarify the regulation of the BBB and to test specific drugs designed to act in the CNS diseases (273).

The BBB consists of brain microvascular endothelial cells interconnected by tight junctions. These are key features of the BBB and are responsible to reduce the paracellular diffusion of solutes between endothelial cells from the blood plasma to the brain extracellular fluid (241).

In addition to endothelial cells pericytes and astrocytes are responsible for the formation of tight junctions (395,396), and thus are critical for maintaining normal BBB physiology and function as a barrier (233,246,265,273,397–412). Moreover, true formation of a BBB requires the presence of shear stresses which are experienced from blood circulation and contribute to differentiation of vascular endothelial cells into a BBB phenotype (244,413).

BBB dysfunction is implicated in various neurodegenerative diseases, including Alzheimer's disease (AD), which is characterized by a progressive deterioration of cognitive functions due to degeneration of synapses and the death of neurons (218,219). This results in a significant reduction of the volume of the brain in AD patients as compared to healthy subjects. Additionally, one of the hallmarks of AD is the presence of amyloid plaques. The major component of amyloid plaques is the amyloid β (Aβ) peptide which has a central role in AD pathology (218). Aβ is a peptide of 36–43 amino acids that is processed from the Amyloid precursor protein (414). The peptide Aβ1-40 is the predominant form in blood and cerebrospinal fluid, and represents the major constituent of

cerebrovascular amyloid plaques. Whereas the peptide Aβ1-42 predominate in senile plaques (415–420). Neurotoxicity of Aβ1-42 peptide fragment have been widely investigated on neurons (421–423). However, toxicity of Aβ1-42 on BBB cells (*i.e.,* endothelial cells, astrocytes and pericytes) is poorly understood.

Therefore, there is a tremendous interest in developing *in vitro* models to closely mimic BBB alterations such as those observed in AD. Traditional *in vitro* models use culture of brain endothelial cells in Transwell inserts (272,424,425). Those models have several limitations (see Section 2.3.2) and do not replicate the physiological characteristics of the barrier *in vivo*. In this contest, microfluidic techniques have been applied to create more complex *in vitro* models which can be successfully used for permeability and toxicity studies of the CNS (264,267,426). Those models have the considerable advantage of lower required cell number and can provide flow of the culture medium to recreate physiological shear forces that induce proper barrier formation.

An ideal microfluidic or OoC model of the BBB would include all the blood and brain derived cells, and would allow mechanistic studies of the full functions of the BBB, such as tight junctions, transporters, enzymes, macromolecular and immune cell trafficking and signalling. The most recent OoC models (as discussed in Section 2.3.2.1) present co-culture of blood and brain derived cells, with suboptimal ratios between cell types (273). Those designs lead to overgrowth of astrocytes and pericytes and do not allow for extended culture of the whole microvascular unit. Additionally, the perfusion of the vascular compartment does not allow for polarization and effective establishment of a tight endothelium only with high flow rates. While these are sustainable by the perfusion hardware and by the microfluidic system, the recirculation of medium into the compartment leads to a dilution of the secreted molecules and affects the diffusion of molecules into the brain compartment.

A first step towards the design of such a complex system thus consists in the optimization of the endothelium, which is the essential component of the BBB and is *per se* informative and suitable for rapid screening of new drug candidates.

In the present study, a simple *in vitro* microfluidic model was designed and developed to reproduce the endothelial barrier, where culture and maintenance conditions were optimized in order to induce endothelial cell alignment and differentiation into a more specific BBB phenotype. In contrast to currently

available models, this system did not require the use of complex liquid handling systems which can favour its adoption in conventional cell culture laboratories without the need of extensive technical trainings. Different device designs have been tested including an individual culture chamber and a multiple channels configuration. The latter allowed to obtain shear stress levels able to induce cell alignment and elongation, without the need of high flow rates and thus without causing excessive dilution of nutrients and soluble factors in the culture media. In addition, an improved culture medium was used in combination with the optimal flow rate to promote tight junctions formation was identified.

Furthermore, effects of Aβ1-42 (0.1, 0.5, 1 μM) peptide on viability of individual human primary BBB cells (astrocytes, pericytes and endothelial cells) were investigated to study peptide neurotoxicity. This experiment was repeated for endothelial cells using flow and measuring production of pro-inflammatory and anti-inflammatory cytokines – *i.e.,* Interleukin 6 (IL-6), Interleukin 8 (IL-8), Tumor Necrosis Factor alpha (TNF-α) – since studies reported that Aβ1-42 can induce secretion of those cytokines in BBB cells *in vitro* (427,428).

Different types of endothelial cells have been used in this study. First, human umbilical vein endothelial cells have been used to test the optimal dynamic culture conditions, then brain microvascular endothelial cells were used to investigate the effect of Aβ1-42.

4.2 Material and Methods

4.2.1 Device fabrication

The microfluidic devices used in this work were fabricated by soft lithography (58) in polydimethylsiloxane (PDMS, Sylgard® 184, Dow Corning, MI, USA). In the following sections are reported details for each photolithographic step: (i) mask design and fabrication, (ii) master (or mold) fabrication, and (iii) PDMS layer fabrication.

4.2.1.1 Mask design and fabrication

Masks were designed using computer-aided design (CAD) software (AutoCAD) and saved as .dwg file. Different device designs have been created in order to test each geometry and select the more suitable for the desired culture applications. Microfluidic chambers and channels were designed according to acceptable aspect ratios, to avoid channels collapsing after fabrication. Specifically, channels dimensions were adapted to obtain aspect ratios above 1:10 and below 4:1(69). Masks were printed on 9” × 12” emulsion film photomask by JD Photo Data (Photodata House, Hitchin, United Kingdom).

Each device design consisted of a cell culture chamber, one inlet and one outlet ports with diameter 1/16” and two microchannels which link the central chamber with the ports. The mask design included an array of round pillars (100 μm in diameter) to provide structural support for the PDMS chamber. Two different geometries has been tested (Figure 4.1):

1. Rectangular chamber with dimensions 4.75 mm and 6.2 mm (length × height), as seen in (273). Chamber dimensions were chosen in accordance to the surface area of a well in a 96 well plate (0.32 cm^2), to reproduce cell seeding density similar to those of traditional cell culture systems.
2. Rhombus-shaped chamber with 60° angled inlet and outlet microchannels, to allow better flow distribution within the chamber. This design was also created to increase the culture surface area and reduce the edge effect at the corners of the microfluidic chamber.

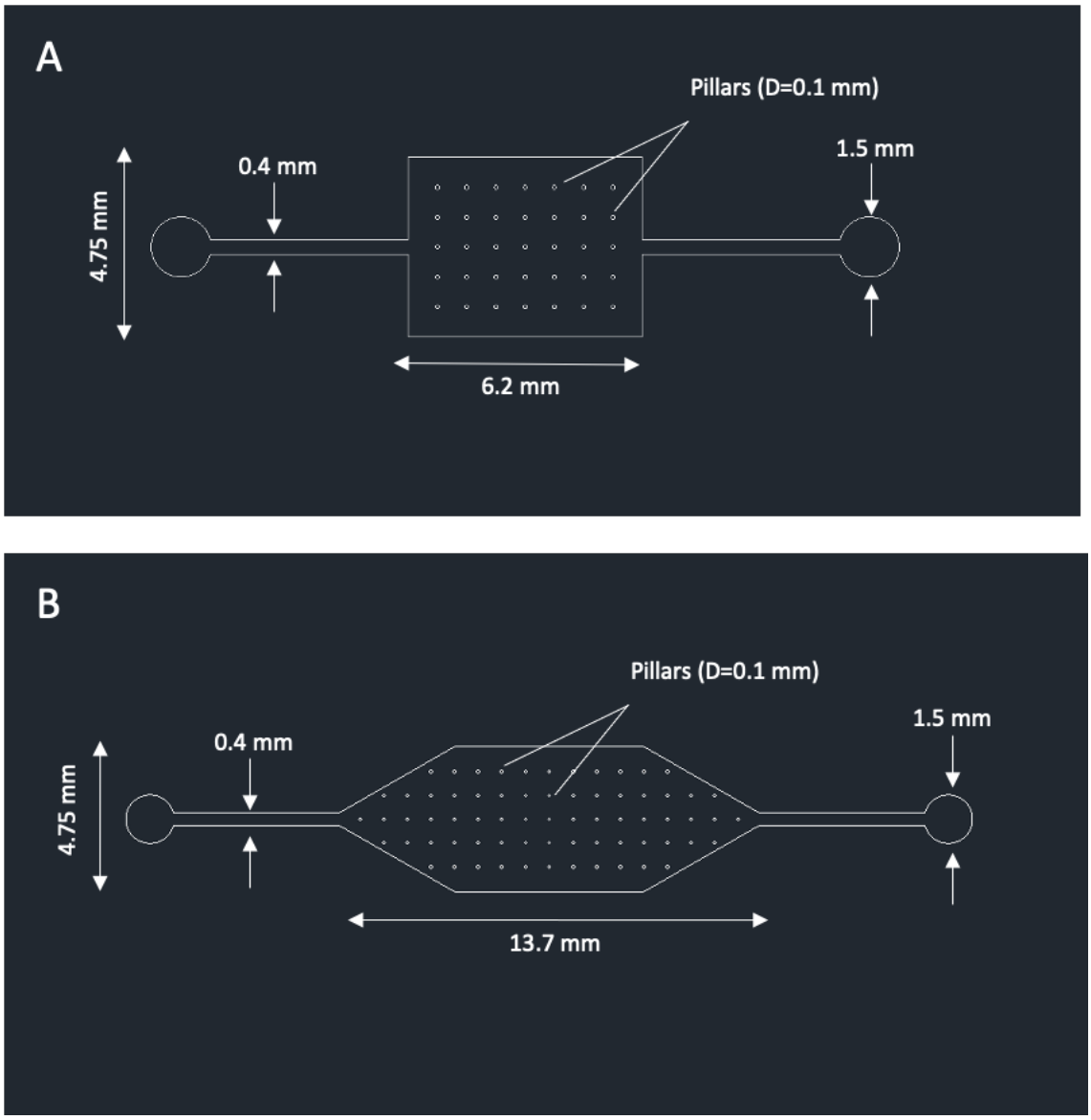

Figure 4.1 Emulsion film mask designs for the microfluidic device. (A) Rectangular chamber design. (B) Rhombus-shaped chamber design.

Values of areas and volumes of microfluidic chambers that can be obtained with the different designs are presented in Table 4.1, considering a final layer thickness of 150 μm. This was selected to optimize the master aspect ratios and prevent lateral collapse of relief structure of the PDMS replica layer (55). The angled geometry should allow a more uniform distribution of cells during seeding and medium into the chamber. The increased cell culture surface might also result beneficial for cell growth and proliferation.

Table 4.1 Values of areas and volumes of microfluidic for different designs, considering a layer thickness (height of the chamber) of 150 µm.

	Area (mm^2)	Volume (µL)
Rectangular chamber	29.45	4.42
Rhombus-shaped chamber	48.85	7.33

4.2.1.2 Mold fabrication

Molds were fabricated following the protocol described in (429) in Class 100 cleanroom (Nanotechnology Cleanroom, University of Leeds, School of Electronic and Electrical Engineering) with SU-8 2100 negative photoresist (MicroChem, USA) on 3" silicon wafers (Si-Mat, Kaufering, Germany). Wafers were cleaned firstly with acetone and then with isopropanol using a ultrasonic bath for 5 min at a power of 10 % and then dried with blow air. A thin layer of SU-8 negative photoresist was dispensed from a viscous solution of the polymer onto the wafer lying on a wafer platen in a resist spinner. A vacuum chuck held the wafer in place. The wafer was then spun at high speed to make a uniform film using a two steps program. The first step consists on the SU-8 spreading onto the wafer surface while the second step is the effective spinning.

Resist spin coating parameters (speed rate and time) were determined based on the viscosity of SU-8 2100 and optimized in order to obtain a final SU-8 relief height of 150 µm (Table 4.2). The final thickness was measured at the end of the soft lithography process by means of a surface profiler. The parameters which allowed to obtain the desired thickness were selected and SU-8 negative photoresist was then spin coated on the wafer for 10 s at 500 rpm and then for 30 s at 200 rpm.

Table 4.2 Spinning parameters tested to obtain the desired resist thickness of 150 µm.*

		Speed rate	Time	Final thickness
1)	Step 0: Spreading	500 rpm	30 s	180 ± 5 µm
	Step 1: Spinning	1800 rpm	60 s	
2)	Step 0: Spreading	500 rpm	30 s	120 ± 5 µm
	Step 1: Spinning	2000 rpm	60 s	
3)	Step 0: Spreading	500 rpm	10 s	150 ± 5 µm
	Step 1: Spinning	2000 rpm	30 s	

*** Values expressed as mean ± SD.**

The spinning process is of primary importance to the effectiveness of pattern transfer because the quality of the resist coating determines the density of defects transferred to the PDMS stamp. For that reason, the quantity of resist that was placed onto the wafer was optimized to reduce the formation of defects.

After resist spin coating, samples were “soft-baked” at 65 ˚C for 5 min and then at 95 ˚C for 20 min, to allow complete evaporation of the solvent and to make the SU-8 photoresist more solid, promoting the adhesion of the resist layer to the wafer. The evaporation slightly change the thickness of the layer and prepare the SU-8 photoresist to the ultraviolet (UV) exposure. Subsequently, the film photomask containing the desired pattern was placed in direct contact with the resist-coated surface and the wafer was exposed to UV radiation using a mask aligner. The exposure to the UV light enables the activation of the photoactive component in the SU-8.

Exposure time (*s*) expressed in seconds is obtained dividing the incident energy across the surface of the resist film (J/cm^2) by the incident light intensity (W/cm^2).

According to SU-8 2100 datasheets, an incident energy of 250 mJ/ cm^2 is needed to ensure exposure necessary to obtain a resist thickness of 150 μm. The exposure time was then calculated measuring the incident light intensity generated by the instrument.

Post-exposure baking, which is necessary to halt the reactions which have initiated after exposure but not have run to completion, was then performed at 65 ˚C for 5 min and then at 95 ˚C for 12 min. After cooling down for 30 min, the unexposed resist was developed using SU-8 developer solution (EC-Solvent). The exposed wafer was placed in a beaker with the developer solution and gently shaken for 10 min, then the exhausted developer solution was replaced with fresh solvent and gently shaken for another 10 min. The wafer was lift out from the beaker with tweezers, rinsed with isopropanol and dried with blow air. The development left on the wafer surface the pattern of photoresist which contains the negative relief image of the final PDMS microfluidic chamber (Figure 4.2). The last step of the process, the “Hard-bake”, is optional and aims at improving the hardness of the film heating the SU-8 at high temperature (more than 120 °C) for approx. 5 min. This step allows to suppress the strengths that remain inside the SU-8 photoresist at the end of the process which can create cracks on the

surface. Finally, the thickness of the SU-8 layer was measured with surface profiler Alpha step.

Molds used for the preparation of devices whose design included parallel microchannels (see Section 4.3.3.1) were prepared by using a maskless aligner lithography system MLA150 (Heidelberg Instruments, Heidelberg, Germany). This system enables to expose the pattern directly on the wafer by means of a guided laser beam (wavelength 375 nm), without fabricating a mask. This results in a significantly easier and faster photolithography step an overall shorter prototyping cycle (430). This technique also guarantees high resolution and minimum feature size of 1 μm. For this device, we selected a resist thickness of 100 μm to optimize features aspect ratios and guarantee appropriate channels volume and flow properties. To obtain this thickness, SU-8 50 negative photoresist was spin coated on a cleaned 3" silicon wafer at 600 rpm for 10s and then at 1500 rpm for 40s. Samples were then "soft-baked" for 7 min at 65 °C and then for 20 min at 95 °C. Mask exposure was then performed with the MLA150 system using an energy dose of 2000 mJ/cm^2 and a defocus (parameter which defines where the focus is done) of 8. Post-exposure baking treatment was done at 65 °C for 5 min and then at 95 °C for 12 min. Resist development was obtained in EC-solvent for 4 min followed by 1 min rinse in fresh solvent. Finally, wafers were washed in Isopropyl alcohol (IPA) for 2 min and resist was ramp "hard-bake" between 95-150 °C for 5 min on a hot plate to increase the mechanical strength of the photoresist.

To facilitate detachment of PDMS layers from the master, molds were treated with a fluorinated silane [(tridecafluoro-1,1,2,2-tetrahydrooctyl)-1-trichlorosilane] (Sigma, UK) for 10 min under a fume hood.

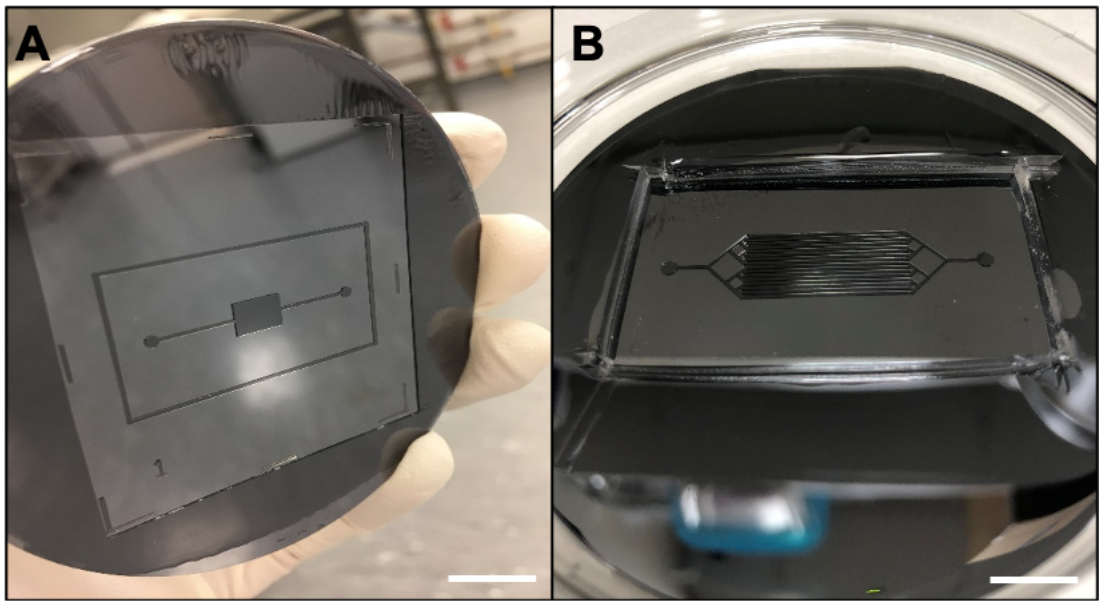

Figure 4.2 Final SU-8 molds on a silicon wafer having the relief chamber structure on its surface. Scalebar: 1 cm.

4.2.1.3 PDMS layer fabrication and device assembly

The PDMS layer fabrication process was carried out in the Bioelectronics Laboratory (School of Electronic and Electrical Engineering, University of Leeds) and is schematized in Figure 4.3A. In detail, PDMS prepolymer was mixed with a curing agent at a weight ratio of 10:1 (prepolymer: curing agent), poured onto the SU-8 master and placed in a vacuum chamber to remove trapped air. After degassing, samples were cured at 70 ˚C overnight. The PDMS layer was peeled off from the SU-8 master (Figure 4.3B) and ports to access the microfluidic chamber were opened by punching 1/16'' holes with a stainless-steel round punch (Integra Myltex, NJ, USA). For the device assembly, the PDMS layer and a glass slide were oxygen-plasma treated (600 mTorr, 100 W, 45 s) and bonded together (Figure 4.3C). Oxygen-plasma treatment renders the exposed surfaces hydrophilic (65). Hence, once assembled, the devices were immediately filled with deionized sterile water and stored at 4 ˚C until use, to maintain PDMS hydrophilicity (431). For static experiments, 500 µl Pyrex cloning cylinders (Fisher Scientific, Pittsburgh, PA, USA) were bonded with liquid PDMS to the inlet/outlet regions of each channel to form small reservoirs for cell media (Figure 4.3D). To avoid evaporation of liquids at the ports of the microfluidic device and through the PDMS layer, inlet and outlet reservoirs were filled with deionized water before cell seeding. Prior to use, devices were sterilized by UV (wavelength 254 nm) exposure for 20 min.

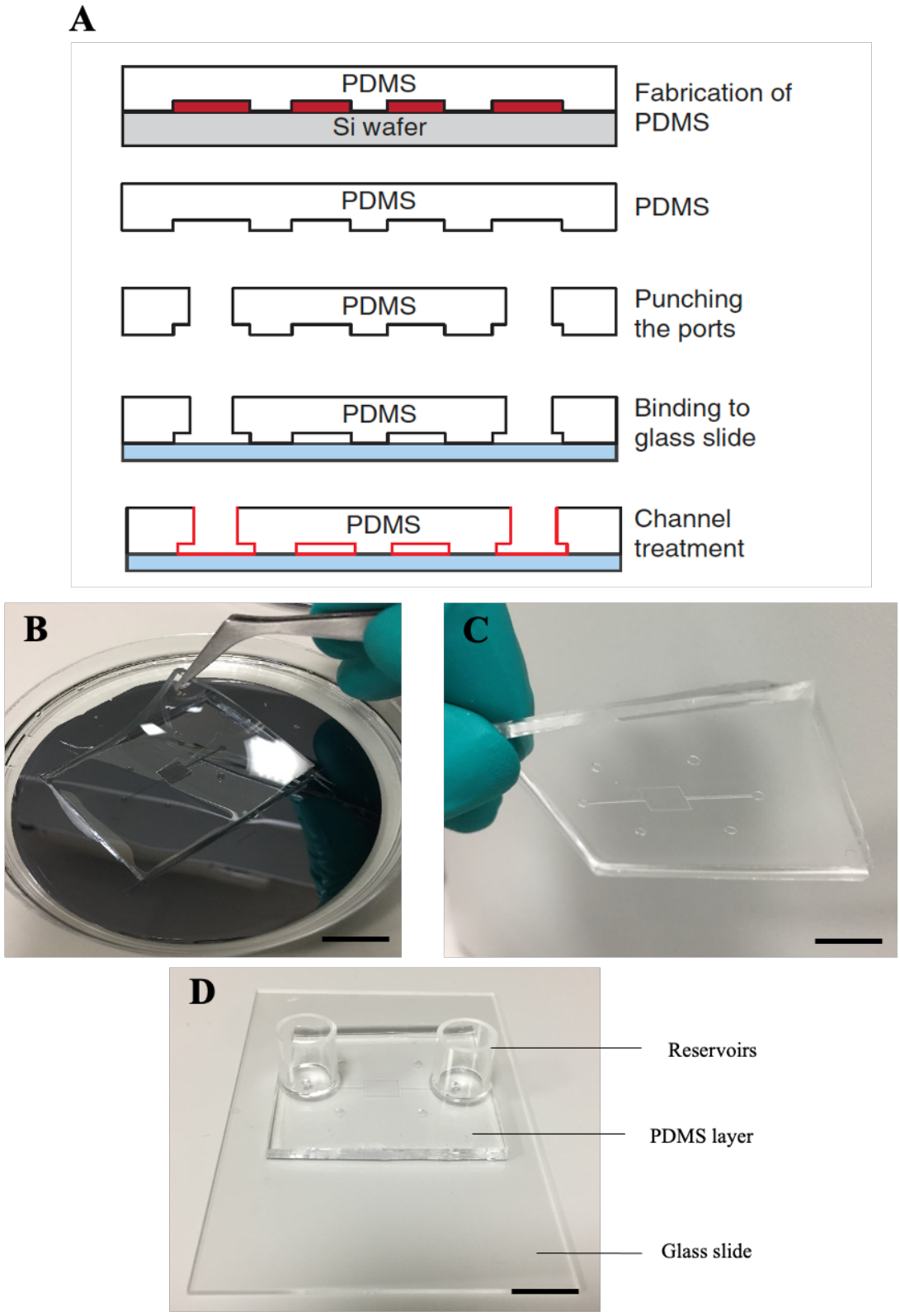

Figure 4.3 Soft lithographic process and PDMS layer fabrication.

A) Schematic of the process: fabrication of a PDMS layer and device assembly. (432) (B) After curing, the PDMS layer was peeled off from the SU-8 master and, C) an elastomeric stamp containing the inverse replica of the master was obtained. D) After opening inlet and outlet ports, the PDMS layer was plasma treated and bonded with a glass slide. Medium reservoirs were then bonded with the PDMS layer. Scalebar: 1 cm.

4.2.2 Flow simulation and prediction of the wall shear stress

In order to predict the resultant wall shear stress levels that cells experience in the chamber, fine-mesh 3D COMSOL (COMSOL Multiphysics® v.5.2a) simulations were performed to obtain velocity profiles at different heights from the bottom wall. Microfluidic channels geometry was imported from a .dwg file produced by AutoCAD software and extruded to obtain the desired height of 3D channels (100 and 150 μm). Shear rate dU/dz at the wall was calculated by COMSOL and used to obtain shear stress values, by multiplying it with the proportionality constant μ, or viscosity, as in the following equation (Figure 4.4):

$$\tau = \frac{dU}{dz}\,\mu \qquad (4.1)$$

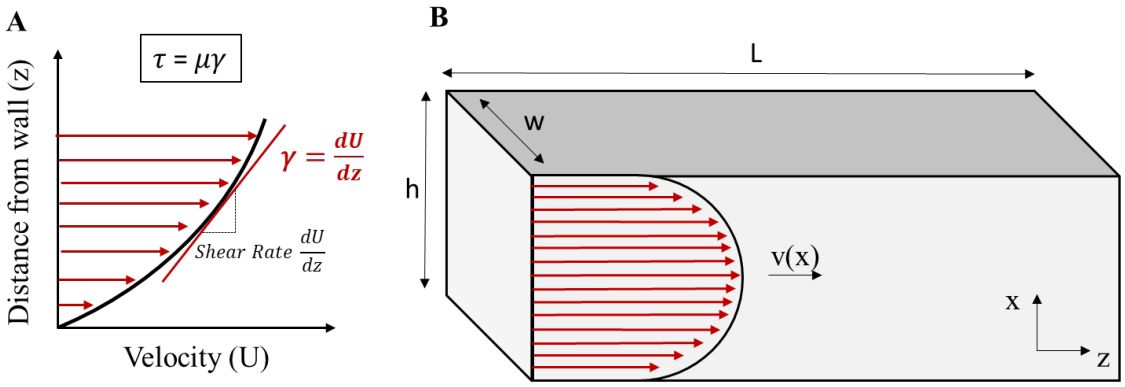

Figure 4.4 Shear stress calculation method.

A) Wall shear stress (τ) was calculated by COMSOL based on the vertical velocity gradient dU/dz multiplied by the dynamic viscosity μ. **B)** Definition of coordinates and scale parameters of a rectangular microchannel with a height h, a width w and a length L. The arrows represent the velocity of the fluid along the chamber.

COMSOL simulations were performed using the steady state Navier-Stokes model, and fluid characteristics were chosen to be the same as water (density, ρ = 1000 kg m^{-3} and viscosity , μ = 1x10^{-3} Pa s). The assumptions used in the model were: (i) Newtonian, incompressible and homogeneous fluid, (ii) no-slip condition at the wall and zero pressure at the outlet, (iii) flows completely laminar at all relevant flow-rates, with a Reynolds number several orders of magnitude lower than the turbulent threshold (2300), (iv) negligible effects of channel wall deformation induced by the flow (433) at all relevant flow-rates, and (v) rigid

channel walls in each experimental condition for the purpose of wall shear stress calculations.

As a comparison, for microfluidic perfusion culture in 2D Poiseuille flow systems, the average wall shear stress can be also approximately calculated by the formula: (434)

$$\tau = \frac{6\mu Q}{h^2 w} \quad (4.2)$$

where μ = viscosity (0.001 Pa s), Q = flow rate ($m^3\ s^{-1}$), h = chamber height (m), and w = chamber width (m). This equation is valid for a channels with w greater than h and for fully developed flows (435). For this reason, these assumptions are more appropriate for channels with a rectangular section, a relatively flat geometry and length sufficient to ensure formation of a fully developed flow.

Other assumptions to consider are that Navier-Stokes equations are valid for channels with length ≥ 0.1 µm (436), which make them appropriate to describe the flow within our models. However, those equations do not consider effects of surface roughness and fluid temperature changes which may affect Reynolds number and the friction factor. Those considerations identify limits of the model and appropriateness of the assumptions which are specific to conditions considered in this work.

4.2.3 Cell culture

Human umbilical vein endothelial cells (HUVECs), widely used in cell culture studies of endothelial cells (437,438), were used in this work as a cellular model to optimize perfusion culture conditions. In order to reproduce *in vitro* the physiological characteristics of the blood brain barrier (BBB), primary human brain astrocytes, pericytes and microvascular endothelial cells were used. HUVECs were both commercially obtained from Lonza (USA) or isolated from umbilical vein vascular wall by enzymatic treatment as described in the following paragraph.

4.2.3.1 Acquisition of human umbilical cords and cell isolation

Umbilical cords were obtained from non-laboring patients who underwent elective cesarean sections between 37 and 39 weeks of gestation. Tissue were collected by Dr. Nicolas Orsi, following an ethical process approved by the

University of Leeds and the NHS and used in this period for training purposes. The patient was tested for blood borne viral infections during pregnancy and checked to make sure they did not have the evidence of congenital malformation, genital aberration or severe diseases. The protocol was carried out under sterile conditions and is summarized in Figure 4.5. Collected umbilical cords were conserved and transported in a sterile container filled with 50 mL of buffer solution (50 mL PBS with 1% of 5000 U/mL penicillin-streptomycin and kept at 4 °C. Hematic or damaged cords and cords from infected parturient women were not considered. Umbilical cords were delivered to the laboratory and placed in a biological safety cabinet in a sterile stainless-steel dish. HUVECs were then isolated from collected umbilical cord using an existing protocol (439). Both ends of the cord were cut using forceps. The umbilical vein, that is easy distinguishable from the two umbilical arteries, was washed with PBS solution using a 10 mL syringe to remove red blood cells. Next, 10 mL of a collagenase solution (0.2 % weight/volume in PBS) was injected at one extremity of the vein using a 10 mL syringe until the whole cord was filled, clumping the other extremity. The cord was incubated in a water bath for ten min and then squeezed to facilitate cell detachment. Cells were collected washing the vein with 40 mL of PBS solution and suspended in 10 mL of complete medium (Dulbecco's Modified Eagle Medium (DMEM) with 20 % fetal calf serum (FCS) and 1% antibiotic) in a 50 mL conical tube. Cell suspension was centrifuged at 750 *g* for 10 min, supernatant was discharged and the pellet of cells was resuspended in 14 mL of complete medium. After cell counting the correct amount of cell suspension (2×10^6 cells) was plated in cell culture flasks and maintained at 37 ° C in a 95 % air / 5 % CO_2 atmosphere saturated with H_2O. Growth medium was changed less than 24 h after seeding and every 48 h thereafter. Typically, cell confluence is achieved in 6-8 days and special treatment, such as addition of drugs, should start after 48 h.

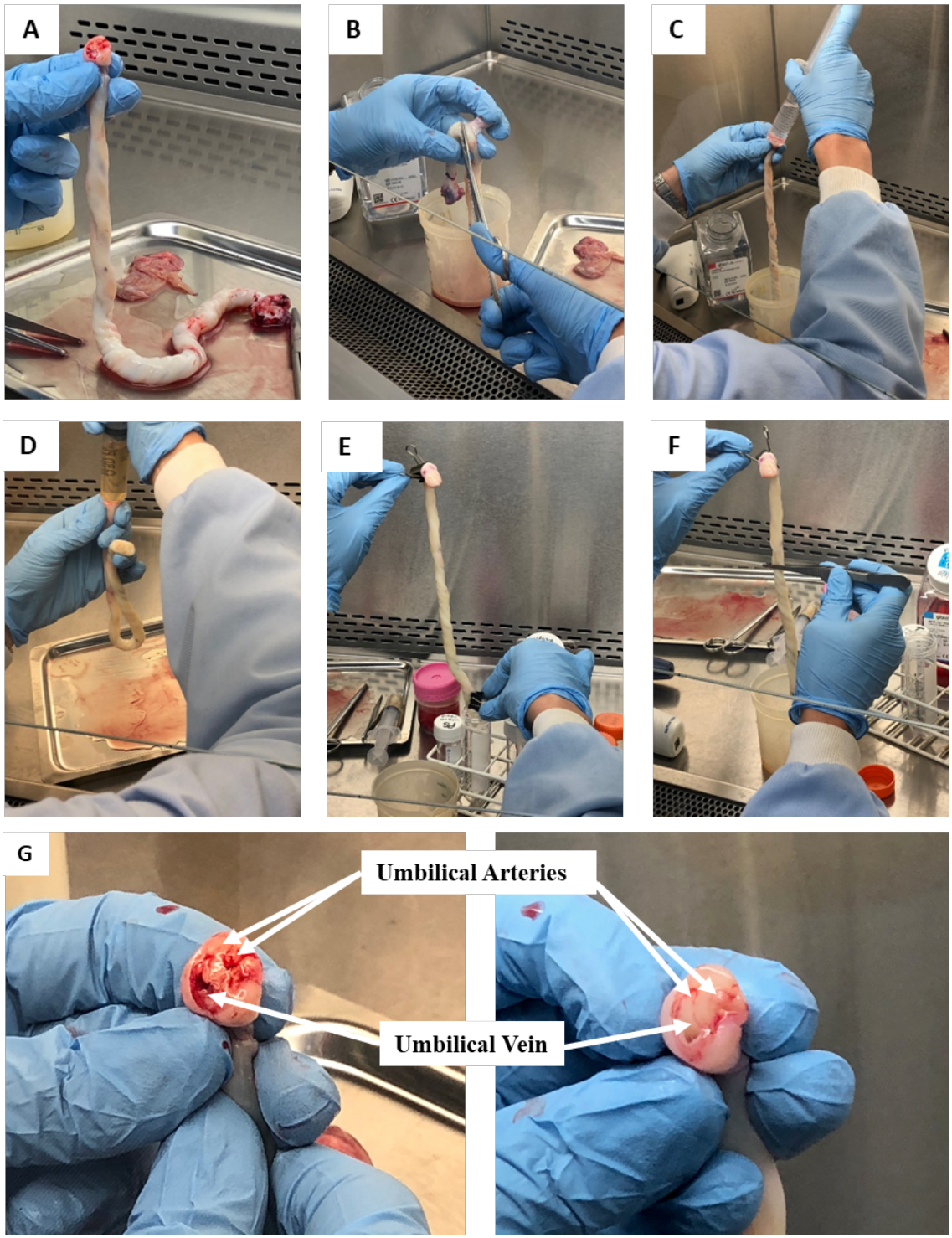

Figure 4.5 Isolation of HUVECs from umbilical cord.

A) The umbilical cord is placed in a biological safety cabinet in a sterile stainless-steel dish; B) Both ends of the cord are cut with a scalpel; C) The umbilical vein is washed with 1XPBS; D) 0.2% collagenase solution is injected at one extremity; E) both end of the cord were tightly clamped with surgical clamps; F) gently squeeze the cord with a pair of forceps to facilitate cell detachment. Keep the extremities of the cord closed with the clips during this step. G) The umbilical vein is easy distinguishable from the two umbilical arteries. The picture shows the cord extremity before (left) and after (right) cell isolation.

4.2.3.2 HUVECs culture protocol

Commercially obtained HUVECs were initially plated from cryopreservation with a seeding density of 2,500 cells/cm^2. Cells were then cultured in Endothelial Basal Medium-2 (EBM-2) supplemented with EGM™-2 Single Quots™ Kit growth factors (Lonza, USA) and maintained in a saturated humidity atmosphere containing 95 % air / 5 % CO2. Before cell loading into the microfluidic device, HUVECs were sub-cultured before reaching 60-70 % confluence up to passage 7.

4.2.3.3 Human brain primary cells (astrocytes, pericytes and endothelial cells) culture protocol

Human primary cells were purchased from available commercial firms, which are committed to the highest ethical and legal standards and approvals. Human brain microvascular endothelial cells (HBMECs, Catalog 1000), astrocytes (HAs, Catalogs1800-5) and pericytes (HBVPs, Catalog 1200) were purchased from ScienCell (UK). In all cases, cells were cultured in T75 flasks until 85-90% confluence to avoid possible cell differentiation or inhibition processes HBMECs were cultured in Endothelial Cell Growth Medium (ScienCell, USA) following the protocol described in a previous study (440). Both HAs and HBVPs were cultured with DMEM/Ham's Nutrient mixture F12 (Sigma Aldrich, UK), supplemented with 10% sterile filtered foetal bovine serum (FBS) of South American Origin (Labtech.com), 1% antibiotics (Penicillin – Streptomycin, P/S) and 1% L-Glutamine (Sigma Aldrich, UK). Astrocyte medium from a primary human astrocyte (HA) culture (conditioned medium) was combined with endothelial cell medium as previously described by other groups (258) in a 1/3 proportion. The medium was filtered using Millipore Express polyethersulfone (PES) Membrane (pore size 0.22 μm, diameter 33 mm, sterile, γ-irradiated) and Terumo syringes and stored at -80ºC until use. HBMECs and Human Brain Vascular Pericytes (HBVPs) conditioned media were also collected and stored in the same way for further experiments. Passage of cells was carried out by standard trypsinisation (Sigma Aldrich, UK). After centrifugation, the pellet was re-suspended and cells counted using a haemocytometer. All flasks, plates and coverslips were coated beforehand with collagen type I from rat tail (Sigma Aldrich, UK) for the culture of

HBMECs, and with poly-d-lysine hydrobromide (Sigma Aldrich, UK) for the culture of HAs and HBVPs. Cells were only used cells up to passage 7.

4.2.3.4 Cell seeding method

Prior to cell seeding, the chamber was coated with a thin layer of 1:50 dilution of Matrigel (BD Bioscience, USA) or 300 µg/mL collagen type I from rat tail (Sigma Aldrich, UK) for 3 hours, and washed three times with PBS and once in cell culture medium, to enhance cell adhesion, growth and proliferation (107,441). Upon achieving approximately 80% confluent monolayers, cells in conventional flasks were trypsinized, pelleted by centrifugation at 220 rcf for 10 min, counted using a hemocytometer (Neubauer - Improved cell counting chamber) and then suspended in complete growth medium at the desired concentration. Cells were subsequently loaded into the chamber using a 1 mL syringe (BD Biosciences) (approximately µL of cell suspension in each device) and allowed to adhere in a 37 °C, 5% CO2, 90% humidity incubator for at least 30 min. Once cells have established firm attachment, 300 µL of complete growth medium, was added to the inlet reservoir. Spent media from the reservoirs was collected and replaced with fresh media every day throughout all static experiments. The cells generally began to spread after one day and reached confluence after 3–4 days.

After medium addition to the inlet reservoir, the culture chamber is filled by means of capillary forces which creates a negative pressure in front of the liquid that draw the liquid into the channel. The flow rate of the liquid filling the microchannel can be expressed with this equation:

$$Q = \frac{1}{\eta}\frac{\Delta P}{R_f} \tag{4.3}$$

where η is the viscosity of the liquid, ΔP is the difference in pressure inside and in front of the liquid, and R_f is the resistance to flow of the microchannel (442)(431). The resulting capillary pressure Pc of a liquid–air meniscus can also be calculated with the following equation:

$$P_c = -\gamma\left(\frac{\cos\theta_b+\cos\theta_t}{d} + \frac{\cos\theta_l+\cos\theta_r}{w}\right) \tag{4.4}$$

where γ is the surface tension of the liquid, $\theta_{b,\,t,\,l,\,r}$ are the contact angles of the liquid on the bottom, top, left, and right walls, respectively, and *d* and *w* are the depth and width of the microchannel, respectively. Thus, from equation 2 is

possible to predict the flow rate within the chamber (443) and the time that the liquid takes to travel a length *l* in the chamber can be calculated by (59):

$$t = \frac{\eta}{2\Delta P C_g} l^2 \quad (4.5)$$

where,

$$C_g = \frac{1}{8}\left(\frac{dw}{d+w}\right)^2 \quad (4.6)$$

is a geometric term which approximate the influence of channel dimensions on the capillary friction, for channels with aspect ratio in the range 0.25< *w/d* <4 (59).

4.2.3.5 Perfusion system

In order to promote the differentiation of vascular endothelial cells into typical BBB phenotype with increased formation of tight junctions and membrane transporters (244), endothelial cells were exposed to flow-mediated shear stress using the following protocol. HUVECs and HBMECs were seeded in collagen-coated microfluidic devices at a density of 2 × 10^6 cells/mL allowed to adhere under static conditions for 72 h. Culture media were changed daily. Cells were then exposed to shear stress for 24 h, testing different input flow rates (1, 2, 5 and 10 µl/min). The endothelial cell-covered microfluidic channels were connected to a syringe pump using Tygon tubing with internal diameter (ID) 0.020" and outer diameter (OD) 0.060" (Cole Parmer, USA) and 24G blunt needle connections (Sai infusion technologies, USA). Spent media was collected by outlet tubing in reservoirs. The shear stress medium was EGM™-2 Endothelial Cell Growth Medium-2 BulletKit™ (Lonza, USA) and Endothelial Cell Growth Medium (ScienCell, USA), for HUVEC and HBMECs, respectively. The entire experimental setup (pump, devices and reservoirs) was placed in a CO_2 incubator (Figure 4.6). Different flow rates were used to test effect of shear stress on endothelial cell function and proliferation. For comparison, endothelial cells were cultured in the chips without exposure to flow under static conditions over the same period.

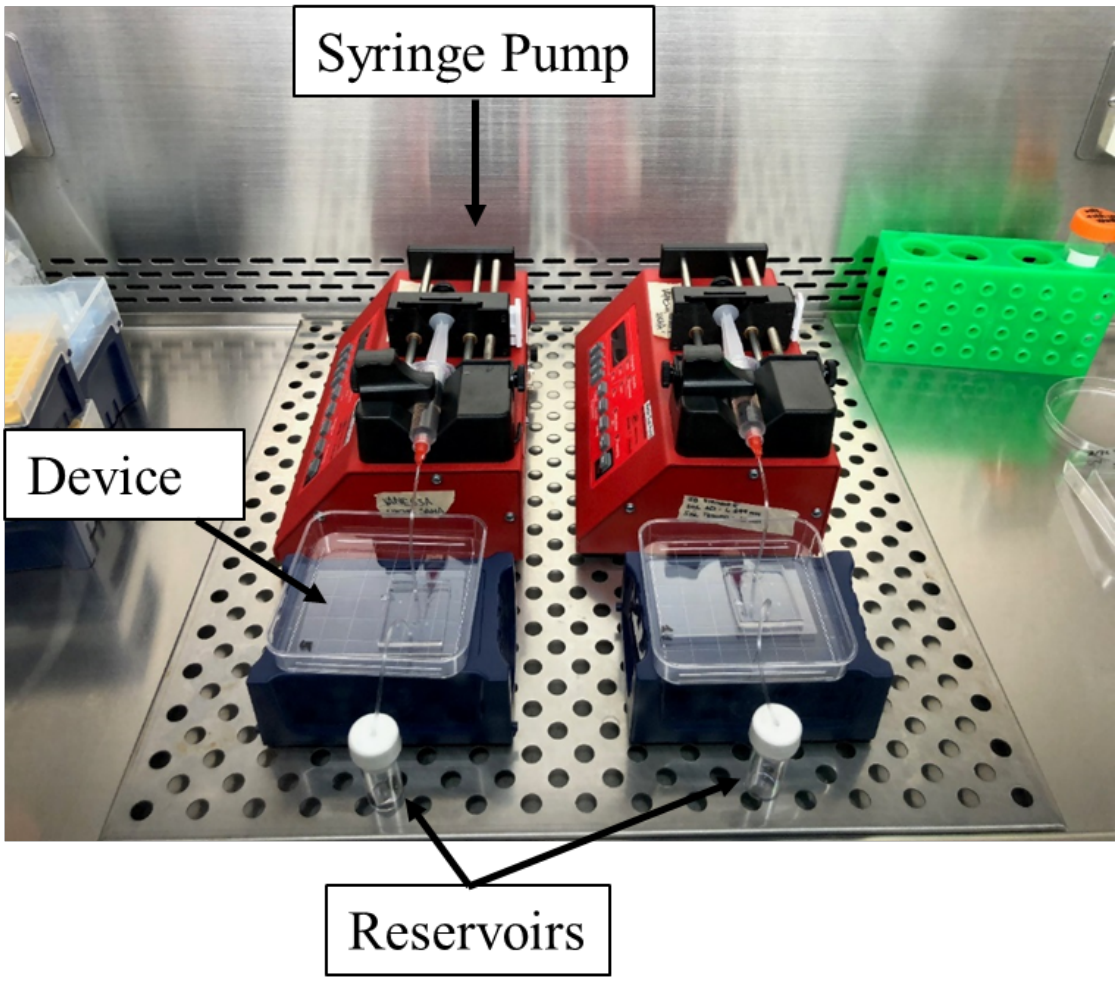

Figure 4.6 Experimental setup preparation.

Devices were connected to a syringe pump using Tygon tubings (left). Outlet tubings were connected to reservoirs to collect spent media for quantitative assays. The entire setup was placed in a CO_2 incubator (right).

4.2.3.6 Culture medium optimization

Endothelial cells were first cultured in Endothelial Cell Medium (ScienCell, #1001), containing 5% FBS, 1% P/S. To better reproduce the *in vivo* environment, HBMECs were cultured in an improved medium containing HAs- and HBVPs-conditioned media. The conditioned media was filtered using Millipore Express (PES) Membrane (pore size 0.22 µm, diameter 33 mm, sterile, γ-irradiated) and stored at −80 °C until use. The final improved medium consisted of 40% filtered conditioned media obtained from the two cell types and 60% fresh media (440).

4.2.3.7 Immunofluorescence Staining

Briefly, cells were washed twice in 0.1 M PBS (pH 7.6) and fixed with fresh 4% paraformaldehyde (PFA) for 10 min. The PFA was discarded and cells were

washed three times in PBS for 5 min each. To prevent non-specific antibody binding, fixed cells were re-suspended in 10% horse serum for 1 hour at room temperature. Primary antibody incubation was carried out for 2 hours at room temperature or overnight at 4 °C with gentle agitation. HBMECs were identified by using primary antibodies against *Cluster of differentiation 31* (CD31) and *Zonula Occludens* (Rb anti ZO-1) (Thermo Fisher, UK). After incubation with the primary antibody, the samples were washed in PBS three times for 5 min. The corresponding secondary antibody conjugated to Alexa Fluor 488 (1:1000) was added to the cells for 1 hour at room temperature with gentle agitation. Cells were washed in PBS three times for 5 min, stained with 5 µg/mL Hoechst 33342 (Invitrogen, UK) to label the nucleous and stored at 4 °C.

The immunostained cells were viewed under fluorescence microscope (ZEISS Axiovision) using appropriate excitations for each fluorophore. All images were imported into ImageJ program for minor adjustment of brightness and contrast, resizing or cropping and assembling into figures.

4.2.3.8 Imaging analysis for measurement of cell alignment and elongation

After shear stress application, HUVECs were stained with phalloidin (ActinGreen™ 488 Ready Probes™, ThermoFisher Scientific, UK) to label F-actin. Images of cells were acquired in phase contrast mode using a Olympus IX70 inverted microscope system (Olympus, USA). Fluorescence images were acquired using a ZEISS Axiovison fluorescence microscope (ZEISS, Germany) equipped with ZEISS ZEN 2.3 (blue edition) software and exported into ImageJ v.1.52n (444) for analysis. Cell morphology was quantified using shape descriptors and cell alignment measurements. In order to obtain the precise morphologies of the cells, the cell boundaries were outlined manually using ImageJ freehand line tool. Actin filament alignment was quantified using an ImageJ based plug-in, FibrilTool, which measures fibrils alignment and a score of anisotropy structures in a given region of interest (ROI) (445). Images were aligned horizontally considering 0° the direction of the flow. The anisotropy score was quantified between 0.0 for no order (purely isotropic arrays) and 1.0 for perfectly ordered fibril distribution (purely anisotropic arrays). For each measurement, ten different ROIs were selected in each image and three different

images were selected for each experimental group. Using this approach we also measured parameters such as the length of the long axis of the cell, the inverse aspect ratio (IAR) which represents length of the short axis divided by the length of long axis (Figure 4.7), and the orientation angle of the cell long axis with respect to the flow direction (θ).

As a measure of elongation, it was used the shape descriptor circularity in ImageJ, which is measured by the formula: $C=4\pi A/P^2$, where A is the area and P the perimeter of the projected cell. A value of 1.0 indicates a perfect circle while a value close to 0.0 (*i.e.*, 0.01 - 0.02) indicates an elongated cell shape. For instance, the cell highlighted in Figure 4.7 has a circularity value of 0.02, which is characteristic of elongated cells.

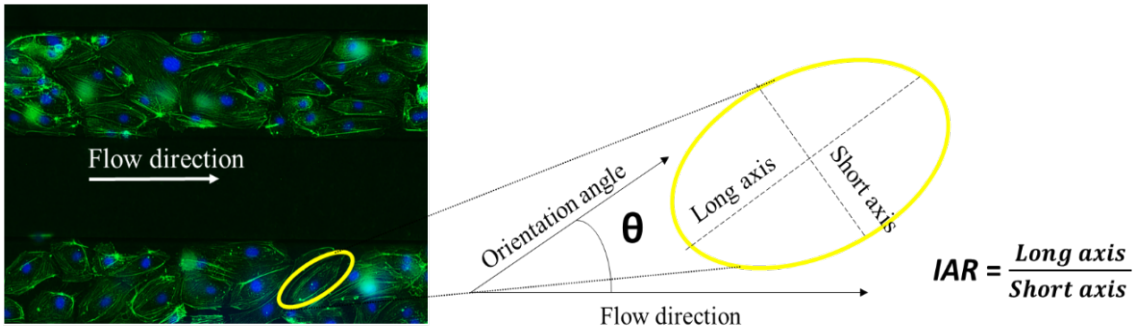

Figure 4.7 Cell morphology calculations.

4.2.4 Amyloid Beta (Aβ) treatment

Amyloid beta protein fragment 1-42, Aβ1-42, (Sigma, A9810) was initially dissolved in dimethyl sulfoxide (DMSO) at a concentration of 0.22 mM. Aβ1-42 stocks were stored at -20 °C. Before the experiment, 10 µl Aβ1-42 was combined with 12 µl PBS to generate 100 µM Aβ1-42 solution, which was further diluted in culture medium to obtain the desired concentration. In detail, three different Aβ1-42 concentrations were tested: 0.1 µM, 0.5 µM, 1 µM.

Cells were incubated in the presence and absence of Aβ1-42 at different concentrations (0.1, 0.5 and 1 µM) for 24, 48 and 72 h to assess the possible effect of the peptide on cell viability. MTT assay (30006, Biotium, UK) was carried out by adding 10 µL of 3-(4,5-dimethylthiazol-2-yl)-2,5-diphenyl tetrazolium bromide (MTT) solution to each well on a 96 well plate and cells were incubated for 4 hours at 37 °C protected from light. Then, 200 µl of dimethyl sulfoxide (DMSO) was added to the cells to dissolve the crystals formed.

4.2.4.1 Live dead assay

Cell survival was measured using ReadyProbes® Cell Viability Imaging Kit (ThermoFisher Scientific, USA) in accordance with manufacturer's instructions. Briefly, the cultures were incubated in the presence of the combined solution at room temperature for 15 min protected from light. Using fluorescence microscopy, cells showed the blue florescence of NucBlue® Live (Hoechst 33342) which stains the nuclei of all cells whilst nuclei of dead cells were indicated by the green florescence of NucGreen® Dead. The extent of the cell survival was than quantified over the amount of the total cells.

4.2.4.2 MTT assay

To assess cell viability it was used MTT assay (Biotium, Catalog 30006) using standard microplate absorbance readers. The MTT assay is based on the cleavage of the yellow tetrazolium salt MTT to purple formazan crystal by metabolic active cells (446). The formazan is then solubilized, and the concentration determined by optical density at 570 nm. The result is a sensitive assay with a colorimetric signal proportional to the cell number. Cells were seeded into 96-well tissue culture plates at a density of 10,000 cells per well in order to reach optimal density within 48 to 72 hours. After 72 h, cells were treated with Aβ1-42 as described above with a final volume of culture medium in each well of 100 μL. The MTT solution was heated to 37 °C and mixed gently to obtain a clear solution, and 10 μL MTT solution was added to the 100 μL of medium in each well. Cells were then incubated at 37 °C for 4 hours protected from light. After incubation with MTT solution, 200 μL of DMSO was added directly into the medium in each well and pipetted up and down several times to dissolve the formazan salt, reaching a final volume of 300 μL in each well. Finally, the optical density (OD) was measured on an IMark absorbance microplate reader (Bio-Rad, UK) with a test wavelength of 570 nm. Background absorbance at 630 nm was subtracted from signal absorbance to obtain normalized absorbance values. For comparison, MTT assay results were compared with live/dead assay cell viability data.

4.2.4.3 Cytokine ELISA for IL-6, IL-8 and TNF-α

Effluent samples from devices were taken after 24 h of Aβ1-42 exposure or after 24 h with no treatment, spun at 500 x g for 5 min at 4 °C and supernatant was stored at -20 °C. Samples were diluted 1:10 and cytokine analysis was performed using enzyme-linked immunosorbent assay (ELISA) for TNF-α, IL-8 and IL-6 (R&D Systems, Inc., Minneapolis, MN, USA). Before use, all ELISA reagents were brought to room temperature and all standards, samples and controls were assayed in duplicate. To prepare the plate, the respective capture antibody was diluted to the working concentration according to the manufacturer's instructions (4 µg/mL for TNF-α and IL-8, 2 µg/mL for IL-6) in PBS without carrier protein and immediately used for coating a 96-well microplate by adding 100 µL per well. The plate was sealed and incubated overnight at room temperature. Each well was aspirated and washed with buffer (400 µL), repeating the process three times for a total of four washes. After removing any remaining wash buffer by aspirating or decanting, the plate was inverted and blotted against clean paper towels. Plates were then blocked by adding 300 µL of reagent diluent to each well and incubated at room temperature for a minimum of 1 hour. The aspiration/wash was repeated and 100 µL of diluted sample or standards were added to each well. Plates were covered and incubated 2 hours at room temperature. After washing, 100 µL of the respective detection antibody (50 ng/mL for TNF-α andIL-6, 20 ng/mL for IL-8) were added to each well and plates were incubated 2 hours at room temperature. Plates were washed and 100 µL of the working dilution (1:40) of Streptavidin-horseradish peroxidase (HRP) were added to each well. After 20 min incubation at room temperature in the dark, plates were washed and 100 µL of substrate solution were added to each well. Following other 20 min incubation at room temperature in the dark, 50 µL of stop solution were added to each well. Finally, the optical density was determined for each well, using a microplate reader set to 450 nm, subtracting readings at 540 nm. For calculation of results, the duplicate readings for each standard and sample were averaged and the average zero standard optical density (O.D.) were subtracted. Standard curves were created by reducing the data using a computer software capable of generating a four parameter logistic (4-PL) curve-fit (Assayfit Pro, Assay Cloud, The Netherlands). The concentration read from the standard

curve was then multiplied by the sample dilution factor (10) to obtain the final sample concentration.

4.2.5 Statistical analysis

Data are presented as mean ± SD of independent experiments performed in triplicate. Data were analysed by one-way ANOVA, with differences between groups assessed by Tukey's post hoc tests using GraphPad Prism 7.05 software (GraphPad, SanDiego, California). Statistical significance was determined when $p < 0.05$.

4.3 Results and Discussions

4.3.1 Device design and fabrication

For the *in vitro* culture of BBB cells shear stress levels were first modelled by computation simulation using COMSOL. To culture microvascular brain endothelial cells, the design has been improved in order to optimize flow rate distribution and shear stress levels to more closely reproduce typical capillary-like shear stress levels (6.2 dynes/cm^2) (447,448) observed *in vivo.*

4.3.2 COMSOL simulation and measurement of shear stress

In order to quantitatively evaluate the velocity field and shear stresses in the microfluidic chamber, the fluid flow was simulated with COMSOL. Different flow rates (0.5, 1, 2, 3, 5 and 10 µl/min) at the inlet of the chamber and zero pressure (relative pressure) at the outlet were considered in this experiment. The absolute pressure at the outlet is equal to 1 atm as the atmospheric pressure was considered as reference pressure.

Each geometry was characterized by the calculation of the average velocity in the chamber calculated along a line defined in the middle of the chamber at $z=h/2$, and average and maximum values of shear stress at the bottom of the chamber along a line at $z=0$, where z is vertical axis and h is the height of the chamber. COMSOL simulation results are summarized in Table 4.3. Average shear stresses at the bottom of the chamber were found to be in the range between 5 and 80 × 10^{-3} dyne/cm^2 and maximum at the lateral walls of the chamber.

Table 4.3 COMSOL simulation results for the two chamber designs.

Design	Flow rate [µl/min] (m^3/s)	Average Velocity [mm/s]	Average Shear stress at the bottom wall [$dyne/cm^2$]	Maximum Shear stress at the bottom wall [$dyne/cm^2$]
Rectangular chamber	0.5 (0.9×10^{-11})	1.45×10^{-2}	3.16×10^{-3}	3.62×10^{-3}
	1 (1.7×10^{-11})	2.84×10^{-2}	6.35×10^{-3}	7.32×10^{-3}
	2 (3.4×10^{-11})	5.79×10^{-2}	12.26×10^{-3}	14.46×10^{-3}
	3 (5.1×10^{-11})	8.77×10^{-2}	19.61×10^{-3}	22.44×10^{-3}
	5 (8.3×10^{-11})	1.41×10^{-1}	30.93×10^{-3}	35.42×10^{-3}
	7 (11.9×10^{-11})	2.05×10^{-1}	45.75×10^{-3}	52.76×10^{-3}
	10 (1.7×10^{-10})	2.92×10^{-1}	71.90×10^{-3}	75.37×10^{-3}
Rhombus-shaped chamber	0.5 (0.89×10^{-11})	1.45×10^{-2}	3.21×10^{-3}	3.34×10^{-3}
	1 (1.7×10^{-11})	2.92×10^{-2}	6.52×10^{-3}	6.88×10^{-3}
	2 (3.4×10^{-11})	5.82×10^{-2}	12.84×10^{-3}	13.56×10^{-3}
	3 (5.1×10^{-11})	8.76×10^{-2}	19.58×10^{-3}	22.61×10^{-3}
	5 (8.3×10^{-11})	1.41×10^{-1}	30.93×10^{-3}	32.31×10^{-3}
	7 (11.9×10^{-11})	2.04×10^{-1}	45.69×10^{-3}	48.19×10^{-3}
	10 (1.7×10^{-10})	2.92×10^{-1}	65.28×10^{-3}	68.84×10^{-3}

Figures 4.8, 4.9, 4.10 and 4.11 present a graphical rendering of COMSOL simulations of the velocity field and shear stress for the two different chip designs at an input flow rate of 10 µl/min. Figure 4.8A and Figure 4.9A show the velocity magnitude distribution in the middle of the chamber from blue (0 mm/s) to red (1 mm/s). The rectangular chamber design is characterized by the presence of zero-velocity corners where biomolecules or cells can be trapped for long period. Those areas can be minimized using a rhombus-shaped chamber which allows to obtain a more homogeneous flow distribution and velocity field. The velocity magnitude profile along the width of the chamber in the central area of the chamber (z=h/2) is displayed on Figure 4.8B and Figure 4.9B. This velocity distribution obtained by COMSOL confirms the one calculated by the Navier-Stokes equation which shows that the fluid velocity is maximum in the middle of the chamber and minimal at the side-walls. However, it presents velocity

fluctuations of approximately 18% due to the presence of micropillars, which determine a reduction of the flow in those areas. A more uniform velocity distibution is observed along the height of the chamber in the middle of the analysis area (Figure 4.8C and Figure 4.9C).

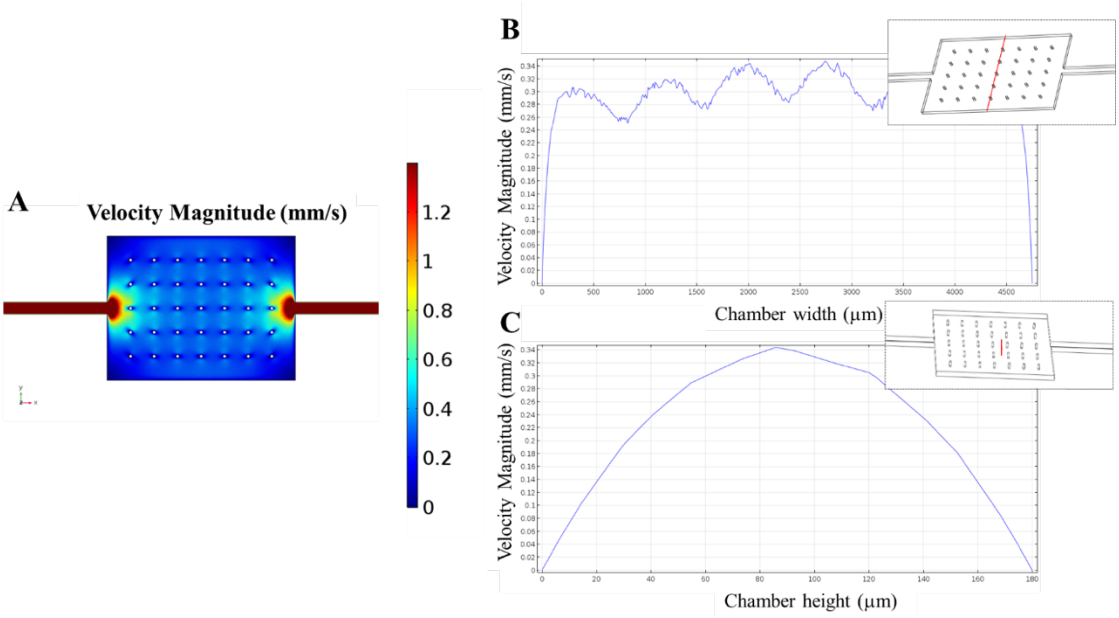

Figure 4.8 COMSOL simulation of fluid flow in a microfluidic rectangular chamber with depth 150 μm at 10 μl/min input flow.

A) Velocity magnitude distribution in the middle of the microfluidic chamber. B) velocity profile across the chamber along the red line highlighted on the insert (middle of the chamber, z=h/2). C) velocity profile across the chamber along the vertical red line highlighted on the insert.

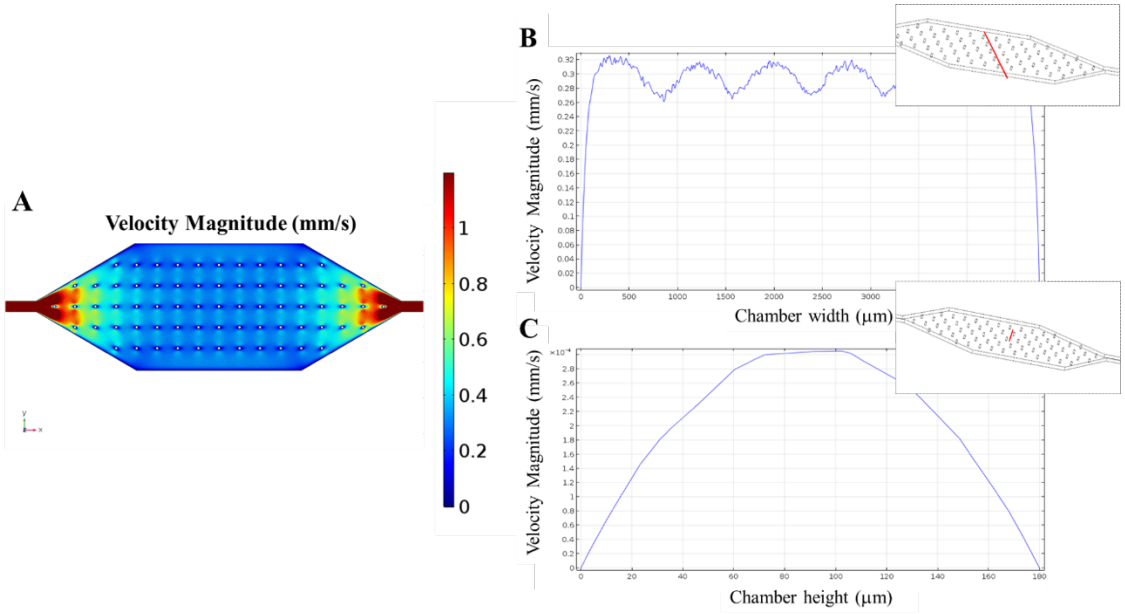

Figure 4.9 COMSOL simulation of fluid flow in a microfluidic rhombus-shaped chamber with depth 150 μm at 10 μl/min input flow.

A) Velocity magnitude distribution in the middle of the microfluidic chamber. B) velocity profile across the chamber along the red line highlighted on the insert (middle of the chamber, z=h/2). C) velocity profile across the chamber along the vertical red line highlighted on the insert.

COMSOL simulation results of the shear stress observed at the bottom of the chamber are shown in Figure 4.10 and Figure 4.11. Comparison between the two designs revealed a similar range of shear stress, comprised between 0 Pa (blue) and 3×10^{-2} Pa (red), but a more even distribution of shear stress in the rhombus-shaped design. Results indicated also that the horizontal profile of shear stress within the chamber (Figure 4.10B and Figure 4.11B) is mostly uniform except for regions near the lateral walls within a distance of ~ 200 μm and for low fluctuations generated by the presence of pillars. This uniform distribution helps optimize the homogeneity of the shear stress experienced by the cells in the chamber, that is essential in experiments which investigate effects of flow on cell morphology and functions. Moreover, as expected, shear stresses along the height of the chamber are higher at the walls and zero in centre of the chamber (Figure 4.10C and Figure 4.11C).

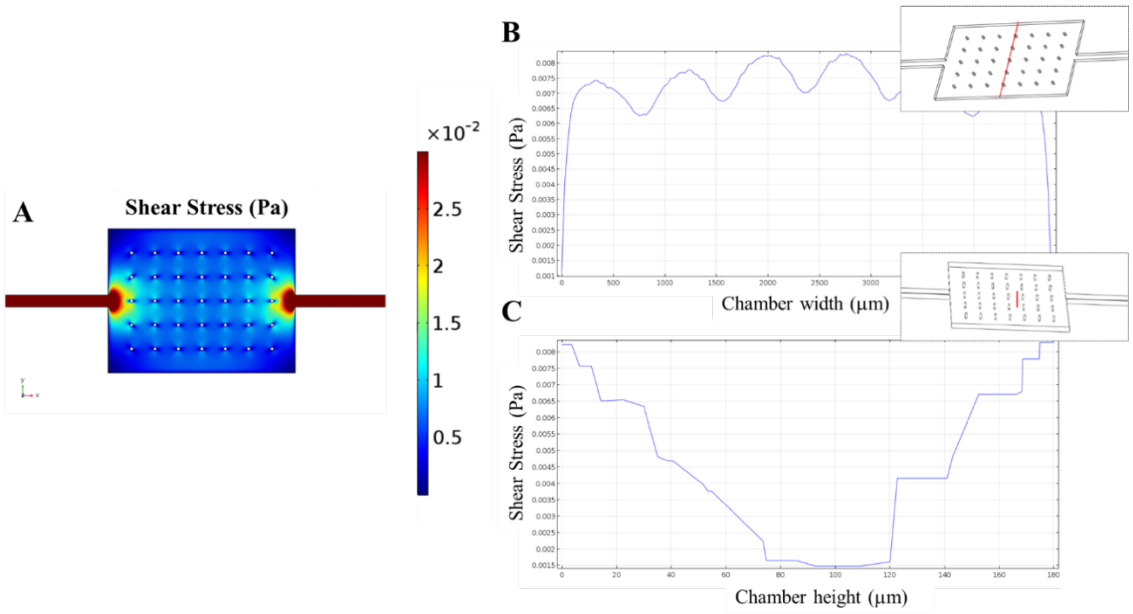

Figure 4.10 COMSOL simulation of fluid flow in a microfluidic rectangular chamber with depth 150 μm 10 μl/min input flow.

A) Shear stress distribution at the bottom of the microfluidic chamber. B) shear stress profile across the chamber along the red line highlighted on the insert (middle of the chamber, z=0). C) shear stress profile across the chamber along the vertical red line highlighted on the insert.

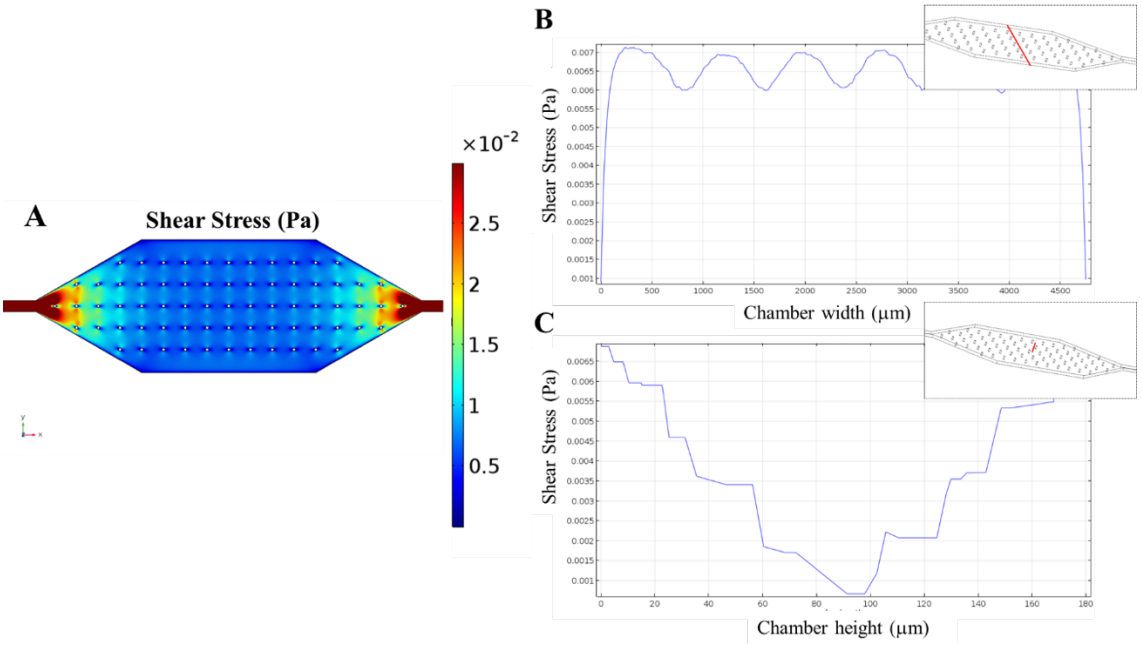

Figure 4.11 COMSOL simulation of fluid flow in a microfluidic rhombus-shaped chamber with depth 150 μm at 10 μl/min input flow.

A) Shear stress distribution at the bottom of the microfluidic chamber. B) shear stress profile across the chamber along the red line highlighted on the insert (middle of the chamber, z=0). C) shear stress profile across the chamber along the vertical red line highlighted on the insert.

Considering the Navier-Stokes equation used to calculate the velocity distribution in a rectangular microchannel and assuming Poiseuille flow, the mean velocity along a line in the middle of the analysis area can be approximated by the following equation (449):

$$v_m = \frac{1}{w}\int_0^w v(y)dy = \frac{4v_{max}}{w^3}\int_0^w y(w-y)dy = \frac{4v_{max}}{w^3}\left[\frac{wx^2}{2} - \frac{x^3}{3}\right]_0^w = \frac{2v_{max}}{3} \qquad (4.7)$$

From this calculation it can be deduced that the flow rate only reaches 2/3 of the maximum theoretical rate, and this limits the levels of shear stress which cells experience within the chamber.

However, **the rhombus-shaped design allows to avoid the zero-velocity areas present in a rectangular chamber design and to create a more uniform environment where cells are exposed to a homogeneous wall shear stress profile**. Thus, this design results suitable to culture cells which are not exposed to high level of shear stress *in vivo,* such as astrocytes and pericytes, while to *in vitro* replicate the tight endothelium which characterizes the BBB, some modifications need to be done to improve the chamber design.

4.3.3 Design of a microfluidic device for culture of endothelial cells

From COMSOL simulation results, it was possible to conclude that a rhombus-shaped chamber is not ideal for the culture of endothelial cells, due to the reduced shear stresses within the chamber. A simple solution to this problem would be to modify the chamber geometry building a tree-like architecture that splits the flow into multiple channels. With this configuration, each channel still presents a Poiseuille distribution but it is possible to obtain an increased mean velocity and flow velocity uniformity in the chamber. There is also a need to adapt the chamber design in order to better mimic dimensions of human BBB vasculature *in vivo*, where arterioles and venules are characterized by a diameter of 20-90 μm and capillaries by a diameter of 6-10 μm (450). Following these considerations, was created a design which includes an inlet microchannel that sequentially splits the flow into several sub-channels. This improved strategy allowed to obtain a high shear rate microfluidic device which also provides a better uniformity of shear distribution and of the velocity field.

4.3.3.1 Device design

Different device designs were created using AutoCAD software and are displayed in Figure 4.12. The design consisted on an inlet microchannel 400 μm-wide which then was being splitted into two subchannels at each level of the tree-like architecture, to allow an equal distribution of the flow within the chamber. The final number of microchannels obtained is 16 and those merge together at the outlet following the same tree-like splitting rules. With the aim to better mimic BBB arterioles and venules dimensions, two different channel widths, 200 μm and 400 μm were compared. The height of the channels was chosen to be 100 μm to enable the Hele-Shaw flow approximation of the Navier-Stokes equation, which is specifically important for flows at the micro-scale and for modelling purposes. Finally, to increase cell seeding area, thus the amount of cells available for following analysis such as proteomic, genomic or transcriptomic studies, two channel lengths, 10 mm and 20 mm were compared.

In detail, the different designs that have been considered are:

- 400 μm wide microchannel, 10 mm long and 100 μm high
- 200 μm wide microchannel, 10 mm long and 100 μm high
- 400 μm wide microchannel, 20 mm long and 100 μm high
- 200 μm wide microchannel, 20 mm long and 100 μm high

All the subchannels have parallel walls and in each split a channels is divided into two perpendicular subchannels. The diameter of the inlet and outlet ports is 2 mm and the spacing between each channel is 200 μm.

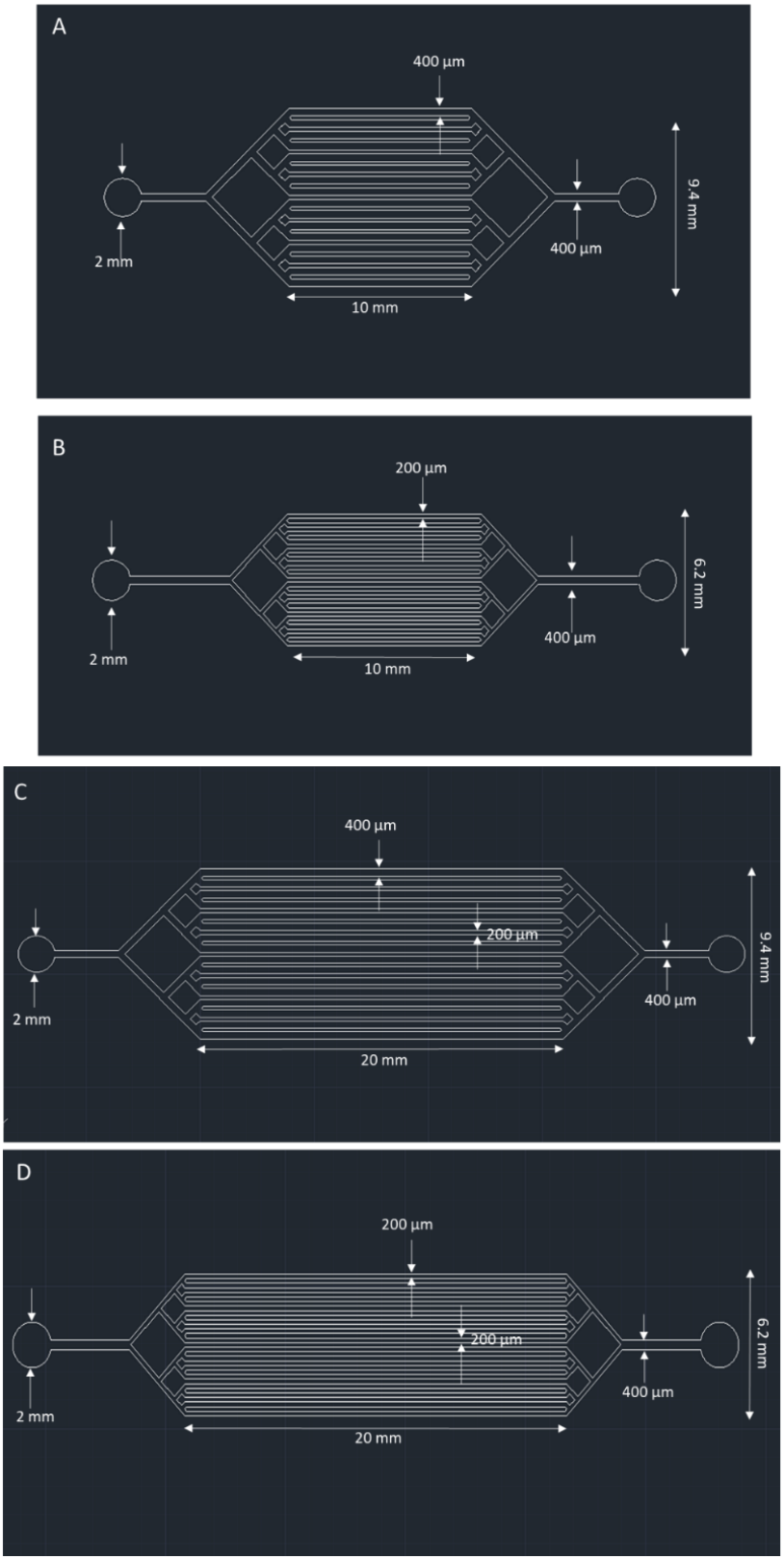

Figure 4.12 Emulsion film masks design for the different microfluidic chamber designs.

A) 400 µm wide microchannel, 10 mm long and 100 µm high. B) 200 µm wide microchannel, 10 mm long and 100 µm high. C) 400 µm wide microchannel, 10 mm long and 100 µm high D) 400 µm wide microchannel, 20 mm long and 100 µm high.

Table 4.4 Comparison of different microfluidic chamber designs in terms of culture area (mm^2), culture volume of medium (µl) and cell seeding density (number of cells / device).

	Area (mm^2)		**Volume (µl)**		**Cell seeding density**
	Each channel	All channels	Each channel	All channels	All channels
Rectangular chamber	29.45		4.4		8.8×10^3
Rhombus-shaped chamber	48.85		7.3		14.7×10^3
200 µm channels, L=10mm	2	32	0.2	3.2	6.4×10^3
400 µm channels, L=10mm	4	64	0.4	6.4	12.8×10^3
200 µm channels, L=20mm	4	64	0.4	6.4	12.8×10^3
400 µm channels, L=20mm	8	128	0.8	12.8	25.6×10^3

4.3.3.2 COMSOL simulation of shear stress

The flow within each of the chamber design was characterize by COMSOL simulations, to quantitatively measure shear levels that cells would experience within each device. Simulation results indicated a uniform distribution of shear stress among the different channels (Figure 4.13) and along the entire length of the channel, with maximum values at the lateral walls of the chamber. Different input flow rates (0.5, 1, 2, 5 and 10 µl/min) at the inlet of the chamber and zero pressure at the outlet were considered. COMSOL simulation results are summarized in Table 4.5. The 200 µm channels configuration allowed, as expected, to obtain shear stress distribution two times higher than the one obtained with the 400 µm channels design. For instance, with an input flow rate of 5 µl/min shear stresses at the bottom of the chamber are approximately 0.2 dyne/cm^2 in the 200 µm channels design (Figure 4.13A), while they drop to ~ 0.08 dyne/cm^2 in the 400 µm channels design (Figure 4.13C).

From computational simulation, wall shear stress distributions were five times the maximum value obtained for the previous rectangular or rhombus-

shaped design. **These results demonstrate that this design is more suitable for the culture of endothelial cells to expose them to shear stress which impact the development of properties and functions of the BBB cells.**

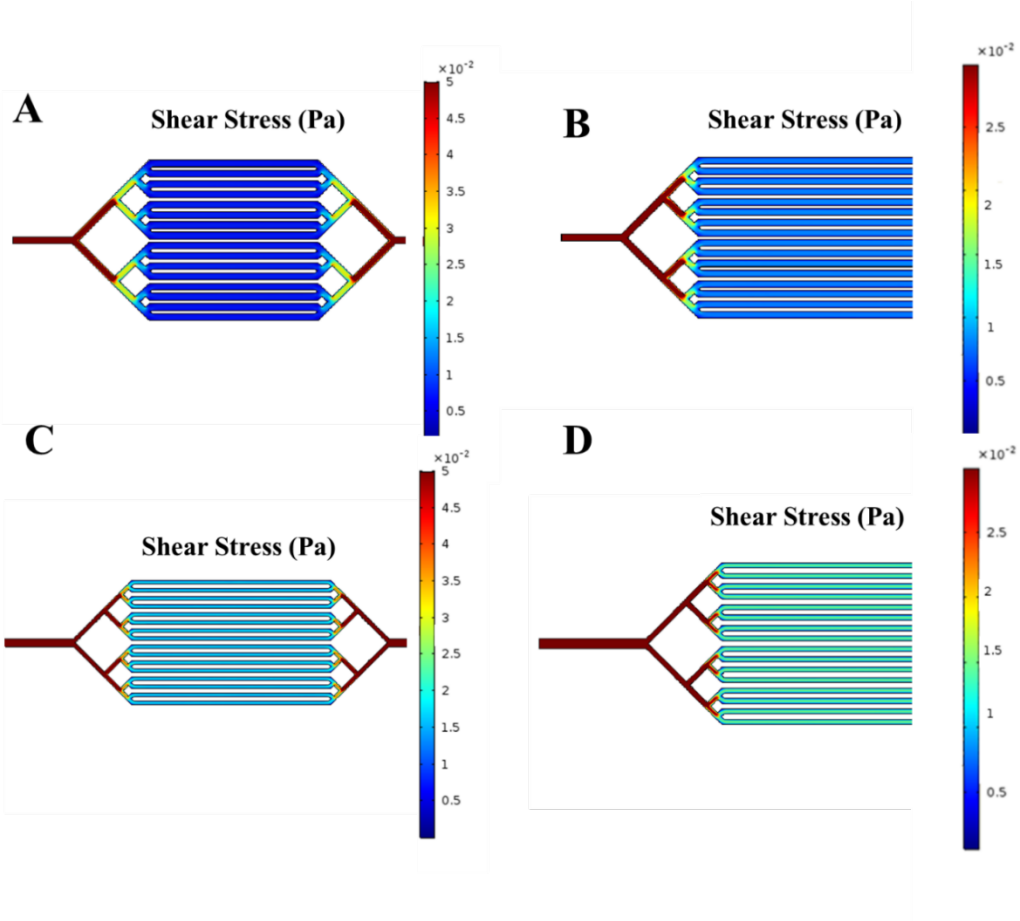

Figure 4.13 COMSOL simulations of fluid flow in different chip designs with depth 100 µm and with an input flow rate of 5 µl/min.

Shear stress distribution at the bottom (z=0) of the microfluidic chip composed of (A) 400 µm-wide channels with length of 10 mm, (B) 400 µm-wide channels with length of 20 mm, (C) 200 µm-wide channels with length of 10 mm or (D) 200 µm-wide channels with length of 20 mm.

Table 4.5 COMSOL simulation results for each chamber design. Computationally measured values of flow rate, average and maximum shear stresses in the bottom wall are provided for each chamber design. W=width, H=height and L=length of the channel.

Design	**Flow rate [µl/min]**	**Average Shear stress in the bottom wall [dyne/cm^2]**	**Maximum Shear stress in the bottom wall [dyne/cm^2]**
W=200 µm H=100 µm L=10 mm	0.5 (0.85×10^{-11} m^3/s)	15.10×10^{-3}	18.92×10^{-3}
	1 (1.7×10^{-11} m^3/s)	30.19×10^{-3}	37.84×10^{-3}
	2 (3.4×10^{-11} m^3/s)	60.39×10^{-3}	75.67×10^{-3}
	5(8.33×10^{-11} m^3/s)	147.95×10^{-3}	185.39×10^{-3}
	10 (16.7×10^{-11} m^3/s)	295.92×10^{-3}	370.78×10^{-3}
W=400 µm H=100 µm L=10 mm	0.5 (0.85×10^{-11} m^3/s)	6.94×10^{-3}	8.39×10^{-3}
	1 (1.7×10^{-11} m^3/s)	13.87×10^{-3}	16.79×10^{-3}
	2 (3.4×10^{-11} m^3/s)	27.75×10^{-3}	33.57×10^{-3}
	5 (8.33×10^{-11} m^3/s)	67.98×10^{-3}	82.26×10^{-3}
	10 (16.7×10^{-11} m^3/s)	135.96×10^{-3}	164.51×10^{-3}
W=200 µm H=100 µm L=20 mm	0.5 (0.85×10^{-11} m^3/s)	15.43×10^{-3}	18.51×10^{-3}
	1 (1.7×10^{-11} m^3/s)	30.86×10^{-3}	37.03×10^{-3}
	2 (3.4×10^{-11} m^3/s)	61.712×10^{-3}	74.05×10^{-3}
	5 (8.33×10^{-11} m^3/s)	151.20×10^{-3}	181.42×10^{-3}
	10 (16.7×10^{-11} m^3/s)	302.4×10^{-3}	662.84×10^{-3}
W=400 µm H=100 µm L20=mm	0.5 (0.85×10^{-11} m^3/s)	7.41×10^{-3}	8.49×10^{-3}
	1 (1.7×10^{-11} m^3/s)	14.83×10^{-3}	16.98×10^{-3}
	2 (3.4×10^{-11} m^3/s)	29.67×10^{-3}	33.97×10^{-3}
	5 (8.33×10^{-11} m^3/s)	72.68×10^{-3}	83.22×10^{-3}
	10 (16.7×10^{-11} m^3/s)	145.72×10^{-3}	166.84×10^{-3}

Figure 4.14 shows COMSOL simulation results for the shear stress, comparing the four microchannel designs using different input flow rates. Shear stress levels were found to be sufficiently equivalent in the short (10 mm) (Figure 4.13A,C) and long (20 mm) (Figure 4.13B,D) configuration of the chip. For this reason, **the 20 mm-long channels design was used in the following**

experiments as it allows to obtain uniform distribution of flow velocity, high level of shear stress and increased surface cell culture area.

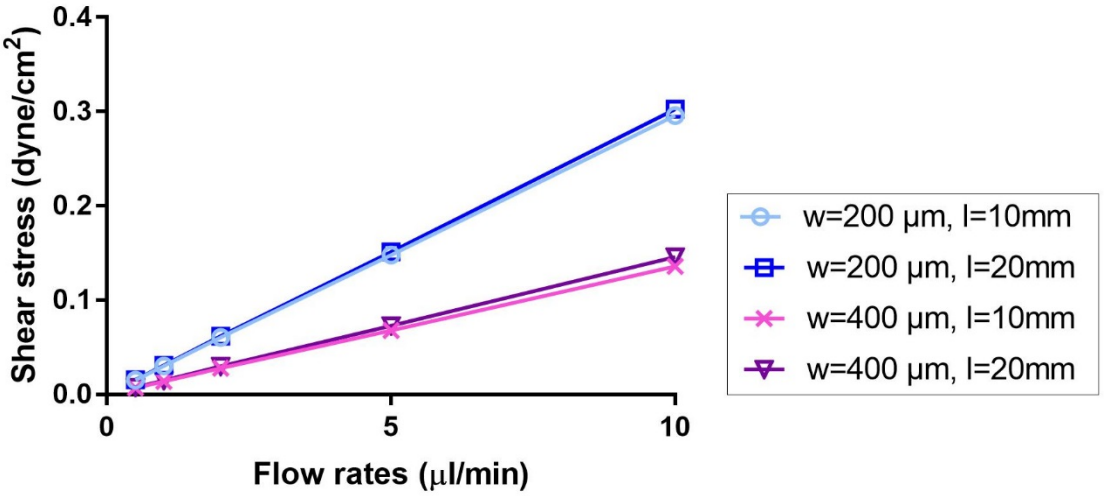

Figure 4.14 Shear stress distibutions between the four device configurations at different input flow rates obtained by COMSOL simulations.

4.3.4 Cell culture

In this chapter, the culture of different cell types will be discussed. HUVECs were cultured in the microfluidic device to optimize perfusion culture in order to induce endothelial cell alignment and differentiation into more specific BBB phenotype. After optimization of device design and flow conditions, HBMECs were cultured in the microfluidic device and exposed to flow to investigate their morphological response to shear. Finally, effects of Aβ1-42 on the viability of all the three BBB cells types, astrocytes, pericytes and endothelial cells, were investigated to identify potential toxicity of the peptide which represents the main component of amyloid plaques in AD brains.

4.3.4.1 HUVECs seeding and perfusion culture

HUVECs were seeded in collagen-coated microfluidic devices and cultured for 3 days to allow cell confluence and optimal cell anchorage. Cells were then exposed to shear stress for 24 h, testing different input flow rates (1, 2, 5 and 10 μl/min). Endothelial monolayer were imaged after 24 h of perfusion culture to assess morphological responses to flow within the device, compared to the control (static culture). Figure 4.15 and Figure 4.16 compare HUVECs

morphology in static and flow (5 µl/min) conditions in a 200 µm- and a 400 µm-wide channels device, respectively.

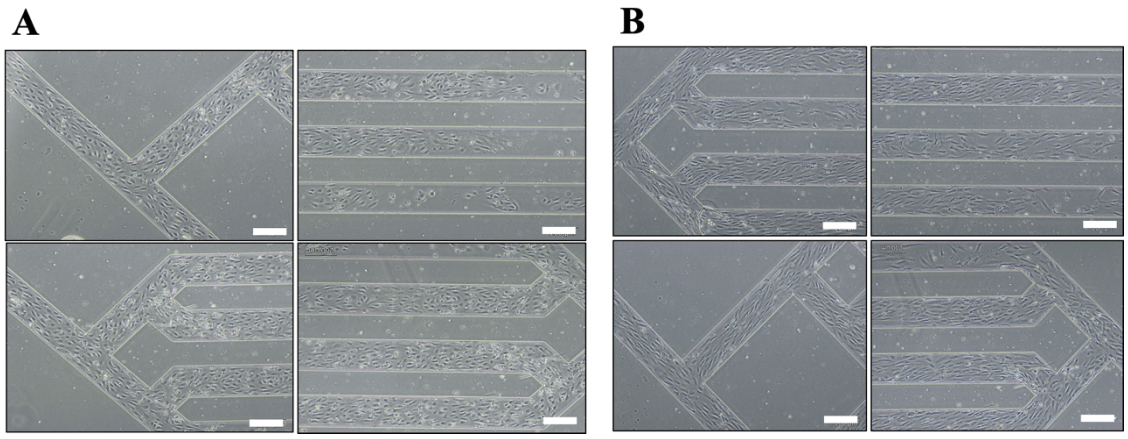

Figure 4.15 Phase contrast images of HUVECs cultured in the 200 µm-wide channels device in static (A) or under flow (5 µl/min) (B). 4X magnification, scalebar: 200 µm.

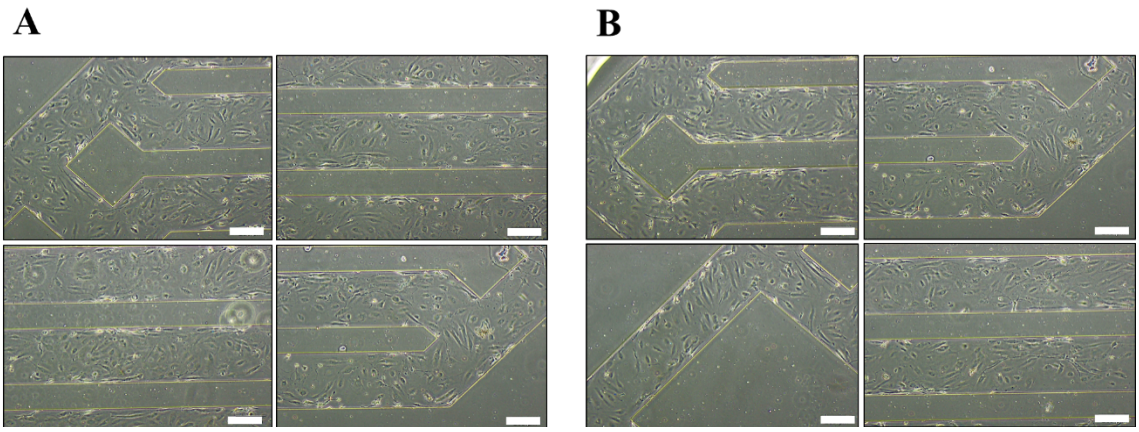

Figure 4.16 Phase contrast images of HUVECs cultured in the in the 400 µm-wide channels device in static (A) or under flow (5 µl/min) (B). 4X magnification, scalebar: 200 µm.

To visualize the cell boundaries, cells were stained for F-Actin and imaged using a fluorescence microscope (Figure 4.17 and Figure 4.18). 4′,6-diamidino-2-phenylindole (DAPI) was used to stain the cell nucleus. Immunofluorescence images show that HUVECs respond to flow by slowly elongating in the direction of shear and by formation of numerous stress fibers. Figure 4.17 shows HUVECs cultured in 200 µm- wide channels in static or under flow using input flow rates of 1, 2 or 5 µl/min for 24 h. Similarly, Figure 4.18 shows HUVECs cultured in 400 µm- width channels in static conditions or using input flow rates of 2, 5 or 10 µl/min for 24 h. The influence of shear on cell alignment is more evident in the narrower channels, where cells are characterized by an elongated shape and horizontal fiber alignment. However, increased cell proliferation under flow was

observed when compared to static culture. This might be explained by the continuous replenishment of culture medium and waste removal offered by perfusion culture.

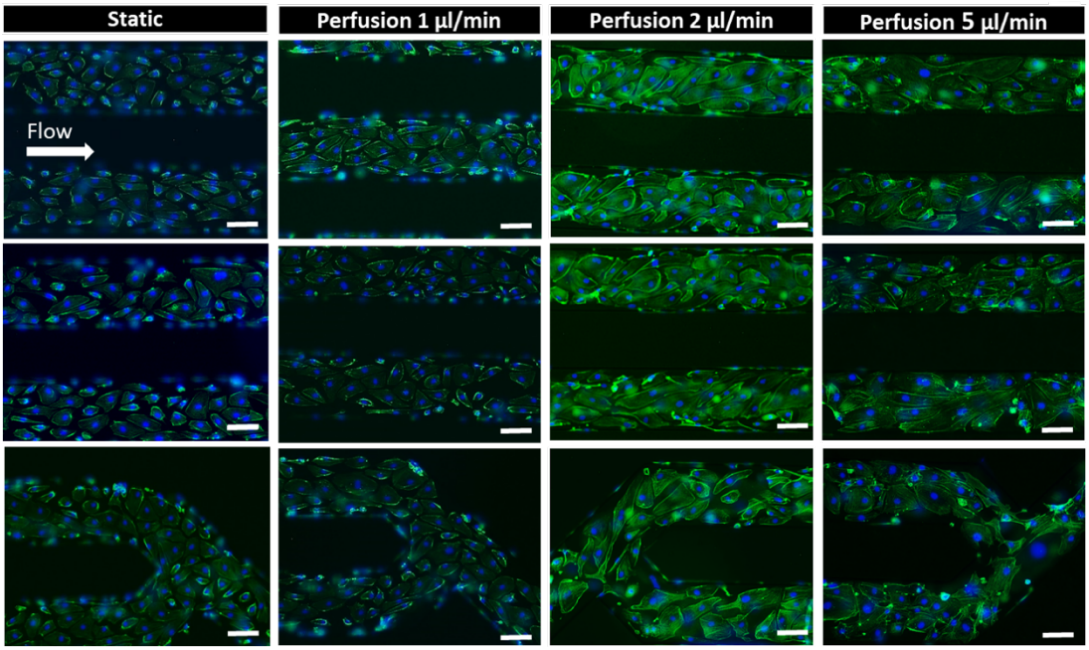

Figure 4.17 Fluorescence images of confluent monolayers of HUVECs.

Green staining represents F-Actin, and blue staining demonstrates cell nuclei (DAPI). HUVECs are cultured in the microfluidic 200 µm-wide channels device with no flow (left) or with input flow rate of 1 µl/min (left), 2 µl/min (middle) or 5 µl/min (right). Scalebar: 100 µm.

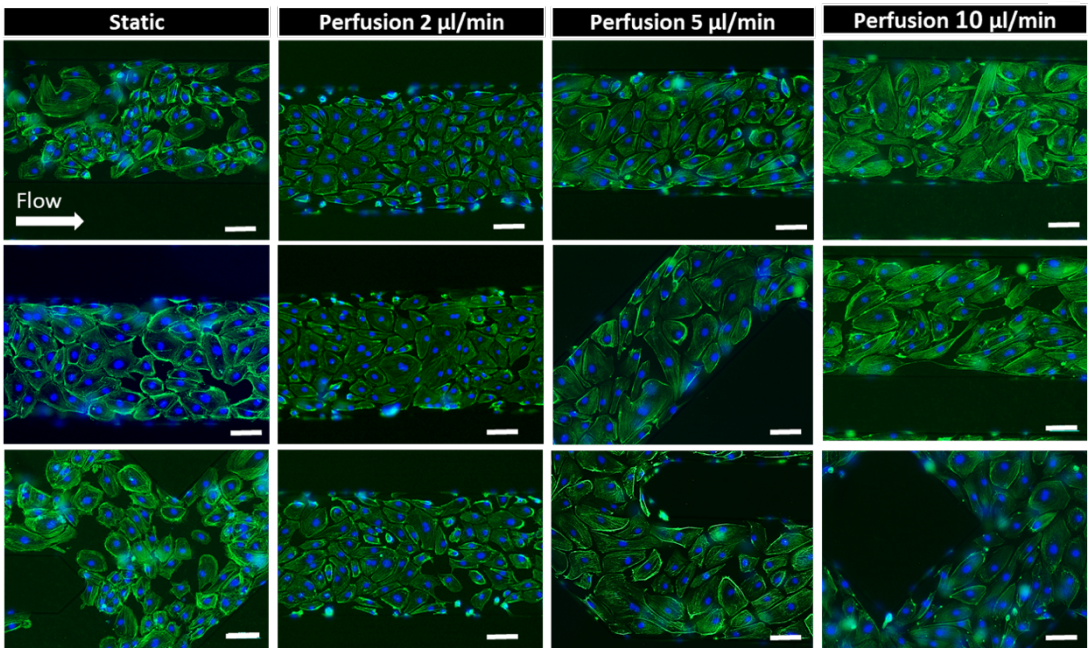

Figure 4.18 Fluorescence images of confluent monolayers of HUVECs

Green staining represents F-Actin, and blue staining demonstrates cell nuclei (DAPI). HUVECs are cultured in the microfluidic 400 µm-wide channels device with no flow (left) or with input flow rate of 2 µl/min (left), 5 µl/min (middle) or 10 µl/min (right). Scalebar: 100 µm.

From morphological analysis of HUVECs cultured in the different channels designs in static or flow condition, it was observed that the higher shear stress generated by reduced channel width induces cell alignment along the flow direction, whereas this effect is less evident in the 400 μm- wide channels device.

4.3.4.1.1 Cell elongation and alignment measurement

Morphological analysis was performed on the immunofluorescence images using ImageJ. In order to obtain the precise morphologies of the cells, the cell boundaries were outlined manually (Figure 4.19). Using this approach it was possible to quantitatively determine parameters associated with cell morphology such as cell elongation and cell alignment in the direction of the flow.

To quantify the axial alignment of cells, was measured the orientation angle of the cell long axis with respect to the flow direction. For doing this, was used the Feret angle measurement calculated by ImageJ. The Feret angle is in fact the angle (0-180 degrees) of the Feret's diameter, which represents the longest distance between any two points along the selection boundary. For comparison, actin fibril orientation was determined using Fibriltool, an ImageJ-based plugin which measures how well actin fibers are aligned and gives a score of anisotropy. A series of ROIs (N=10) were identified in each florescence image, and the angle of fibril orientation (degrees) in the ROI with respect to the horizontal direction (flow direction) as well as the anisotropy scoring of actin filaments were measured.

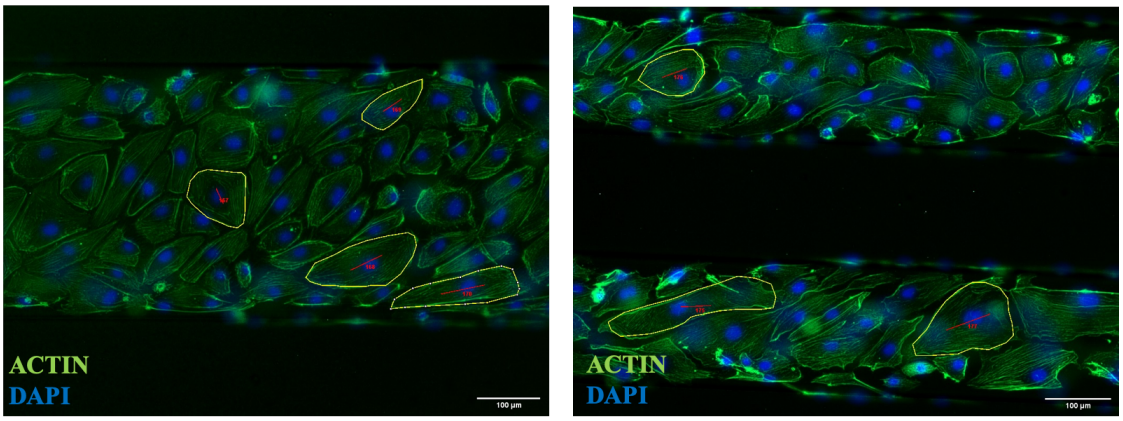

Figure 4.19 Examples of images and ROIs for measuring anisotropy.

Shape descriptors parameters such as circularity, a parameter commonly used in measuring cell morphology, and the inverse aspect ratio (IAR), obtained by dividing the length of short axis by the length of long axis (Figure 4.7), were used as a measurement of cell elongation. Those were significantly reduced in the presence of flow for both the designs for the highest input flow rates (Figure 4.20D,E, and Figure 4.21D,E).

Using those tools, it was confirmed that actin filaments are better aligned under flow. In static conditions the average orientation angle (θ) of cells is 25° in the 200 μm-wide channel design and 45°, which is characteristic of a random distribution, in the 400 μm-wide channel design (Figure 4.21B). This means that cells cultured in the narrower channels tend to align along the channel axis even without the presence of flow. Indeed, when media is added to the inlet reservoir in static conditions, capillary forces create a slow flow (Equation 4.3) which likely affects cell alignment in the microchannel. Minimum θ values of around 15° are obtained in the 200 μm-wide channel design when cell are cultured using 5 μl/min perfusion flow rate (Figure 4.20B). A significant increase in cell elongation under flow was also observed, when compared to static conditions. This was demonstrated by the measurement of circularity (static: 0.03, flow:0.02) and of the IAR which significantly drops from around 0.6 to 0.3 in the 200 μm-wide channel design.

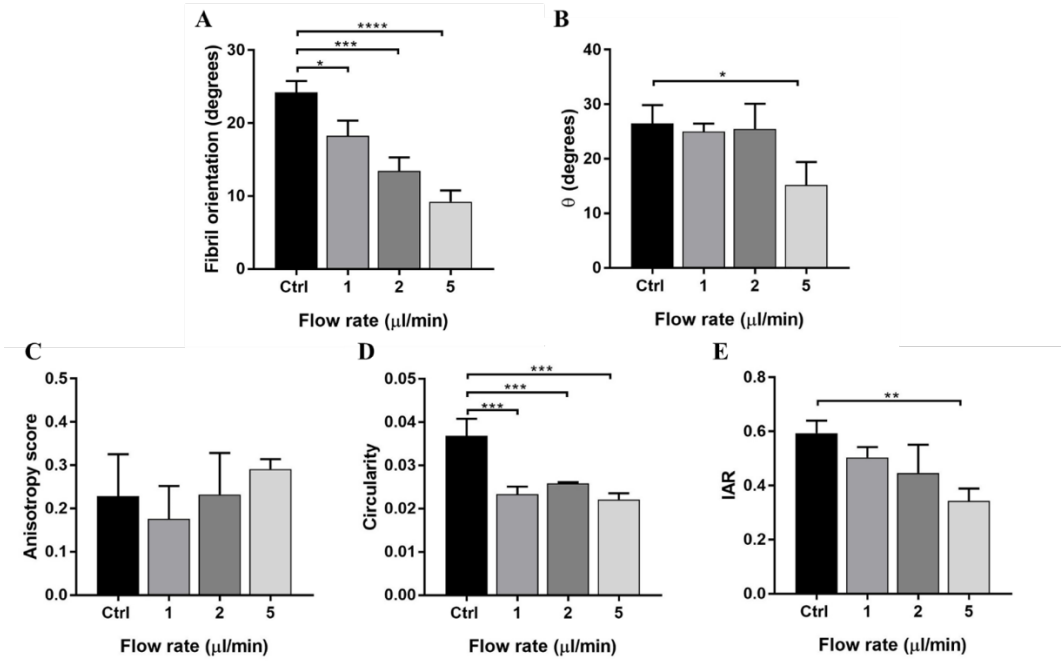

Figure 4.20 Influence of shear stress on cell morphology.

Cells were seeded in the 200 µm-wide channels device and subjected to shear stress for 24 h using input flow rates of 1, 2, and 5 µl/min. Results were compared with control (static, no flow). (A) Fibril orientation (B) average orientation angle (θ) (C) Anisotropy score (D) Circularity (E) IAR. *$p < 0.05$, **$p < 0.005$ *** $p < 0.001$, **** $p < 0.0001$. Error bars represent SD.

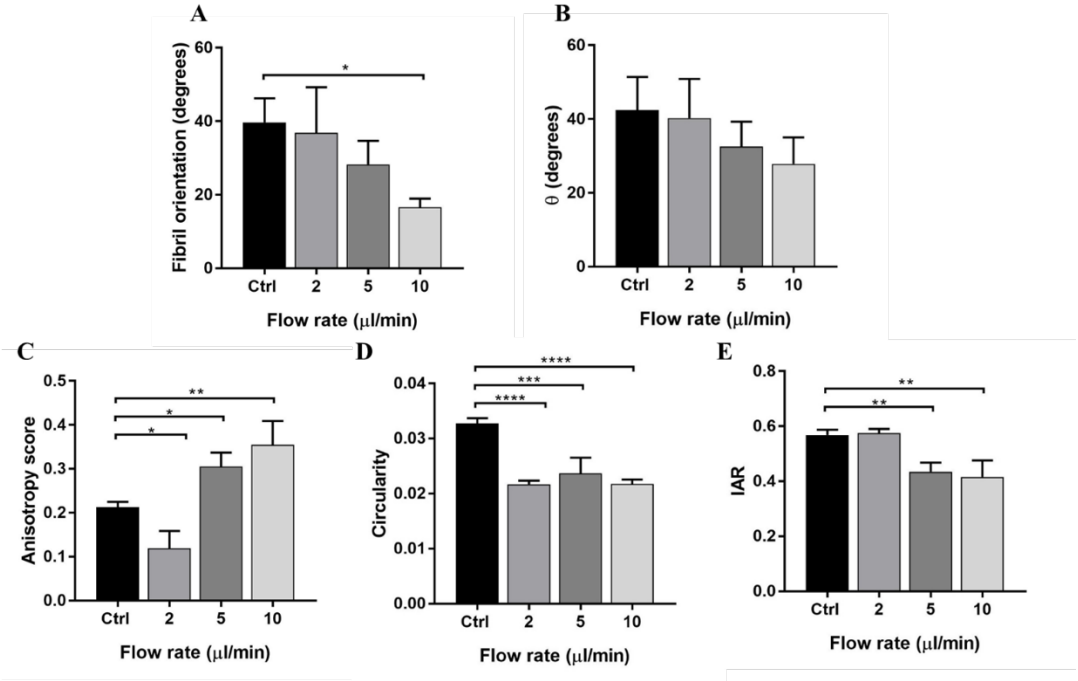

Figure 4.21 Influence of shear stress on cell morphology.

Cells were seeded in the 400 µm-wide channels device and subjected to shear stress for 24 h using input flow rates of 2, 5, and 10 µl/min. Results were compared with control (static, no flow). (A) angle of orientation of actin fibril respect to flow direction (B) average orientation angle (θ) (C) anisotropy scoring of actin filament (D) Circularity (E) IAR. *$p < 0.05$, **$p < 0.005$ *** $p < 0.001$, **** $p < 0.0001$. Error bars represent SD.

4.3.4.2 HBMECs culture

4.3.4.2.1 Immunofluorescence staining of HBMECs

HBMECs were cultured in collagen-coated coverslips in a 24 well plate with seeding density 0.05 × 10^6 cells/well. After reaching 80 % confluence, cells were immunostained for tight junctions (CD31 and ZO-1) using two different primary antibody concentrations, 1:50 and 1:100. After secondary antibody (1:1000) incubation, coverslips were mounted on a microscope slide using VECTASHIELD Antifade Mounting Medium with DAPI (Vector Laboratories, UK) and imaged using a ZEISS Axiovision fluorescence microscope (ZEISS, Germany). Images were analysed using ZEN 2 (blue edition) software and adjusted for brightness and contrast using ImageJ software (Figure 4.22). Primary antibody volume ratio 1:100 revealed optimal for tight junction labelling and selected for further experiments.

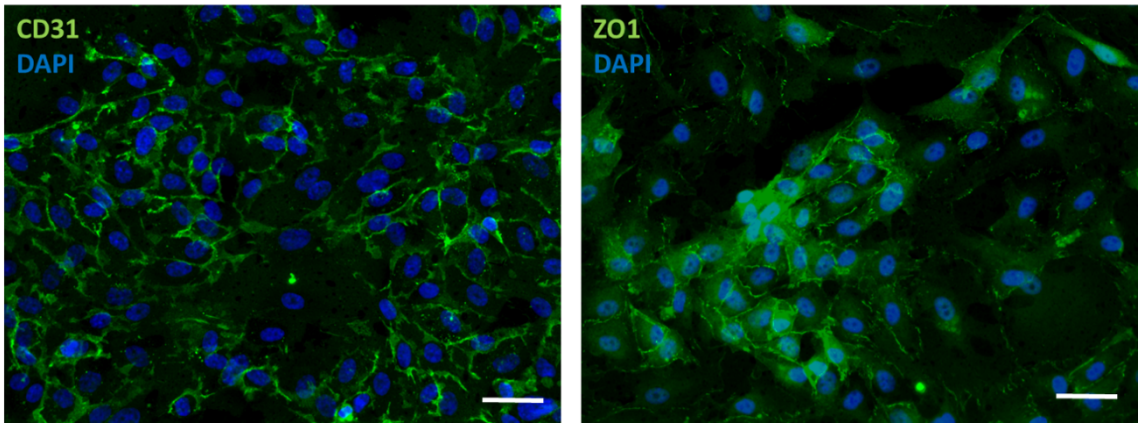

Figure 4.22 Immunofluorescence images of tight junctions of HBMECs cultured in coverslips.

HBMECs were stained for CD-31(1:100) (left) and ZO-1 (1:100) (right). Nucleus was stained using DAPI. 20 x magnification, scalebar: 50 µm.

4.3.4.2.2 HBMECs perfusion culture

HBMECs were cultured in the microfluidic device at a seeding density of 2 × 10^6 cells/mL for 72 h under static conditions and then exposed to perfusion for 24 h at 5 µl/min. Similarly to what observed for HUVECs, HBMECs were able to align and elongate in the direction of the flow as shown in Figure 4.23B. In addition, significant increase in cell proliferation was observed compared to static culture (Figure 4.23A), which reveals beneficial effects of dynamic culture on the formation of a tightly connected endothelium.

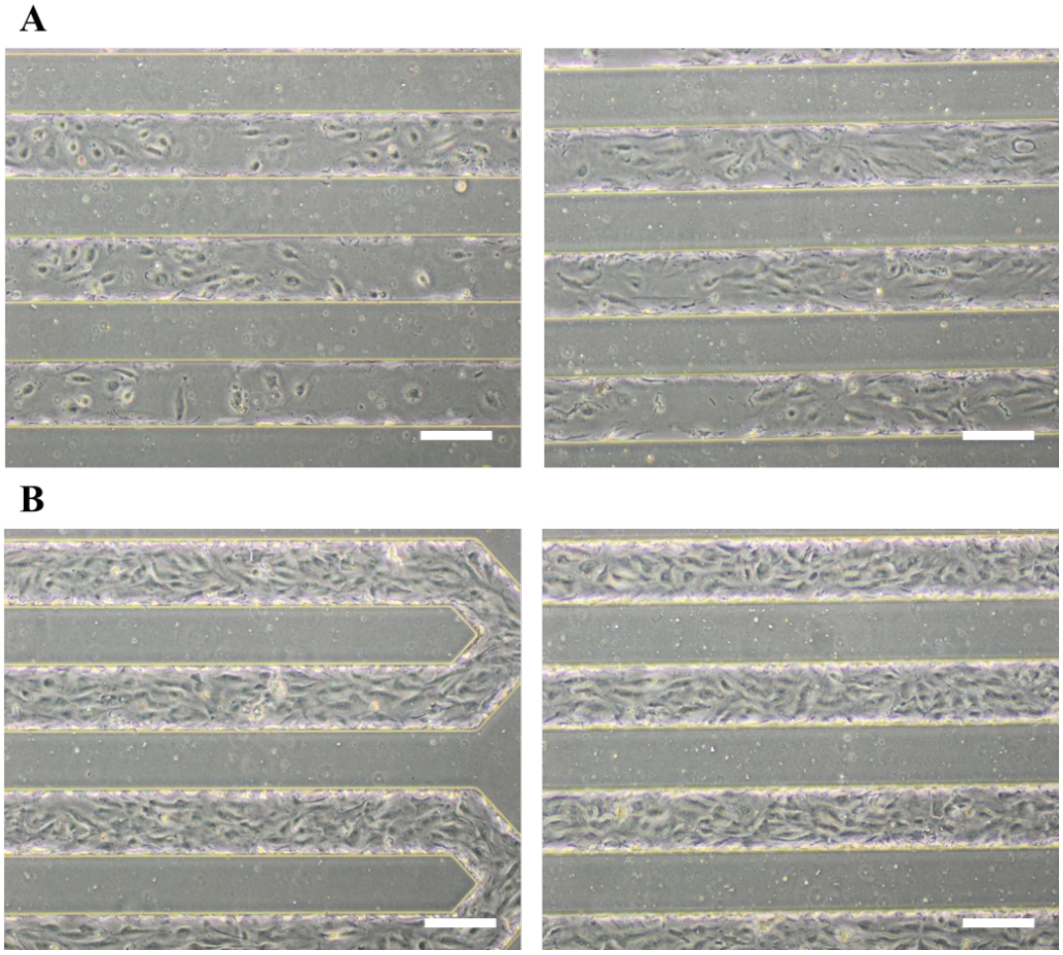

Figure 4.23 Phase contrast images of HBMEC cultured in the device under static (A) or dynamic (5 µl/min) conditions (B) for 24 h. 4X magnification, scalebar: 200 µm.

4.3.4.3 Aβ treatment of human brain primary cells

From the analysis of cell viability, it was observed that $A\beta_{1-42}$ treatment differentially affected the BBB cells when, compared with the control (absence of $A\beta_{1-42}$). In detail, HAs were significantly ($p<0.005$, n=3) affected by the presence of $A\beta_{1-42}$ after only 24 h (Figure 4.24). At the different time points, there is not a significant difference among the different concentrations of the peptide, meaning that even low concentrations can result in toxicity to HAs. Similarly, HBVPs viability was significantly ($p<0.05$, n=3) reduced after 24 h, but only by treatment with high concentrations of $A\beta_{1-42}$ (0.5 and 1 µM) (Figure 4.25), when compared with control. Both MTT assay and Live/Dead assay showed that HBMECs maintained the same viability after 24 h treatment with Aβ1-42, whereas after 48 h treatment a reduction in viability was observed (Figure 4.26). However, when

compared with control, this reduction appears to be statistically significant only with high concentration (1 μM) of Aβ1-42.

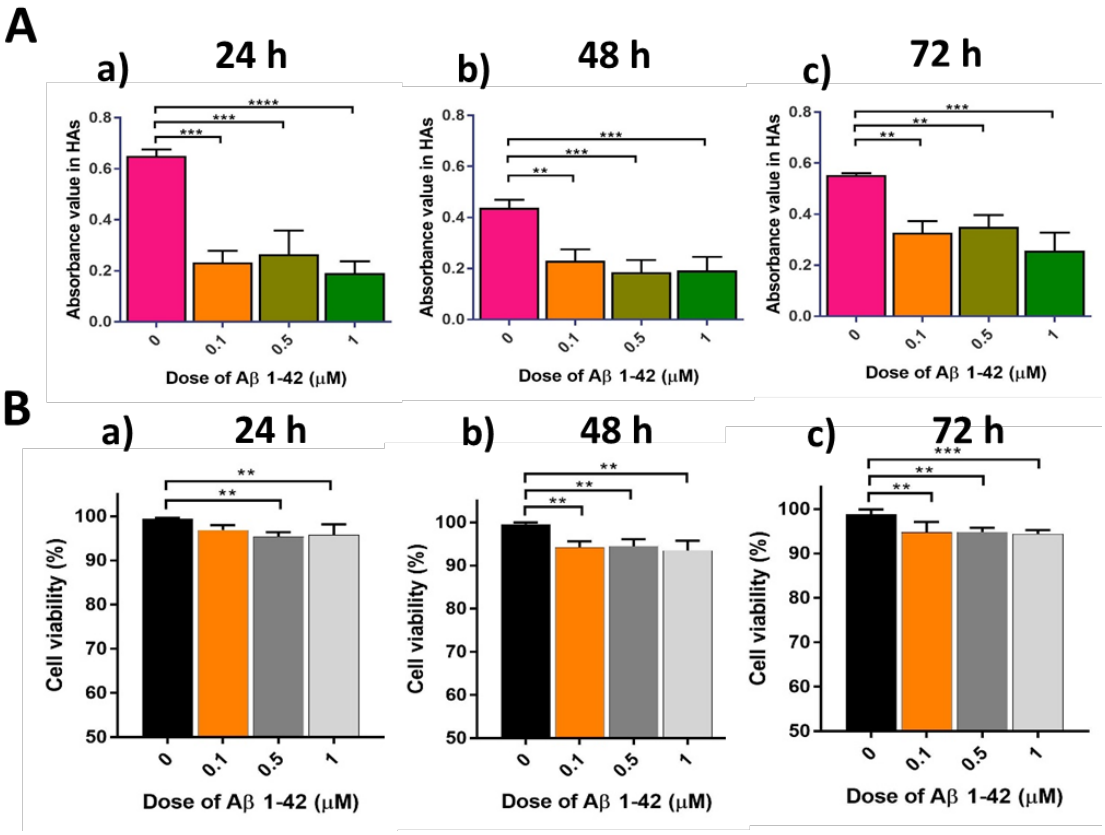

Figure 4.24 Viability of HAs after treatment with different concentrations of $A\beta_{1-42}$ after 24 h (a), 48 h (b) and 72 h (c) measured with A) MTT assay and B) Live/dead cell viability assay.

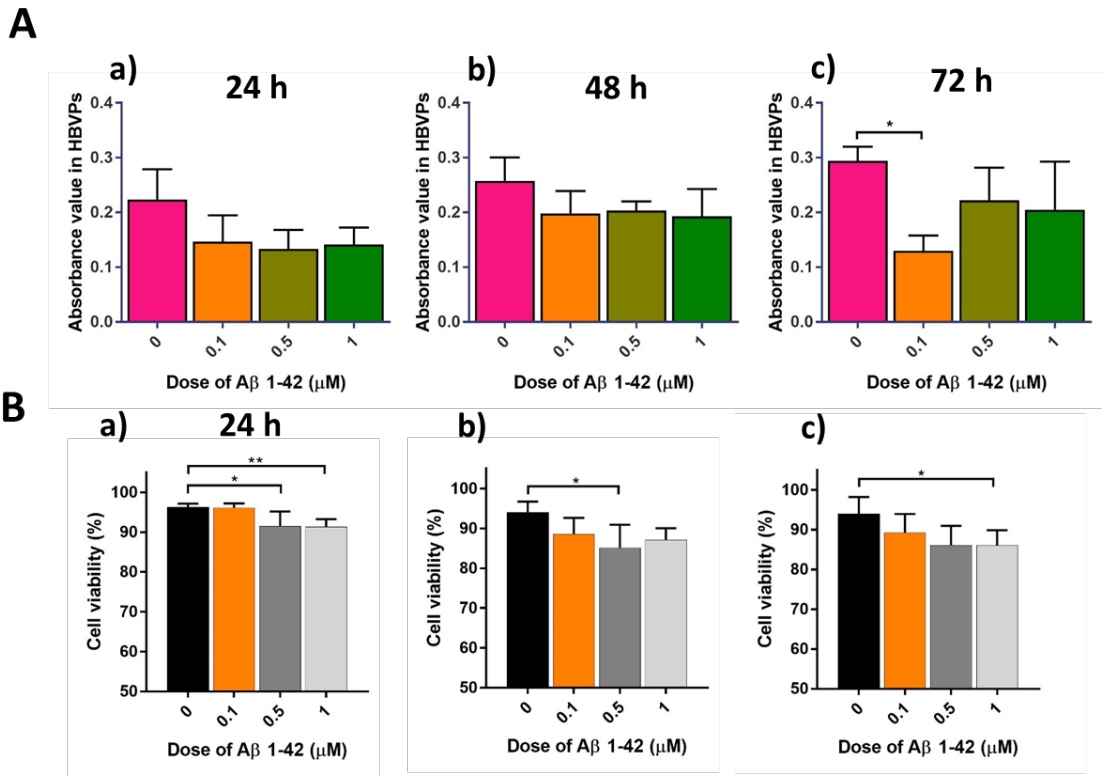

Figure 4.25 Viability of HBVPs after treatment with different concentrations of Aβ1-42 after 24 h (a), 48 h (b) and 72 h (c) measured with A) MTT assay and B) Live/dead cell viability assay.

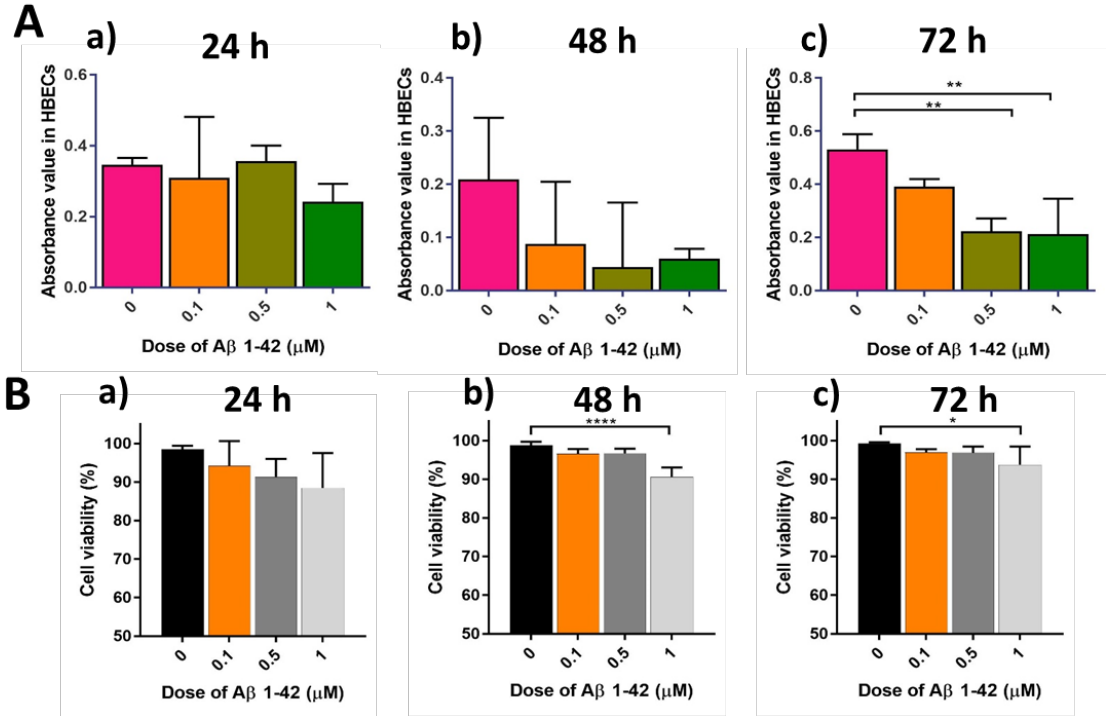

Figure 4.26 Viability of HBMECs after treatment with different concentrations of Aβ1-42 after 24 h (a), 48 h (b) and 72 h (c) measured with A) MTT assay and B) Live/dead cell viability assay.

These results reveal differential toxic effects of Aβ1-42 on the BBB cells. However, further studies are needed to investigate the effect of the peptide on different BBB cell types co-cultured together. Similarly, the presence of the flow, which mimics the physiological blood flow and the *in vivo* microenvironment, should be assessed to further investigate the harmful effect of Aβ1-42 on the BBB.

4.3.4.4 Aβ treatment of HBMECs using flow

Since endothelial cells are the one exposed to shear forces *in vivo*, effects of Aβ1-42 peptide on endothelial cells cultured in the device using flow were investigated. Perfusion culture conditions which provided higher level of shear stresses and increased cell alignment and orientation were used for this experiment. HBMECs were thus cultured in a 200 μm- wide channels device for 24h and then exposed to Aβ1-42 for 24 h using flow or in static conditions. From previous results, it was observed no significant difference among the different peptide concentrations on HBMECs viability. For this reason, in this experiment was used the lowest peptide concentration (0.1 μM), to investigate if even at low concentrations the presence of flow can have an impact on cell viability.

4.3.4.4.1 Live dead assay

HBMECs were cultured in devices and exposed to medium containing Aβ1-42 (0.1 μM) for 24 h in static or under flow (5 μl/min). As a control, cells were cultured in the same conditions using medium without the peptide. To assess HBMECs viability, a cell viability imaging kit was used and cells were imaged with a ZEISS Axiovison fluorescent microscope. Experiments were performed in triplicate (N=3 devices) and repeated three times. Results showed no significant decrease in cell viability after Aβ1-42 treatment for 24 h either in static or dynamic conditions, when compared to control (no treatment) (Figure 4.27). Moreover, Aβ1-42 treatment using flow induced no significant reduction in cell viability compared to static culture. Thus, **the presence of shear forces which mimic those found *in vivo* did not affect HBMECs viability using Aβ1-42 concentration of 0.1 μM.** Further investigations will consider higher concentrations of the peptide as well a longer exposure times.

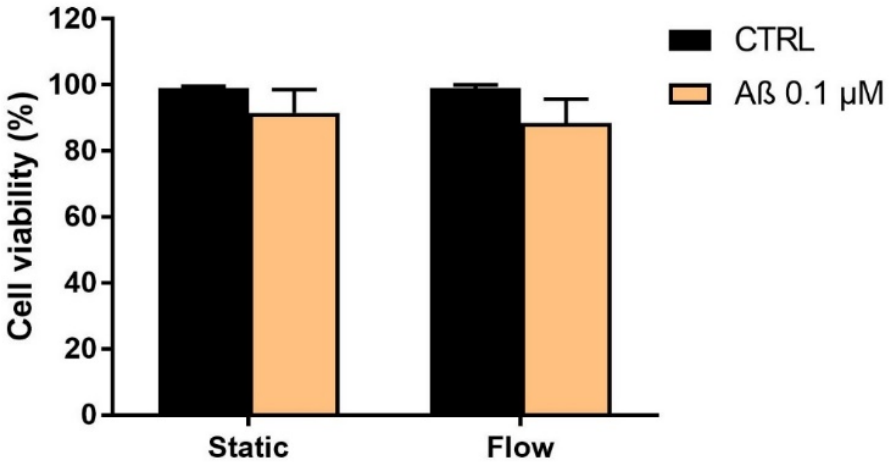

Figure 4.27 HBMECs viability after Aβ1-42 (0.1 µM) treatment using static or perfusion culture.

4.3.4.4.2 ELISA for IL-6, IL-8 and TNF-α

Despite no significant changes in HBMECs viability were observed, measurements of pro-inflammatory and anti-inflammatory cytokines production were carried out to further investigate effects of Aβ1-42. Concentration of cytokines IL-6, IL-8, and TNF- α were measured in spent media samples collected from devices after 24 h dynamic culture (5 µl/min) or static culture using specific ELISA kits (Figure 4.28). Each experiment was repeated four times and each sample was assayed in duplicate. Results showed that IL-6 and IL-8 production were reduced in HBMECs cultured under flow, compared to static. Specifically, IL-6 was significantly reduced when cells were exposed to flow both without Aβ1-42 ($p<0.005$) and with Aβ1-42 ($p<0.05$), when compared to static culture. However, for cells cultured using flow there was no significant decrease in cell viability after Aβ1-42 treatment, compared to control (no treatment). Surprisingly, TNF-α was not detected either in static or flow condition, even though there are no previous studies investigating the expression of this cytokine following Aβ1-42 treatment.

These results showed that **presence of flow might help in reducing inflammation generated by treatment with amyloid peptide or by *in vitro* culture conditions.** Other considerations include that cytokine concentration in effluents collected after perfusion culture might be reduced due to the higher

volume of media used throughout the culture (7.2 mL in dynamic, *vs.* 300 μL in static).

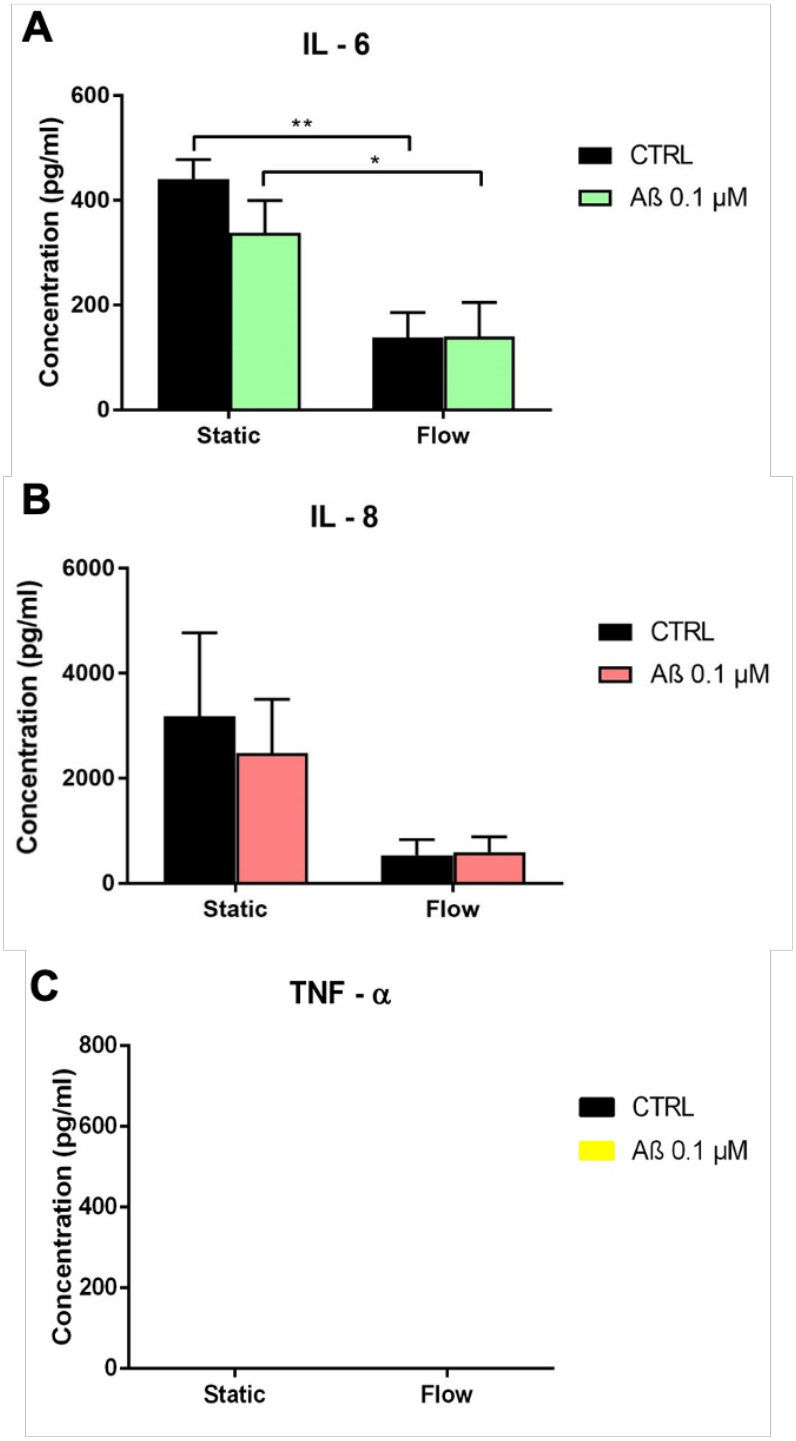

Figure 4.28 ELISA. IL-6 (A), IL-8 (B) and TNF-α (C) concentrations in spent media samples collected from devices in static or perfusion culture, after treatment with Aβ1-42 (0.1 μM) compared to control (0 μM). *p<0.05, **p<0.005

4.4 Summary

This Chapter describes the design, fabrication and development of a microfluidic device for the study of BBB cells. The device was optimized to culture endothelial cells and to induce cell differentiation into a BBB phenotype. Results demonstrated that by culturing endothelial cells in microchannels with a diameter of 200 μm and by using a flow rate of 5 μl/min (flow speed in the channel: 2.6×10^{-4} m/s; shear stress at the wall: 0.18 dyne/cm^2) it was possible to induce cell alignment and elongation in the direction of flow. To further prove the formation of a tightly interconnected endothelial barrier are required additional assessments such as TEER measurements and barrier permeability studies. Those could be implemented by culturing cells on a more complex system which includes two microfluidic chambers separated by a monolayer of endothelial cells cultured on a physical supports such as a permeable membrane.

There is increasing evidence that AD induces complex changes in barrier functions (451), but the individual contribution of BBB cell types in the disease mechanisms is not clear. Thus, another aim of the present work was to explore possible effects of Aβ1-42 peptide on BBB individual cell types under static or dynamic conditions. Aβ1-42 was chosen as a proof of concept, because this fragment has been shown to induce toxicity on neuronal cells (421–423), but its effect on BBB cells (*i.e.,* endothelial cells, astrocytes and pericytes) is poorly understood. In this study, astrocytes were affected by Aβ1-42 exposure after only 24 h under static conditions, whereas endothelial cells and pericytes viability was not affected in the early stages of Aβ1-42 toxicity. Since endothelial cells are the one exposed to shear forces *in vivo*, effects of Aβ1-42 (0.1 μM) peptide on endothelial cells cultured in the device using flow were investigated. After 24 h of culture in the device under dynamic conditions, any effect over the cell viability was observed, suggesting that the presence of shear does not affect Aβ1-42 toxicity. Since studies reported that Aβ1-42 can induce secretion of inflammatory cytokines in BBB cells *in vitro* (427,428), level of IL-6, IL-8 and TNF-α were measured in spent culture medium samples collected from devices. Although no significant differences were observed between treatment (Aβ1-42 0.1μM) and control, there was a significant effect on cytokine production due to the presence of flow. Those results indicate that the concentration of those cytokines might be

affected by the flow rate, media volumes and PDMS absorption, and that the perfusion has a beneficial effect on inflammation. This study represents the first evaluation of Aβ toxicity on brain microvascular endothelial cells cultured in a microfluidic device, and further studies are required to better understand the potential effect of microfluidic culture on BBB cells when treated with the peptide. Moreover, further research is needed to explore the mechanism of action of Aβ1-42 on BBB cells and investigate if different peptide concentrations could determine a decrease in cell viability or could affect the permeability of the BBB.

In conclusion, this microfluidic system provides a viable platform to culture brain microvascular endothelial cells and to test effects of toxic compounds on BBB functions. This model allows the generation of fluidic shear stress without the need of the complex liquid handling systems that are typically used in lab on chip technologies, which is actually one of the biggest obstacles for the widespread use of those technologies. In contrast to currently available BBB microfluidic models, the present system allows to obtain optimal shear stress with low flow rates and reduced perfusion time, with minimal reagent use and optimal cell seeding densities. However, limitations of this platform include the possibility to use only one shear stress at a time, due to channels configuration, and the inlet branching cell loading is not 100% efficient. Further development of the device could be to include multiple primary BBB cell types and to enable the measurement of BBB integrity would allow for the creation a dynamic BBB model to be used for toxicity screening.

Conclusions and Future Work

The emerging growth of microfluidic-based technologies observed over the past two decades have led to the development of innovative 3D cell-culture models. Since the nineties, several microfluidic-based systems have been proposed to support IVF procedures, such as *in vitro* embryo development. However, implantation rates are comparable to conventional culture systems and most of those models still require the use of mineral oil whose quality has been correlated with embryo developmental competence and viability. The main aim of this work was to develop a user-friendly microfluidic device for the culture of murine zygotes to produce viable and competent blastocysts and for complete assessment of their developmental competence. The microfluidic device used to culture mouse embryos described in Chapter 3 was not toxic and able to support embryo development to the blastocysts stage. However, analysis of genetic profile of individual developed blastocysts revealed that the system affected the expression of genes fundamental during embryo development. It is currently unknown whether this could have an effect on embryo quality and there is need of further investigations by increasing the sample size *i.e.,* the number of analyzed blastocysts. Importantly, from the study of metabolic profile of spent embryo culture media was not observed a significant difference between blastocyst developed into the microfluidic device and those cultured using traditional microdrops. Furthermore, this work showed that the use of an improved media consisting on traditional embryo culture media (KSOM) conditioned by uterine epithelial cells for 24 h had the potential to enhance blastocyst development (blastocysts rates in CM were 71.8 ± 4.3%, *vs.* control 54.6 ± 6.6%) and to significantly alter the expression of some of the DNA methylation and genomic imprinting genes. Additionally, untargeted RPLC/MS data showed that metabolic pathways of several amino acids and DNA bases, that have a critical role in embryo development, were enriched for the metabolites consumed by the embryos during culture in microfluidic devices using conditioned media. Therefore, those results revealed that the use of uterine epithelial cells-conditioned media could have a significant impact on embryo developmental competence and quality.

Thus, the main objectives of this research project were successfully achieved since the herein developed microfluidic device supported embryo development and showed developmental rates comparable to those obtained by using traditional embryo culture platforms (blastocysts rates in microfluidic devices were 90.48 ± 3.2%, *vs.* control 86.40 ± 4.6%). Specifically, this microfluidic platform allows to directly visualize morphological changes during embryo growth, due to the material transparency, and to sample spent media for non-invasive analysis of the embryo development. Moreover, it allowed to identify endogenous and exogenous factors as well as organic and inorganic compounds, which may have an impact on embryo growth and competence, in small volume samples of medium by global untargeted mass spectrometry. However, further studies are needed to enable the correlation of these species with normal or altered expression of genes associated with embryo development. It would therefore be interesting to focus on the impact of specific metabolic pathways identified in this study on embryo development and implantation potential. This will allow to clarify how microfluidic culture alters the composition of the culture medium and the embryo's metabolome.

In regard to the specific device design selected for this work, this is currently relatively simple in terms of principle of operation and fabrication methods. That can have a positive impact on the usability of the platform and can reduce time for training for inexperienced embryologist and practitioners which typically use conventional techniques and culture systems. On the other hand, such a simple design does not directly allow for complex culture conditions and real-time and multiparametric monitoring of embryo development. Thus, future works might consider combination of the current microfluidic structure with non-invasive dedicated sensors for on-line measurements of parameters crucial during embryo culture (*e.g.*, pH, oxygen, glucose, temperature).

In terms of future applications of the microfluidic device described in Chapter 3, the design could be adapted to support optimal growth and development of high quality human IVF embryos with the aim to improve the efficiency of assisted reproduction technologies (success rate of human IVF cycles is currently 22-23%). To this intent, pre-clinical evaluation of the efficacy of this device is needed and could be initially performed on IVF-derived bovine embryos as a model for human embryos. If the clinical implementation will reveal successful, such an

innovative system for *in vitro* human embryo culture will aid the current need of new tools and technique to improve outcomes, and optimize efficacy of human IVF cycles and treatment for infertility.

In the second main chapter of this thesis (Chapter 4) is described the design and development of a microfluidic device for the culture of brain microvascular endothelial cells to reproduce the properties of the BBB *in vitro*. The device design was optimized and dynamic culture conditions were implemented testing different flow rates, to induce desired shear stresses on ECs and consequently trigger cell polarization and tightening of the endothelium. Additionally, Aβ1-42 peptide was used as a toxicant model in this study to investigate potential cytotoxic effect on BBB cells at low concentrations. This was performed as a proof of concept investigation which could shed light to the use of this system for testing different toxic agents or drugs of particular interest for the CNS homeostasis.

Overall, the objectives established for this project were largely accomplished since the microfluidic device supported the formation of an endothelial cell layer that was able to align in the direction of flow under optimal shear stress. Additionally, the model was used to study effect of a toxicant agent (Aβ 1-42) on viability of individual BBB cells and could therefore be applied for future BBB toxicology studies. Finally, this platform allows the integration with biochemical analysis of small volume sample collected from the microfluidic device (*i.e.,* ELISA and immunofluorescence staining). Thus, this work provides an informative study for researchers that intend to apply microfluidic technology for generating biological knowledge.

As discussed in Section 4.4 this model might need to be further improved and integrated with additional measurement systems such as TEER for a more comprehensive assessment of barrier functions and stability. In addition, it would be interesting to assess barrier formation by immunocytochemistry to localize other specific tight junction markers expressed by endothelial cells (*e.g.*, ZO-1, CD-31, occludin). Thus, there is still progress to be made in terms of device design and integration of multiparametric analyses, which will aid the development of innovative platforms to study the BBB and the transport of toxic substances into the CNS.

In conclusion, the work described in this thesis showed the development of different microfluidic models for specific applications and their integration with

downstream analysis techniques, which could open the door to future applications in drug screening as well as IVF procedures to be performed *in vitro* under controlled and optimized culture condition.

4.5 Final conclusion and personal perspective

In this thesis I completed the design, fabrication and optimisation of two microfluidic devices that support *in vitro* development of embryonic, glial and endothelial cells in standard or perturbed states. Multiparametric “omic” analyses was performed to evaluate the effect of the microenvironment on the metabolomic, genetic and secretome profiles.

This thesis is intended to serve as a starting point for further applications in medicine and reproductive biology and the presented study aimed to provide an insight into the possible integration of microfluidics over current technologies. To better understand the implications of those results, future research is needed to fully understand the potential of the engineered platforms used in this work and their potential introduction into clinical applications.

From a personal perspective, over the course of this project I had the opportunity to actively participate in different research projects and to learn new techniques and procedures in different disciplines, such as engineering, biology and reproductive biology. With this, I had the chance to have a deep insight into potential and limitations of current microfluidic technology and traditional culture platforms. This allowed the fabrication of in-house microfluidic devices and to use them for culture of either murine embryos or human cells. Additionally, I had the chance to learn a broad range of analytical techniques and to acquire expertise on the analysis of complex datasets. The acquired ability to critically interpret results, experimental data and scientific literature provided an efficient tool to establish progress in this PhD project. Last but not least, the possibility to work in multi-disciplinary and cross-functional teams allowed me to extend my knowledge further from the classical biomedical engineering formation, and from this I also learnt how to communicate results to different audiences, such as engineers and biologists.

Working on this project I had novel insights into the research field I have been working on and I discovered many aspects to carefully take into account when working on scientific research projects. Those include the choice of material

properties and characteristics, the selection of microfabrication techniques, the establishment of culture conditions and analytical techniques to analyse individual cells or culture media.

Together with the acquisition of novel expertise and precious knowledge, I became aware of the limits of this technology and available methods. In the process of development of new technologies there are indeed many aspects to take into account. As it is complex to think about a new design, likewise it is difficult to have the system fully working and available to other practitioners and biologists. Also, testing the device with various species is not straightforward and require adjustments in the procedures and experimental plans. For instance, for the use of human samples is required the approval of specific and very detailed ethical procedures. Moreover, the need for a reproducible and repeatable fabrication process and culture procedure is fundamental and often not simple to achieve. Finally, it might result difficult to combine knowledge from cross-functional area of research and generate protocols and results that can be fully understand to diverse researcher profiles.

At the same time, this study also shed light on limitations already in place in this area of research which are actually limiting the widespread use of those models. For instance, is currently very unlikely the possibility to use PDMS-based microfluidic chip in clinical environment and medical practices. Thus, this further drive the need of novel materials, which could ideally be simultaneously effective and eco-friendly.

Despite the huge potential of those models, it has to be taken into consideration that currently it can result very critical to see a direct application of these models into the clinic or to have access to clinical trials. A first step towards this will be the commercialization of the device to make it available to a broader range of users and applications with mammalian embryos. Next, it has to be adapted to culture human embryos so that could potentially be introduced into human IVF clinics practice.

As a final remark, I would like to express my personal enthusiasm over the potential of those systems. Even though there is much work to do and much progress to achieve, the future applications in IVF or toxicology studies for the NCS are mind-blowing. It is absolutely exciting to think that in the near future similar platforms could really help medical research and implement techniques

and procedures currently not efficient, thus have a direct effect on people health and lives.

List of references

1. Huh D, Hamilton GA, Ingber DE. From 3D cell culture to organs-on-chips. Trends Cell Biol. 2011;21(12):745–54.
2. Sackmann EK, Fulton AL, Beebe DJ. The present and future role of microfluidics in biomedical research. Nature. 2014;507(7491):181–9.
3. Li R, Lv X, Zhang X, Saeed O, Deng Y. Microfluidics for cell-cell interactions: A review. Front Chem Sci Eng. 2016;10(1):90–8.
4. Auroux PA, Iossifidis D, Reyes DR, Manz A. Micro total analysis systems. 2. Analytical standard operations and applications. Anal Chem. 2002 Jun 15;74(12):2637–52.
5. Ohno K, Tachikawa K, Manz A. Microfluidics: Applications for analytical purposes in chemistry and biochemistry. Electrophoresis. 2008 Nov 1;29(22):4443–53.
6. Jakeway SC, De Mello AJ, Russell EL. Miniaturized total analysis systems for biological analysis. Fresenius J Anal Chem. 2000;366(6–7):525–39.
7. Yu Z, Lu S, Huang Y. Microfluidic whole genome amplification device for single cell sequencing. Anal Chem. 2014 Oct 7;86(19):9386–90.
8. Lion N, Rohner TC, Dayon L, Arnaud IL, Damoc E, Youhnovski N, et al. Microfluidic systems in proteomics. Electrophoresis. 2003 Nov 1;24(21):3533–62.
9. Lenshof A, Laurell T. Emerging Clinical Applications of Microchip-Based Acoustophoresis. J Lab Autom. 2011 Dec 1;16(6):443–9.
10. Wlodkowic D, Cooper JM. Microfluidic cell arrays in tumor analysis: New prospects for integrated cytomics. Expert Rev Mol Diagn. 2010 May;10(4):521–30.
11. Hatch A, Hansmann G, Murthy SK. Engineered alginate hydrogels for effective microfluidic capture and release of endothelial progenitor cells from whole blood. Langmuir. 2011 Apr 5;27(7):4257–64.
12. Gray BL, Lieu DK, Collins SD, Smith RL, Barakat AI. Microchannel Platform for the Study of Endothelial Cell Shape and Function. Biomed Microdevices. 2002;4(1):9–16.
13. Reece A, Xia B, Jiang Z, Noren B, McBride R, Oakey J. Microfluidic techniques for high throughput single cell analysis. Curr Opin Biotechnol. 2016 Aug 1;40:90–6.
14. Huh D, Leslie DC, Matthews BD, Fraser JP, Jurek S, Hamilton G a, et al. A Human Disease Model of Drug Toxicity – Induced Pulmonary Edema in a Lung-on-a-Chip Microdevice. Sci Transl Med. 2012;4(159):1–9.
15. Kim HJ, Huh D, Hamilton G, Ingber DE. Human gut-on-a-chip inhabited by microbial flora that experiences intestinal peristalsis-like motions and flow. Lab Chip. 2012;12(12):2165.
16. van Duinen V, Trietsch SJ, Joore J, Vulto P, Hankemeier T. Microfluidic 3D

cell culture: From tools to tissue models. Curr Opin Biotechnol. 2015 Dec 1;35:118–26.

17. Booth R, Noh S, Kim H. A multiple-channel, multiple-assay platform for characterization of full-range shear stress effects on vascular endothelial cells. Lab Chip. 2014 Jun 7;14(11):1880–90.

18. Squires TM, Quake SR. Microfluidics: Fluid physics at the nanoliter scale. Rev Mod Phys. 2005 Jul 6;77(3):977–1026.

19. Halldorsson S, Lucumi E, Gómez-Sjöberg R, Fleming RMT. Advantages and challenges of microfluidic cell culture in polydimethylsiloxane devices. Biosens Bioelectron. 2015;63:218–31.

20. Gupta N, Liu JR, Patel B, Solomon DE, Vaidya B, Gupta V. Microfluidics-based 3D cell culture models: Utility in novel drug discovery and delivery research. Bioeng Transl Med. 2016 Mar 1;1(1):63–81.

21. Inamdar NK, Borenstein JT. Microfluidic cell culture models for tissue engineering. Curr Opin Biotechnol. 2011;22(5):681–9.

22. Kim L, Toh Y-C, Voldman J, Yu H. A practical guide to microfluidic perfusion culture of adherent mammalian cells. Lab Chip. 2007 May 30;7(6):681.

23. Toh YC, Zhang C, Zhang J, Khong YM, Chang S, Samper VD, et al. A novel 3D mammalian cell perfusion-culture system in microfluidic channels. Lab Chip. 2007 Mar 1;7(3):302–9.

24. Irimia D, Liu SY, Tharp WG, Samadani A, Toner M, Poznansky MC. Microfluidic system for measuring neutrophil migratory responses to fast switches of chemical gradients. Lab Chip. 2006 Jan 31;6(2):191–8.

25. Wei-Cheng T, Finehout E. Microfluidics for Biological Applications. Vol. 16, Springer Science & Business Media. 2009.

26. Jang K-J, Suh K-Y. A multi-layer microfluidic device for efficient culture and analysis of renal tubular cells. Lab Chip. 2010;10(1):36–42.

27. Galbraith CG, Sheetz MP. A micromachined device provides a new bend on fibroblast traction forces. Proc Natl Acad Sci U S A. 1997 Aug 19;94(17):9114–8.

28. Shamloo A, Ma N, Poo MM, Sohn LL, Heilshorn SC. Endothelial cell polarization and chemotaxis in a microfluidic device. Lab Chip. 2008 Jul 24;8(8):1292–9.

29. Van Engeland NCA, Pollet AMAO, Den Toonder JMJ, Bouten CVC, Stassen OMJA, Sahlgren CM. A biomimetic microfluidic model to study signalling between endothelial and vascular smooth muscle cells under hemodynamic conditions. Lab Chip. 2018 Jun 7;18(11):1607–20.

30. Rothbauer M, Zirath H, Ertl P. Recent advances in microfluidic technologies for cell-to-cell interaction studies. Lab Chip. 2018 Jan 21;18(2):249–70.

31. Walker GM, Zeringue HC, Beebe DJ. Microenvironment design considerations for cellular scale studies. Lab Chip. 2004;4(2):91.

32. Whitesides GM. The origins and the future of microfluidics. Nature. 2006;442(7101):368–73.

33. Brody JP, Yager P, Goldstein RE, Austin RH. Biotechnology at Low Reynolds Numbers. Biophys J. 1996;71(6):3430–41.

34. White FM. Fluid Mechanics. McGraw-Hill, New York, NY, 7th edition edition; 2011.

35. Gravesen P, Branebjerg J, Jensen OS. Microfluidics-a review. J micromechanics microengineering. 1993;3(3):168–82.

36. Beebe DJ, Mensing GA, Walker GM. Physics and Applications of Microfluidics in Biology. Annu Rev Biomed Eng. 2002 Aug 28;4(1):261–86.

37. Bettinger C, Borenstein JT, Tao SL. Microfluidic Cell Culture Systems. Microfluidic Cell Culture Systems. Elsevier Inc.; 2012. 1–433 p.

38. Deen WM. Analysis of transport phenomena. New York, NY: Oxford University Press; 1998.

39. Oh K, And CA. A review of microvalves. J micromechanics microengineering. 2006;16(5):R13.

40. Lu H, Koo LY, Wang WM, Lauffenburger DA, Griffith LG, Jensen KF. Microfluidic shear devices for quantitative analysis of cell adhesion. Anal Chem. 2004 Sep 15;76(18):5257–64.

41. Korin N, Bransky A, Dinnar U, Levenberg S. A parametric study of human fibroblasts culture in a microchannel bioreactor. Lab Chip. 2007 May 2;7(5):611–7.

42. Maluf N, Williams K. Introduction to Microelectromechanical Systems Engineering. Artech House. 2004.

43. Becker H, Locascio LE. Polymer microfluidic devices. Talanta. 2002 Feb 11;56(2):267–87.

44. Madou MJ. Fundamentals of Microfabrication and Nanotechnology. CRC Press; 2018.

45. Xia Y, McClelland JJ, Gupta R, Qin D, Zhao X-M, Sohn LL, et al. Replica molding using polymeric materials: A practical step toward nanomanufacturing. Adv Mater. 1997 Feb 1;9(2):147–9.

46. Kricka LJ, Fortina P, Panaro NJ, Wilding P, Alonso-Amigo G, Becker H. Fabrication of plastic microchips by hot embossing. Lab Chip. 2002 Feb 1;2(1):1–4.

47. Shiu, Pun-Pang et al. Rapid fabrication of tooling for microfluidic devices via laser micromachining and hot embossing. J Micromechanics Microengineering. 2008;18(2):025012.

48. Giboz J, Copponnex T, Mélé P. Microinjection molding of thermoplastic polymers: a review. J Micromechanics Microengineering. 2007;17(6):R96.

49. Gale B, Jafek A, Lambert C, Goenner B, Moghimifam H, Nze U, et al. A Review of Current Methods in Microfluidic Device Fabrication and Future Commercialization Prospects. Inventions. 2018 Aug 28;3(3):60.

50. Becker H, Gärtner C. Polymer microfabrication methods for microfluidic analytical applications. Electrophoresis. 2000 Jan 1;21(1):12–26.

51. Abgrall P, Gue A. Lab-on-chip technologies: making a microfluidic network and coupling it into a complete microsystem—a review. J Micromechanics Microengineering. 2007 Apr 24;17(5):R15.

52. Waldbaur A, Rapp H, Länge K, Methods BR-A, 2011 U. Let there be chip—towards rapid prototyping of microfluidic devices: one-step manufacturing processes. Anal Methods. 2011;3(12):2681–716.

53. Waheed S, Cabot JM, Macdonald NP, Lewis T, Guijt RM, Paull B, et al. 3D printed microfluidic devices: Enablers and barriers. Lab Chip. 2016 May 24;16(11):1993–2013.

54. Xia Y. Soft Lithography. Annu Rev Mater Sci. 1998;28(1):153–84.

55. Qin D, Xia Y, Whitesides GM. Soft lithography for micro- and nanoscale patterning. Nat Protoc. 2010;5(3):491–502.

56. Linder V, Wu H, Jiang X, Whitesides GM. Rapid prototyping of 2D structures with feature sizes larger than 8 μm. Anal Chem. 2003 May 15;75(10):2522–7.

57. Faustino V, Catarino SO, Lima R, Minas G. Biomedical microfluidic devices by using low-cost fabrication techniques: A review. J Biomech. 2016 Jul 26;49(11):2280–92.

58. Whitesides GM, Ostuni E, Jiang X, Ingber DE. Soft Lithography in Biology and Biochemistry. Annu Rev Biomed Eng. 2001;3:335–73.

59. Delamarche E, Bernard A, Schmid H, Bietsch A, Michel B, Biebuyck H. Microfluidic networks for chemical patterning of substrates: Design and application to bioassays. J Am Chem Soc. 1998 Jan 28;120(3):500–8.

60. Martin RS, Gawron AJ, Lunte SM, Henry CS. Dual-electrode electrochemical detection for poly(dimethylsiloxane)-fabricated capillary electrophoresis microchips. Anal Chem. 2000 Jul 15;72(14):3196–202.

61. Schmid H, Michel B. Siloxane polymers for high-resolution, high-accuracy soft lithography. Macromolecules. 2000 Apr 18;33(8):3042–9.

62. Chaudhury MK, Whitesides GM. Direct Measurement of Interfacial Interactions between Semispherical Lenses and Flat Sheets of Poly(dimethylsiloxane) and Their Chemical Derivatives. Langmuir. 1991 May 22;7(5):1013–25.

63. Gale BK, Eddings MA, Sundberg SO, Hatch A, Kim J, Ho T, et al. Low-Cost MEMS Technologies. In: Reference Module in Materials Science and Materials Engineering. Elsevier; 2016.

64. Jessamine Ng Lee, Xingyu Jiang, Declan Ryan A, Whitesides* GM. Compatibility of Mammalian Cells on Surfaces of Poly(dimethylsiloxane). Langmuir. 2004;20(26):11684–91.

65. Tan SH, Nguyen NT, Chua YC, Kang TG. Oxygen plasma treatment for reducing hydrophobicity of a sealed polydimethylsiloxane microchannel. Biomicrofluidics. 2010;4(3):1–8.

66. Fritz JL, Owen MJ. Hydrophobic recovery of plasma-treated polydimethylsiloxane. J Adhes. 1995;54(1–4):33–45.

67. Duffy DC, McDonald JC, Schueller OJA, Whitesides GM. Rapid prototyping of microfluidic systems in poly(dimethylsiloxane). Anal Chem. 1998 Dec 1;70(23):4974–84.

68. Bodas D, Khan-Malek C. Hydrophilization and hydrophobic recovery of PDMS by oxygen plasma and chemical treatment-An SEM investigation. Sensors Actuators, B Chem. 2007 Apr 10;123(1):368–73.

69. Lake MA, Narciso CE, Cowdrick KR, Storey TJ, Zhang S, Zartman JJ, et al. Microfluidic device design, fabrication, and testing protocols. Protoc Exch. 2015;

70. Delamarche E, Schmid H, Michel B, Biebuyck H. Stability of molded polydimethylsiloxane microstructures. Adv Mater. 1997 Jul 4;9(9):741–6.

71. Regehr KJ, Domenech M, Koepsel JT, Carver KC, Ellison-Zelski SJ, Murphy WL, et al. Biological implications of polydimethylsiloxane-based microfluidic cell culture. Lab Chip. 2009;9(15):2132.

72. Lee JN, Park C, Whitesides GM. Solvent Compatibility of Poly(dimethylsiloxane)-Based Microfluidic Devices. Anal Chem. 2003;75(23):6544–54.

73. Sasaki H, Onoe H, Osaki T, Kawano R, Takeuchi S. Parylene-coating in PDMS microfluidic channels prevents the absorption of fluorescent dyes. Sensors Actuators, B Chem. 2010 Oct 21;150(1):478–82.

74. Ren K, Zhao Y, Su J, Ryan D, Wu H. Convenient method for modifying poly(dimethylsiloxane) to be airtight and resistive against absorption of small molecules. Anal Chem. 2010 Jul 15;82(14):5965–71.

75. Berthier E, Young EWK, Beebe D. Engineers are from PDMS-land, Biologists are from Polystyrenia. Lab Chip. 2012 Mar;12(7):1224.

76. Young EWK, Beebe DJ. Fundamentals of microfluidic cell culture in controlled microenvironments. Chem Soc Rev. 2010;39(3):1036.

77. Brinster RL. Studies on the development of mouse embryos in vitro. I. The effect of osmolarity and hydrogen ion concentration. J Exp Zool. 1965 Feb 1;158(1):49–57.

78. Takagi M, Hayashi H, Yoshida T. The effect of osmolarity on metabolism and morphology in adhesion and suspension chinese hamster ovary cells producing tissue plasminogen activator. Cytotechnology. 2000;32(3):171–9.

79. Yun SH, Cabrera LM, Song JW, Futai N, Tung YC, Smith GD, et al. Characterization and resolution of evaporation-mediated osmolality shifts that constrain microfluidic cell culture in poly(dimethylsiloxane) devices. Anal Chem. 2007 Feb 1;79(3):1126–34.

80. Chisti Y. Hydrodynamic damage to animal cells. Crit Rev Biotechnol. 2001;21(2):67–110.

81. Mohammed MI, Haswell S, Gibson I. Lab-on-a-chip or Chip-in-a-lab: Challenges of Commercialization Lost in Translation. Procedia Technol. 2015;20:54–9.

82. Becker H. Chips, money, industry, education and the “killer application.”

Lab Chip. 2009 Jun 21;9(12):1659–60.

83. Jeon JS, Chung S, Kamm RD, Charest JL. Hot embossing for fabrication of a microfluidic 3D cell culture platform. Biomed Microdevices. 2011 Apr 27;13(2):325–33.

84. Huang J-H, Kim J, Agrawal N, Sudarsan AP, Maxim JE, Jayaraman A, et al. Rapid Fabrication of Bio-inspired 3D Microfluidic Vascular Networks. Adv Mater. 2009 Sep 18;21(35):3567–71.

85. Ogończyk D, Wgrzyn J, Jankowski P, Dąbrowski B, Garstecki P. Bonding of microfluidic devices fabricated in polycarbonate. Lab Chip. 2010 May 5;10(10):1324–7.

86. Ongaro AE, Di Giuseppe D, Kermanizadeh A, Miguelez Crespo A, Mencattini A, Ghibelli L, et al. Polylactic is a sustainable, low absorption, low auto-fluorescence, alternative to other plastics for Microfluidic and Organ-On-Chip applications. Anal Chem. 2020 Apr 1;92(9):6693–701.

87. Chen CS, Breslauer DN, Luna JI, Grimes A, Chin WC, Lee LP, et al. Shrinky-Dink microfluidics: 3D polystyrene chips. Lab Chip. 2008 Mar 27;8(4):622–4.

88. Wu MH, Huang S Bin, Lee G Bin. Microfluidic cell culture systems for drug research. Lab Chip. 2010 Apr 1;10(8):939–56.

89. Lee P, Ghorashian N, Gaige T, Hung P. Microfluidic System for Automated Cell-Based Assays. J Assoc Lab Autom. 2007 Dec 27;12(6):363–7.

90. Reichen M, Veraitch FS, Szita N. Development of a multiplexed microfluidic platform for the automated cultivation of embryonic stem cells. J Lab Autom. 2013 Dec 22;18(6):519–29.

91. Bhatia SN, Ingber DE. Microfluidic organs-on-chips. Nat Biotechnol. 2014;32(8):760–72.

92. Kola I, Landis J. Can the pharmaceutical industry reduce attrition rates? Nat Rev Drug Discov. 2004 Aug;3(8):711–5.

93. Adams CP, Van Brantner V. Market watch : Estimating the cost of new drug development: Is it really $802 million? Health Aff. 2006 Mar 2;25(2):420–8.

94. Mullard A. 2017 FDA drug approvals. 2018;

95. Esch MB, King TL, Shuler ML. The Role of Body-on-a-Chip Devices in Drug and Toxicity Studies. Annu Rev Biomed Eng. 2011;13(1):55–72.

96. LaBonia GJ, Lockwood SY, Heller AA, Spence DM, Hummon AB. Drug penetration and metabolism in 3D cell cultures treated in a 3D printed fluidic device: assessment of irinotecan via MALDI imaging mass spectrometry. Proteomics. 2016 Jun 1;16(11–12):1814–21.

97. Lei KF, Chang CH, Chen MJ. Paper/PMMA Hybrid 3D Cell Culture Microfluidic Platform for the Study of Cellular Crosstalk. ACS Appl Mater Interfaces. 2017 Apr 19;9(15):13092–101.

98. Kim JH, Park JY, Jin S, Yoon S, Kwak J-Y, Jeong YH. A Microfluidic Chip Embracing a Nanofiber Scaffold for 3D Cell Culture and Real-Time Monitoring. Nanomaterials. 2019 Apr 10;9(4):588.

99. Xiao S, Coppeta JR, Rogers HB, Isenberg BC, Zhu J, Olalekan SA, et al. A microfluidic culture model of the human reproductive tract and 28-day menstrual cycle. Nat Commun. 2017;8:1–13.

100. Huh D, Matthews BD, Mammoto A, Montoya-Zavala M, Yuan Hsin H, Ingber DE. Reconstituting organ-level lung functions on a chip. Science (80-). 2010 Jun 25;328(5986):1662–8.

101. Lee PJ, Hung PJ, Lee LP. An artificial liver sinusoid with a microfluidic endothelial-like barrier for primary hepatocyte culture. Biotechnol Bioeng. 2007 Aug 1;97(5):1340–6.

102. Jang KJ, Suh KY. A multi-layer microfluidic device for efficient culture and analysis of renal tubular cells. Lab Chip. 2010 Jan 7;10(1):36–42.

103. Wilmer MJ, Ng CP, Lanz HL, Vulto P, Suter-Dick L, Masereeuw R. Kidney-on-a-Chip Technology for Drug-Induced Nephrotoxicity Screening. Trends Biotechnol. 2016 Feb 1;34(2):156–70.

104. Agarwal A, Goss JA, Cho A, McCain ML, Parker KK. Microfluidic heart on a chip for higher throughput pharmacological studies. Lab Chip. 2013 Sep 21;13(18):3599–608.

105. Griep LM, Wolbers F, De Wagenaar B, Ter Braak PM, Weksler BB, Romero IA, et al. BBB on CHIP: Microfluidic platform to mechanically and biochemically modulate blood-brain barrier function. Biomed Microdevices. 2013 Feb 6;15(1):145–50.

106. Li WX, Liang GT, Yan W, Zhang Q, Wang W, Zhou XM, et al. Artificial uterus on a microfluidic chip. Fenxi Huaxue/ Chinese J Anal Chem. 2013;41(4):467–72.

107. Gnecco JS, Pensabene V, Li DJ, Ding T, Hui EE, Bruner-Tran KL, et al. Compartmentalized Culture of Perivascular Stroma and Endothelial Cells in a Microfluidic Model of the Human Endometrium. Ann Biomed Eng. 2017;45(7):1758–69.

108. Laronda MM, Rutz AL, Xiao S, Whelan KA, Duncan FE, Roth EW, et al. A bioprosthetic ovary created using 3D printed microporous scaffolds restores ovarian function in sterilized mice. Nat Commun. 2017;8(May):1–10.

109. Mancini V, Pensabene V. Organs-On-Chip Models of the Female Reproductive System. Bioengineering. 2019 Nov 7;6(4):103.

110. European Commission. Directorate-General for Employment SA and I, Statistical Office of the European Communities. Short analytical web note : demography report. Publications Office; 2015.

111. Kupka MS, Ferraretti AP, De Mouzon J, Erb K, D'hooghe T, Castilla JA, et al. Assisted reproductive technology in Europe, 2010: results generated from European registers by ESHRE †. Hum Reprod. 2014;29(10):2099–113.

112. Gardner DK, Vella P, Lane M, Wagley L, Schlenker T, Schoolcraft WB. Culture and transfer of human blastocysts increases implantation rates and reduces the need for multiple embryo transfers. Fertil Steril. 1998 Jan 1;69(1):84–8.

113. Thompson JG, Kind KL, Roberts CT, Robertson SA, Robinson JS. DEBATE-continued Epigenetic risks related to assisted reproductive technologies Short-and long-term consequences for the health of children conceived through assisted reproduction technology: more reason for caution? Vol. 17, Human Reproduction. 2002.

114. Taft RA. Virtues and limitations of the preimplantation mouse embryo as a model system. Theriogenology. 2008 Jan 1;69(1):10–6.

115. Waterston RH, Lander ES, Sulston JE. On the sequencing of the human genome. Proc Natl Acad Sci. 2002;99(6).

116. Ménézo YJR, Hérubel F. Mouse and bovine models for human IVF. Reprod Biomed Online. 2002 Jan 1;4(2):170–5.

117. Quinn P, Horstman FC. Is the mouse a good model for the human with respect to the development of the preimplantation embryo in vitro? Hum Reprod. 1998;13:173–83.

118. Silver L. Mouse genetics: concepts and applications. Oxford University Press; 1995.

119. Robinson NB, Krieger K, Khan F, Huffman W, Chang M, Naik A, et al. The current state of animal models in research: A review. Int J Surg. 2019 Dec 1;72:9–13.

120. Duran AL, Potter P, Wells S, Kirkwood T, Von Zglinicki T, McArdle A, et al. Shared Ageing Research Models (ShARM): A new facility to support ageing research. Biogerontology. 2013 Dec;14(6):789–94.

121. Yuan R, Peters LL, Paigen B. Mice as a Mammalian Model for Research on the Genetics of Aging. ILAR J. 2011 Jan 1;52(1):4–15.

122. Drost R, Jonkers J. Opportunities and hurdles in the treatment of BRCA1-related breast cancer. Oncogene. 2014 Jul 17;33(29):3753–63.

123. Drost RM, Jonkers J. Preclinical mouse models for BRCA1-associated breast cancer. Br J Cancer. 2009 Nov;101(10):1651–7.

124. Barr J, Vázquez-Chantada M, Alonso C, Pérez-Cormenzana M, Mayo R, Galán A, et al. Liquid Chromatography−Mass Spectrometry-Based Parallel Metabolic Profiling of Human and Mouse Model Serum Reveals Putative Biomarkers Associated with the Progression of Nonalcoholic Fatty Liver Disease. J Proteome Res. 2010 Sep 3;9(9):4501–12.

125. von Herrath M, Nepom GT. Remodeling rodent models to mimic human type 1 diabetes. Eur J Immunol. 2009 Aug;39(8):2049–54.

126. Brinster RL. A Method for in vitro cultivation of mouse ova from two-cell to blastocyst. Exp Cell Res. 1963;32(1):205–8.

127. Bin Ali R, van der Ahé F, Braumuller TM, Pritchard C, Krimpenfort P, Berns A, et al. Improved pregnancy and birth rates with routine application of nonsurgical embryo transfer. Transgenic Res. 2014;23(4):691–5.

128. Mahabir E, Volland R, Landsberger A, Manz S, Na E, Urban I, et al. Reproductive Performance after Unilateral or Bilateral Oviduct Transfer of 2-Cell Embryos in Mice. J Am Assoc Lab Anim Sci. 2018;57(2):110–4.

129. Rossant P. J& T. Mouse Development, Patterning, Morphogenesis, and Organogenesis. Acad Press. 2002;136(1):371–89.

130. Minot CS. A laboratory text-book of embryology. Nabu Press; 2011.

131. Kovacs G, Rutherford A, Gardner DK. How to Prepare the Egg and Embryo to Maximize IVF Success. Cambridge University Press; 2019.

132. Canseco RS, Sparks AET, Pearson RE, Gwazdauskas FC. Embryo density and medium volume effects on early murine embryo development. J Assist Reprod Genet. 1992 Oct;9(5):454–7.

133. Gopichandran N, Leese HJ. The effect of paracrine/autocrine interactions on the in vitro culture of bovine preimplantation embryos. Reproduction. 2006;131:269–77.

134. Richter KS. The importance of growth factors for preimplantation embryo development and in-vitro culture. Curr Opin Obstet Gynecol. 2008 Jun;20(3):292–304.

135. Paria BC, Dey SK. Preimplantation embryo development in vitro: Cooperative interactions among embryos and role of growth factors. Proc Natl Acad Sci U S A. 1990;87(12):4756–60.

136. Lane M, Gardner DK. Effect of incubation volume and embryo density on the development and viability of mouse embryos in vitro. Hum Reprod. 1992 Apr;7(4):558–62.

137. Vajta G, Peura TT, Holm P, Paldi A, Greve T, Trounson AO, et al. New method for culture of zona-included or zona-free embryos: The Well of the Well (WOW) system. Mol Reprod Dev. 2000 Mar 1;55(3):256–64.

138. Thouas GA, Jones GM, Trounson AO. The “GO” system-A novel method of microculture for in vitro development of mouse zygotes to the blastocyst stage. Reproduction. 2003;126:161–9.

139. Abdullah JABM. Continuous ultra micro-drop (cUMD) culture yields higher pregnancy and implantation rates than either larger-drop culture or fresh-medium replacement. Clin Embryol. 2004;(7):1–23.

140. Sugimura S, Akai T, Somfai T, Hirayama M, Aikawa Y, Ohtake M, et al. Time-Lapse Cinematography-Compatible Polystyrene-Based Microwell Culture System: A Novel Tool for Tracking the Development of Individual Bovine Embryos1. Biol Reprod. 2010 Dec 1;83(6):970–8.

141. Swain JE, Smith GD. Advances in embryo culture platforms: Novel approaches to improve preimplantation embryo development through modifications of the microenvironment. Hum Reprod Update. 2011;17(4):541–57.

142. Sakkas D, Katz JM, Sueldo CE. Gamete and Embryo Selection Genomics, Metabolomics and Morphological Assessment. Springer New York Heidelberg Dordrecht London; 2014.

143. Kim J, Kim SH, Jun JH. Prediction of blastocyst development and implantation potential in utero based on the third cleavage and compaction times in mouse pre-implantation embryos. J Reprod Dev. 2017;63(2):117–25.

144. Sakkas D, Gardner DK. Noninvasive methods to assess embryo quality. Curr Opin Obstet Gynecol. 2005 Jun;17(3):283–8.

145. Leese HJ. Metabolism of the preimplantation embryo: 40 Years on. Reproduction. 2012;143(4):417–27.

146. Sturmey RG, Brison DR, Leese HJ. Assessing embryo viability by measurement of amino acid turnover. Reprod Biomed Online. 2008 Jan 1;17(4):486–96.

147. Houghton FD, Thompson JG, Kennedy CJ, Leese HJ. Oxygen consumption and energy metabolism of the early mouse embryo. Mol Reprod Dev. 1996 Aug 1;44(4):476–85.

148. Leese HJ. What does an embryo need? Hum Fertil. 2003;6(4):180–5.

149. Israel S, Ernst M, Psathaki OE, Drexler HCA, Casser E, Suzuki Y, et al. An integrated genome-wide multi-omics analysis of gene expression dynamics in the preimplantation mouse embryo. Sci Rep. 2019 Dec 1;9(1):1–15.

150. Fu Z, Wang B, Wang S, Wu W, Wang Q, Chen Y, et al. Integral Proteomic Analysis of Blastocysts Reveals Key Molecular Machinery Governing Embryonic Diapause and Reactivation for Implantation in Mice1. Biol Reprod. 2014 Mar 1;90(3):52–1.

151. Katz-Jaffe MG, McReynolds S, Gardner DK, Schoolcraft WB. The role of proteomics in defining the human embryonic secretome. Mol Hum Reprod. 2009 May 1;15(5):271–7.

152. Hamatani T, Carter MG, Sharov AA, Ko MSH. Dynamics of global gene expression changes during mouse preimplantation development. Dev Cell. 2004 Jan;6(1):117–31.

153. Wang QT, Piotrowska K, Ciemerych MA, Milenkovic L, Scott MP, Davis RW, et al. A genome-wide study of gene activity reveals developmental signaling pathways in the preimplantation mouse embryo. Dev Cell. 2004 Jan;6(1):133–44.

154. Tanaka TS, Jaradat SA, Lim MK, Kargul GJ, Wang X, Grahovac MJ, et al. Genome-wide expression profiling of mid-gestation placenta and embryo using a 15,000 mouse developmental cDNA microarray. Proc Natl Acad Sci. 2000 Aug 1;97(16):9127–32.

155. Parks JC, McCallie BR, Janesch AM, Schoolcraft WB, Katz-Jaffe MG. Blastocyst gene expression correlates with implantation potential. Fertil Steril. 2011 Mar 15;95(4):1367–72.

156. Yin X, Tan K, Vajta G, Jiang H, Tan Y, Zhang C, et al. Massively Parallel Sequencing for Chromosomal Abnormality Testing in Trophectoderm Cells of Human Blastocysts1. Biol Reprod. 2013 Mar 1;88(3):69–1.

157. Treff NR, Krisher RL, Tao X, Garnsey H, Bohrer C, Silva E, et al. Next Generation Sequencing-Based Comprehensive Chromosome Screening in Mouse Polar Bodies, Oocytes, and Embryos1. Biol Reprod. 2016 Apr 1;94(4):76–1.

158. Seli E, Botros L, Sakkas D, Burns DH. Noninvasive metabolomic profiling of embryo culture media using proton nuclear magnetic resonance

correlates with reproductive potential of embryos in women undergoing in vitro fertilization. Fertil Steril. 2008 Dec 1;90(6):2183–9.

159. Bromer JG, Seli E. Assessment of embryo viability in assisted reproductive technology: shortcomings of current approaches and the emerging role of metabolomics. Curr Opin Obstet Gynecol. 2008 Jun;20(3):234–41.

160. Hardarson T, Ahlström A. Non-invasive metabolomic profiling of Day 2 and 5 embryo culture medium: a prospective randomized trial. Hum Reprod. 2012;27(1):89–96.

161. Aydiner F, Yetkin C, Seli E. Perspectives on Emerging Biomarkers for Non-Invasive Assessment of Embryo Viability in Assisted Reproduction. Curr Mol Med. 2010 Mar 18;10(2):206–15.

162. Huang SM, Xu F, Lam SH, Gong Z, Ong CN. Metabolomics of developing zebrafish embryos using gas chromatography- and liquid chromatography-mass spectrometry. Mol Biosyst. 2013 May 7;9(6):1372–80.

163. Krisher RL, Heuberger AL, Paczkowski M, Stevens J, Pospisil C, Prather RS, et al. Applying metabolomic analyses to the practice of embryology: physiology, development and assisted reproductive technology. Reprod Fertil Dev. 2015 May 8;27(4):602.

164. Cortezzi SS, Cabral EC, Trevisan MG, Ferreira CR, Setti AS, De Almeida Ferreira Braga DP, et al. Prediction of embryo implantation potential by mass spectrometry fingerprinting of the culture medium. Reproduction. 2013;145(5):453–62.

165. Ellis DI, Goodacre R. Metabolic fingerprinting in disease diagnosis: Biomedical applications of infrared and Raman spectroscopy. Analyst. 2006;131(8):875–85.

166. Scott R, Seli E, Miller K, Sakkas D, Scott K, Burns DH. Noninvasive metabolomic profiling of human embryo culture media using Raman spectroscopy predicts embryonic reproductive potential: a prospective blinded pilot study. Fertil Steril. 2008 Jul 1;90(1):77–83.

167. Seli E, Sakkas D, Scott R, Kwok SC, Rosendahl SM, Burns DH. Noninvasive metabolomic profiling of embryo culture media using Raman and near-infrared spectroscopy correlates with reproductive potential of embryos in women undergoing in vitro fertilization. Fertil Steril. 2007 Nov 1;88(5):1350–7.

168. Li XX, Cao PH, Han WX, Xu YK, Wu H, Yu XL, et al. Non-invasive metabolomic profiling of culture media of ICSI- and IVF-derived early developmental cattle embryos via Raman spectroscopy. Anim Reprod Sci. 2018 Sep 1;196:99–110.

169. Liang B, Gao Y, Xu J, Song Y, Xuan L, Shi T, et al. Raman profiling of embryo culture medium to identify aneuploid and euploid embryos. Fertil Steril. 2019 Apr 1;111(4):753-762.e1.

170. Nagy ZP, Sakkas D, Behr B. Non-invasive assessment of embryo viability by metabolomic profiling of culture media ('metabolomics'). Reprod Biomed Online. 2008 Jan 1;17(4):502–7.

171. Botros L, Sakkas D, Seli E. Metabolomics and its application for non-

invasive embryo assessment in IVF. Mol Hum Reprod. 2008 Dec 1;14(12):679–90.

172. Thompson JG, Brown HM, Sutton-McDowall ML. Measuring embryo metabolism to predict embryo quality. Reprod Fertil Dev. 2016 Jan 27;28(2):41.

173. Biassoni R, Raso A. Quantitative Real-Time PCR. Vol. 2065. New York, NY: Humana Press; 2016.

174. Bustin S, Benes V. Quantitative real-time RT-PCR–a perspective. J Mol Endocrinol. 2005;34(3):597–601.

175. Ivan Bower N, Joachim Moser R, Robert Hill J, Arabella Lehnert S. Universal reference method for real-time PCR gene expression analysis of preimplantation embryos. Biotechniques. 2007 Feb 16;42(2):199–206.

176. Picelli S, Faridani OR, Björklund ÅK, Winberg G, Sagasser S, Sandberg R. Full-length RNA-seq from single cells using Smart-seq2. Nat Protoc. 2014;9(1):171–81.

177. Krisher RL, Schoolcraft WB, Katz-Jaffe MG. Omics as a window to view embryo viability. Fertil Steril. 2015 Feb 1;103(2):333–41.

178. D'Souza F, Uppangala S, Asampille G, Salian SR, Kalthur G, Talevi R, et al. Spent embryo culture medium metabolites are related to the in vitro attachment ability of blastocysts. Sci Rep. 2018 Dec 1;8(1):1–10.

179. West PR, Weir AM, Smith AM, Donley ELR, Cezar GG. Predicting human developmental toxicity of pharmaceuticals using human embryonic stem cells and metabolomics. Toxicol Appl Pharmacol. 2010 Aug 15;247(1):18–27.

180. Dettmer K, Aronov PA, Hammock BD. Mass spectrometry-based metabolomics. Mass Spectrom Rev. 2007 Jan 1;26(1):51–78.

181. Gika HG, Theodoridis GA, Plumb RS, Wilson ID. Current practice of liquid chromatography-mass spectrometry in metabolomics and metabonomics. J Pharm Biomed Anal. 2014;87:12–25.

182. Singh R, Sinclair KD. Metabolomics: Approaches to assessing oocyte and embryo quality. Theriogenology. 2007 Sep 1;68(SUPPL. 1):S56–62.

183. Qi BL, Liu P, Wang QY, Cai WJ, Yuan BF, Feng YQ. Derivatization for liquid chromatography-mass spectrometry. TrAC - Trends Anal Chem. 2014 Jul 1;59:121–32.

184. Pham-Tuan H, Kaskavelis L, Daykin CA, Janssen HG. Method development in high-performance liquid chromatography for high-throughput profiling and metabonomic studies of biofluid samples. J Chromatogr B Anal Technol Biomed Life Sci. 2003 Jun 15;789(2):283–301.

185. Patti GJ, Yanes O, Siuzdak G. Metabolomics: the apogee of the omics trilogy. Nat Rev Mol Cell Biol. 2012 Apr 22;13(4):263–9.

186. Schrimpe-Rutledge AC, Codreanu SG, Sherrod SD, McLean JA. Untargeted Metabolomics Strategies—Challenges and Emerging Directions. J Am Soc Mass Spectrom. 2016 Dec 13;27(12):1897–905.

187. Sainiemi L, Sikanen T, Kostiainen R. Integration of fully microfabricated, three-dimensionally sharp electrospray ionization tips with microfluidic glass chips. Anal Chem. 2012 Nov 6;84(21):8973–9.

188. Lin S-L, Lin T-Y, Fuh M-R. Microfluidic chip-based liquid chromatography coupled to mass spectrometry for determination of small molecules in bioanalytical applications: An update. Electrophoresis. 2014 May;35(9):1275–84.

189. Wang X, Yi L, Mukhitov N, Schrell AM, Dhumpa R, Roper MG. Microfluidics-to-Mass Spectrometry: A review of coupling methods and applications. J Chromatogr A. 2015;1382:98–116.

190. Ascari IJ, Martins SC, Camargo LSA, Mendez-Otero R, Jasmin. Development of bovine embryos in vitro in coculture with murine mesenchymal stem cells and embryonic fibroblasts. Mol Biol Rep. 2018;45(6):1827–37.

191. Bavister BD. Role of oviductal secretions in embryonic growth in vivo and in vitro. Theriogenology. 1988 Jan 1;29(1):143–54.

192. Gardner DK, Sakkas D. Mouse embryo cleavage, metabolism and viability: role of medium composition. Hum Reprod. 1993 Feb;8(2):288–95.

193. Gardner DK, Leese HJ. Concentrations of nutrients in mouse oviduct fluid and their effects on embryo development and metabolism in vitro. Reproduction. 1990;88(1):361–8.

194. Biggers JD. Thoughts on embryo culture conditions. Reprod Biomed Online. 2002;4 Suppl 1:30–8.

195. Gruber I, Klein M. Embryo culture media for human ivf: Which possibilities exist? J Turkish Ger Gynecol Assoc. 2011;12(2):110–7.

196. Lane M, Gardner DK. Embryo culture medium: which is the best? Best Pract Res Clin Obstet Gynaecol. 2007 Feb;21(1):83–100.

197. Ménézo YJ, Hamamah S, Hazout A, Dale B. Time to switch from co-culture to sequential defined media for transfer at the blastocyst stage. Hum Reprod. 1998 Aug;13(8):2043–4.

198. Simopoulou M, Sfakianoudis K, Rapani A, Giannelou P, Anifandis G, Bolaris S, et al. Considerations regarding embryo culture conditions: From media to epigenetics. Vol. 32, In Vivo. International Institute of Anticancer Research; 2018. p. 451–60.

199. Lawitts JA, Biggers JD. Culture of preimplantation embryos. Methods Enzymol. 1993;225:153–64.

200. Gardner DK, Lane M, Spitzer A, Batt PA. Enhanced Rates of Cleavage and Development for Sheep Zygotes Cultured to the Blastocyst Stage in Vitro in the Absence of Serum and Somatic Cells: Amino Acids, Vitamins, and Culturing Embryos in Groups Stimulate Development1. Biol Reprod. 1994 Feb 1;50(2):390–400.

201. Devreker F, Hardy K. Amino acids promote human blastocyst development in vitro. Hum Reprod. 2001;16(4):749–56.

202. Ho Y, Wigglesworth K, Eppig JJ, Schultz RM. Preimplantation development

of mouse embryos in KSOM: Augmentation by amino acids and analysis of gene expression. Mol Reprod Dev. 1995 Jun 1;41(2):232–8.

203. Sakkas D, Trounson a O. Co-culture of mouse embryos with oviduct and uterine cells prepared from mice at different days of pseudopregnancy. J Reprod Fertil. 1990;90(1):109–18.

204. Freeman MR, Bastias MC, Hill GA, Osteen KG. Coculture of mouse embryos with cells isolated from the human ovarian follicle, oviduct, and uterine endometrium. Fertil Steril. 1993 Jan 1;59(1):138–42.

205. Bagheban Eslami Nejad MR, Rezazadeh M, Kazemy Ashtiani S, Eftekhary P. Effect of polarized human uterine epithelial cells on mouse embryo development and blastocyst cellularity. Yakhteh. 2005;7(25).

206. Azadbakht M, Valojerdi MR, Mowla SJ. Development of mouse embryos co-cultured with polarized or non-polarized uterine epithelial cells using sequential culture media. Anim Reprod Sci. 2007 Jul;100(1–2):141–57.

207. Joo BS, Kim MK, Na YJ, Moon HS, Lee KS, Kim H Do. The mechanism of action of coculture on embryo development in the mouse model: Direct embryo-to-cell contact and the removal of deleterious components. Fertil Steril. 2001 Jan 1;75(1):193–9.

208. Desai N, Goldfarb J. Co-cultured human embryos may be subjected to widely different microenvironments: pattern of growth factor/ cytokine release by Vero cells during the co-culture interval. Hum Reprod. 1998;13(6):1600–5.

209. Orsi NM, Reischl JB. Mammalian embryo co-culture: Trials and tribulations of a misunderstood method. Theriogenology. 2007;67(3):441–58.

210. Ramos-Ibeas P, Calle A, Pericuesta E, Laguna-Barraza R, Moros-Mora R, Lopera-Vásquez R, et al. An Efficient System to Establish Biopsy-Derived Trophoblastic Cell Lines from Bovine Embryos1. Biol Reprod. 2014 Jul 1;91(1):15–1.

211. Wang LW. Effect of condition medium and glucose concentration the in vitro development of early bovine embryos. Theriogenology. 1990;33:343.

212. Rieger D, Grisart B, Semple E, Langendonckt A Van, Betteridge KJ, Dessy F. Comparison of the effects of oviductal cell co-culture and oviductal cell-conditioned medium on the development and metabolic activity of cattle embryos. J Reprod Fertil. 1995;105:91–8.

213. Lopera-Vasquez R, Hamdi M, Fernandez-Fuertes B, Maillo V, Beltran-Brena P, Calle A, et al. Extracellular Vesicles from BOEC in In Vitro Embryo Development and Quality. PLoS One. 2016 Feb 1;11(2):e0148083.

214. Lee YL, Xu JS, Chan STH, Ho PC, Yeung WSB. Animal Experimentation: Vero Cells, But Not Oviductal Cells, Increase the Hatching Frequency and Total Cell Count of Mouse Blastocysts Partly by Changing Energy Substrate Concentrations in Culture Medium. J Assist Reprod Genet. 2001;18(10):566–74.

215. World Health Organization. Neurological disorders: public health challenges. 2006.

216. Feigin VL, Nichols E, Alam T, Bannick MS, Beghi E, Blake N, et al. Global, regional, and national burden of neurological disorders, 1990–2016: a systematic analysis for the Global Burden of Disease Study 2016. Lancet Neurol. 2019 May 1;18(5):459–80.

217. 2020 Alzheimer's disease facts and figures. Alzheimer's Dement. 2020 Mar 1;16(3):391–460.

218. Cheignon C, Tomas M, Bonnefont-Rousselot D, Faller P, Hureau C, Collin F. Oxidative stress and the amyloid beta peptide in Alzheimer's disease. Redox Biol. 2018;14(October 2017):450–64.

219. Mattson MP. Pathways towards and away from Alzheimer's disease. Nature. 2004 Aug 5;430(7000):631–9.

220. Pardridge WM. CSF, blood-brain barrier, and brain drug delivery. Expert Opin Drug Deliv. 2016 Jul 2;13(7):963–75.

221. Abbott NJ, Patabendige AAK, Dolman DEM, Yusof SR, Begley DJ. Structure and function of the blood-brain barrier. Neurobiol Dis. 2010 Jan 1;37(1):13–25.

222. Abbott NJ, Rönnbäck L, Hansson E. Astrocyte-endothelial interactions at the blood-brain barrier. Nat Rev Neurosci. 2006 Jan;7(1):41–53.

223. Tietz S, Engelhardt B. Brain barriers: Crosstalk between complex tight junctions and adherens junctions. J Cell Biol. 2015 May 25;209(4):493–506.

224. Daneman R. The blood-brain barrier in health and disease. Ann Neurol. 2012 Nov 1;72(5):648–72.

225. Gupta S, Dhanda S, Sandhir R. Anatomy and physiology of blood-brain barrier. In: Brain Targeted Drug Delivery System. Elsevier; 2019. p. 7–31.

226. Abbott NJ. Blood-brain barrier structure and function and the challenges for CNS drug delivery. J Inherit Metab Dis. 2013 May 23;36(3):437–49.

227. Iadecola C. The Neurovascular Unit Coming of Age: A Journey through Neurovascular Coupling in Health and Disease. Neuron. 2017 Sep 27;96(1):17–42.

228. Obermeier B, Daneman R, Ransohoff RM. Development, maintenance and disruption of the blood-brain barrier. Nat Med. 2013 Dec 5;19(12):1584–96.

229. Wong AD, Ye M, Levy AF, Rothstein JD, Bergles DE, Searson PC. The blood-brain barrier: An engineering perspective. Front Neuroeng. 2013 Aug 30;6(JUL):7.

230. Janzer RC, Raff MC. Astrocytes induce blood-brain barrier properties in endothelial cells. Nature. 1987;325(6101):253–7.

231. Zonta M, Angulo MC, Gobbo S, Rosengarten B, Hossmann KA, Pozzan T, et al. Neuron-to-astrocyte signaling is central to the dynamic control of brain microcirculation. Nat Neurosci. 2003 Jan 1;6(1):43–50.

232. Gee JR, Keller JN. Astrocytes: Regulation of brain homeostasis via apolipoprotein E. Int J Biochem Cell Biol. 2005 Jun 1;37(6):1145–50.

233. Abbott NJ. Astrocyte-endothelial interactions and blood-brain barrier

permeability. J Anat. 2002;200(6):629–38.

234. Allt G, Lawrenson JG. Pericytes: Cell Biology and Pathology. Cells Tissues Organs. 2001;169(1):1–11.

235. Winkler EA, Bell RD, Zlokovic B V. Central nervous system pericytes in health and disease. Nat Neurosci. 2011 Nov 26;14(11):1398–405.

236. Thanabalasundaram G, Schneidewind J, Pieper C, Galla HJ. The impact of pericytes on the blood-brain barrier integrity depends critically on the pericyte differentiation stage. Int J Biochem Cell Biol. 2011 Sep 1;43(9):1284–93.

237. Cornford EM, Hyman S. Localization of brain endothelial luminal and abluminal transporters with immunogold electron microscopy. NeuroRx. 2005 Jan 1;2(1):27–43.

238. Correale J, Villa A. Cellular elements of the blood-brain barrier. Neurochem Res. 2009 Dec 25;34(12):2067–77.

239. Dejana E, Tournier-Lasserve E, Weinstein BM. The Control of Vascular Integrity by Endothelial Cell Junctions: Molecular Basis and Pathological Implications. Vol. 16, Developmental Cell. Cell Press; 2009. p. 209–21.

240. Hawkins BT, Davis TP. The blood-brain barrier/neurovascular unit in health and disease. Vol. 57, Pharmacological Reviews. American Society for Pharmacology and Experimental Therapeutics; 2005. p. 173–85.

241. Wolburg H, Noell S, Mack A, Wolburg-Buchholz K, Fallier-Becker P. Brain endothelial cells and the glio-vascular complex. Vol. 335, Cell and Tissue Research. 2009. p. 75–96.

242. Cecchelli R, Berezowski V, Lundquist S, Culot M, Renftel M, Dehouck MP, et al. Modelling of the blood - Brain barrier in drug discovery and development. Nat Rev Drug Discov. 2007;6(8):650–61.

243. Ohashi T, Sato M. Remodeling of vascular endothelial cells exposed to fluid shear stress: Experimental and numerical approach. Fluid Dyn Res. 2005;37(1-2 SPEC. ISS.):40–59.

244. Cucullo L, Hossain M, Puvenna V, Marchi N, Janigro D. The role of shear stress in Blood-Brain Barrier endothelial physiology. BMC Neurosci. 2011 May 11;12:40.

245. Lee SW, Kim WJ, Choi YK, Song HS, Son MJ, Gelman IH, et al. SSeCKS regulates angiogenesis and tight junction formation in blood-brain barrier. Nat Med. 2003 Jul 1;9(7):900–6.

246. Siddharthan V, Kim Y V., Liu S, Kim KS. Human astrocytes/astrocyte-conditioned medium and shear stress enhance the barrier properties of human brain microvascular endothelial cells. Brain Res. 2007 May 25;1147(1):39–50.

247. Abbott NJ. Prediction of blood-brain barrier permeation in drug discovery from in vivo, in vitro and in silico models. Drug Discov Today Technol. 2004 Dec 1;1(4):407–16.

248. Abbott A. More than a cosmetic change. Nature. 2005 Nov 10;438(7065):144–6.

249. Pankevich DE, Altevogt BM, Dunlop J, Gage FH, Hyman SE. Improving and accelerating drug development for nervous system disorders. Neuron. 2014 Nov 5;84(3):546–53.

250. Nakagawa S, Deli MA, Kawaguchi H, Shimizudani T, Shimono T, Kittel Á, et al. A new blood-brain barrier model using primary rat brain endothelial cells, pericytes and astrocytes. Neurochem Int. 2009 Mar 1;54(3–4):253–63.

251. Coisne C, Dehouck L, Faveeuw C, Delplace Y, Miller F, Landry C, et al. Mouse syngenic in vitro blood-brain barrier model: A new tool to examine inflammatory events in cerebral endothelium. Lab Investig. 2005 Jun 19;85(6):734–46.

252. Dehouck M -P, Méresse S, Delorme P, Fruchart J -C, Cecchelli R. An Easier, Reproducible, and Mass-Production Method to Study the Blood–Brain Barrier In Vitro. J Neurochem. 1990 May 1;54(5):1798–801.

253. Franke H, Galla HJ, Beuckmann CT. An improved low-permeability in vitro-model of the blood-brain barrier: Transport studies on retinoids, sucrose, haloperidol, caffeine and mannitol. Brain Res. 1999 Feb 6;818(1):65–71.

254. Franke H, Galla HJ, Beuckmann CT. Primary cultures of brain microvessel endothelial cells: A valid and flexible model to study drug transport through the blood-brain barrier in vitro. Brain Res Protoc. 2000 Jul 1;5(3):248–56.

255. Patabendige A, Skinner RA, Abbott NJ. Establishment of a simplified in vitro porcine blood-brain barrier model with high transendothelial electrical resistance. Brain Res. 2013 Jul 12;1521:1–15.

256. Hatherell K, Couraud PO, Romero IA, Weksler B, Pilkington GJ. Development of a three-dimensional, all-human in vitro model of the blood-brain barrier using mono-, co-, and tri-cultivation Transwell models. J Neurosci Methods. 2011 Aug 15;199(2):223–9.

257. Marroni M, Kight KM, Hossain M, Cucullo L, Desai SY, Janigro D. Dynamic in vitro model of the blood-brain barrier. Gene profiling using cDNA microarray analysis. Methods Mol Med. 2003;89:419–34.

258. Helms HC, Abbott NJ, Burek M, Cecchelli R, Couraud P-O, Deli MA, et al. In vitro models of the blood-brain barrier: An overview of commonly used brain endothelial cell culture models and guidelines for their use. J Cereb Blood Flow Metab. 2016 May 11;36(5):862–90.

259. Sivandzade F, Cucullo L. In-vitro blood–brain barrier modeling: A review of modern and fast-advancing technologies. J Cereb Blood Flow Metab. 2018 Oct 1;38(10):1667–81.

260. Lippmann ES, Weidenfeller C, Svendsen CN, Shusta E V. Blood-brain barrier modeling with co-cultured neural progenitor cell-derived astrocytes and neurons. J Neurochem. 2011 Nov 1;119(3):507–20.

261. Xue Q, Liu Y, Qi H, Ma Q, Xu L, Chen W, et al. A novel brain neurovascular unit model with neurons, astrocytes and microvascular endothelial cells of rat. Int J Biol Sci. 2013;9(2):174–89.

262. Nakagawa S, Deli MA, Kawaguchi H, Shimizudani T, Shimono T, Kittel Á, et al. A new blood-brain barrier model using primary rat brain endothelial

cells, pericytes and astrocytes. Neurochem Int. 2009 Mar 1;54(3–4):253–63.

263. Török M, Huwyler J, Gutmann H, Fricker G, Drewe J. Modulation of transendothelial permeability and expression of ATP-binding cassette transporters in cultured brain capillary endothelial cells by astrocytic factors and cell-culture conditions. Exp Brain Res. 2003 Dec 12;153(3):356–65.

264. Kaisar MA, Abhyankar V V., Cucullo L. In Vitro BBB Models: Working with Static Platforms and Microfluidic Systems. In: Neuromethods. Humana Press Inc.; 2019. p. 55–70.

265. Cucullo L, McAllister MS, Kight K, Krizanac-Bengez L, Marroni M, Mayberg MR, et al. A new dynamic in vitro model for the multidimensional study of astrocyte-endothelial cell interactions at the blood-brain barrier. Brain Res. 2002 Oct 4;951(2):243–54.

266. Cucullo L, Couraud P-O, Weksler B, Romero I-A, Hossain M, Rapp E, et al. Immortalized human brain endothelial cells and flow-based vascular modeling: a marriage of convenience for rational neurovascular studies. J Cereb Blood Flow Metab. 2008;28:312–28.

267. Oddo A, Peng B, Tong Z, Wei Y, Tong WY, Thissen H, et al. Advances in Microfluidic Blood–Brain Barrier (BBB) Models. Trends Biotechnol. 2019 Dec 1;37(12):1295–314.

268. Jiang L, Li S, Zheng J, Li Y, Huang H. Recent Progress in Microfluidic Models of the Blood-Brain Barrier. Micromachines. 2019 Jun 5;10(6):375.

269. Bang S, Lee SR, Ko J, Son K, Tahk D, Ahn J, et al. A Low Permeability Microfluidic Blood-Brain Barrier Platform with Direct Contact between Perfusable Vascular Network and Astrocytes. Sci Rep. 2017 Dec 1;7(1):1–10.

270. Booth R, Kim H. Characterization of a microfluidic in vitro model of the blood-brain barrier (μBBB). Lab Chip. 2012 Apr 24;12(10):1784–92.

271. Achyuta AKH, Conway AJ, Crouse RB, Bannister EC, Lee RN, Katnik CP, et al. A modular approach to create a neurovascular unit-on-a-chip. Lab Chip. 2013;13(4):542–53.

272. Wilhelm I, Krizbai IA. In vitro models of the blood-brain barrier for the study of drug delivery to the brain. Mol Pharm. 2014 Jul 7;11(7):1949–63.

273. Brown JA, Pensabene V, Markov DA, Allwardt V, Diana Neely M, Shi M, et al. Recreating blood-brain barrier physiology and structure on chip: A novel neurovascular microfluidic bioreactor. Biomicrofluidics. 2015 Sep 1;9(5):054124.

274. Prabhakarpandian B, Shen MC, Nichols JB, Mills IR, Sidoryk-Wegrzynowicz M, Aschner M, et al. SyM-BBB: A microfluidic blood brain barrier model. Lab Chip. 2013 Mar 21;13(6):1093–101.

275. Deosarkar SP, Prabhakarpandian B, Wang B, Sheffield JB, Krynska B, Kiani MF. A novel dynamic neonatal blood-brain barrier on a chip. PLoS One. 2015 Nov 10;10(11).

276. Terrell-Hall TB, Ammer AG, Griffith JIG, Lockman PR. Permeability across

a novel microfluidic blood-tumor barrier model. Fluids Barriers CNS. 2017 Jan 23;14(1):3.

277. Adriani G, Ma D, Pavesi A, Kamm RD, Goh ELK. A 3D neurovascular microfluidic model consisting of neurons, astrocytes and cerebral endothelial cells as a blood-brain barrier. Lab Chip. 2017 Feb 7;17(3):448–59.

278. Xu H, Li Z, Yu Y, Sizdahkhani S, Ho WS, Yin F, et al. A dynamic in vivo-like organotypic blood-brain barrier model to probe metastatic brain tumors OPEN. Sci Rep. 2016;6:36670.

279. van der Helm MW, van der Meer AD, Eijkel JCT, van den Berg A, Segerink LI. Microfluidic organ-on-chip technology for blood-brain barrier research. Tissue Barriers. 2016 Jan 2;4(1):e1142493.

280. Chrobak KM, Potter DR, Tien J. Formation of perfused, functional microvascular tubes in vitro. Microvasc Res. 2006 May 1;71(3):185–96.

281. Kim JA, Kim HN, Im SK, Chung S, Kang JY, Choi N. Collagen-based brain microvasculature model in vitro using three-dimensional printed template. Biomicrofluidics. 2015 Apr 15;9(2):024115.

282. Herland A, Van Der Meer AD, FitzGerald EA, Park TE, Sleeboom JJF, Ingber DE. Distinct contributions of astrocytes and pericytes to neuroinflammation identified in a 3D human blood-brain barrier on a chip. PLoS One. 2016 Mar 1;11(3).

283. Wevers NR, Kasi DG, Gray T, Wilschut KJ, Smith B, Vught R, et al. A perfused human blood-brain barrier on-a-chip for high-throughput assessment of barrier function and antibody transport. Fluids Barriers CNS. 2018 Aug 31;15(1):1–12.

284. Wang YI, Abaci HE, Shuler ML. Microfluidic blood-brain barrier model provides in vivo-like barrier properties for drug permeability screening. Biotechnol Bioeng. 2017 Jan 1;114(1):184–94.

285. Brown JA, Codreanu SG, Shi M, Sherrod SD, Markov DA, Neely MD, et al. Metabolic consequences of inflammatory disruption of the blood-brain barrier in an organ-on-chip model of the human neurovascular unit. J Neuroinflammation. 2016 Dec 12;13(1):306.

286. Koo Y, Hawkins BT, Yun Y. Three-dimensional (3D) tetra-culture brain on chip platform for organophosphate toxicity screening. Sci Rep. 2018 Dec 1;8(1):1–7.

287. Czupalla CJ, Liebner S, Devraj K. In Vitro Models of the Blood–Brain Barrier. Methods Mol Biol. 2014;1135:415–37.

288. Wheeler MB, Rubessa M. Integration of microfluidics in animal in vitro embryo production. Mol Hum Reprod. 2017 Apr 1;23(4):248–56.

289. Beebe D, Wheeler M, Zeringue H, Walters E, Raty S. Microfluidic technology for assisted reproduction. Theriogenology. 2002 Jan;57(1):125–35.

290. Han C, Zhang Q, Ma R, Xie L, Qiu T, Wang L, et al. Integration of single oocyte trapping, in vitro fertilization and embryo culture in a microwell-

structured microfluidic device. Lab Chip. 2010;10(21):2848.

291. Ma R, Xie L, Han C, Su K, Qiu T, Wang L, et al. In vitro fertilization on a single-oocyte positioning system integrated with motile sperm selection and early embryo development. Anal Chem. 2011;83(8):2964–70.

292. Smith GD, Takayama S, Swain JE. Rethinking In Vitro Embryo Culture: New Developments in Culture Platforms and Potential to Improve Assisted Reproductive Technologies. Biol Reprod. 2012;86(3):1–10.

293. Esteves TC, Van Rossem F, Nordhoff V, Schlatt S, Boiani M, Le Gac S. A microfluidic system supports single mouse embryo culture leading to full-term development. RSC Adv. 2013 Dec 28;3(48):26451–8.

294. Glasgow IK, Zeringue HC, Beebe DJ, Choi SJ, Lyman JT, Chan NG, et al. Handling individual mammalian embryos using microfluidics. IEEE Trans Biomed Eng. 2001;48(5):570–8.

295. Wheeler MB, Beebe DJ, Walters EM, Raty S. Microfluidic technology for in vitro embryo production. In: 2nd Annual International IEEE-EMBS Special Topic Conference on Microtechnologies in Medicine and Biology - Proceedings. Institute of Electrical and Electronics Engineers Inc.; 2002. p. 104–8.

296. Kieslinger DC, Hao Z, Vergouw CG, Kostelijk EH, Lambalk CB, Le Gac S. In vitro development of donated frozen-thawed human embryos in a prototype static microfluidic device: A randomized controlled trial. Fertil Steril. 2015;103(3):680-686.e2.

297. Melin J, Lee A, Foygel K, Leong DE, Quake SR, Yao MWM. In vitro embryo culture in defined, sub-microliter volumes. Dev Dyn. 2009 Apr;238(4):950–5.

298. Raty S, Walters EM, Davis J, Zeringue H, Beebe DJ, Rodriguez-Zas SL, et al. Embryonic development in the mouse is enhanced via microchannel culture. Lab Chip. 2004;4:186–90.

299. Heo YS, Cabrera LM, Bormann CL, Shah CT, Takayama S, Smith GD. Dynamic microfunnel culture enhances mouse embryo development and pregnancy rates. Hum Reprod. 2010;25(3):613–22.

300. Hickman DL, Beebe DJ, Rodriguez-Zas SL, Wheeler MB. Comparison of Static and Dynamic Medium Environments for Culturing of Pre-implantation Mouse Embryos. Comp Med. 2002;52(2):122–6.

301. Cabrera L, Heo Y, Ding J, … ST-F and, 2006 U. Improved blastocyst development with microfluidics and Braille pin actuator enabled dynamic culture. Fertil Steril. 2006;86(3):S43.

302. Swain JE, Lai D, Takayama S, Smith GD. Thinking big by thinking small: Application of microfluidic technology to improve ART. Lab Chip. 2013 Apr 7;13(7):1213–24.

303. Wale PL, Gardner DK. The effects of chemical and physical factors on mammalian embryo culture and their importance for the practice of assisted human reproduction. Hum Reprod Update. 2016;22(1):2–22.

304. Zarmakoupis-Zavos PN, Zavos PM. Factors that May Influence the Mouse

Embryo Bioassay. Tohoku J Exp Med. 1996;179(3):141–9.

305. Holyoak GR, Wang S, Liu Y, Bunch TD. Toxic effects of ethylene oxide residues on bovine embryos in vitro. Toxicology. 1996 Apr 15;108(1–2):33–8.

306. Naz RK, Janousek JT, Moody T, Stillman RJ. Factors influencing murine embryo bioassay: effects of proteins, aging of medium, and surgical glove coatings. Fertil Steril. 1986;46(5).

307. Nijs M, Franssen K, Cox A, Wissmann D, Ruis H, Ombelet W. Reprotoxicity of intrauterine insemination and in vitro fertilization-embryo transfer disposables and products: a 4-year survey. Fertil Steril. 2009 Aug;92(2):527–35.

308. Colucci F, McKeegan P, Picton HM, Pensabene V. Mouse embryo assay to evaluate polydimethylsiloxane (PDMS) embryo-toxicity∗. In: Proceedings of the Annual International Conference of the IEEE Engineering in Medicine and Biology Society, EMBS. Institute of Electrical and Electronics Engineers Inc.; 2018. p. 4484–7.

309. Tae JC, Kim EY, Lee WD, Park SP, Lim JH. Sterile filtered paraffin oil supports in vitro developmental competence in bovine embryos comparable to co-culture. J Assist Reprod Genet. 2006 Mar 13;23(3):121–7.

310. Morbeck DE. Mouse embryo assay for quality control in the IVF laboratory. In: Principles of IVF Laboratory Practice: Optimizing Performance and Outcomes. Cambridge University Press; 2017. p. 69–72.

311. Balaban B, Urman B. Effect of oocyte morphology on embryo development and implantation. Reprod Biomed Online. 2006;12(5):608–15.

312. Ebner T. Selection based on morphological assessment of oocytes and embryos at different stages of preimplantation development: a review. Hum Reprod Update. 2003 May 1;9(3):251–62.

313. Yu Y, Mai Q, Chen X, Wang L, Gao L, Zhou C, et al. Assessment of the developmental competence of human somatic cell nuclear transfer embryos by oocyte morphology classification. Hum Reprod. 2008 Dec 4;24(3):649–57.

314. Coticchio G, Sereni E, Serrao L, et al. What Criteria for the Definition of Oocyte Quality? Ann N Y Acad Sci. 2004 Dec;1034(1):132–44.

315. Krisher RL. The effect of oocyte quality on development. J Anim Sci. 2004;82:E14–23.

316. Guerif F, Mckeegan PJ, Leese HJ, Sturmey RG. A simple approach for COnsumption and RElease (CORE) analysis of metabolic activity in single mammalian embryos. PLoS One. 2013 Jan;8(8):e67834.

317. Leese HJ, Guerif F, Allgar V, Brison DR, Lundin K, Sturmey RG. Biological optimization, the Goldilocks principle, and how much is lagom in the preimplantation embryo. Mol Reprod Dev. 2016 Jul;83(9):748–54.

318. McKeegan PJ, Sturmey RG. Metabolomic Screening of Embryos to Enhance Successful Selection and Transfer. In: Rutherford A, Gardner DK,

Kovacs G, editors. How to Prepare the Egg and Embryo to Maximize IVF Success. Cambridge: Cambridge University Press; 2019. p. 295–304.

319. Schultz JF, Armant DR. β1- and β3-class integrins mediate fibronectin binding activity at the surface of developing mouse peri-implantation blastocysts: Regulation by ligand-induced mobilization of stored receptor. J Biol Chem. 1995 May 12;270(19):11522–31.

320. Thouas GA, Trounson AO, Wolvetang EJ, Jones GM. Mitochondrial dysfunction in mouse oocytes results in preimplantation embryo arrest in vitro. Biol Reprod. 2004 Dec;71(6):1936–42.

321. Leppens G, Gardner DK, Sakkas D. Co-culture of 1-cell outbred mouse embryos on bovine kidney epithelial cells: effect on development, glycolytic activity, inner cell mass: trophectoderm ratios and viability. Hum Reprod. 1996 Mar;11(3):598–600.

322. Binder NK, Hannan NJ, Gardner DK. Paternal diet-induced obesity retards early mouse embryo development, mitochondrial activity and pregnancy health. PLoS One. 2012 Jan;7(12):e52304.

323. Hannan NJ, Paiva P, Meehan KL, Rombauts LJF, Gardner DK, Salamonsen LA. Analysis of Fertility-Related Soluble Mediators in Human Uterine Fluid Identifies VEGF as a Key Regulator of Embryo Implantation. Endocrinology. 2011 Dec;152(12):4948–56.

324. Manbachi A, Shrivastava S, Cioffi M, Chung BG, Moretti M, Demirci U, et al. Microcirculation within grooved substrates regulates cell positioning and cell docking inside microfluidic channels. Lab Chip. 2008 Apr;8(5):747.

325. Livak KJ, Schmittgen TD. Analysis of Relative Gene Expression Data Using Real-Time Quantitative PCR and the 2−ΔΔCT Method. Methods. 2001 Dec 1;25(4):402–8.

326. Adjaye J, Huntriss J, Herwig R, BenKahla A, Brink TC, Wierling C, et al. Primary Differentiation in the Human Blastocyst: Comparative Molecular Portraits of Inner Cell Mass and Trophectoderm Cells. Stem Cells. 2005;23(10):1514–25.

327. Ozawa M, Sakatani M, Yao J, Shanker S, Yu F, Yamashita R, et al. Global gene expression of the inner cell mass and trophectoderm of the bovine blastocyst. BMC Dev Biol. 2012 Nov 6;12(1):33.

328. Cui X-S, Shen X-H, Kim N-H. Dicer1 expression in preimplantation mouse embryos: Involvement of Oct3/4 transcription at the blastocyst stage. Biochem Biophys Res Commun. 2007 Jan;352(1):231–6.

329. Chazaud C, Yamanaka Y. Lineage specification in the mouse preimplantation embryo. Development. 2016 Apr 1;143(7):1063–74.

330. Watanabe Y, Miyasaka KY, Kubo A, Kida YS, Nakagawa O, Hirate Y, et al. Notch and Hippo signaling converge on Strawberry Notch 1 (Sbno1) to synergistically activate Cdx2 during specification of the trophectoderm. Sci Rep. 2017 May 12;7(1):46135.

331. Lin SCJ, Wani MA, Whitsett JA, Wells JM. Klf5 regulates lineage formation in the pre-implantation mouse embryo. Development. 2010;137(23):3953–63.

332. Yagi R, Kohn MJ, Karavanova I, Kaneko KJ, Vullhorst D, DePamphilis ML, et al. Transcription factor TEAD4 specifies the trophectoderm lineage at the beginning of mammalian development. Development. 2007 Nov 1;134(21):3827–36.

333. Ng RK, Dean W, Dawson C, Lucifero D, Madeja Z, Reik W, et al. Epigenetic restriction of embryonic cell lineage fate by methylation of Elf5. 2008;10(11):1280–90.

334. Home P, Ray S, Dutta D, Bronshteyn I, Larson M, Paul S. GATA3 Is Selectively Expressed in the Trophectoderm of Peri-implantation Embryo and Directly Regulates Cdx2 Gene Expression. J Biol Chem. 2009;284(42):28729.

335. Gibson CL, Codreanu SG, Schrimpe-Rutledge AC, Retzlaff CL, Wright J, Mortlock DP, et al. Global untargeted serum metabolomic analyses nominate metabolic pathways responsive to loss of expression of the orphan metallo b-lactamase, MBLAC1. Omics. 2018;14:142.

336. May JC, Gant-Branum RL, McLean JA. Targeting the untargeted in molecular phenomics with structurally-selective ion mobility-mass spectrometry. Curr Opin Biotechnol. 2016 Jun 1;39:192–7.

337. Sherrod SD, Mclean JA. Systems-Wide High-Dimensional Data Acquisition and Informatics Using Structural Mass Spectrometry Strategies. Clin Chem. 2015;62(1):77–83.

338. Wishart D, Jewison T, Guo A. HMDB 3.0 - the human metabolome database in 2013. Nucleic Acids Res. 2013;41(D1):D801–7.

339. METLIN: a metabolite mass spectral database. journals.lww.com.

340. Horai H, Arita M, Kanaya S, Nihei Y, Ikeda T, Suwa K, et al. MassBank: a public repository for sharing mass spectral data for life sciences. J Mass Spectrom. 2010 Jul 7;45(7):703–14.

341. Jablonski A. NIST Standard Reference Database 64 NIST Electron Elastic-Scattering Cross-Section Database. 2010.

342. Xia J, Wishart DS. Using MetaboAnalyst 3.0 for Comprehensive Metabolomics Data Analysis. Curr Protoc Bioinforma. 2016 Sep 1;55(1):14.10.1-14.10.91.

343. Xie Y, Wang F, Zhong W, Puscheck E, Shen H, Rappolee D a. Shear stress induces preimplantation embryo death that is delayed by the zona pellucida and associated with stress-activated protein kinase-mediated apoptosis. Biol Reprod. 2006;75(1):45–55.

344. Bao J-B, Jed Harrison D. Measurement of flow in microfluidic networks with micrometer-sized flow restrictors. AIChE J. 2006 Jan;52(1):75–85.

345. Gopichandran N, Leese HJ. The effect of paracrine/autocrine interactions on the in vitro culture of bovine preimplantation embryos. Reproduction. 2006 Feb;131(2):269–77.

346. Lavranos TC, Rathjen PD, Seamark RF. Trophic effects of myeloid leukaemia inhibitory factor (LIF) on mouse embryos. J Reprod Fertil. 1995 Nov 1;105(2):331–8.

347. Rappolee DA, Sturm KS, Behrendtsen O, Schultz GA, Pedersen RA, Werb Z. Insulin-like growth factor II acts through an endogenous growth pathway regulated by imprinting in early mouse embryos. Genes Dev. 1992 Jun 1;6(6):939–52.

348. Brice EC, Wu J-X, Muraro R, Adamson ED, Wiley LM. Modulation of mouse preimplantation development by epidermal growth factor receptor antibodies, antisense RNA, and deoxyoligonucleotides. Dev Genet. 1993 Jan 1;14(3):174–84.

349. Österlund C, Wramsby H, Pousette Å. Preimplantation embryology. Mol Hum Reprod. 1996 Jul 1;2(7):507–12.

350. Atkins P, De Paula J. Physical chemistry. W. H. Freeman and Company New York. 2006.

351. Yildiz-Ozturk E, Yesil-Celiktas O. Diffusion phenomena of cells and biomolecules in microfluidic devices. Biomicrofluidics. 2015;9(5).

352. Thorne RG, Hrabětová S, Nicholson C. Diffusion of epidermal growth factor in rat brain extracellular space measured by integrative optical imaging. J Neurophysiol. 2004 Dec;92(6):3471–81.

353. Ma Y, Zhu C, Ma P, Yu KT. Studies on the diffusion coefficients of amino acids in aqueous solutions. J Chem Eng Data. 2005 Jul;50(4):1192–6.

354. Dandekar P V., Glass RH. Development of mouse embryos in vitro is affected by strain and culture medium. Gamete Res. 1987 Aug 1;17(4):279–85.

355. Uysal F, Akkoyunlu G, Ozturk S. Dynamic expression of DNA methyltransferases (DNMTs) in oocytes and early embryos. Biochimie. 2015.

356. Reik W, Dean W, Walter J. Epigenetic reprogramming in mammalian development. Science (80-). 2001 Aug 10;293(5532):1089–93.

357. Bird A. DNA methylation patterns and epigenetic memory. Genes Dev. 2002 Jan 1;16(1):6–21.

358. Bestor TH. The DNA methyltransferases of mammals. Hum Mol Genet. 2000 Oct 1;9(16):2395–402.

359. Okano M, Xie S, Li E. Cloning and characterization of a family of novel mammalian DNA (cytosine-5) methyltransferases [1]. Nat Genet. 1998;19(3):219–20.

360. Okano M, Bell DW, Haber DA, Li E. DNA methyltransferases Dnmt3a and Dnmt3b are essential for de novo methylation and mammalian development. Cell. 1999;99(3):247–57.

361. Kato Y, Kaneda M, Hata K, Kumaki K, Hisano M, Kohara Y, et al. Role of the Dnmt3 family in de novo methylation of imprinted and repetitive sequences during male germ cell development in the mouse. Hum Mol Genet. 2007 Oct 1;16(19):2272–80.

362. Hansen RS, Wijmenga C, Luo P, Stanek AM, Canfield TK, Weemaes CMR, et al. The DNMT3B DNA methyltransferase gene is mutated in the ICF immunodeficiency syndrome. Proc Natl Acad Sci U S A. 1999 Dec

7;96(25):14412–7.

363. Ueda Y. Roles for Dnmt3b in mammalian development: a mouse model for the ICF syndrome. Development. 2006;133(6):1183–92.

364. Santos F, Hendrich B, Reik W, Dean W. Dynamic reprogramming of DNA methylation in the early mouse embryo. Dev Biol. 2002 Jan 1;241(1):172–82.

365. Watanabe D, Suetake I, Tada T, Tajima S. Stage- and cell-specific expression of Dnmt3a and Dnmt3b during embryogenesis. Mech Dev. 2002 Oct;118(1–2):187–90.

366. Barau J, Teissandier A, Zamudio N, Roy S, Nalesso V, Hérault Y, et al. The DNA methyltransferase DNMT3C protects male germ cells from transposon activity. Science (80-). 2016;354(6314):909–12.

367. Reik W, Walter J. Genomic imprinting: Parental influence on the genome. Nat Rev Genet. 2001 Jan;2(1):21–32.

368. Kagitani F, Kuroiwa Y, Wakana S, Shiroishi T, Miyoshi N, Kobayashi S, et al. Peg5/Neuronatin is an imprinted gene located on sub-distal chromosome 2 in the mouse. Nucleic Acids Res. 1997;25(17):3428–32.

369. Joe MK, Lee HJ, Suh YH, Han KL, Lim JH, Song J, et al. Crucial roles of neuronatin in insulin secretion and high glucose-induced apoptosis in pancreatic β-cells. Cell Signal. 2008 May 1;20(5):907–15.

370. Millership SJ, Tunster SJ, Van de Pette M, Choudhury AI, Irvine EE, Christian M, et al. Neuronatin deletion causes postnatal growth restriction and adult obesity in 129S2/Sv mice. Mol Metab. 2018 Dec 1;18:97–106.

371. Du Z wei, Cong H chien, Yao Z. Identification of putative downstream genes of Oct-4 by suppression-subtractive hybridization. Biochem Biophys Res Commun. 2001 Apr 6;282(3):701–6.

372. Sahi VP, Wadekar HB, Ravi NS, Arumugam TU, Morita EH, Abe S. A molecular insight into darwin's "plant brain hypothesis" through expression pattern study of the MKRN gene in plant embryo compared with mouse embryo. Plant Signal Behav. 2012 Mar;7(3):375–81.

373. Mohammad F, Pandey GK, Mondal T, Enroth S, Redrup L, Gyllensten U, et al. Long noncoding RNA-Mediated maintenance of DNA methylation and transcriptional gene silencing. J Cell Sci. 2012 Aug 1;125(15):2792–803.

374. Green K, Lewis A, Dawson C, Dean W, Reinhart B, Chaillet JR, et al. A developmental window of opportunity for imprinted gene silencing mediated by DNA methylation and the Kcnq1ot1 noncoding RNA. Mamm Genome. 2007;18:32–42.

375. Higashimoto K, Soejima H, Saito T, Okumura K, Mukai T. Imprinting disruption of the CDKN1C/KCNQ1OT1 domain: The molecular mechanisms causing Beckwith-Wiedemann syndrome and cancer. Cytogenet Genome Res. 2006 Mar;113(1–4):306–12.

376. Doornbos ME, Maas SM, McDonnell J, Vermeiden JPW, Hennekam RCM. Infertility, assisted reproduction technologies and imprinting disturbances: a Dutch study. Hum Reprod. 2007 Jun 28;22(9):2476–80.

377. Owen C, Segars J. Imprinting Disorders and Assisted Reproductive Technology. Semin Reprod Med. 2009 Sep 26;27(05):417–28.

378. Bird AP, Wolffe AP. Methylation-induced repression-belts, braces, and chromatin. Cell. 1999 Nov 24;99(5):451–4.

379. Nagarajan P, Ge Z, Sirbu B, Doughty C, Agudelo Garcia PA, Schlederer M, et al. Histone Acetyl Transferase 1 Is Essential for Mammalian Development, Genome Stability, and the Processing of Newly Synthesized Histones H3 and H4. PLoS Genet. 2013 Jun;9(6).

380. Chawengsaksophak K, De Graaff W, Rossant J, Deschamps J, Beck F. Cdx2 is essential for axial elongation in mouse development. Proc Natl Acad Sci U S A. 2004 May 18;101(20):7641–5.

381. Leonardi R, Zhang YM, Rock CO, Jackowski S. Coenzyme A: Back in action. Prog Lipid Res. 2005 Mar;44(2–3):125–53.

382. Dansie LE, Reeves S, Miller K, Zano SP, Frank M, Pate C, et al. Physiological roles of the pantothenate kinases. Biochem Soc Trans. 2014;42(4):1033–6.

383. McKiernan SH, Bavister BD. Culture of one-cell hamster embryos with water soluble vitamins: Pantothenate stimulates blastocyst production. Hum Reprod. 2000;15(1):157–64.

384. Gardner DK. Changes in requirements and utilization of nutrients during mammalian preimplantation embryo development and their significance in embryo culture. Theriogenology. 1998 Jan 1;49(1):83–102.

385. Leese HJ, Baumann CG, Brison DR, McEvoy TG, Sturmey RG. Metabolism of the viable mammalian embryo: quietness revisited. Mol Hum Reprod. 2008 Dec 1;14(12):667–72.

386. Troike DE, Brinster RL. De novo pyrimidine nucleotide synthesis in the preimplantation mouse embryo. Exp Cell Res. 1981 Aug 1;134(2):481–4.

387. Nureddin A, Epsaro E, Kiessling AA. Purines inhibit the development of mouse embryos in vitro. J Reprod Fertil. 1990;90(2):455–64.

388. Alexiou M, Leese HJ. Purine utilisation, de novo synthesis and degradation in mouse preimplantation embryos. Development. 1992;114(1):185–92.

389. Gupta S, Banerjee J, Agarwal A. The Impact of Reactive Oxygen Species on Early Human Embryos: A Systematic Review of the Literature. Embryo Talk 1. 2006;1(2):87–98.

390. Ducker GS, Rabinowitz JD. One-Carbon Metabolism in Health and Disease. Cell Metab. 2017;25:27–42.

391. Avila MA, García-Trevijano ER, Lu SC, Corrales FJ, Mato JM. Methylthioadenosine. Int J Biochem Cell Biol. 2004 Nov 1;36(11):2125–30.

392. Green MA, Bass S, Spear BT. A device for the simple and rapid transcervical transfer of mouse embryos eliminates the need for surgery and potential post-operative complications. Biotechniques. 2009 Nov;47(5):919–24.

393. Steele KH, Hester JM, Stone BJ, Carrico KM, Spear BT, Fath-Goodin A.

Nonsurgical embryo transfer device compared with surgery for embryo transfer in mice. J Am Assoc Lab Anim Sci. 2013;52(1):17–21.

394. Takeshita Y, Kanda T. The blood-brain barrier (BBB) and in vitro BBB Models. Brain and Nerve. 2015 Aug 1;67(8):1035–42.

395. Vandenhaute E, Dehouck L, Boucau M-C, Sevin E, Uzbekov R, Tardivel M, et al. Modelling the Neurovascular Unit and the Blood-Brain Barrier with the Unique Function of Pericytes. Curr Neurovasc Res. 2011 Nov 7;8(4):258–69.

396. Al Ahmad A, Taboada CB, Gassmann M, Ogunshola OO. Astrocytes and pericytes differentially modulate blood-brain barrier characteristics during development and hypoxic insult. J Cereb Blood Flow Metab. 2011 Feb 8;31(2):693–705.

397. Daneman R, Zhou L, Kebede AA, Barres BA. Pericytes are required for blood-brain barrier integrity during embryogenesis. Nature. 2010 Nov 25;468(7323):562–6.

398. Dore-Duffy P. Pericytes: Pluripotent Cells of the Blood Brain Barrier. Curr Pharm Des. 2008 Jun 24;14(16):1581–93.

399. Gautam J, Zhang X, Yao Y. The role of pericytic laminin in blood brain barrier integrity maintenance. Sci Rep. 2016 Nov 3;6(1):1–13.

400. Hellström M, Gerhardt H, Kalén M, Li X, Eriksson U, Wolburg H, et al. Lack of pericytes leads to endothelial hyperplasia and abnormal vascular morphogenesis. J Cell Biol. 2001 Feb 5;152(3):543–53.

401. Katyshev V, Dore-Duffy P. Pericyte coculture models to study astrocyte, pericyte, and endothelial cell interactions. Methods Mol Biol. 2012;814:467–81.

402. Nakagawa S, Deli MA, Nakao S, Honda M, Hayashi K, Nakaoke R, et al. Pericytes from brain microvessels strengthen the barrier integrity in primary cultures of rat brain endothelial cells. Cell Mol Neurobiol. 2007 Sep 6;27(6):687–94.

403. Sweeney MD, Ayyadurai S, Zlokovic B V. Pericytes of the neurovascular unit: Key functions and signaling pathways. Nat Neurosci. 2016 Apr 26;19(6):771–83.

404. Cucullo L, Hossain M, Tierney W, Janigro D. A new dynamic in vitro modular capillaries-venules modular system: Cerebrovascular physiology in a box. BMC Neurosci. 2013 Feb 6;14(1):18.

405. Abbott NJ, Dolman DEM, Drndarski S, Fredriksson SM. An improved in vitro blood-brain barrier model: Rat brain endothelial cells co-cultured with astrocytes. Methods Mol Biol. 2012;814:415–30.

406. Thomsen LB, Burkhart A, Moos T. A triple culture model of the blood-brain barrier using porcine brain endothelial cells, astrocytes and pericytes. PLoS One. 2015 Aug 4;10(8):e0134765.

407. Bai Y, Zhu X, Chao J, Zhang Y, Qian C, Li P, et al. Pericytes contribute to the disruption of the cerebral endothelial barrier via increasing VEGF expression: Implications for stroke. PLoS One. 2015 Apr

17;10(4):e0124362.

408. Liu S, Agalliu D, Yu C, Fisher M. The Role of Pericytes in Blood-Brain Barrier Function and Stroke. Curr Pharm Des. 2012 Jul 25;18(25):3653–62.

409. de Majo M, Koontz M, Rowitch D, Ullian EM. An update on human astrocytes and their role in development and disease. Glia. 2020 Apr 1;68(4):685–704.

410. Gökçinar-Yagci B, Uçkan-Çetinkaya D, Çelebi-Saltik B. Pericytes: Properties, functions and applications in tissue engineering. Stem Cell Rev Reports. 2015 Aug 1;11(4):549–59.

411. Armulik A, Genové G, Mäe M, Nisancioglu MH, Wallgard E, Niaudet C, et al. Pericytes regulate the blood-brain barrier. Nature. 2010 Nov 25;468(7323):557–61.

412. Bonkowski D, Katyshev V, Balabanov RD, Borisov A, Dore-Duffy P. The CNS microvascular pericyte: Pericyte-astrocyte crosstalk in the regulation of tissue survival. Fluids Barriers CNS. 2011 Jan 18;8(1):1–12.

413. Seebach J, Dieterich P, Luo F, Schillers H, Vestweber D, Oberleithner H, et al. Endothelial barrier function under laminar fluid shear stress. Lab Investig. 2000 Dec 1;80(12):1819–31.

414. Strazielle N, Ghersi-Egea J-F, Ghiso J, Dehouck M-P, Frangione B, Patlak C, et al. In Vitro Evidence That β-Amyloid Peptide 1–40 Diffuses Across the Blood–Brain Barrier and Affects Its Permeability. J Neuropathol Exp Neurol. 2000 Jan 1;59(1):29–38.

415. Prelli F, Castano E, Glenner GG, Frangione B. Differences Between Vascular and Plaque Core Amyloid in Alzheimer's Disease. J Neurochem. 1988 Aug 1;51(2):648–51.

416. Miller DL, Papayannopoulos IA, Styles J, Bobin SA, Lin YY, Biemann K, et al. Peptide Compositions of the Cerebrovascular and Senile Plaque Core Amyloid Deposits of Alzheimer′s Disease. Arch Biochem Biophys. 1993 Feb 15;301(1):41–52.

417. Roher AE, Lowenson JD, Clarke S, Woods AS, Cotter RJ, Gowing E, et al. β-amyloid-(1-42) is a major component of cerebrovascular amyloid deposits: Implications for the pathology of Alzheimer disease. Proc Natl Acad Sci U S A. 1993 Nov 15;90(22):10836–40.

418. Gravina SA, Ho L, Eckman CB, Long KE, Otvos L, Younkin LH, et al. Amyloid β protein (Aβ) in Alzheimer's disease brain. Biochemical and immunocytochemical analysis with antibodies specific for forms ending at Aβ40 or Aβ42(43). J Biol Chem. 1995 Mar 31;270(13):7013–6.

419. Savage MJ, Kawooya JK, Pinsker LR, Emmons TL, Mistretta S, Siman R, et al. Elevated aβ levels in Alzheimer's disease brain are associated with selective accumulation of aβ42 in parenchymal amyloid plaques and both aβ40 and aβ42 in cerebrovascular deposits. Amyloid. 1995;2(4):234–40.

420. Shinkai Y, Yoshimura M, Ito Y, Odaka A, Suzuki N, Yanagisawa K, et al. Amyloid β-proteins 1—40 and 1—42(43) in the soluble fraction of extra- and intracranial blood vessels. Ann Neurol. 1995 Sep 1;38(3):421–8.

421. Cárdenas-Aguayo M, Silva-Lucero M. Physiological role of amyloid beta in neural cells: the cellular trophic activity. In: IntechOpen. 2014.

422. Tanokashira D, Mamada N, Yamamoto F, Taniguchi K, Tamaoka A, Lakshmana MK, et al. The neurotoxicity of amyloid β-protein oligomers is reversible in a primary neuron model. Mol Brain. 2017;10(1):1–10.

423. Alhibshi AH, Odawara A, Suzuki I. Neuroprotective efficacy of thymoquinone against amyloid beta-induced neurotoxicity in human induced pluripotent stem cell-derived cholinergic neurons. Biochem Biophys Reports. 2019 Mar 1;17:122–6.

424. Grant GA, Abbott NJ, Janigro D. Understanding the Physiology of the Blood-Brain Barrier: In Vitro Models. Physiology. 1998 Dec;13(6):287–93.

425. Wilhelm I, Fazakas C, Krizbai IA. In vitro models of the blood-brain barrier. Acta Neurobiol Exp. 2011;71(1):113–28.

426. Shin Y, Choi SH, Kim E, Bylykbashi E, Kim JA, Chung S, et al. Blood–Brain Barrier Dysfunction in a 3D In Vitro Model of Alzheimer's Disease. Adv Sci. 2019 Oct 12;6(20):1900962.

427. Fiala M, Zhang L, Gan X, Sherry B, Taub D, Graves MC, et al. Amyloid-β induces chemokine secretion and monocyte migration across a human blood-brain barrier model. Mol Med. 1998 Jul 1;4(7):480–9.

428. Rogers J, O'Barr S. Inflammatory Mediators in Alzheimer's Disease. In: Molecular Mechanisms of Dementia. Humana Press; 1997. p. 177–98.

429. Microchem. Permanent Epoxy Negative Photoresist processing guidelines for: SU-8 2100 and SU-8 2150.

430. Diez S. The next generation of maskless lithography. In: Douglass MR, King PS, Lee BL, editors. Emerging Digital Micromirror Device Based Systems and Applications VIII. SPIE; 2016. p. 976102.

431. Delamarche E, Juncker D, Schmid H. Microfluidics for processing surfaces and miniaturizing biological assays. Adv Mater. 2005 Dec 16;17(24):2911–33.

432. Mazutis L, Gilbert J, Ung WL, Weitz DA, Griffiths AD, Heyman JA. Single-cell analysis and sorting using droplet-based microfluidics. Nat Protoc. 2013;8(5):870–91.

433. Gervais T, El-Ali J, Günther A, Jensen KF. Flow-induced deformation of shallow microfluidic channels. Lab Chip. 2006;6(4):500–7.

434. Kim L, Vahey MD, Lee HY, Voldman J. Microfluidic arrays for logarithmically perfused embryonic stem cell culture. Lab Chip. 2006;6(3):394–406.

435. Sung JH, Shuler ML. Microtechnology for Mimicking In Vivo Tissue Environment. Ann Biomed Eng. 2012;40(6):1289–300.

436. Koo J, Kleinstreuer C. Liquid flow in microchannels: experimental observations and computational analyses of microfluidics effects. Vol. 13, INSTITUTE OF PHYSICS PUBLISHING JOURNAL OF MICROMECHANICS AND MICROENGINEERING J. Micromech. Microeng. 2003.

437. Cao Y, Gong Y, Liu L, Zhou Y, Fang X, Zhang C, et al. The use of human umbilical vein endothelial cells (HUVECs) as an *in vitro* model to assess the toxicity of nanoparticles to endothelium: a review. J Appl Toxicol. 2017 Dec 1;37(12):1359–69.

438. Walshe TE, dela Paz NG, D'Amore PA. The role of shear-induced transforming growth factor-β signaling in the endothelium. Arterioscler Thromb Vasc Biol. 2013 Nov;33(11):2608–17.

439. Baudin B, Bruneel A, Bosselut N, Vaubourdolle M. A protocol for isolation and culture of human umbilical vein endothelial cells. Nat Protoc. 2007 Mar 15;2(3):481–5.

440. Miranda-Azpiazu P, Panagiotou S, Jose G, Saha S. A novel dynamic multicellular co-culture system for studying individual blood-brain barrier cell types in brain diseases and cytotoxicity testing OPEN. Sci Rep. 2018;8(1):1–10.

441. Patabendige A, Abbott NJ. Primary Porcine Brain Microvessel Endothelial Cell Isolation and Culture. In: Current Protocols in Neuroscience. Hoboken, NJ, USA: John Wiley & Sons, Inc.; 2014. p. 3.27.1-3.27.17.

442. Tachibana H, Saito M, Tsuji K, Yamanaka K, Hoa LQ, Tamiya E. Self-propelled continuous-flow PCR in capillary-driven microfluidic device: Microfluidic behavior and DNA amplification. Sensors Actuators, B Chem. 2015;206:303–10.

443. West GB, Brown JH, Enquist BJ. A general model for the structure and allometry of plant vascular systems. Nature. 1999 Aug 12;400(6745):664–7.

444. Abràmoff MD, Magalhães PJ, Ram SJ. Image Processing with ImageJ Second Edition. Vol. 11, Biophotonics International. Laurin Publishing; 2004. 36–42 p.

445. Boudaoud A, Burian A, Borowska-Wykręt D, Uyttewaal M, Wrzalik R, Kwiatkowska D, et al. FibrilTool, an ImageJ plug-in to quantify fibrillar structures in raw microscopy images. Nat Protoc. 2014 Feb;9(2):457–63.

446. Liu Y, Peterson DA, Kimura H, Schubert D. Mechanism of Cellular 3-(4,5-Dimethylthiazol-2-yl)-2,5-Diphenyltetrazolium Bromide (MTT) Reduction. J Neurochem. 2002 Nov 18;69(2):581–93.

447. Koutsiaris AG, Tachmitzi S V., Batis N, Kotoula MG, Karabatsas CH, Tsironi E, et al. Volume flow and wall shear stress quantification in the human conjunctival capillaries and post-capillary venules in vivo. Biorheology. 2007;44(5–6):375–86.

448. Dewey CF, Bussolari SR, Gimbrone MA, Davies PF. The dynamic response of vascular endothelial cells to fluid shear stress. J Biomech Eng. 1981;103(3):177–85.

449. Saias L, Autebert J, Malaquin L, Viovy JL. Design, modeling and characterization of microfluidic architectures for high flow rate, small footprint microfluidic systems. Lab Chip. 2011 Mar 7;11(5):822–32.

450. Bell RD, Zlokovic B V. Neurovascular mechanisms and blood-brain barrier disorder in Alzheimer's disease. Acta Neuropathol. 2009;118(1):103–13.

451. Saunders NR, Ek CJ, Habgood MD, Dziegielewska KM. Barriers in the brain: a renaissance? Trends Neurosci. 2008 Jun 1;31(6):279–86.

Appendix A

Below are reported tables listing the compounds that were identified from the Venn diagrams described in Section 3.3.4.1 and were significantly different in the pairwise comparisons as stated.

Table A.1. List of compounds that were released from PDMS into the medium after 24 h and 5 days. Those compounds had increased expression ($p<0.05$, FC>2) in both the 24 h KSOM and the day 5 KSOM compared to control.*

(-)-11-hydroxy-9,10-dihydrojasmonic acid 11-beta-D-glucoside	Echitamine
(1S,2S,4R,8R)-p-Menthane-1,2,9-triol	Ethanol, 2-[2-(2-butoxyethoxy)ethoxy]-
(2E)-hexenedioylcarnitine	Fluoxymesterone
(2R,3R)-heptane-1,2,3-triol	Flupirtine
(3S,4S)-3-hydroxytetradecane-1,3,4-tricarboxylic acid	Gamma-glutamyl-L-putrescine
(4E)-6-hydroxy-1-(4-hydroxy-3-methoxyphenyl)tetradec-4-en-3-one	Glutamyltyrosine
(S)-2-Acetolactate	Glutamylvaline
(S)-3-Mercaptohexyl pentanoate	Glycerol
(S)-a-Amino-2,5-dihydro-5-oxo-4-isoxazolepropanoic acid N2-glucoside	Glycerol tripropanoate
(S)C(S)S-S-Methylcysteine sulfoxide	Hexanethioic acid S-propyl ester
(S)-Homostachydrine	Homocysteinesulfinic acid
(S1)-Methoxy-3-heptanethiol	Hydroxyprolyl-Isoleucine
1-(2-Thienyl)-1-heptanone	Indoleacetaldehyde
10-Hydroxy-8-nor-2-fenchanone glucoside	Isopropyl beta-D-glucoside
1-Aminocyclopropanecarboxylic acid	Isovalerylalanine
2-(1-Ethoxyethoxy)propanoic acid	Itaconic acid
2,3-Butanediol glucoside	L-(-)-Arabitol, permethyl-
2-Phthalimidoglutaric acid	L-Hexanoylcarnitine
3,4-Methyleneadipic acid	L-Kynurenine
3,5-Bis(trifluoromethyl)diphenylamine	Margaric acid(d3)
3''-Chloro-3''-deoxytriphasiol	Methionyl-Methionine
3-hydroxynonanoyl carnitine	Mytilin B
3-Isopropenylpentanedioic acid	N-(1-Deoxy-1-fructosyl)glycine
3-Mercapto-3-methylbutyl formate	N-(1-Deoxy-1-fructosyl)isoleucine
3-Methyl-.gamma.-butyrolactone	N-(1-Deoxy-1-fructosyl)leucine
3-O-Methyl-a-methyldopa	N-(1-Deoxy-1-fructosyl)phenylalanine
3-Oxo-1,8-octanedicarboxylic acid	N-(Carbethoxyacetyl)-4-chloro-L-tryptophan
5-Aminoorotic acid	N-.alpha.-(tert-Butoxycarbonyl)-L-Histidine
5-Geranyloxy-7-methoxycoumarin	N1,N8-Diacetylspermidine
5-Methoxytryptophan	N-Acetyldjenkolic acid
5-Nitrobarbituric acid	N-Acetyl-L-alanine
5-O-p-Coumaroylnigrumin	N-acetyltryptophan
6-(Hydroxymethyl)-2,4(1H,3H)-pteridinedione	N-Alpha-acetyllysine
6-{[3-(6,7-dimethoxy-2H-1,3-benzodioxol-5-yl)prop-2-enoyl]oxy}-3,4,5-trihydroxyoxane-2-carboxylic acid	N-Deisopropyl-fluvastatin
7-Aminoflunitrazepam	Necatorine
8-Deoxy-11,13-dihydroxygrosheimin	N-Fluorenylacetamide
	N-Heptanoylglycine
	N-Methoxyspirobrassinol
	N-Nonanoylglycine
	N-Phenylacetylglutamic acid
	O-sebacoylcarnitine
	Pentadecylic acid

8-Hydroxy-5,6-octadienoic acid	Pentaethylene glycol
9,9-dimethoxy-nonanoic acid	Pirbuterol
Acetazolamide	Prenyl glucoside
Acuminoside	Propionylcarnitine
Alfuzosin	Pterolactam
Alizapride	Pyridoxamine
Arginyl-Hydroxyproline	Pyroglutamic acid
Armillaripin	Quinaprilat
Beta-Guanidinopropionic acid	R-2-Hydroxy-3-methylbutanoic acid 3-Methy lbutanoyl
Butyl ethyl malonate	Ribothymidine
Calystegine B5	Semilepidinoside A
Carnitine-d3	Seryllysine
Casomorphin	S-Propyl 1-propanesulfinothioate
Cibulins	Succinic acid
Deoxyribose	Sufentanil
Deoxythymidine diphosphate-l-rhamnose	Sulfallate
D-glycero-L-galacto-Octulose	Swainsonine
Dibromodichloromethane	Tetraethylene glycol
Dibutyl malate	Thiiranebutanenitrile
Didesmethyl doxepin	Triethyl citrate
Diethyl oxalpropionate	Triethylene glycol
Dihydro-2,4,6-tris(2-methylpropyl)-4h-1,3,5-dithiazine	Trifluridine
Dihydroergocornine	Valyl-Valine
Dihydrolipoamide	xi-2,5-Dihydro-2,4-dimethylthiazole
Dimethicone	Zanamivir
Dimethyl sulfoxide	Zapotidine
Deoxyuridine-5'-diphosphate	

* Only compound with confidence level L2 and L3a are listed out of the 408 total compounds.

Table A.2. List of compounds absorbed by PDMS after 24 h and 5 days incubation from culture medium. Those compounds had decreased expression ($p<0.05$, FC >2) in both the 24 h KSOM and the day 5 KSOM compared to control.*

4-O-alpha-D-Galactopyranosylcalystegine B2
(2xi,6xi)-7-Methyl-3-methylene-1,2,6,7-octanetetrol
1-Isopropyl citrate
2-Methoxyestrone 3-glucuronide
Austinol
Geranyl-PP
Isoleucyl-Isoleucine
Isoleucyl-Leucine
Isoleucyl-Phenylalanine
Muramic acid
N-(1-Deoxy-1-fructosyl)alanine

* Annotation confidence level of the listed compounds: L3a and L3b.

Table A.3. List of compounds released by PDMS in medium after 5 days. Those compounds had increased expression (p<0.05, FC>2) in both the day 5 embryo culture KSOM and the day 5 KSOM compared to control.*

(-)-11-hydroxy-9,10-dihydrojasmonic acid 11-beta-D-glucoside	Ethanol, 2-[2-(2-butoxyethoxy)ethoxy]-
(2E)-hexenedioylcarnitine	Fluoxymesterone
(2R,3R)-heptane-1,2,3-triol	Flupirtine
(3S,4S)-3-hydroxytetradecane-1,3,4-tricarboxylic acid	Gamma-glutamyl-L-putrescine
(4E)-6-hydroxy-1-(4-hydroxy-3-methoxyphenyl)tetradec-4-en-3-one	Glutamyltyrosine
(S)-2-Acetolactate	Glutamylvaline
(S)-3-Mercaptohexyl pentanoate	Glycerol
(S)-a-Amino-2,5-dihydro-5-oxo-4-isoxazolepropanoic acid N2-glucoside	Glycerol tripropanoate
(S)C(S)S-S-Methylcysteine sulfoxide	Hexanethioic acid S-propyl ester
(S)-Homostachydrine	Homocysteinesulfinic acid
(S1)-Methoxy-3-heptanethiol	Hydroxyprolyl-Isoleucine
1-(2-Thienyl)-1-heptanone	Indoleacetaldehyde
1-[2-Methyl-3-(methylthio) allyl]cyclohex-2-enol	Isopropyl beta-D-glucoside
10-Hydroxy-8-nor-2-fenchanone glucoside	Isovalerylalanine
1-Aminocyclopropanecarboxylic acid	Itaconic acid
2-(1-Ethoxyethoxy)propanoic acid	L-(-)-Arabitol, permethyl-
2,3-Butanediol glucoside	L-cis-Cyclo(aspartylphenylalanyl)
2-Phthalimidoglutaric acid	L-Cystathionine
3,4-Methyleneadipic acid	L-Hexanoylcarnitine
3,5-Bis(trifluoromethyl)diphenylamine	Lipoyllysine
3''-Chloro-3''-deoxytriphasiol	L-Kynurenine
3-Hydroxymethylglutaric acid	Methionyl-Methionine
3-hydroxynonanoyl carnitine	Mytilin B
3-Isopropenylpentanedioic acid	N-(1-Deoxy-1-fructosyl)glycine
3-Mercapto-3-methylbutyl formate	N-(1-Deoxy-1-fructosyl)isoleucine
3-Methyl-.gamma.-butyrolactone	N-(1-Deoxy-1-fructosyl)leucine
3-O-Methyl-a-methyldopa	N-(1-Deoxy-1-fructosyl)phenylalanine
3-Oxo-1,8-octanedicarboxylic acid	N-.alpha.-(tert-Butoxycarbonyl)-L-Histidine
5-Geranyloxy-7-methoxycoumarin	N1,N8-Diacetylspermidine
5-Methoxytryptophan	N2-Maltulosylarginine
5-Nitrobarbituric acid	N-Acetyldjenkolic acid
5-O-p-Coumaroylnigrumin	N-Acetyl-L-alanine
6-(Hydroxymethyl)-2,4(1H,3H)-pteridinedione	N-acetyltryptophan
6-{[3-(6,7-dimethoxy-2H-1,3-benzodioxol-5-yl)prop-2-enoyl]oxy}-3,4,5-trihydroxyoxane-2-carboxylic acid	N-Alpha-acetyllysine
7-Aminoflunitrazepam	N-Deisopropyl-fluvastatin
8-Deoxy-11,13-dihydroxygrosheimin	Necatorine
8-Hydroxy-5,6-octadienoic acid	N-Fluorenylacetamide
9,9-dimethoxy-nonanoic acid	N-Heptanoylglycine
Acetazolamide	N-Methoxyspirobrassinol
Acuminoside	N-Methylethanolaminium phosphate
	N-Nonanoylglycine
	N-Phenylacetylglutamic acid
	O-sebacoylcarnitine
	Pentaethylene glycol
	Pirbuterol
	Prenyl glucoside
	Propionylcarnitine
	Pterolactam

Alfuzosin	Pyridoxamine
Alizapride	Pyroglutamic acid
alpha-Methylphenylalanine	Quinaprilat
Arginyl-Hydroxyproline	R-2-Hydroxy-3-methylbutanoic acid 3-Methylbutanoyl
Armillaripin	Ribothymidine
Beta-Guanidinopropionic acid	S-Adenosylmethionine
Butyl ethyl malonate	Seryllysine
Calystegine B5	S-Propyl 1-propanesulfinothioate
Casomorphin	Succinic acid
Cibulins	Sufentanil
Creatine	Sulfadiazine
Deoxyribose	Sulfallate
Deoxythymidine diphosphate-l-rhamnose	Swainsonine
D-glycero-L-galacto-Octulose	Tetraethylene glycol
Dibromodichloromethane	Thiiranebutanenitrile
Dibutyl malate	Toxin T2 tetrol
Didesmethyl doxepin	Triethyl citrate
Diethyl oxalpropionate	Triethylene glycol
Dihydro-2,4,6-tris(2-methylpropyl)-4h-1,3,5-dithiazine	Trifluridine
Dihydroergocornine	Tyrosyl-Tyrosine
Dihydrolipoamide	Valyl-Valine
Dimethicone	xi-2,5-Dihydro-2,4-dimethylthiazole
Dimethyl sulfoxide	Zanamivir
Deoxyuridine-5'-diphosphate	Zapotidine
Echitamine	

* Only compounds with annotation confidence level L2 and L3a are listed out of the total 433.

Table A.4. List of compounds that were absorbed by PDMS from the culture medium after 5 days. Those compounds had decreased expression ($p<0.05$, FC>2) in both the day 5 embryo culture KSOM and the day 5 KSOM compared to control.*

(2xi,6xi)-7-Methyl-3-methylene-1,2,6,7-octanetetrol
1H-Indole-3-acetamide
1-Isopropyl citrate
1-Phenyl-1,2-propanedione
2-{4-[(1E)-1,2-diphenylbut-1-en-1-yl]phenoxy}acetic acid
Austinol
Curcumin II
Cytarabine
Disperse Blue 7
Erysothiopine
Furazolidone
gamma-Glutamyl-S-methylcysteine sulfoxide
Geranyl-PP
Kinetin-9-N-glucoside
L-Agaridoxin
LMPK12020251
Muramic acid
N-(1-Deoxy-1-fructosyl)alanine
N,N-Bis(2-hydroxyethyl)-2-aminoethanesulfonic acid
N-[2-(3,4-dihydroxyphenyl)ethyl]-3-(4-hydroxy-3-methoxyphenyl)propanimidic acid

N-[2-(3,4-dimethoxyphenyl)ethyl]-3-(3-hydroxy-4-methoxyphenyl)propanimidic acid
N-Acetylgalactosamine 4-sulphate
N-desalkyludenafil
Paroxetine
TamsulosinN-(1-Deoxy-1-fructosyl)alanine

* Annotation confidence level of the listed compounds: L3a and L3b.

Table A.5. List of compounds that were released by embryos after 5 days of culture in the microfluidic device. Those compounds had decreased expression (p<0.05, FC>2) in both control and day 5 KSOM compared to day 5 embryo culture KSOM.*

(-)-11-hydroxy-9,10-dihydrojasmonic acid 11-beta-D-glucoside	Ethyl beta-D-glucopyranoside
(5-Chloro-1H-indol-2-yl)(4-methyl-1-piperazinyl)methanone	Furcelleran
(S)-Reticuline	gamma-Glutamylisoleucine
1-(2-Thienyl)-1-heptanone	gamma-Glutamylleucine
1,2-Dehydrosalsolinol	gamma-Glutamylvaline
1,7-Dimethylguanosine	Gingerenone B
1-[2-Methyl-3-(methylthio) allyl]cyclohex-2-enol	Glutamylglutamine
1-Methylinosine	Glutamylmethionine
1-Octen-3-yl glucoside	Glycerol
2-amino-4-({1-[(carboxymethyl)-C-hydroxycarbonimidoyl]-2-[(1,3-dihydroxy-1-phenylpropan-2-yl)sulfanyl]ethyl}-C-hydroxycarbonimidoyl)butanoic acid	Glycyltyrosine
2-Hydroxyfelbamate	Hydromorphone-3-glucuronide
2-Piperidinone	Hypoxanthine
3''-Chloro-3''-deoxytriphasiol	Isoleucylproline
3-Cyano-4,7-dimethylcoumarin	L-Acetylcarnitine
3-Deoxy-D-glycero-D-galacto-2-nonulosonic acid	L-Cystathionine
3-hydroxyhexanoyl carnitine	Lepidine D
3-O-Methyl-a-methyldopa	L-Formylkynurenine
3'-O-Methylguanosine	Lipoyllysine
4-{1-hydroxy-3-[4-hydroxy-2-methoxy-3-(3-methylbut-2-en-1-yl)phenyl]propyl}benzene-1,2-diol	L-Kynurenine
4-Phosphopantothenoylcysteine	L-Lysopine
5-Hydroxy-6-methoxycoumarin 7-glucoside	L-Tryptophan
5-Hydroxy-7-(4-hydroxy-3-methoxyphenyl)-1-phenyl-3-heptanone	Meglumine
5-Hydroxy-L-tryptophan	Meticillin
5-Methoxytryptophan	N-(1-Deoxy-1-fructosyl)glycine
5'-Methylthioadenosine	N,N-Bis(2-hydroxyethyl)-2-aminoethanesulfonic acid
5-O-p-Coumaroylnigrumin	N-[2-(3,4-dimethoxyphenyl)ethyl]-3-(3-hydroxy-4-methoxyphenyl)propanimidic acid
6-Hydroxyfluvastatin	N2-Maltulosylarginine
7-Aminonitrazepam	N8-Acetylspermidine
Abiraterone sulfate	N-Acetylarylamine
Acetohexamide	N-acetyltryptophan
Ajmaline	N-Decanoylglycine
Allyl thiohexanoate	N-Deisopropyl-fluvastatin
alpha-Methylphenylalanine	Neosaxitoxin
	Nepafenac
	Niacinamide
	Nigakinone
	N-m-Tolyloxyacetyl-benzenesulfonamide
	Orciprenaline
	Pantothenamide

Asymmetric dimethylarginine	Pantothenic acid
Botrydial	Penicillin G
Bumetanide	Penicillin V
Caffeoyl tyrosine	Penicilloic acid
Carisoprodol	Pirbuterol
Casomorphin	Pyridine N-oxide glucuronide
Chitotriose	Pyroglutamic acid
cis-4-Hydroxyproline	Quinaprilat
Creatine	Ribothymidine
Cycloalliin	SAICAR
Cytosine	Salbutamol 4-O-sulfate
Dehydromatricaric acid	Sulfadiazine
Deoxycytidine	Tetrapropylene glycol
Deoxythymidine diphosphate-l-rhamnose	Theobromine
D-Glucosaminic acid	Thymine
D-Glucosaminide	trans-S-(1-Propenyl)-L-cysteine
D-glycero-L-galacto-Octulose	Tyrosine methylester
Diacetone-D-galacturonic acid	Tyrosyl-Hydroxyproline
Dibromodichloromethane	Tyrosyl-Tyrosine
Divinyl sulfide	Xanthine
Echothiophate	

*Annotation confidence level of the listed compounds: L2, L3a, L3b.

Table A.6. List of compounds uptaken by embryos from culture medium after 5 days of culture in the microfluidic device. Those compounds had increased expression (p<0.05, FC>2) in both control and day 5 KSOM compared to day 5 embryo culture KSOM.*

1-Isopropyl citrate
1-Methylxanthine
2-Hydroxychlorpropamide
4-Hydroxy-4-(3-pyridyl)-butanoic acid
4-Nitro-3-(trifluoromethyl)aniline
5-Phosphoribosylamine
7-Methylxanthine
Clemastine
Furazolidone
Geranyl-PP
Muramic acid
N-(1-Deoxy-1-fructosyl)alanine
N-(4-aminobutyl)-3-(3,4-dihydroxyphenyl)propanimidic acid
N,N-Dimethylformamide
N-Acetylgalactosamine 4-sulphate
N-Acetyl-L-phenylalanine
Sinalexin
Thiomorpholine 3-carboxylate

*Annotation confidence level of the listed compounds: L3a and L3b.

Table A.7. List of compounds that were released by embryos after 5 days of culture using CM in the microfluidic device. Those compounds had increased expression (p<0.05, FC>2) in day 5 embryo culture CM, when compared to either control or day 5 CM.*

(2S)-2-amino-3-(4-hydroxy-3-methoxyphenyl)-2-methylpropanoic acid	3,4-Dihydroxy-2-hydroxymethyl-1-pyrrolidinepropanamide
(5-Chloro-1H-indol-2-yl)(4-methyl-1-piperazinyl)methanone	4-octenoylglycine
{4-[(E)-2-(2,3,5-trihydroxyphenyl)ethenyl]phenyl}oxidanesulfonic acid	5-Aminoorotic acid
2-amino-4-({1-[(carboxymethyl)-C-hydroxycarbonimidoyl]-2-{[1-hydroxy-1-(4-methoxyphenyl)-4-methyl-3-oxopentan-2-yl]sulfanyl}ethyl}-C-hydroxycarbonimidoyl)butanoic acid	5-Nitrobarbituric acid
2-amino-4-({1-[(carboxymethyl)-C-hydroxycarbonimidoyl]-2-{[1-hydroxy-1-(4-methoxyphenyl)-4-methyl-3-oxopentan-2-yl]sulfanyl}ethyl}-C-hydroxycarbonimidoyl)butanoic acid	7-Aminonitrazepam
2-Phthalimidoglutaric acid	Glutamylmethionine
3-octenoylglycine	Glutarylcarnitine
	L-Cysteinylglycine disulfide
	Lepidine D
	LysoPA(8:0/0:0)
	N-.alpha.-(tert-Butoxycarbonyl)-L-Histidine
	Pseudoecgonine
	Pyroglutamic acid
	Retrofractamide D
	Ribothymidine
	Tetrapropylene glycol
	Xanthine

* Annotation confidence level of the listed compounds: L3a, L3b.

Table A.8. List of increased compounds (p<0.05, FC>2) unique to the pairwise comparison between day 5 embryo culture CM and day 5 embryo culture KSOM.

Clemastine	Sulfamerazine
4-(Dimethylamino)azobenzene n-oxide	3-octenoylglycine
2-(4-Chlorophenyl)-3-methylbutyric acid, 1,1,1,3,3,3-hexafluoro-2-propyl ester	(Â±)-2-Methylthiazolidine
Thiomorpholine 3-carboxylate	Cytidine 2'-phosphate
Mimosine	1-Isopropyl citrate
S-Adenosylmethionine	F-Amidine
5-Hydroxy-L-tryptophan	4-octenoylglycine
4-Hydroxy-4-(3-pyridyl)-butanoic acid	Acetyl tributyl citrate
N-Acetylgalactosamine 4-sulphate	(S)-10,16-Dihydroxyhexadecanoic acid
5-Phosphoribosylamine	7-Methylxanthine
Furazolidone	13,14-dihydroxy-octadecanoic acid
N,N-Dimethylformamide	Tuberostemonone
N-Acetylgalactosamine 4-sulphate	

Table A.9. List of decreased compounds (p<0.05, FC>2) unique to the pairwise comparison between day 5 embryo culture CM and day 5 embryo culture KSOM.

	L-cis-Cyclo(aspartylphenylalanyl)
Prolyl-Tryptophan	Pro Lys Asn
L-Carnitine	Phaseolic acid
N-(1-Deoxy-1-fructosyl)glycine	D-Glucosaminide
Divinyl sulfide	Dodecanoic acid
Glutamylmethionine	Quinaprilat
Glutamyltyrosine	Phe Tyr Val
9-Methylxanthine	alpha-Fluoro-beta-ureidopropionic acid
N5-Carboxyaminoimidazole ribonucleotide	DL-Phenylalanine
N-Acetyldjenkolic acid	Polypropylene glycol
1-(sn-Glycero-3-phospho)-1D-myo-inositol	Penicilloic acid
trans-S-(1-Propenyl)-L-cysteine	Ala Ala Ile
Theobromine	Tripropylene glycol

N,N-Bis(2-hydroxyethyl)-2-aminoethanesulfonic acid	Lipoyllysine Sulfinpyrazone sulphide

Appendix B

Below are reported tables listing the compounds that were identified from the Venn diagrams described in Section 3.3.4.2 and were significantly different in the pairwise comparisons as stated.

Table B.1. List of compounds that were increased in spent media collected from culture microdrops and associated with the culture environment. Those compounds had increased expression ($p<0.05$, FC>2) in both the day 4 embryo culture KSOM and the day 4 KSOM compared to control.*

(2R*,3R*)-1,2,3-Butanetriol	Cycloalliin
(S)C(S)S-S-Methylcysteine sulfoxide	Dimethylallylpyrophosphate
(Z)-1-(Methylthio)-5-phenyl-1-penten-3-yne	Eriobofuran
1-(4-Fluorobenzyl) piperazine	Ethyl beta-D-glucopyranoside
1-(4-hydroxyphenyl)-7-phenylheptane-3,5-dione	Flavoxate
1-Aminocyclopropanecarboxylic acid	Glutamyltyrosine
1-Octen-3-yl glucoside	Histidinyl-Hydroxyproline
1,2,3-Tris(1-ethoxyethoxy)propane	Isogemichalcone B
1,9-Nonanedithiol	Isoginkgetin
18-Carboxy-dinor-LTE4	Lanthionine ketimine
2-hydroxymethylolanzapine	Mevalonic acid
3-Carbamoyl-2-phenylpropionic acid	N-Acetyl-L-methionine
3-Deaza-2'-deoxyadenosine	N-Acetyldjenkolic acid
3b,8b-Dihydroxy-6b-(3-chloro-2-hydroxy-2-methylbutanoyloxy)-7(11)-eremophilen-12,8-olide	N-Caffeoyltryptophan
	N-Deisopropyl-fluvastatin
	Nb-Feruloyltryptamine
	o-succinyl-l-homoserine-34
4-Ethyl-2-methylthiazole	Pantoyllactone glucoside
4,8 Dimethylnonanoyl carnitine	Parvisoflavone A
5-O-p-Coumaroylnigrumin	Penicilloic acid
5-Oxoprolinate	Phentolamine
Acetohexamide	Phenylacetylglycine
Acetylpterosin C	Phlorin
Arginyl-Glycine	Pinocembrin 7-apiosyl-(1->5)-apiosyl-(1->2)-glucoside
Arginyl-Lysine	Polypropylene glycol (m w 1,200-3,000)
Arginyl-Tyrosine	Pyroglutamic acid
Aspartylphenylalanine	Ribothymidine
Avenanthramide C	S-Allylcysteine
Botrydial	Saccharopine
Chrycorin	Salbutamol 4-O-sulfate
Cilastatin	Talaromycin A
cis-2-Methylaconitate	Theaflavin
Citreoviridin C	Tryptophyl-Gamma-glutamate
Creatine	Tyramine glucuronide

* Annotation confidence level of the listed compounds: L3a, L3b.

Table B.2. List of compounds that were decreased in spent media collected from culture microdrops and associated with the culture environment. Those compounds had increased expression (p<0.05, FC>2) in both the day 4 embryo culture KSOM and the day 4 KSOM compared to control.*

(1alpha,2alpha,4betaH,6alpha,8R)-p-Menthane-2,6,8,9-tetrol	Melleolide
4,5-Dimethylthiazole	Meticillin
Aspartylphenylalanine	Muramic acid
Citpressine II	N-Deisopropyl-fluvastatin
Cycloalliin	Penicillin G
Deoxyadenosine	Penicillin V
Fluconazole	Phenylacetylglycine
Glu Thr Gly 13696	Pranlukast 25682
Glucotropaeolin	prednisolone-16alpha-carboxylic acid
Glutamyllysine	Semilicoisoflavone B
Glycodiazine	Sulfametopyrazine
Isogingerenone B	Threoninyl-Histidine
L-Galacto-2-heptulose	Trimeprazine
L-Tyrosine	

* Annotation confidence level of the listed compounds: L3a, L3b.

Table B.3. List of compounds that were released by embryos after 4 days of culture in KSOM microdrops. Those compounds had decreased expression (p<0.05, FC>2) in both control and day 4 KSOM compared to day 4 embryo culture KSOM.*

(9xi,10xi,12xi)-9,10-Dihydroxy-12-octadecenoic acid	Creatine
1-Methylinosine	Cytosine
1,2,3,4-Tetrahydro-b-carboline-1,3-dicarboxylic acid	Deoxycytidine
15(R)-hydroperoxy-EPE	Gancaonin A
2-Methoxy-3-methyl-9H-carbazole	Homolanthionine
3,4,5-trihydroxy-6-[(2-methylpropanoyl)oxy]oxane-2-carboxylic acid	Hydroxyprolyl-Threonine
3'-O-Methylguanosine	Hypoxanthine
5'-Methylthioadenosine	Indanone
Alpha-Lactose	L-2-Amino-3-(oxalylamino)propanoic acid
alpha-Methylphenylalanine	L-Proline
Carisoprodol	Leucyl-Leucine
	Niacinamide
	Ornithine
	Parvisoflavone A
	Valyl-Isoleucine

* Annotation confidence level of the listed compounds: L2, L3a, L3b.

Table B.4. List of compounds released into the culture medium by embryos after 4 days of culture in CM microdrops. Those compounds had increased expression in day 4 embryo culture CM, when compared to either control or day 4 CM.*

4,8 Dimethylnonanoyl carnitine	N-(1-Deoxy-1-fructosyl)phenylalanine
5-Hydroxy-L-tryptophan	N-(1-Deoxy-1-fructosyl)tyrosine
Alpha-Lactose	N-(1-Deoxy-1-fructosyl)valine
alpha-Methylphenylalanine	Neosaxitoxin
Carisoprodol	O-succinyl-L-homoserine
Cys Phe Ser	Ornithine

Hydroxytyrosol 1-O-glucoside	Pro Pro Ser
L-2-Amino-3-(oxalylamino)propanoic acid	Tetrahydropentoxyline
N-(1-Deoxy-1-fructosyl)leucine	Val Pro Val 4198
N-(1-Deoxy-1-fructosyl)methionine	

* Annotation confidence level of the listed compounds: L2, L3a, L3b.